V. 122, NO. 4
JULY 2025

ACI MATERIALS JOURNAL

A JOURNAL OF THE AMERICAN CONCRETE INSTITUTE

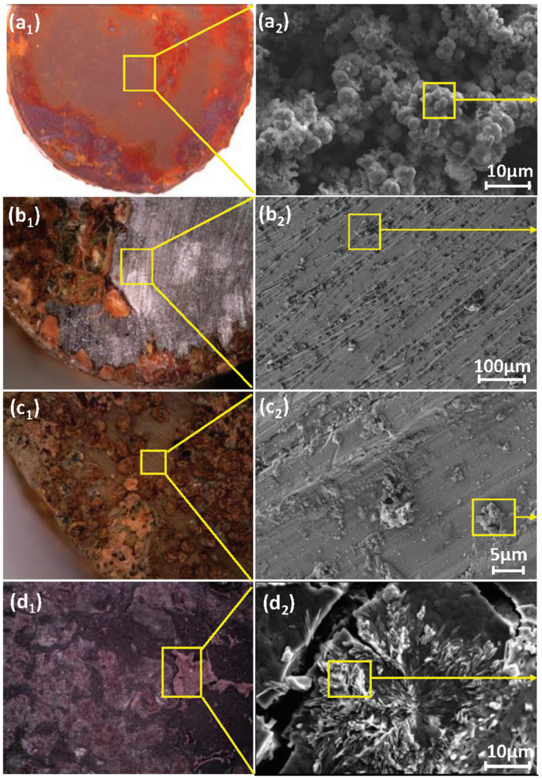

Element	Atomic %	Element	Atomic %
Fe	45.72%	K	1.32
C	7.58%	Na	1.35
O	42.47%	Cl	1.56

Element	Atomic %	Element	Atomic %
Fe	22.4	K	3.32
C	29.24	Na	2.52
O	42.19	Cl	0.33

Element	Atomic %	Element	Atomic %
Fe	20.4	K	4.98
C	31.11	Na	5.20
O	38.25	Cl	0.06

Element	Atomic %	Element	Atomic %
Fe	1.09	K	5.90
C	11.29	Na	23.12
O	58.22	Cl	0.38

American Concrete Institute

CONTENTS

Editorial Board

Shiho Kawashima, Editor-in-Chief,
Columbia University
Liberato Ferrara,
Polytechnic University of Milan
Raissa Ferron,
The University of Texas at Austin
O. Burkan Isgor,
Oregon State University
Prannoy Suraneni,
University of Miami

Board of Direction

President
Maria Juenger

Vice Presidents
Scott M. Anderson
Matthew R. Sherman

Directors
Michael Ahern
Corina-Maria Aldea
Oscar R. Antommattei
Peter Barlow
Arturo Gaytan Covarrubias
James H. Hanson
Carol Hayek
Werner K. Hellmer
Mary Beth Diesz Hueste
Kimberly Waggle Kramer
Enrique Pasquel
Xiomara Sapón-Roldán

Past President Board Members
Charles K. Nmai
Antonio Nanni
Michael J. Paul

Executive Vice President
Frederick H. Grubbe

Staff

Publisher
John C. Glumb

Senior Managing Director of Technical Operations
Michael L. Tholen

Engineers
Will J. Gold
Matthew R. Senecal
Michael L. Tholen
Gregory M. Zeisler

Managing Editor
Lauren E. Mentz

Associate Editor
Kimberly K. Olesky

Editors
Erin N. Azzopardi
Lauren C. Brown
Kaitlyn J. Dobberteen
Tiesha Elam
Angela R. Noelker
Kelli R. Slayden

ACI MATERIALS JOURNAL

JULY 2025, V. 122, NO. 4

A JOURNAL OF THE AMERICAN CONCRETE INSTITUTE
AN INTERNATIONAL TECHNICAL SOCIETY

ACI Materials Journal
© 2025 American Concrete Institute. All rights reserved.

This material may not be reproduced or copied, in whole or in part, in any form or by any means, including making copies by any photo process, or by electronic or mechanical device, printed, written, graphic, or oral, or recording for sound or visual reproduction for use in any knowledge or retrieval system or device, without the written consent of ACI. This material may not be used by data mining, robots, screen scraping, or similar data gathering and extraction tools such as artificial intelligence ("AI") for purposes of developing or training a machine learning or AI model, conducting computer analysis or creating derivatives of this material, without the written consent of ACI.

American Concrete Institute®, ACI®, Always Advancing®, *ACI Structural Journal*®, and *ACI Materials Journal*® are registered trademarks of American Concrete Institute.

The *ACI Materials Journal* (ISSN 0889-325x) is published bimonthly by the American Concrete Institute. Publication office: 38800 Country Club Drive, Farmington Hills, MI 48331. Periodicals postage paid at Farmington, MI, and at additional mailing offices. Subscription rates: $210 per year, payable in advance. POSTMASTER: Send address changes to: *ACI Materials Journal*, 38800 Country Club Drive, Farmington Hills, MI 48331.

Canadian GST: R 1226213149.

Direct correspondence to 38800 Country Club Drive, Farmington Hills, MI 48331. Telephone: +1.248.848.3700.
Website: http://www.concrete.org.

MEETINGS

AUGUST 2025

10-13—4th International Conference on Sustainable Building Materials (ICSBM 2025), Eindhoven, the Netherlands, https://susbuildmat.com

10-15—28th International Conference on Structural Mechanics in Reactor Technology (SMiRT28), Toronto, ON, Canada, https://smirt28.com

12-14—ACI Foundation 2025 Concrete Innovation Forum, Denver, CO, www.acifoundation.org/technology/forums.aspx

24-29—79th RILEM Annual Week and the International Conference on Advances in Engineering and Technology for Sustainable Development (ICONS 2025), Hanoi, Vietnam, https://rilemweek2025.sciencesconf.org/?lang=en

SEPTEMBER 2025

7-10—Concrete Institute of Australia's Biennial National Conference, Concrete 2025, Adelaide, SA, Australia, https://ciaconference.com.au

10-13—ASCC Annual Conference 2025, Indianapolis, IN, https://ascconline.org/events

11-12—2nd International RILEM Conference on Early-Age and Long-Term Cracking in RC Structures (CRC2025), Katowice, Poland, https://crc2025.org

15-16—44th Cement & Concrete Science Conference, Leeds, UK, www.iom3.org/events-awards/44th-cement-concrete-science-conference.html

15-19—19th World Conference on Seismic Isolation, Energy Dissipation and Active Vibration Control of Structures (19WCSI), Berkeley, CA, https://19wcsi.org

16-18—3rd International Workshop on Durability and Sustainability of Concrete Structures (DSCS 2025), Naples, Italy, www.rilem.net/agenda/3rd-international-workshop-ondurability-and-sustainability-of-concrete-structuresdscs-2025-1613

16-20—2025 PCI Committee Days, Rosemont, IL, www.pci.org/CommitteeDays

18-19—6th Ibero-American Congress on Special Concretes – Concrete and Sustainability (HACBAC2025), Faro, Portugal, https://hacbac2025.ualg.pt/en

26-29—APA 2025 Annual Convention, Austin, TX, www.archprecast.org/2025-convention

ACI CONCRETE CONVENTION: FUTURE DATES

2025—Oct. 26-29, Hilton Baltimore & Baltimore Marriott Inner Harbor, Baltimore, MD
2026—Mar. 29-Apr. 1, Hyatt Regency O'Hare Chicago, Rosemont/Chicago, IL
2026—Oct. 11-14, Hilton Atlanta, Atlanta, GA
2027—Mar. 21-24, Caesars Palace Las Vegas, Las Vegas, NV

For additional information, contact:
Event Services, ACI
38800 Country Club Drive
Farmington Hills, MI 48331
Telephone: +1.248.848.3795
email: conventions@concrete.org

ON FRONT COVER: 122-M22, p. 33, Fig. 4—Optical microscopy images of: (a1) control (inhibitor-free); (b1) 4-Aminobenzoic acid (ABA); (c1) 2-Aminopyridine (AP); and (d1) Salicylaldehyde (SA); and scanning electron microscopy (SEM) images with energy-dispersive X-ray spectroscopy (EDX) results of: (a2) control (inhibitor-free); (b2) ABA; (c2) AP; and (d2) SA admixed in pore solution.

Papers appearing in the *ACI Materials Journal* are reviewed according to the Institute's Publication Policy by individual experts in the subject area of the papers.

Contributions to *ACI Materials Journal*

The *ACI Materials Journal* is an open forum on concrete technology and papers related to this field are always welcome. All material submitted for possible publication must meet the requirements of the "American Concrete Institute Publication Policy" and "Author Guidelines and Submission Procedures." Prospective authors should request a copy of the Policy and Guidelines from ACI or visit ACI's website at **www.concrete.org** prior to submitting contributions.

Papers reporting research must include a statement indicating the significance of the research.

The Institute reserves the right to return, without review, contributions not meeting the requirements of the Publication Policy.

All materials conforming to the Policy requirements will be reviewed for editorial quality and technical content, and every effort will be made to put all acceptable papers into the information channel. However, potentially good papers may be returned to authors when it is not possible to publish them in a reasonable time.

Discussion

All technical material appearing in the *ACI Materials Journal* may be discussed. If the discussion is received within four months of the paper's print publication, it will appear in the issue dated ten months from this journal's date. Discussion material received after specified dates will be considered individually for publication or private response. ACI Standards published in ACI Journals for public comment have discussion due dates printed with the Standard. Discussion should be complete and ready for publication, including finished, reproducible illustrations. Discussion must be confined to the scope of the paper and meet the ACI Publication Policy.

Follow the style of the current issue. Discussions should not exceed 1800-word equivalents (illustrations and tables count as 300 words each). References should be complete. Do not repeat references cited in original paper; cite them by original number. Numbering of additional references, figures, tables, and equations should follow sequentially from the original manuscript throughout the discussion. The discusser must indicate the month, year, volume number, issue number, authors' names, and manuscript number of the original manuscript. Closures responding to a single discussion should not exceed 1800-word equivalents in length, and to multiple discussions, approximately one half of the combined lengths of all discussions. Closures are published together with the discussions.

Discuss the paper, not some new or outside work on the same subject. Use references wherever possible instead of repeating available information.

Discussion offered for publication should offer some benefit to the general reader. Discussion which does not meet this requirement will be returned or referred to the author for private reply.

Send manuscripts to:
http://mc.manuscriptcentral.com/aci

Send discussions to:
Journals.manuscripts@concrete.org

ACI MATERIALS JOURNAL TECHNICAL PAPER

Title No. 122-M20

Influence of Different Factors on Thermal Behavior of Permeable Concrete Pavement

by Chaoguo Wu, Xudong Chen, Chen Chen, Tao Ji, and Chang Jin

Pavement hardening has a significant impact on urban ecological environments and intensifies urban heat island (UHI) effect, and permeable pavement is considered an effective solution to alleviate UHI effect. However, the evaluation of solar evaporative cooling performance is still controversial after use. It is necessary to study the influence of different factors on the thermal performance of permeable concrete pavement. The indoor simulation test results show that in the cycle of simulated heating and cooling, permeable pavement with large aggregate particle size has a greater impact on the near-surface thermal environment. The air temperature near the surface of dry permeable concrete is higher, and the increase of water content can exert the evaporative cooling effect to a greater extent. Compared with changing the aggregate particle size of the structural layer, the addition of a sand layer has a certain impact. Changing the surface color of the test specimen has a great effect on the reflectivity of the pavement, delaying the rise of the surface temperature and the vertical transfer of heat radiation.

Keywords: evaporative cooling; indoor simulation experiments; pavement temperature; permeable concrete pavement; thermal behaviors.

INTRODUCTION

In the process of rapid urbanization, more and more natural soil is replaced by concrete pavement, and traditional concrete pavement has characteristics of high density and high heat capacity.[1-3] It absorbs more solar radiation than natural soil under the same conditions. At the same time, its evaporative cooling effect cannot be compared with natural soil, so it is one of the main causes of urban heat island (UHI) effect.[4-7] The evaporative cooling effect of permeable concrete pavement is an effective solution to alleviate UHI effect. Research on the mechanical and permeable properties of permeable concrete has been carried out and some achievements have been made. The strength of permeable concrete mainly comes from the mutual extrusion of aggregates and bonding of cementitious materials.[8-11] Compared with ordinary concrete, the mechanical properties and durability have become important factors restricting the development of permeable concrete. Therefore, many scholars have focused on the mechanical properties, mixture ratio design, molding process, and permeable properties of permeable concrete,[12-18] while the mechanism of alleviating UHI effect of permeable concrete has been studied relatively late.

At present, there has been much research on the influence of permeable pavement on heat island effect. Among them, Santamouris[19] summarized the influence of external environment (solar radiation, convective heat transfer coefficient, air humidity, and temperature) and the material itself (thermal conductivity and specific heat capacity) on the surface temperature of permeable pavement. Liu et al.[20] found that compared with traditional permeable pavement, capillary evaporation enhanced pavement can effectively use the capillary effect to transfer deeper water to the road surface for evaporation and extend the cooling time. Chen et al.[21] added materials such as iron powder to permeable paving surface materials to increase their thermal conductivity. The test results showed that the temperature could be reduced by 1 to 3°C compared to the traditional permeable concrete. Asaeda and Ca[22] proposed a one-dimensional heat and humidity transfer model of a permeable pavement structure to analyze the relationship between surface temperature and heat balance of the structure under different porosities. This was done to understand the thermal performance of permeable pavement. Similarly, Garcia et al.[23] used infrared lamps to simulate solar radiation and measured the changes of surface and bottom surface temperature, heat flow, and evaporation rate of asphalt mixtures with different porosities under the irradiation of infrared lamps indoors. In actual working conditions, affected by the water-bearing characteristics of permeable pavement surface materials, the evaporative cooling effects of various permeable pavement are also different.[24] Nemirovsky et al.[25] tested the effect of the water level of the structural layer at four depths of 0, 25, 76, and 152 mm on evaporation and cooling through the indoor simulation test. The results showed that the water at a depth of 152 mm could hardly maintain a certain evaporation and cooling effect, and an aboveground water supply was still needed to ensure a certain evaporation rate. The moisture near the surface can maintain a certain evaporative cooling effect. Syrrakou and Pinder[26] conducted scale tests on common permeable concrete pavement structures with polyvinyl chloride (PVC) pipes and found that the maximum evaporation rate could reach 0.0216 mm/h and gradually decreased to zero with the decrease of water content. Liu et al.[20] invented a new permeable pavement structure: by inserting a capillary column capable of absorbing water, the water at the bottom of the structural layer is raised to the surface layer by capillary force for rapid evaporation. The results showed that compared with traditional permeable pavement, this type of pavement can reduce the temperature by up to 9.4°C and can continue to reduce the temperature

---

ACI Materials Journal, V. 122, No. 4, July 2025.
MS No. M-2023-177.R1, doi: 10.14359/51746812, received March 27, 2024, and reviewed under Institute publication policies. Pertinent discussion including author's closure, if any, will be published ten months from this journal's date if the discussion is received within four months of the paper's print publication.

Table 1—Cement performance indicators

Density, g/cm^3	Condensation time, h:min		Flexural strength, MPa		Compressive strength, MPa	
	First condensation	Final condensation	3 days	28 days	3 days	28 days
3.05	2:45	3:50	4.7	7.8	18	≥42.5

Table 2—Coarse aggregates technical index

Crushing value	Dust content	Elongated and flaky particle content	Maximum particle size
≤30%	≤1%	≤15%	≤Two-thirds of layer thickness

for up to 7 days in sunny summer weather. Doulos et al.[27] tested the thermal behavior of 93 kinds of pavement materials and found that the thermal behavior was mainly determined by the surface reflectivity. For example, the rougher the surface, the darker the color of the tile, which would absorb more solar radiation. Li et al.[28] tested the reflectance of permeable concrete brick pavement, asphalt pavement, and concrete pavement outdoors and found that the reflectance of the pavement surface material measured fluctuated up and down, but was not fixed, which was greatly related to the roughness of the material and the angle of the sun incident. Li et al.[28-31] conducted a series of indoor and field studies on the thermal behavior of permeable concrete pavement and its influence on the surrounding environment under various conditions.

This paper studies the influence of different factors on the thermal behavior and cooling performance of permeable concrete pavement through indoor simulation tests, analyzing the influence of test material aggregate particle size, moisture content, pavement structure, and surface color on the temperature of permeable concrete pavement, and the measured air temperature near the surface of the specimen and temperature at different depths inside the specimen during the heating and cooling cycle. The thermal energy change of the specimen was calculated to evaluate the effect of different factors on the cooling and cooling effect of permeable pavement, which provided help for the subsequent qualitative and quantitative evaluation of the thermal impact of permeable pavement on the surrounding environment under different factors.

RESEARCH SIGNIFICANCE

With the development of urbanization and the transportation industry, permeable pavements have been identified by the U.S. Environmental Protection Agency (EPA) as one of the solutions to mitigate the heat island effect. At present, studies on the influence of permeable concrete's thermal behavior focus mainly on pavement materials and meteorological factors. The study of the influence of aggregate particle size, moisture content, pavement structure, and surface color on the thermal behavior of permeable pavement is helpful to deepen the understanding of the thermal effect of permeable pavement on the surrounding environment and provide a reference for its practical application.

Table 3—Permeable concrete mixture ratio, kg/m^3

Cement	Aggregate	Silica fume	Water	Water-reducing agent
435	1549	23	138	2

EXPERIMENTAL INVESTIGATION

Materials

To analyze the influence of different factors on the thermal performance of permeable concrete pavement, silicate cement, silica fume, macadam, water, and high-range water-reducing admixture (HRWRA) were used to prepare permeable concrete, in which P.O 42.5 ordinary silicate cement was used for cement (detailed index as shown in Table 1), the silica fume particle size was 0.1 to 0.3 μm, burning loss was 6%, crushed stone was used as coarse aggregate, particle size range was 5 to 20 mm (detailed index is shown in Table 2), laboratory tap water was used, admixture was a polycarboxylic acid HRWRA, and the water-reducing rate was 37%. The mixture ratio of permeable concrete is shown in Table 3.

Test protocol and specimen preparation

Aggregate particle size is a key factor affecting the porosity and pore state of permeable concrete, and water content affects the size of evaporation resistance, which plays an important role in evaporative cooling. Reasonable pavement structures can not only enable water to penetrate the lower layer smoothly, but also enable part of the water to be preserved in the surface material for evaporative cooling. The reflectivity is greatly affected by the color of the surface material, which has a significant effect on the evaporative cooling effect. To study the thermal performance of permeable concrete pavement with different parameter configurations, four variables of aggregate particle size, moisture content, pavement structure, and surface color were set up in this paper, and the influence of each variable was investigated and comprehensively analyzed. Among them, the aggregate size ranges were 5 to 10 mm, 10 to 15 mm, and 15 to 20 mm, and the water contents were 0%, 16.3%, and 25.9%, respectively. The pavement structures were divided into three distinct categories: 1) single-layer pervious concrete; 2) double-layer pervious concrete consisting of an upper layer with 10 to 15 mm aggregates and a lower layer with 20 to 25 mm aggregates; and 3) double-layer with sand pervious concrete comprising an upper layer with 10 to 15 mm aggregates and a lower sand subbase. There were three surface colors: natural color, red, and blue, of which red and blue were achieved with spray paint. The test scheme and specimen numbers are shown in Table 4.

To study the influence of different factors on the cooling effect of permeable concrete pavement, permeable concrete specimens with a size of 300 x 180 x 140 mm were formed according to the mixture ratio in Table 3. A foam box with

Table 4—Test protocol and test piece number

Group	Aggregate size, mm	Water content, %	Pavement structure	Surface color	Specimen number
A	5 to 10	0	Single layer	Natural color	A1
	10 to 15	0	Single layer	Natural color	A2
	15 to 20	0	Single layer	Natural color	A3
W	10 to 15	0	Single layer	Natural color	W1
	10 to 15	16.3	Single layer	Natural color	W2
	10 to 15	25.9	Single layer	Natural color	W3
P	10 to 15	0	Single layer	Natural color	P1
	10 to 15	0	Double layer	Natural color	P2
	10 to 15	0	Double layer with sand	Natural color	P3
C	10 to 15	0	Single layer	Natural color	C1
	10 to 15	0	Single layer	Red	C2
	10 to 15	0	Single layer	Blue	C3

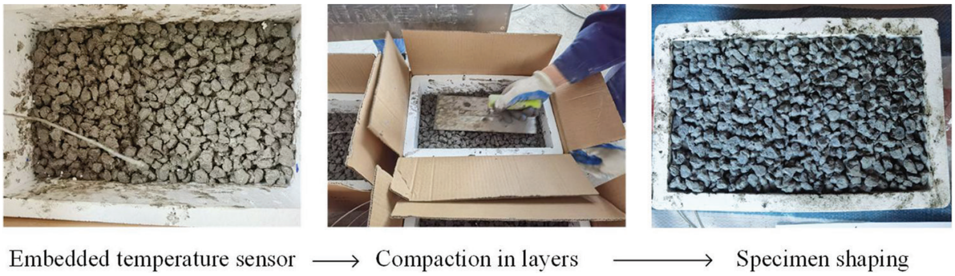

Fig. 1—Test piece fabrication process.

the same inner size was used as the template, and three calibrated temperature sensors were embedded in the foam box in advance for measuring the internal temperature of the specimen during the test. The mixture was divided into three layers and injected into the foam box for layered compaction. After forming, it was covered with plastic film and foam cover for curing until the test began; the production process is shown in Fig. 1.

Test method

In this paper, indoor simulation testing is used to study the thermal performance of permeable pavement under different factors. The simulation test was carried out in a closed chamber. A tungsten iodide lamp light source placed on the surface of the specimen at a certain height was used as a heat source, and it was assumed that the light source uniformly radiated on the surface of the specimen to simulate solar radiation, as shown in Fig. 2.

Fig. 2—Indoor heat source: tungsten iodine lamp.

The simulated thermal radiation test device in this paper is shown in Fig. 3. K-type temperature sensors were placed at 10, 70, and 130 mm below the upper layer of permeable concrete to measure the internal temperature of the specimen. The numbers are 1, 2, and 3, respectively, and the measuring range is –100°C to 1000°C. The gap between the temperature sensor and the foam box was sealed with silicone to prevent the temperature sensor reading from external temperature interference. Another K-type temperature sensor was placed 35 mm above the specimen surface to measure the near-surface air temperature above the specimen. The four temperature sensors were connected to the temperature tester by 250°C high-temperature-resistant wire and a multichannel temperature tester for temperature acquisition. The test was divided into heating and heating stages and cooling and cooling stages. In the heating and heating stage, the tungsten iodide lamp light source was irradiated and the heat source was turned off after 5 hours to cool the specimen to room temperature (approximately 12 hours). Through the cycle of heating for 5 hours and cooling for 12 hours, the changes of air temperature in different positions inside the specimen and near the surface above the specimen were recorded and observed. The data acquisition system began to work after the test began, and the temperature acquisition

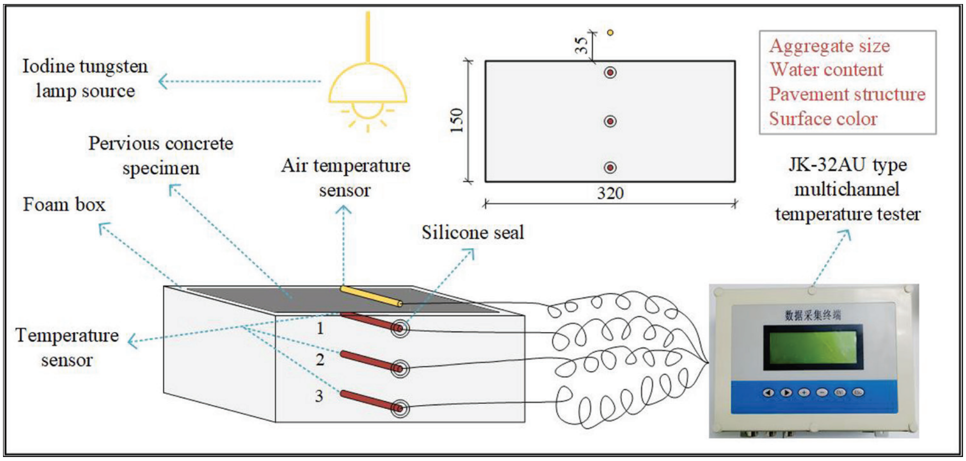

Fig. 3—Simulated thermal radiation test device diagram.

instrument collected the temperature changes during the test in real time.

EXPERIMENTAL RESULTS AND DISCUSSION

Temperature change under thermal radiation

The plotting interval of all the analysis graphs in this paper was 0 to 20 hours, including heating for 5 hours and cooling for 12 hours. Considering that the temperature change of some specimens was not stable after 17 hours, 20 hours was taken as the entire test and plotting interval, as shown in Fig. 4. It can be seen from the results of the indoor simulation test that the temperature changes of all specimens under simulated thermal radiation are reflected. The temperature change trend in different locations of the four groups of specimens was basically the same. The temperature gradually rose after the heating began, and the rate gradually decreased after the heating reached a certain stage. The temperature continued to rise for half an hour after the heating ended (5 hours). It then entered the cooling phase, where the temperature dropped rapidly to the same level as before heating in approximately 12 hours.

Aggregate size—Figure 5 shows the temperature change of each aggregate particle size group under simulated thermal radiation. The aggregate size affects the temperature of the surface, interior, and bottom of the specimen. Under the same circumstances, the temperature rise rate of the A2 specimen (10 to 15 mm) was the fastest, followed by A3 (15 to 20 mm), and finally A1 (5 to 10 mm). Among them, the porosity of A1 was 21.08%, A2 was 30.65%, and A3 was 32.24%, which does not completely follow the order of aggregate particle size thickness, indicating that the aggregate particle size has other effects on the road surface temperature and should be considered when designing the mixture ratio. After 5 hours of thermal radiation, the maximum temperature of A2 was approximately 20.1% and 39.8% higher than that of A3 and A1. In the cooling and cooling stage, A3 had the fastest cooling rate. Under simulated thermal radiation, the large-diameter permeable concrete specimen had the characteristics of fast heating, fast cooling, and poor thermal insulation. In the actual project, the permeable pavement absorbed more heat under the light, and the surface temperature was often higher than that of the ordinary pavement. When night comes, thanks to the porous skeleton structure, the permeable pavement quickly releases heat outward, and the pavement temperature is also reduced. In the range of 5 to 20 mm particle size, the temperature change rate of the specimen with large aggregate particle size was faster than that of the specimen with small aggregate particle size, and the characteristics of rapid heat conduction were more prominent.

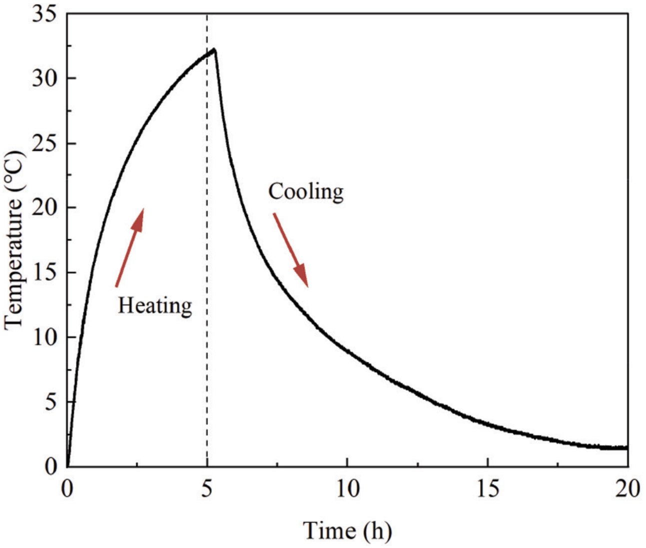

Fig. 4—Temperature change diagram.

Water content—Figure 6 shows the temperature change of the specimen in each water content group under simulated thermal radiation. The moisture content plays an important role in the temperature changes on the surface and inside the specimen. Under the same circumstances, the W1 specimen had the fastest heating rate (0%), followed by W2 (16.3%), and finally W3 (25.9%). After 5 hours of thermal radiation, the maximum temperature of W1 was approximately 21.4% and 36.9% higher than that of W2 and W3. In addition, the surface temperature of W2 was slightly higher than that of W3, and the surface temperature of W1 was significantly higher than that of other specimens at any time. With the increase of water content, the surface temperature of permeable pavement can be significantly reduced. By observing the surface heating rate of each specimen during the heating

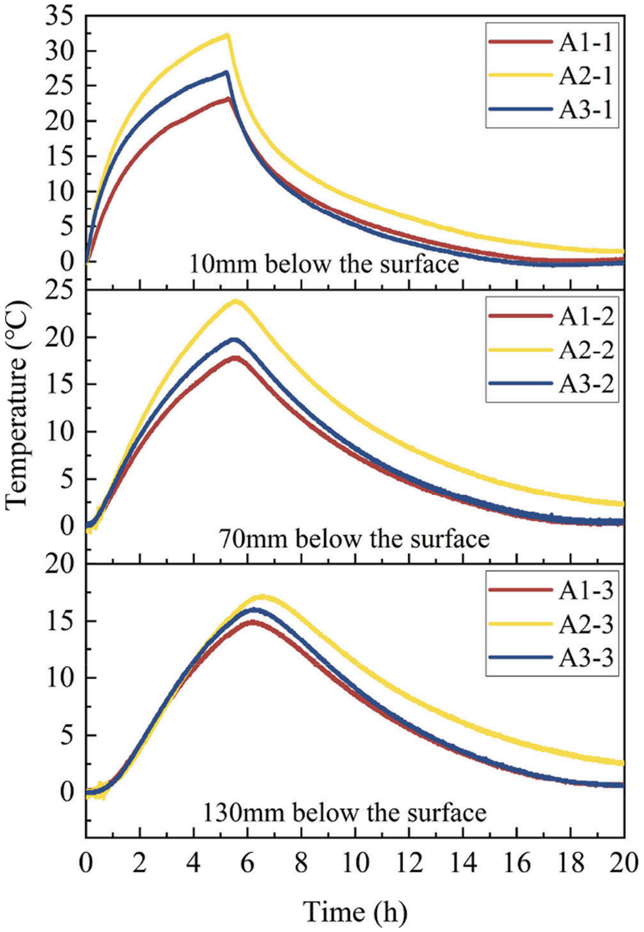

Fig. 5—Temperature change of specimens under action of simulated thermal radiation (aggregate size).

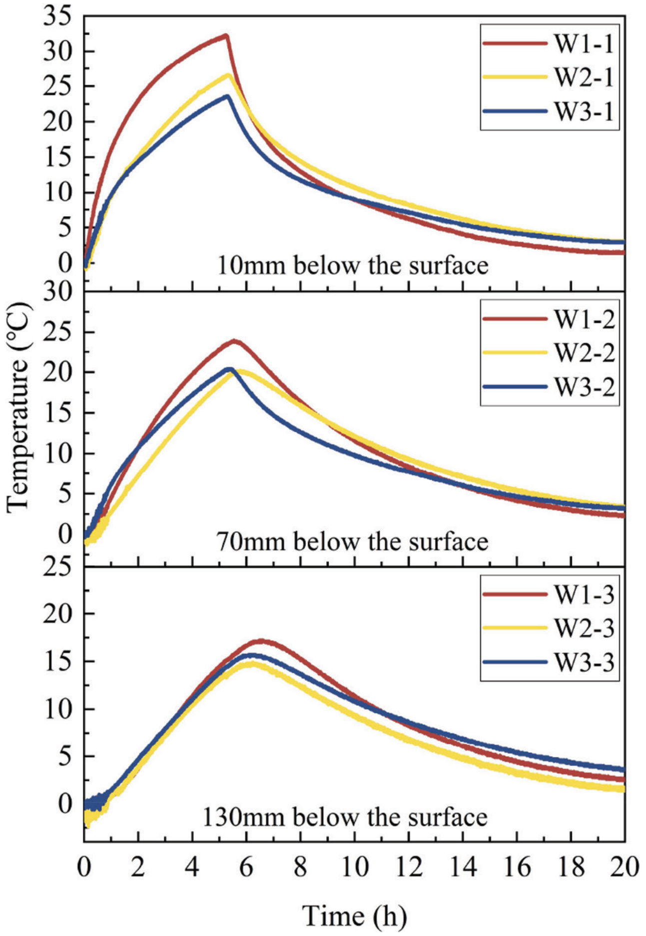

Fig. 6—Temperature change of specimens under action of simulated thermal radiation (water content).

stage, it was found that increasing water content can also significantly change the temperature change rate—that is, reducing the heating rate and increasing the cooling rate. Wang et al.[32] found that increasing the internal moisture content of pavement can effectively improve the evaporation intensity, but there is a time limit of approximately 8 hours, leading the enhancement effect to gradually weaken to a low level. However, the evaporation intensity of permeable pavement can be improved by replenishment of surface water.[33] As shown in Fig. 6, the drop rate of surface temperature of W2 and W3 showed a slow trend after 8 hours, which was significantly lower than the initial cooling stage, and even lower than that of the W1 specimen.

Pavement structure—Figure 7 shows the temperature change of the pavement structure group specimens under simulated thermal radiation. The pavement structure affects the temperature of the surface, interior, and bottom of the specimen. Under the same circumstances, the temperature rise rate of the P1 (single layer) specimen was the fastest, followed by P2 (double layer), and finally P3 (double layer with sand). After 5 hours of thermal radiation, the maximum surface temperature of P1 was approximately 7.3% and 10.2% higher than that of P2 and P3. In addition, the temperature rise rate of P1 and P2 was higher than P3, and the cooling rate was also higher than P3. This indicates that the bottom of the sand-containing double-layer specimen accumulates more heat, attributable to the fact that the sand layer is deeper and the heat dissipation is slow, making the cooling slower. As shown in Fig. 7, the maximum temperature at the bottom of P3 was approximately 23.3% higher than that of P1 and P2. This is because the lower layer of P3 was sandy, and the heat radiation transfer was faster, so the temperature at the bottom rose faster.

Surface color—Figure 8 shows the temperature change of the surface color group specimens under simulated thermal radiation. Surface color plays an important role in the temperature changes on the surface and inside of the specimen. Under the same circumstances, the C1 (natural color) specimen had the fastest heating rate, followed by C2 (red), and finally C3 (blue). After 5 hours of thermal radiation, the maximum temperature of C1 was approximately 23.3% and 30.2% higher than that of C2 and C3. In addition, the surface temperature of C2 was slightly higher than that of C3, and the heating and cooling rates of C1 were significantly higher than those of other specimens. After the radiation began, the surface temperature of C2 and C3 showed a straight line parallel to the horizontal axis, which caused the temperature change of C2 and C3 to lag. This is because C1 had low reflectivity and absorbed more heat in the heating stage, so it heated up faster, while C2 and C3 had high reflectivity and thermal radiation was reflected back to the surrounding environment after irradiation on the surface of the specimen;

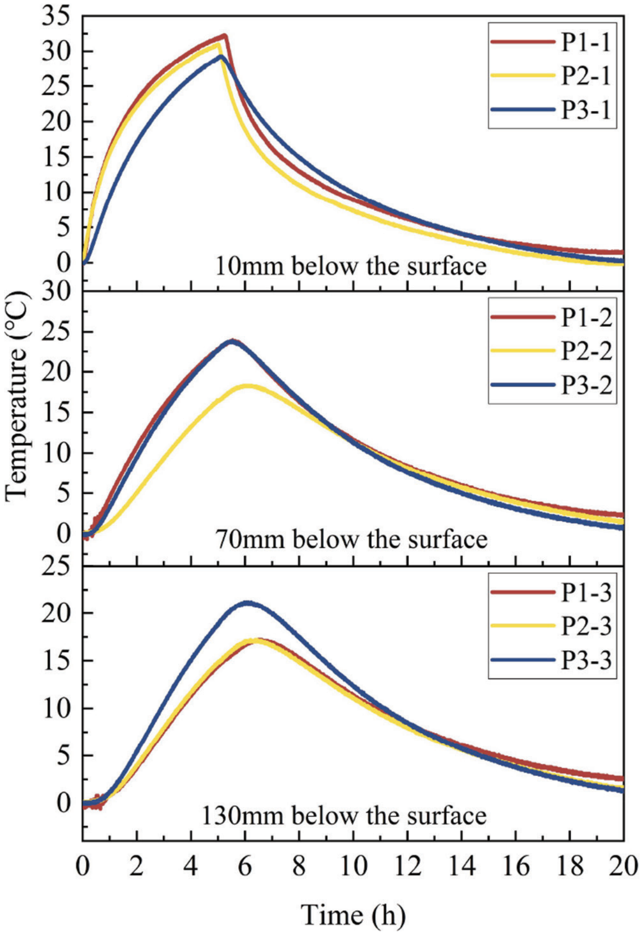

Fig. 7—Temperature change of specimens under action of simulated thermal radiation (pavement structure).

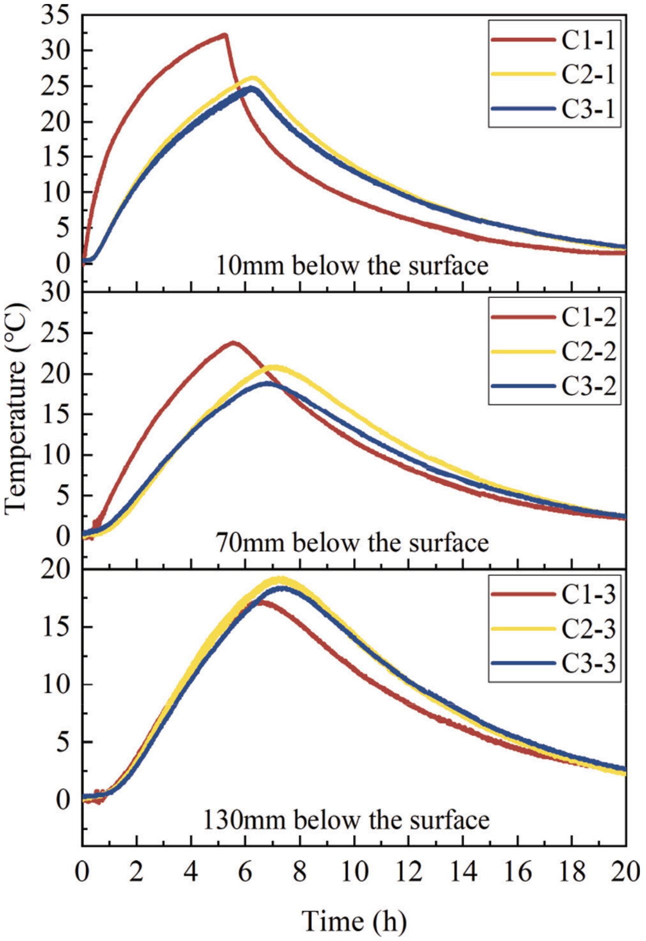

Fig. 8—Temperature change of specimens under action of simulated thermal radiation (surface color).

only a small part of it was absorbed by the specimen in the form of a slow rise in temperature.

Temperature difference change under thermal radiation

Figure 9 shows the difference between the temperature sensor readings at 10 mm below the specimen surface and at 130 mm—that is, the difference between the surface and bottom surface temperatures of the specimen. During the heating phase, the surface temperature was much higher than the bottom surface and the temperature difference was positive. As the light continued, the temperature difference between the surface and the bottom surface increased rapidly. Combined with the analysis of the temperature change graph of permeable concrete, the temperature difference increased rapidly because the surface of the specimen warmed up rapidly, while the bottom temperature was still in the slowly rising phase. This shows that there is a hysteresis phenomenon of heat transfer in the internal structure of the pavement: the heat radiation reaches the surface first and the temperature increases rapidly, but it takes some time for the heat to be conveyed from the surface to the bottom surface, and there is a certain degree of heat loss, which leads to the rapid increase of temperature difference during the early phase of heating. After approximately 2 hours of heating, the curve was more stable than during the initial phase of heating. Combined with the analysis of the temperature change diagram of permeable concrete, the surface heating rate gradually decreased at this phase, while the bottom heating rate remained at the same level as the initial phase of heating. Therefore, the temperature difference in Fig. 9 remains relatively stable or slightly decreases for approximately 2 to 5 hours. It also shows that after continuous heating for 2 hours, the hysteresis of heat transfer from the surface to the bottom of the specimen was balanced.

With the end of lighting, the temperature difference gradually decreased, reaching the lowest negative peak (absolute temperature difference). The reason for this phenomenon is that after the tungsten iodide lamp was turned off, the surface of the specimen lost its heat source, the temperature decreased rapidly, and the rate was significantly higher than that of the bottom. At that time, the bottom was still warming slowly and did not reach the peak temperature, as can be seen in Fig. 5 to 8. When the surface temperature was lower than the bottom temperature, the difference was negative, which was also due to the delay and loss of heat transfer, and the bottom cooled later than the surface at a low rate. When the surface temperature decreased to a certain extent, the convective exchange between the surface and the air near the surface became weak, the cooling rate slowly decreased, the bottom temperature gradually approached it, and the temperature difference was closer to 0.

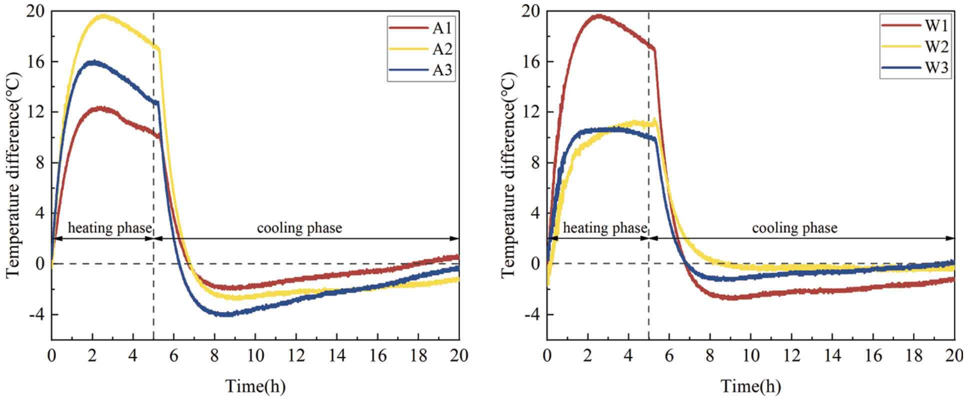

(a) Aggregate size (b) Water content

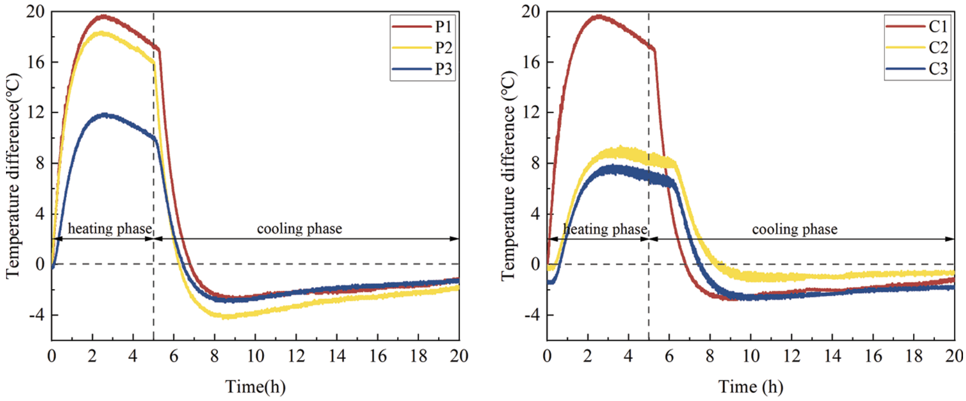

(c) Pavement structure (d) Surface color

Fig. 9—Temperature difference between surface of specimen and bottom surface.

As shown in Fig. 9(a), the three curves of aggregate particle size group had the same change trend. The temperature difference curve was relatively uniform, and the two adjacent curves had similar intervals: from top to bottom, they were A2, A3, and A1, which indicates that porosity has an impact on temperature difference and should be fully considered in the design stage of mixture ratio—but it is not a linear change relationship. As shown in Fig. 9(b), the variation trends of the three curves of the moisture content group were quite different. Among them, the peak temperature difference between the W2 and W3 specimens was close, but the difference was 44.1% between the W1 and W2 specimens, indicating that increasing the internal moisture content of permeable pavement can effectively reduce the temperature difference between the surface and the bottom of the specimen. As shown in Fig. 9(c), the variation trends of the three curves of the pavement structure group were consistent, but the peak temperature difference of the P3 specimen was much lower than that of the P1 and P2 specimens, which indicates that the bottom of the double-layer specimen containing sand accumulated more heat and was located in a deep position so the heat dissipation and temperature drop were slow. As shown in Fig. 9(d), there are three curves of the surface color group, among which C2 and C3 specimens had a plateau period of 0.5 hours at the initial heating stage. Because the red and blue surfaces had much higher color reflectance than the natural surfaces, C1 specimens had a great difference from C2 and C3 specimens.

Near-surface air temperature change

Near-surface air is the main object of convective exchange with road surface, and its temperature will also have a great impact on human thermal comfort. In a study of permeable water and ordinary concrete, Duncan[34] believes that the near-surface air temperature of pavement is considered the main index reflecting the impact of pavement on the surrounding environment and toward evaluating its impact on heat island effect. Therefore, it is necessary to measure the near-surface air temperature of permeable concrete with different parameters. Figure 10 shows the near-surface air temperature 35 mm above the specimen. It can be seen from the figure that the variation trend of near-surface air temperature was basically the same as that of the surface, middle, and bottom temperatures of the specimen. After heating started, the temperature rose slowly at first, and the heating rate increased rapidly with continuous heating. Approximately 1 hour after the end of the illumination, the near-surface air temperature still rose and entered the cooling stage after reaching the peak. Then the rate decreased continuously and gradually trended to 0.

It was observed that the A2 specimen had the highest near-surface air temperature in the four different groups, which was approximately 39.8% higher than the minimum value. This indicates that the large-particle aggregate permeable pavement increased the near-surface air temperature in the process of convective exchange with air due to its fast temperature rise and high peak temperature, thus causing a great impact on the near-surface thermal environment

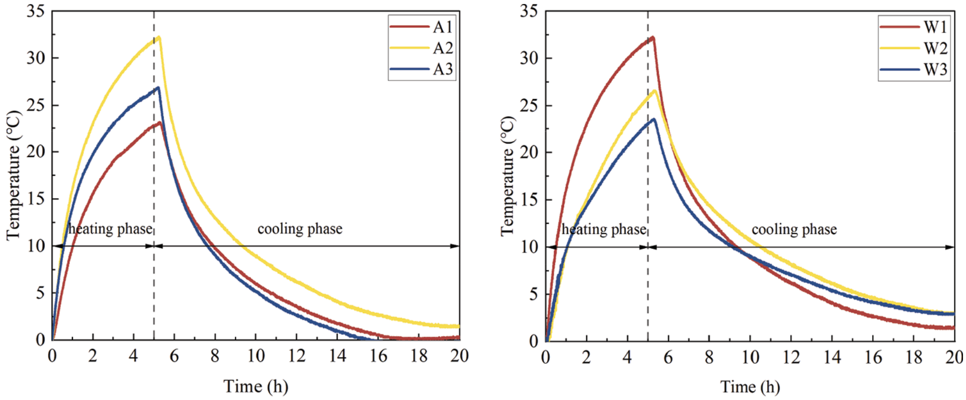

(a) Aggregate size (b) Water content

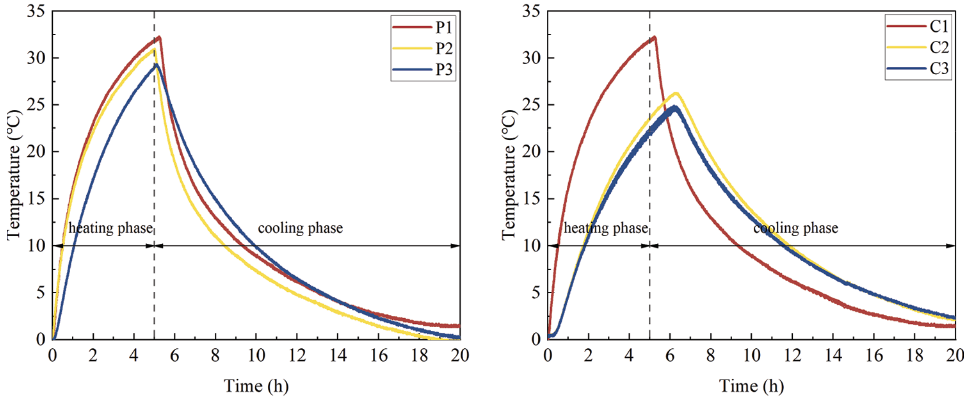

(c) Pavement structure (d) Surface color

Fig. 10—Near-surface air temperature above specimen.

and affecting human thermal comfort. On the other hand, when the internal water content of the pavement increased, the near-surface air temperature was effectively reduced, and the effect was significant. Although large-diameter permeable pavement has the negative effect of increasing the near-surface air temperature, the negative effect can be effectively reduced by sprinkling water onto the pavement and increasing the moisture content. It is worth noting that the change of surface color of the specimen delays the rise of near-surface air temperature and decreases the rate of temperature change.

Thermal energy change

Thermal energy calculation—The composition and proportion of the mixture are different, and its ability to absorb or release heat energy is also different. In general, the heat energy absorbed or released by the material was closely related to its specific heat capacity, and the higher the specific heat capacity of the material, the more heat per unit mass of the material needs to be absorbed at the same temperature. With the change of the external thermal environment, the heat energy absorbed or released by the specimen over a period of time can be calculated using the following formula

$$Q = Cm\Delta t \tag{1}$$

where Q is thermal energy of the material, J; C is specific heat capacity of the material, J/(kg·°C); m is mass of the material, kg; and Δt is the value of temperature change of the material during the measurement phase, °C.

Considering that permeable concrete is composed of a mixture of coarse aggregate, cement, and water, the weighted average specific heat capacity is affected by the mass and proportion of each component in addition to the specific heat capacity of the component itself. Therefore, the specific heat capacity of the mixture is obtained after the weighted average of the specific heat capacity of each component, and the calculation formula is as follows

$$C_p = \frac{\Sigma C_i \omega_i}{\Sigma \omega_i} \tag{2}$$

where C_p is weighted average specific heat capacity, J/(kg·°C); ω_i is mass of each component, kg; and C_i is specific heat capacity of each component, J/(kg·°C).

The specific heat capacity of each component is known, and the weighted specific heat capacity can be obtained according to the percentage of the mixture and then by calculating the thermal energy change of the specimen during the test. The specific heat capacity data of the materials used in this paper are shown in Table 5.

Storage and dissipation of thermal energy—To simplify the calculation of dissipated heat energy of the specimen—assuming that the temperature inside the specimen is linearly distributed along its vertical direction—the average value of the surface, middle, and bottom temperatures of the specimen is taken as the average temperature of the specimen so

Table 5—Specific heat capacity of pavement material, J/(kg·°C)

Material	Water	Cement	Silica ash	Crushed stone	Weighted specific heat capacity
Specific heat capacity	4175	838	920	745	1437.66

as to calculate the dissipated heat energy released into the surrounding environment of each group of specimens during the cooling period, as shown in Fig. 11. The results show that A2 (10 to 15 mm), W1 (0%), P1 (single layer), and C1 (natural color) specimens released more heat energy to the surrounding environment than other specimens in the same group. A2 was 33.2% and 12.4% higher than A1 and A3, respectively, and W1 was 29.3% and 48.5% higher than W2 and W3, respectively. The P1 specimen was 1.0% and 5.8% higher than P2 and P3 specimens, respectively, and C1 specimen was 26.6% and 34.9% higher than C2 and C3 specimens, respectively. The more heat released to the environment during cooling, the greater the impact on the external thermal environment, especially near the surface air. At this time, the dry permeable concrete pavement heated up and cooled down quickly, and the peak temperature was high, so the temperature changed greatly during the cooling stage and more heat was emitted.

The heat energy per unit mass of the specimen and its change can be calculated according to the surface, middle, and bottom temperatures of the specimen, as shown in Fig. 12 to 15. It can be clearly seen that A2 (10 to 15 mm), W1 (0%), P1 (single layer), and C1 (natural color) specimens had the ability to store more heat energy than other test pieces. When the test pieces had the same mass, they could absorb more heat energy under solar radiation (heating phase) and release more heat to the surrounding environment at night (cooling phase). It affects the near-surface thermal environment and reduces the thermal comfort of humans. In addition, permeable concrete pavement is dark gray, has low reflectivity, and will absorb more heat under the same solar radiation, which is also considered to be one of the main reasons for permeable concrete pavement to have a negative impact on the thermal environment.

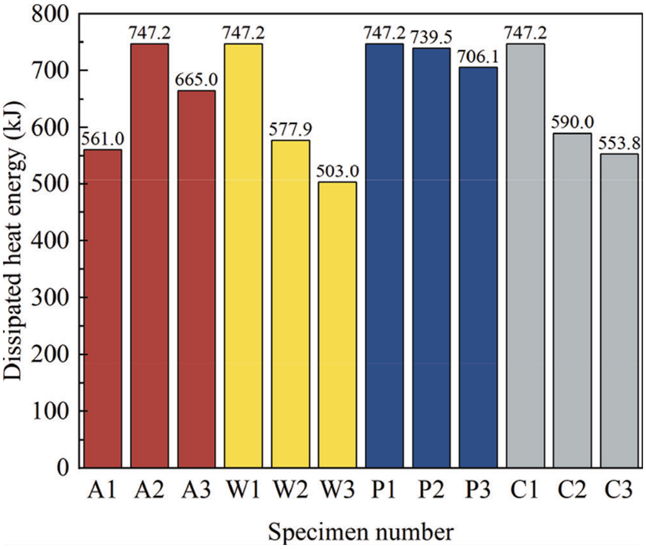

Fig. 11—Effect of air temperature on evaporation capacity of different pavements.

CONCLUSIONS

The influences of aggregate size, water content, pavement structure, and surface color on the thermal behaviors of permeable concrete pavements were investigated by establishing indoor simulated thermal radiation tests. The main conclusions are drawn as follows:

1. The indoor simulation test in this paper can effectively characterize the effects of aggregate particle size, water content, pavement structure, and surface color on the thermal behavior of permeable pavements, which can be used to evaluate their effects on the surrounding environment.

2. The specimens with large aggregate size have better thermal properties. The surface temperature of aggregate particle size group does not follow the order of aggregate particle size completely and should be considered when designing the mixture ratio. Specimens with large aggregate particle size have the characteristics of fast heat absorption. During the heating period, the surface temperature increases rapidly, resulting in a rapid opening of the temperature gap between the surface and the bottom of the specimen, a more obvious temperature gradient, and rapid heat transfer.

3. The specimens with high moisture content have better thermal properties. In the cycles of heating, warming, and cooling, the near-surface air temperature of the dry permeable pavement is higher. When the moisture content of the specimen is increased, the near-surface thermal environment is significantly improved and the thermal impact on the surrounding environment is significantly reduced. Pavement structure has little effect on evaporation and cooling of permeable concrete; only the addition of a sand layer has influence on it.

4. The specimens with high reflectance (red or blue) have better thermal properties. In the initial heating stage, both red and blue specimens show a slow heating characteristic, which is different from that of natural-color specimens. More radiant heat is reflected back to the atmosphere, delaying the rise of near-surface air temperature and reducing the temperature change rate, so there is no significant change in surface temperature.

5. Among the four influencing factors, moisture content and surface color have the most obvious influence on the thermal behavior of permeable pavement, while pavement structure has the weakest influence on the thermal behavior of permeable pavement. Due to the characteristics of high porosity and fast heat absorption, permeable pavement with large particle size leads to high peak temperature and more dissipated heat energy, which easily increases the near-surface air temperature, thus causing a greater impact on the near-surface thermal environment. However, by sprinkling water on the pavement and increasing the moisture content, the negative impact on the nearby human bodies and buildings can be effectively weakened and the role of the large porosity of permeable pavement can be played to a greater extent.

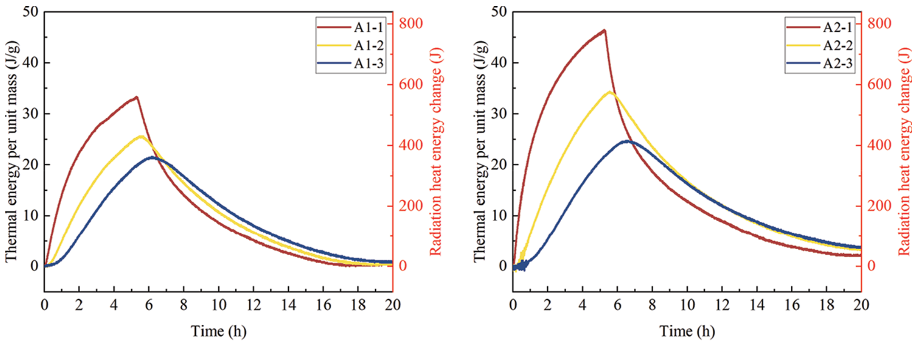

(a) A1

(b) A2

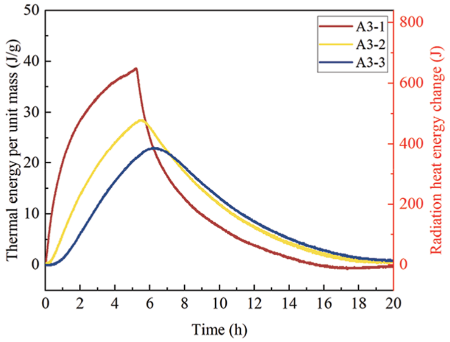

(c) A3

Fig. 12—Unit mass thermal energy and thermal energy change (aggregate size).

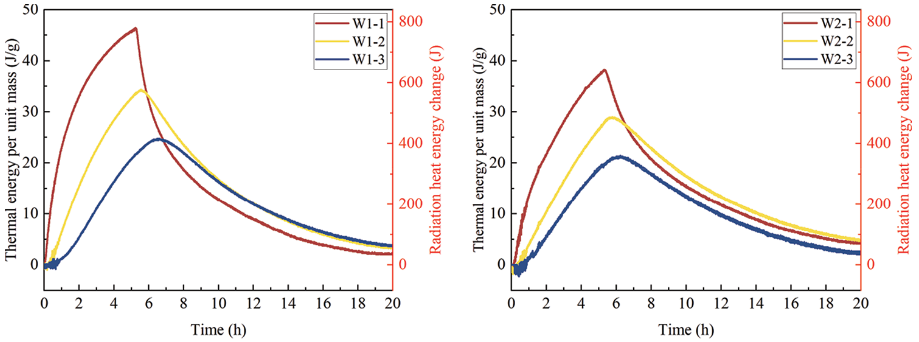

(a) W1

(b) W2

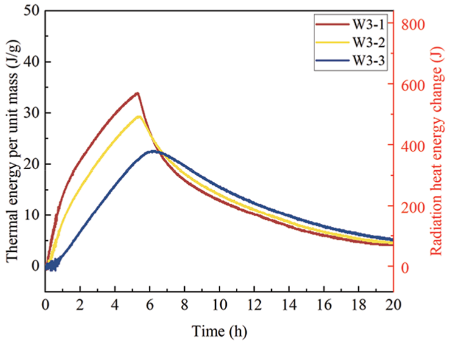

(c) W3

Fig. 13—Unit mass thermal energy and thermal energy change (water content).

AUTHOR BIOS

Chaoguo Wu *is a Doctoral Student in the College of Civil and Transportation Engineering at Hohai University, Nanjing, China. His research interests include the evaporation properties of permeable concrete through indoor and outdoor simulation tests.*

Xudong Chen *is a Professor in the College of Civil and Transportation Engineering at Hohai University, where he received his PhD in 2014. His research interests include experimental and numerical simulation of the mechanical behavior of cement-based materials under impact and earthquake loads.*

Chen Chen *is a Doctoral Student in the College of Civil and Transportation Engineering at Hohai University. His research interests include the damage mechanism of concrete by acoustic emission and digital image correlation.*

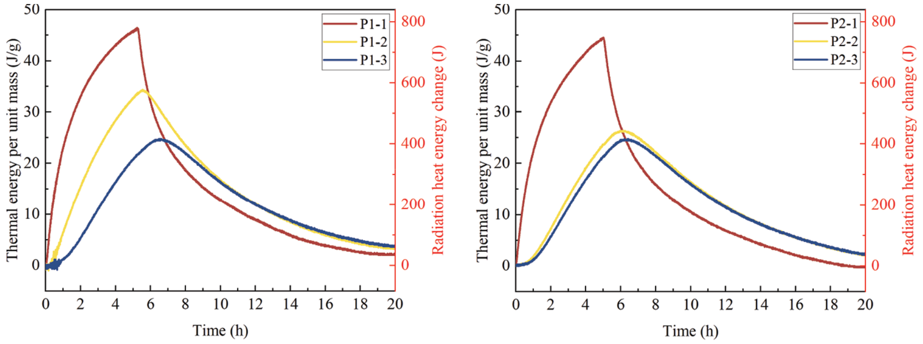

(a) P1

(b) P2

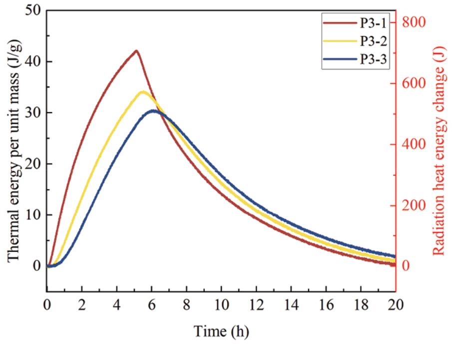

(c) P3

Fig. 14—Unit mass thermal energy and thermal energy change (pavement structure).

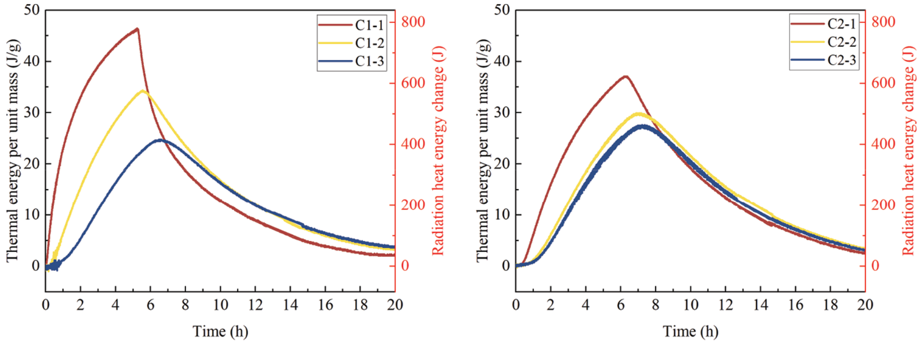

(a) C1

(b) C2

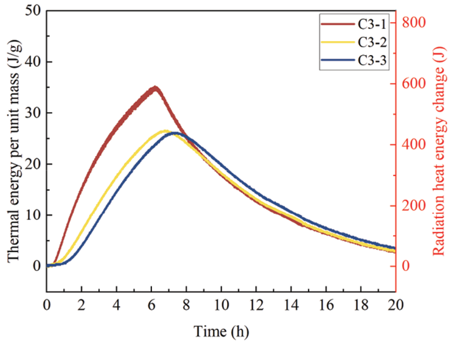

(c) C3

Fig. 15—Unit mass thermal energy and thermal energy change (surface color).

Tao Ji *is a Professor in the College of Civil Engineering at Fuzhou University, Fuzhou, China. His research interests include the efficient use of industrial and municipal solid waste.*

Chang Jin *is a Master's Student in the College of Civil and Transportation Engineering at Hohai University. Her research interests include the evaporation properties of permeable concrete through indoor and outdoor simulation tests.*

ACKNOWLEDGMENTS

The authors are grateful for the financial support from the National Key R&D Program of China (Grant No. 2021YFB2600200), the National Natural Science Foundation of China (Grant No. 51979090), and the State Key Laboratory of High-Performance Civil Engineering Materials (Grant No. 2019CEM002).

REFERENCES

1. Park, J. H.; Kim, Y. U.; Jeon, J.; Wi, S.; Chang, S. J.; and Kim, S., "Effect of Eco-Friendly Pervious Concrete with Amorphous Metallic Fiber on Evaporative Cooling Performance," *Journal of Environmental Management*, V. 297, 2021, p. 113269. doi: 10.1016/j.jenvman.2021.113269

2. Sieffert, Y.; Huygen, J. M.; and Daudon, D., "Sustainable Construction with Repurposed Materials in the Context of a Civil Engineering-Architecture Collaboration," *Journal of Cleaner Production*, V. 67, 2014, pp. 125-138. doi: 10.1016/j.jclepro.2013.12.018

3. Tan, K.; Qin, Y.; and Wang, J., "Evaluation of the Properties and Carbon Sequestration Potential of Biochar-Modified Pervious Concrete," *Construction and Building Materials*, V. 314, 2022, p. 125648. doi: 10.1016/j.conbuildmat.2021.125648

4. Chen, X.; Wu, C.; Chen, Z.; Chen, C.; and Jin, C., "Influence of Meteorological Factors on Evaporative Cooling of Steel Slag Permeable Concrete Pavement," *International Journal of Pavement Engineering*, V. 24, No. 2, 2023, p. 2115493. doi: 10.1080/10298436.2022.2115493

5. Nakayama, T., and Fujita, T., "Cooling Effect of Water-Holding Pavements Made of New Materials on Water and Heat Budgets in Urban Areas," *Landscape and Urban Planning*, V. 96, No. 2, 2010, pp. 57-67.

6. Wang, J.; Meng, Q.; Zhang, L.; Zhang, Y.; He, B. J.; Zheng, S.; and Santamouris, M., "Impacts of the Water Absorption Capability on the Evaporative Cooling Effect of Pervious Paving Materials," *Building and Environment*, V. 151, 2019, pp. 187-197. doi: 10.1016/j.buildenv.2019.01.033

7. Yap, S. P.; Chen, P. Z. C.; Goh, Y.; Ibrahim, H. A.; Mo, K. H.; and Yuen, C. W., "Characterization of Pervious Concrete with Blended Natural Aggregate and Recycled Concrete Aggregates," *Journal of Cleaner Production*, V. 181, 2018, pp. 155-165. doi: 10.1016/j.jclepro.2018.01.205

8. Akkaya, A., and Çağatay, İ. H., "Experimental Investigation of the Use of Pervious Concrete on High Volume Roads," *Construction and Building Materials*, V. 279, 2021, p. 122430. doi: 10.1016/j.conbuildmat.2021.122430

9. Ibrahim, H. A.; Goh, Y.; Ng, Z. A.; Yap, S. P.; Mo, K. H.; Yuen, C. W.; and Abutaha, F., "Hydraulic and Strength Characteristics of Pervious Concrete Containing a High Volume of Construction and Demolition Waste as Aggregates," *Construction and Building Materials*, V. 253, 2020, p. 119251.

10. Wang, S.; Zhang, G.; Wang, B.; and Wu, M., "Mechanical Strengths and Durability Properties of Pervious Concretes with Blended Steel Slag and Natural Aggregate," *Journal of Cleaner Production*, V. 271, 2020, p. 122590. doi: 10.1016/j.jclepro.2020.122590

11. Yu, F.; Sun, D.; Wang, J.; and Hu, M., "Influence of Aggregate Size on Compressive Strength of Pervious Concrete," *Construction and Building Materials*, V. 209, 2019, pp. 463-475. doi: 10.1016/j.conbuildmat.2019.03.140

12. Cui, X.; Zhang, J.; Huang, D.; Jing, Q.; and Hou, F., "Experimental Simulation of Rapid Clogging of Permeable Concrete Pavement Under Effects of Rainstorm," *Zhongguo Gonglu Xuebao*, V. 29, No. 10, 2016, pp. 1-12.

13. Pieralisi, R.; Cavalaro, S. H. P.; and Aguado, A., "Discrete Element Modelling ofthe Fresh State Behavior of Pervious Concrete," *Cement and Concrete Research*, V. 90, 2016, pp. 6-18. doi: 10.1016/j.cemconres.2016.09.010

14. Li, T.-S.; Lu, G.-Y.; Wang, D.-W.; Hong, B.; Yan, T.-Q.; and Oeser, M., "Key Properties of High-Performance Polyurethane Bounded Permeable Mixture," *Zhongguo Gonglu Xuebao*, V. 32, No. 4, 2019, p. 158-169

15. Chen, X.; Wang, J.; Han, Y.-S.; Chen, Q.; and Zhu, G.-R., "Effect of the Cement Paste Rheological Characteristics on the Properties of Pervious Concrete," *Zhongguo Gonglu Xuebao*, V. 32, No. 4, 2019, p. 177-186

16. Xie, X.; Zhang, T.; Wang, C.; Yang, Y.; Bogush, A.; Khayrulina, E.; Hunag, Z.; Wei, J.; and Yu, Q., "Mixture Proportion Design of Pervious Concrete Based on the Relationships Between Fundamental Properties and Skeleton Structures," *Cement and Concrete Composites*, V. 113, 2020, p. 103693. doi: 10.1016/j.cemconcomp.2020.103693

17. Zhang, G.; Wang, S.; Wang, B.; Zhao, Y.; Kang, M.; and Wang, P., "Properties of Pervious Concrete with Steel Slag as Aggregates and Different Mineral Admixtures as Binders," *Construction and Building Materials*, V. 257, 2020, p. 119543. doi: 10.1016/j.conbuildmat.2020.119543

18. Zhong, R., and Wille, K., "Material Design and Characterization of High Performance Pervious Concrete," *Construction and Building Materials*, V. 98, 2015, pp. 51-60. doi: 10.1016/j.conbuildmat.2015.08.027

19. Santamouris, M., "Using Cool Pavements as a Mitigation Strategy to Fight Urban Heat Island—A Review of the Actual Developments," *Renewable and Sustainable Energy Reviews*, V. 26, 2013, pp. 224-240. doi: 10.1016/j.rser.2013.05.047

20. Liu, Y.; Li, T.; and Peng, H., "A New Structure of Permeable Pavement for Mitigating Urban Heat Island," *The Science of the Total Environment*, V. 634, 2018, pp. 1119-1125. doi: 10.1016/j.scitotenv.2018.04.041

21. Chen, J.; Chu, R.; Wang, H.; Zhang, L.; Chen, X.; and Du, Y., "Alleviating Urban Heat Island Effect Using High-Conductivity Permeable Concrete Pavement," *Journal of Cleaner Production*, V. 237, 2019, p. 117722. doi: 10.1016/j.jclepro.2019.117722

22. Asaeda, T., and Ca, V. T., "Characteristics of Permeable Pavement During Hot Summer Weather and Impact on the Thermal Environment," *Building and Environment*, V. 35, No. 4, 2000, pp. 363-375. doi: 10.1016/S0360-1323(99)00020-7

23. Garcia, A.; Hassn, A.; Chiarelli, A.; and Dawson, A., "Multivariable Analysis of Potential Evaporation From Moist Asphalt Mixture," *Construction and Building Materials*, V. 98, 2015, pp. 80-88.

24. Andersen, C. T.; Foster, I. D.; and Pratt, C. J., "The Role of Urban Surfaces (Permeable Pavements) in Regulating Drainage and Evaporation: Development of a Laboratory Simulation Experiment," *Hydrological Processes*, V. 13, No. 4, 1999, pp. 597-609. doi: 10.1002/(SICI)1099-1085(199903)13:4<597::AID-HYP756>3.0.CO;2-Q

25. Nemirovsky, E. M.; Welker, A. L.; and Lee, R., "Quantifying Evaporation from Permeable Concrete Systems: Methodology and Hydrologic Perspective," *Journal of Irrigation and Drainage Engineering*, ASCE, V. 139, No. 4, 2013, pp. 271-277. doi: 10.1061/(ASCE)IR.1943-4774.0000541

26. Syrrakou, C., and Pinder, G. F., "Experimentally Determined Evaporation Rates in Permeable Concrete Systems," *Journal of Irrigation and Drainage Engineering*, ASCE, V. 140, No. 1, 2014, p. 04013003. doi: 10.1061/(ASCE)IR.1943-4774.0000652

27. Doulos, L.; Santamouris, M.; and Livada, I., "Passive Cooling of Outdoor Urban Spaces. The Role of Materials," *Solar Energy*, V. 77, No. 2, 2004, pp. 231-249. doi: 10.1016/j.solener.2004.04.005

28. Li, H.; Harvey, J.; and Kendall, A., "Field Measurement of Albedo for Different Land Cover Materials and Effects on Thermal Performance," *Building and Environment*, V. 59, 2013, pp. 536-546. doi: 10.1016/j.buildenv.2012.10.014

29. Li, H.; Harvey, J. T.; Holland, T. J.; and Kayhanian, M., "The Use of Reflective and Permeable Pavements as a Potential Practice for Heat Island Mitigation and Stormwater Management," *Environmental Research Letters*, V. 8, No. 1, 2013, p. 015023. doi: 10.1088/1748-9326/8/1/015023

30. Li, H.; Harvey, J.; and Jones, D., "Cooling Effect of Permeable Asphalt Pavement under Dry and Wet Conditions," *Transportation Research Record: Journal of the Transportation Research Board*, V. 2372, No. 1, 2013, pp. 97-107. doi: 10.3141/2372-11

31. Li, H.; Harvey, J.; and Ge, Z., "Experimental Investigation on Evaporation Rate for Enhancing Evaporative Cooling Effect of Permeable Pavement Materials," *Construction and Building Materials*, V. 65, 2014, pp. 367-375. doi: 10.1016/j.conbuildmat.2014.05.004

32. Wang, J.; Meng, Q.; Tan, K.; and Santamouris, M., "Evaporative Cooling Performance Estimation of Pervious Pavement Based on Evaporation Resistance," *Building and Environment*, V. 217, 2022, p. 109083. doi: 10.1016/j.buildenv.2022.109083

33. Yokota, K.; Yamaji, T.; and Hirano, S., "Basic Characteristics of Water Permeable/Retainable Porous Paving Bricks for Controlling Urban Heat Island Phenomenon," *Heat Island Institute International*, V. 5, 2010, pp. 40-46.

34. Duncan, D. C., "Influence of Pavement Type on Near Surface Air Temperature," master's thesis, Clemson University, Clemson, SC, 2011.

ACI MATERIALS JOURNAL TECHNICAL PAPER

Title No. 122-M21

Thin Cement-Based Composites for Efficient Neutron Attenuation

by A. D. Patel, J. M. Paris, C. C. Ferraro, J. E. Baciak, K. A. Riding, and E. R. Giannini

Prolonged neutron irradiation can damage concrete biological shields, particularly when nuclear power plants extend reactor lifespans. Retrofitting biological shields with thin and highly efficient neutron shields may limit neutron damage. Portland cement mortars amended with boron carbide and polyethylene powders were assessed for neutron attenuation. Shielding performance was compared to concrete with a similar design and coarse aggregate as a biological shield at an operational nuclear plant. Boron carbide enhanced the shielding performance of specimens under the full energy spectrum of the neutron source. Boron carbide and polyethylene synergistically enhanced neutron attenuation under a purely high-energy neutron flux. Engineered thin composite mortars needed 90% less thickness to achieve similar or better shielding efficiency than the concrete in a typical biological shield under the test conditions. Isothermal calorimetry, compressive strength, and thermal expansion results indicate that mixture design parameters of thin shields can be adjusted to achieve adequate structural properties without diminishing constructability or structural performance.

Keywords: biological shield; boron carbide; high-density polyethylene (HDPE); neutron radiation; portland cement mortar; radiation-induced volumetric expansion (RIVE).

INTRODUCTION

Nuclear power plants (NPPs) in the United States are renewing their operating licenses to extend reactor operations by 20 or 40 years beyond the initial 40-year license. Life extensions have placed aging plant infrastructure under greater scrutiny (Field et al. 2015; Hsiao et al. 2017; Le Pape et al. 2015, 2016; Maruyama et al. 2013; Pignatelli et al. 2016; Remec et al. 2017; Rosseel et al. 2016). Given their proximity to reactor pressure vessels (RPVs), research has focused on radiation damage in concrete biological shields (CBSs) (Fillmore 2004; Le Pape et al. 2016; Maruyama et al. 2013). Concrete shields in NPPs are designed to protect plant personnel from excessive radiation dose uptake, contain radioactivity during accident scenarios, and transfer loads from failure-critical systems such as the RPV to the foundation. Structural degradation of an aging CBS could result in damage to the RPV or radiation containment failure.

Experimental test reactor data indicate that concrete exposed to high neutron radiation levels can undergo strength loss, reduction in the modulus of elasticity, and volumetric expansion (Field et al. 2015; Hilsdorf et al. 1978; Le Pape et al. 2015; Maruyama et al. 2013). This is a result of a damage process known as radiation-induced volumetric expansion (RIVE). Neutrons induce RIVE by damaging the well-ordered crystal lattices in aggregate minerals (Kinchin and Pease 1955). Irradiated minerals amorphize and irreversibly expand as lattice damage accumulates, leading to aggregate expansion (Le Pape et al. 2018; Primak 1958). Irradiation damage to lattice structures may anneal at temperatures above 150°C and delay expansion, but most CBSs in operational reactor plants experience temperatures below this (Le Pape et al. 2018). Aggregate expansion exerts stress and cracking in the surrounding hardened cementitious matrix, ultimately leading to the loss of structural capacity and volumetric expansion. Silicates, the most common types of minerals found in aggregate, tend to be more sensitive to RIVE than other aggregate minerals, such as limestone (Le Pape et al. 2018; Remec et al. 2018; Rosseel et al. 2016; Sindelar et al. 2001). Moreover, RIVE-induced amorphization increases the chemical solubility of silicates in alkaline environments such as concrete pore solution, potentially leading irradiated concrete made with siliceous aggregates to develop alkali-silica reaction (ASR) (Hsiao et al. 2017; Le Pape et al. 2018; Pignatelli et al. 2016). In essence, the extended exposure to neutron radiation converts otherwise innocuous aggregates into ASR-reactive aggregates after decades of service life, potentially creating further deleterious expansion in addition to that caused by RIVE.

Computational modeling has shown that neutron fluences (cumulative exposure over time) necessary to cause RIVE in existing CBSs may be exceeded during the extended operational lifespan of NPP reactors (Remec et al. 2018). Replacement of existing CBSs in the current nuclear reactor fleet would not be economical due to their structural complexity. Retrofitting CBSs with efficient neutron shields may delay the onset or continuation of RIVE damage. However, the tight spatial restrictions between the RPV and CBS, as well as the potential for adhesion failure under high thermal loads and radioactivity, preclude the use of bonded coatings. Concrete coatings designed for nuclear applications have been shown to fail under design-basis accident conditions due to bond degradation under high radiation and temperature (for example, high-temperature fluid interaction with concrete) (Sindelar et al. 2000). Anchored precast panels with high neutron-shielding efficiency are better candidates for retrofits than coatings because they are less likely to fail under thermal loading. Moreover, thin and efficient neutron

---

ACI Materials Journal, V. 122, No. 4, July 2025.

MS No. M-2024-027.R2, doi: 10.14359/51746803, received March 20, 2025, and reviewed under Institute publication policies. Pertinent discussion including author's closure, if any, will be published ten months from this journal's date if the discussion is received within four months of the paper's print publication.

shields have utility in a broad range of applications. The nuclear power industry is trending toward small modular reactors (SMRs) and microreactors. These facilities are expected to have less space available to accommodate large biological shields, but they still need efficient shielding.

Neutrons are difficult to shield because they are chargeless particles with mass that penetrate and damage materials relatively easily compared to charged particles (for example, α and β particles) (Hei et al. 2021). They interact with matter through nuclear collisions, which result in either neutron absorption or scattering. The likelihood of scattering or absorption during collisions depends on the neutron energy. High-energy neutrons, also known as epithermal and fast neutrons, are more likely to undergo scattering. During scattering, high-energy neutrons lose energy through a process known as moderation. Sufficient scattering events with light nuclei, such as hydrogen, can moderate high-energy neutrons into the low-energy range. (Note: Nuclear interactions are dependent on elemental composition and are independent of mineralogy/crystallinity.) Low-energy neutrons, or thermal neutrons, have a higher probability of absorption by atomic nuclei during collision events than more energetic neutrons. High-energy neutrons are mainly responsible for RIVE, while low-energy neutrons still pose a significant biological hazard (Le Pape et al. 2018). Effective shield designs need to account for the entire neutron energy spectrum.

Concrete shields are effective high-energy neutron moderators due to the presence of hydrogen in pore water and cement hydrate phases (Rockwell 1956). Thinner cementitious shields have less moisture and are more prone to drying due to elevated temperatures than larger members; moisture loss can reduce moderation efficiency (Malkapur et al. 2015). Hydrogenous materials such as high-density polyethylene (HDPE) plastic may be added to thin cementitious neutron shields to compensate for moisture loss. Although moderation is important for overall radiation shielding, high moderation can increase the quantity of thermal neutrons by converting fast or epithermal neutrons to thermal neutrons.

Thermal neutron shielding necessitates the use of elements with high thermal neutron absorption cross sections (a probabilistic measure of neutron absorption expressed in units called barns [b]). Though other elements such as gadolinium and cadmium have higher-absorption cross sections, boron is the most economical option for use in cementitious shielding. Table 1 shows the thermal neutron-capture cross sections of boron versus elements commonly found in concrete. Small additions of boron can substantially improve the thermal neutron-shielding ability of cement-based materials (ASTM C1233-15(2021) [2021]). The values in Table 1 represent average capture cross sections for the element. The capture cross section is highly dependent on each element's isotope; therefore, these are averaged based on natural isotopic composition. The boron-10, or ^{10}B, isotope is entirely responsible for the absorption capture cross section of boron. The ^{10}B isotopes release a prompt gamma ray and transmute to a ^{7}Li^{3+} ion and an alpha particle during neutron capture, leaving behind no long-lived radioisotopes.

Table 1—Thermal neutron cross sections of elements found in concrete materials compared to boron (ASTM C1233-15(2021))

Common elements in concrete materials	Thermal neutron absorption cross section, b	Absorber	Thermal neutron absorption cross section, b
Oxygen	0.00019	Boron	768
Calcium	0.43		
Magnesium	0.063		
Sodium	0.53		
Potassium	2.1		
Iron	2.56		
Carbon	0.0035		
Silicon	0.171		
Sulfur	0.53		
Aluminum	0.231		
Hydrogen	0.33		

Though research has shown boron enhances thermal neutron-shielding efficiency in cementitious systems, common boron compounds such as soluble borates can retard setting and limit strength development (Ataie 2019; Glinicki et al. 2018; Kharita et al. 2011; Moradllo et al. 2020; Sindelar et al. 2001). For this application, thermal neutron shielding is dependent only on the amount of boron, specifically the ^{10}B isotope, present and not the boron compound. The adverse effects of soluble borates on hydration and setting time limit the amount of ^{10}B that can be incorporated into cementitious shields.

Boron carbide (B_4C), in contrast, is more chemically stable and does not degrade cementitious properties to the same degree (Chidiac et al. 2021; Glinicki et al. 2018; Mondal et al. 2016; Shin et al. 2014). Chidiac et al. (2021) showed that trace sassolite (boric acid) impurities in boron carbide can retard hydration kinetics and the setting of cementitious systems but had limited effect on strength development (Chidiac et al. 2021). Moreover, boron carbide has a boron mass fraction of 78%, which is substantially higher than those of common soluble borates such as boric acid (17% boron) or borax decahydrate (11% boron), and does not affect setting or hydration (Glinicki et al. 2018). Thus, boron carbide can be used to drastically improve thermal shielding properties without loss of structural properties. To achieve equivalent thermal shielding, far greater quantities of soluble borates are needed than if using boron carbide.

RESEARCH SIGNIFICANCE

This paper presents experimental data on the neutron-shielding performance of thin cementitious panels prepared with boron carbide and HDPE powders. The boron carbide was effective at capturing thermal neutrons, while the hydrogen present in HDPE was effective at moderating faster neutrons into the thermal range for the boron carbide to capture. Specimens were exposed to a collimated neutron flux generated by a plutonium-beryllium alpha-neutron source with and without a cadmium filter. This allowed specimens to be exposed to a neutron energy spectrum containing only high-energy neutrons (purely fast spectrum) and one with both low- and high-energy neutrons (mixed energy spectrum). This enabled the examination of the combined effects of HDPE and boron carbide on neutron-shielding performance across a wide range of neutron energies. Furthermore, shielding performances of the thin panels were compared to concrete (referred to as radiological concrete [RC]) made with the same mixture design and coarse aggregate used in the construction of an existing biological shield. The RC was used to determine the degree of thickness reduction allowed for mortar panels without losing shielding performance.

EXPERIMENTAL PROCEDURE

Materials

A commercially available ASTM C150/C150M-19 (2019) Type I/II portland cement (from Florida) was used for all cementitious systems in this study. A natural quartz silica sand (from Florida) meeting ASTM C33/C33M-18 (2018) fine aggregate gradation was also used for both concrete and mortar preparation. The RC mixture was made with an ASTM C33/C33M-18 No. 67 graded coarse aggregate obtained from a commercial aggregate supplier in North Carolina. The coarse aggregate was from the same quarry and graded to the same size as the aggregate used in the construction of an existing NPP biological shield. ASTM C618-17 (2017) Class F fly ash was used at a cement mass replacement rate of 35% in the RC.

Abrasive boron carbide powder with a median particle size of 12.8 μm was acquired from a materials supplier in Idaho, and HDPE powder with a median particle size of 34.0 μm was obtained from a specialty polymers and chemicals supplier in Ohio. A powdered polycarboxylate ether (PCE)-based high-range water-reducing admixture (HRWRA) was used to improve workability and consolidation of all mortar mixtures.

The elemental oxide profiles of cement and fly ash from X-ray fluorescence (XRF) are shown in Table 2, and the d_{10}, d_{50}, and d_{90} particle-size characteristics of the cement, fly ash, boron carbide, and HDPE are shown in Table 3.

Mixture proportioning and preparation

A summary of the mortar mixture proportions is presented in Table 4. The boron carbide and HDPE powders were incorporated into mortar mixtures as partial fine aggregate replacements on a mass basis. Because ^{10}B is primarily responsible for the neutron-shielding properties of boron, boron carbide dosages were based on the amount of ^{10}B supplied to the cementitious mixture. A natural isotopic mass abundance of 20% was assumed for ^{10}B to calculate the mass proportion of boron carbide in each mixture.

The mixture IDs reference the amount of ^{10}B and HDPE powder in each mixture. For example, the "20B-10P" mixture contained a ^{10}B content of 20 kg/m^3, and HDPE powder constituted 10% of the fine aggregate mass. Boron carbide has a boron mass fraction of 78%, and the natural isotopic abundance of ^{10}B in boron is approximately 20% wt. Thus, the quantity of total boron in each mixture is five times the quantity of ^{10}B outlined in the eighth column of Table 4.

Table 2—Elemental oxide composition of materials by XRF; values in % wt. of sample

Elemental oxide	OPC, %	Fly ash, %
CaO	65.8	2.7
SiO_2	17.3	53.4
Al_2O_3	3.9	22.7
Fe_2O_3	3.0	14.1
SO_3	8.2	0.8
MnO	0.1	0.0
MgO	0.9	1.0
Na_2O	0.1	1.2
K_2O	0.2	2.7
P_2O_5	0.3	0.1
TiO_2	0.2	1.1
Total	100.0	99.8
Loss on ignition	2.1	1.5

Table 3—Summary of particle-size characteristics, μm

Material	d_{10}	d_{50}	d_{90}
OPC	2.3	7.5	21.7
Fly ash	1.7	10.6	47.2
Boron carbide	7.6	12.8	19.9
HDPE	11.4	34.0	73.4

Because HDPE has a lower density than quartz sand, partial mass replacement of sand with HDPE led to lower binder content. Despite the lower water content per unit volume, the hydrogen load of mixtures with HDPE still increased because HDPE contains more hydrogen than water on a mass basis, as shown in Table 4. This was deemed acceptable because hydrogen primarily dictates fast and epithermal neutron moderation.

Preparation of the mortar mixtures was in accordance with ASTM C305-20 (2020), with some modifications to the mixing process. First, the dry constituents (cement, quartz sand, boron carbide, HDPE, and powdered PCE) were added to the mixer and uniformly blended prior to the addition of water. After dry blending, water was slowly added over the course of 30 seconds. The mixing speed was set to 140 rpm during dry component homogenization and the addition of water. This allowed HDPE and boron carbide to uniformly disperse within the cement paste matrix without substantial agglomeration. After the addition of water, the mixer speed was increased to 285 rpm, and the mortar was mixed for 3 minutes, rested for 2 minutes, and mixed again for 3 minutes. These mixing parameters were adjusted to increase the effectiveness of the powdered PCE. Additional powdered PCE was added at the end of the first mixing cycle, as necessary, to adjust mortar flow and allow for proper consolidation.

The RC mixture was prepared following ASTM C192/C192M-19 (2019). The mixture proportions of the RC mixture are shown in Table 5. The RC specimens were cured

Table 4—Mortar mixture proportions; PCE dose values in % wt. of cement

Mixture name	Mixture ID	OPC, kg/m^3 (lb/yd^3)	Sand, kg/m^3 (lb/yd^3)	Water, kg/m^3 (lb/yd^3)	HDPE, kg/m^3 (lb/yd^3)	Boron carbide, kg/m^3 (lb/yd^3)	^{10}B, kg/m^3 (lb/yd^3)	PCE dose, %	H load*, kg/m^3 (lb/yd^3)
Control	Control	999 (1684)	999 (1684)	300 (505)	—	—	—	0.16	34 (56)
4 kg B10	4B	998 (1683)	973 (1640)	300 (505)	—	26 (43)	4 (7)	0.17	33 (56)
11 kg B10	11B	998 (1682)	927 (1563)	299 (505)	—	71 (119)	11 (19)	0.17	33 (56)
20 kg B10	20B	997 (1681)	869 (1465)	299 (504)	—	128 (216)	20 (34)	0.20	33 (56)
40 kg B10	40B	995 (1678)	739 (1246)	299 (503)	—	256 (432)	40 (67)	0.25	33 (56)
80 kg B10	80B	992 (1672)	479 (807)	298 (502)	—	513 (864)	80 (135)	0.52	33 (56)
5%PE	5P	965 (1626)	916 (1545)	289 (488)	48 (81)	—	—	0.15	39 (66)
10%PE	10P	931 (1571)	838 (1414)	279 (471)	93 (157)	—	—	0.23	45 (75)
20%PE	20P	872 (1471)	698 (1176)	261 (441)	174 (294)	—	—	0.31	54 (92)
20 kg B10 + 5%PE	20B-5P	962 (1622)	786 (1324)	289 (486)	48 (81)	128 (216)	20 (34)	0.17	39 (66)
20 kg B10 + 10%PE	20B-10P	929 (1567)	708 (1194)	279 (470)	93 (157)	128 (216)	20 (34)	0.34	45 (75)
20 kg B10 + 20%PE	20B-20P	870 (1467)	568 (958)	261 (440)	174 (293)	128 (216)	20 (34)	0.38	54 (91)

*H load, or hydrogen load, denotes quantity of elemental hydrogen in each mixture, only considering hydrogen from water (H_2O) and HDPE ($(C_2H_4)_n$).

Table 5—Radiological concrete mixture design proportions

Mixture name	Mixture ID	OPC, kg/m^3 (lb/yd^3)	Class F fly ash, kg/m^3 (lb/yd^3)	Sand, kg/m^3 (lb/yd^3)	Coarse aggregate, kg/m^3 (lb/yd^3)	Water, kg/m^3 (lb/yd^3)	Air
Radiological concrete	RC	231 (390)	125 (210)	676 (1140)	1224 (2063)	160 (270)	3%

according to the accelerated moist-curing method in ASTM C1202-19 (2019). This curing method was used to simulate the properties of aged CBS in operating NPPs.

Cement paste mixtures for isothermal conduction calorimetry testing, consisting of boron carbide and HDPE powders, were externally mixed following Method B outlined in ASTM C1702-17 (2017). Boron carbide was added to the mixture to achieve a target ^{10}B mass per 350 kg of cement. This mass proportion was selected to model the cement content in a typical concrete mixture design used for shielding. The HDPE content was proportioned based on the amount of HDPE in the mortar mixture relative to the cement content. Ultrapure water (>18 MΩ·cm) was also used in the production of cement pastes. The mixture proportions of the cement pastes are summarized in Table 6. Isothermal mixture designs were adjusted to match the thermal mass of the reference samples in the calorimeter as necessary.

Testing methods

Isothermal conduction calorimetry—Isothermal conduction calorimetry was conducted using an eight-channel isothermal calorimeter preconditioned to 23°C to qualify the use of boron carbide and HDPE in cementitious systems. Samples were prepared following ASTM C1702-17 (2017) procedures for external mixing. Instantaneous heat flow data, normalized by cement mass (mW/g cement), were collected over a 3-day period to capture the main hydration peaks of each mixture (ASTM C1679-17 [2017]).

Coefficient of thermal expansion—The 7-day coefficient of thermal expansion (CTE) of the mortar mixtures was evaluated using the method outlined in AASHTO T 336-22 (2022) to determine whether the engineering composites will face thermal stability issues in practice. Mortar and concrete specimens were cast in 100 x 200 mm cylindrical molds, consolidated using a vibrating table in two lifts, and cured under sealed conditions for 1 day. After demolding, the mortar specimens were cured in saturated limewater in a 23°C moist room for 6 days. The RC specimens were cured in accordance with the accelerated moist-curing method outlined in ASTM C1202-19 (2019). Prior to testing, specimens were ground to lengths of 178 mm. Two replicates were tested for each mixture composition.

Mortar compression testing—Mortar mixtures were consolidated into cube molds using a vibrating table and placed into a moist room (ASTM C511-19 [2019]). The compressive strengths of the mortar mixtures were evaluated at 3, 7, and 28 days following ASTM C109/C109M-21 (2021). The mortar cubes were demolded 1 day after casting and placed in saturated limewater at 23 ± 2°C until testing. The compressive strength was determined by averaging triplicate specimens at each age.

Neutron attenuation—Mortar specimens were cast into 100 x 200 mm cylindrical molds and consolidated using vibration to remove air voids. After moist curing for 7 days, the mortar specimens were sliced into 10, 30, and 50 mm thick sections using a wet diamond saw prior to measurement. This allowed the measurement of neutron attenuation at thicknesses of 10, 30, 40, 50, 60, 80, and 90 mm by combining slices of varying thickness. Attenuation measurements of each mortar mixture occurred at curing

Table 6—Cement paste mixture designs for isothermal conduction calorimetry

Mixture name	Mixture ID	OPC, g (oz.)	Water, g (oz.)	HDPE, g (oz.)	Boron carbide, g (oz.)	^{10}B*
Control	Control	4 (0.1411)	2 (0.0705)	—	—	—
4 kg B10	4B	4 (0.1411)	2 (0.0705)	—	0.0733 (0.0026)	4 (0.0114)
11 kg B10	11B	4 (0.1411)	2 (0.0705)	—	0.2015 (0.0071)	11 (0.0314)
20 kg B10	20B	4 (0.1411)	2 (0.0705)	—	0.3663 (0.0129)	20 (0.0571)
40 kg B10	40B	4 (0.1411)	2 (0.0705)	—	0.7326 (0.0258)	40 (0.1143)
80 kg B10	80B	4 (0.1411)	2 (0.0705)	—	1.4652 (0.0517)	80 (0.2286)
5%PE	5P	4 (0.1411)	2 (0.0705)	0.2 (0.0071)	—	—
10%PE	10P	4 (0.1411)	2 (0.0705)	0.4 (0.0141)	—	—
20%PE	20P	4 (0.1411)	2 (0.0705)	0.8 (0.0282)	—	—
20 kg B10 + 5%PE	20B-5P	4 (0.1411)	2 (0.0705)	0.2 (0.0071)	0.3663 (0.0129)	20 (0.0571)
20 kg B10 + 10%PE	20B-10P	4 (0.1411)	2 (0.0705)	0.4 (0.0141)	0.3663 (0.0129)	20 (0.0571)
20 kg B10 + 20%PE	20B-20P	4 (0.1411)	2 (0.0705)	0.8 (0.0282)	0.3663 (0.0129)	20 (0.0571)

*^{10}B mass proportion in kg/350 kg OPC (oz./oz. OPC).

ages of 7 days. Neutron attenuation of the mortar mixtures was assessed at 7 days to reflect real-world construction practices. In practice, thin composite panels would need to be installed during reactor downtime, which is limited to approximately 7% of the year, to limit disruption. This provides a short window of time for composite panels to be cast and retrofitted onto aging CBS structures. However, the curing time of the mortar mixtures is unlikely to influence neutron-shielding efficiency because neutron shielding is predominantly dictated by elemental composition.

Specimens were irradiated with a 1 Ci plutonium-beryllium alpha-neutron source (^{239}Pu-Be). The ^{239}Pu-Be source generated a neutron flux of approximately 10^6 n/cm^2·s on contact. The average neutron energy was 5.1 MeV, with a range up to approximately 10 MeV. Neutrons in the thermal range constituted a small fraction of the ^{239}Pu-Be flux energy spectrum. A ^{3}He gas proportional neutron detector was used to measure neutron counts. A 25 mm ^{3}He gas tube under high pressure was paired with a neutron pulse monitoring module. The operating voltage of the detector was tuned to optimize neutron detection efficiency. Neutron counts were measured using a nuclear instrument module (NIM).

An annular, cylindrical drum composed of HDPE (referred to as the collimation drum) was used to collimate neutrons generated by the ^{239}Pu-Be source. The collimation drum consisted of a collimation port with a diameter of 40 mm and a height of 250 mm (collimation ratio of approximately 6.25). The wall thickness of the collimation drum was 180 mm. The neutron source was placed at the bottom of the collimator port to maximize collimation efficiency. To measure the baseline neutron emission of the collimation port, a ^{3}He detector was positioned above the surface of the HDPE collimation drum; the distance between the center of the detector and the top surface of the HDPE drum was approximately 16.5 cm. An annular cadmium sheet (thermal neutron cross section of 2520 b) with an inner diameter of 40 mm, an outer diameter of 400 mm, and a thickness of 0.08 mm was positioned on top of the HDPE collimation port to reduce measurement noise from neutrons moderated by the HDPE drum.

Figure 1 shows the experimental setup for neutron attenuation testing. Neutrons were counted over a 4-minute period to keep measurement uncertainty below 1%. Neutron attenuation was calculated by normalizing neutron counts when a specimen was present to neutron counts of the collimated neutron source. Lower neutron attenuation values indicate that a smaller fraction of the collimated neutrons transmitted through the sample, which means better neutron-shielding efficiency.

The shielding efficiency of mortars exposed to a purely high-energy neutron spectrum was also measured by placing a 0.08 mm thick, square cadmium sheet with a side length of 50 mm between the specimens and the neutron source. The cadmium sheet was used to absorb neutrons with energies up to 0.41 eV, thus exposing mortar specimens to a purely high-energy neutron flux.

EXPERIMENTAL RESULTS AND DISCUSSION

Isothermal calorimetry

Calorimetry data show that mixtures 11B and 20B (11 kg ^{10}B/350 kg ordinary portland cement [OPC] and 20 kg ^{10}B/350kg OPC, respectively) enhanced cement reactivity, as depicted in Fig. 2. Mixtures 4B and 40B generated similar instantaneous heat flow curves with slightly higher main hydration peaks than the control. Moreover, the 4B, 11B, 20B, and 40B mixtures did not show appreciable change in the relative intensities of the main silicate and secondary aluminate peaks. Heat production from the 80B mixture was lower during the main silicate peak compared to the other mixtures. The sulfate depletion peak and the secondary aluminate reactivity peak from the 80B mixture were not as visible as in the other mixtures. During specimen preparation, the high doses of boron carbide powder in mixtures 40B and 80B adversely affected the cohesiveness of fresh paste, which may have affected heat flow measurements. Mixtures with high quantities of boron carbide congealed into globular masses during mixing and made poor contact with the internal surface of the calorimetry vials. Poor contact between the paste and the vial impedes the flow of heat from the pastes to the calorimeter heat sink and could

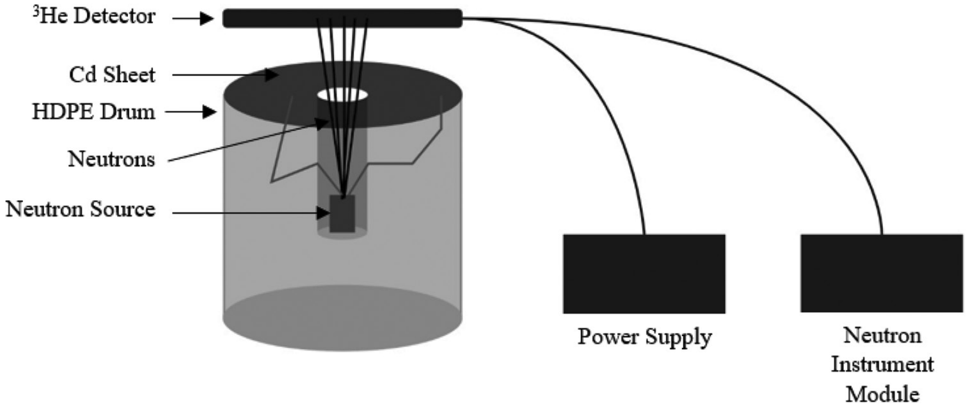

Fig. 1—Schematic of neutron attenuation experiment.

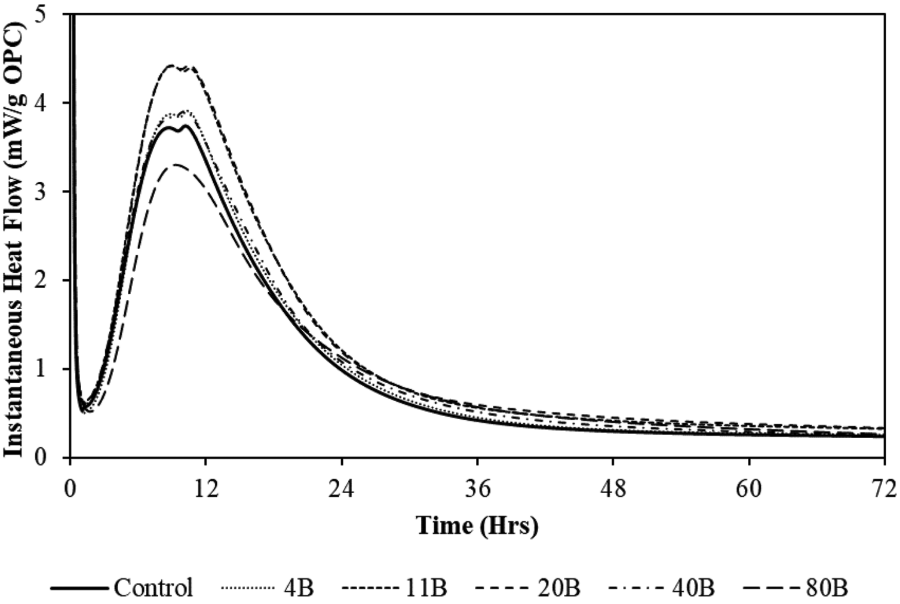

Fig. 2—Instantaneous heat flow curves for boron carbide-amended pastes.

reduce the accuracy of the measurements. Despite operational issues during mixing and measurement for mixtures with high boron carbide content, the results indicate that boron carbide does not induce delays in hydration, which is consistent with previous literature (Glinicki et al. 2018).

The control, 5P, 10P, 20B-5P, 20B-10P, and 20B-20P mixtures produced nearly identical heat profiles, as shown in Fig. 3. Mixture 20P, however, moderately reduced heat production during the main peak. Similar to the mixtures made with high boron carbide content, paste mixtures with high quantities of HDPE had poor workability during mixing and made poor contact with the calorimetry vials.

Boron carbide and HDPE powders were not found to delay hydration at the test dosages. The length of the induction and acceleration periods was similar for the control and boron carbide-amended mixtures. The main peaks occurred at approximately the same time as well. In contrast, relatively small additions of borate compounds can delay the occurrence of the main peak for several days (Ataie 2019; Glinicki et al. 2018; Li et al. 2021). The presence, quantity, and uniformity of ^{10}B within the cement matrix only impact shielding performance and not its chemical environment.

Coefficient of thermal expansion

The mortar mixtures had higher CTE values than the RC, as shown in Table 7. The relative difference between the RC mixture and the mortar mixtures is due to the contributions from coarse aggregate in concrete, which is known to have a lower CTE than cement paste (Mehta and Monteiro 2014). The inclusion of HDPE increases the CTE of mortars due to the comparatively high CTE of HDPE, which typically ranges from 100 to 200 $\mu\varepsilon$/°C, while aggregates used in concrete have approximate CTE values in the range of 7 to 12 $\mu\varepsilon$/°C (Davis 1930; Kumar et al. 2011; Ferraro et al. 2015). This further supports the concern that a coating would experience high differential thermal strains if bonded to a concrete substrate; mechanically fastened panels would not produce the same concerns. Boron carbide lowered CTE values relative to the control mortar mixtures, likely resulting from the lower CTE of boron carbide (approximately 5.7 to 5.9 $\mu\varepsilon$/°C) relative to other components in the mortar matrix (Yakel 1973). Although boron carbide reduced thermal sensitivity in the HDPE-amended mortars, the CTE of mixtures with boron carbide and HDPE was still significantly higher than that of the control mortar or RC mixtures.

Mortar compressive strength

The compressive strengths of mortars containing boron carbide are shown in Fig. 4. Mortars containing boron carbide powder were found to develop sufficient strength for structural applications at 3 days, despite exhibiting lower 28-day strengths than the control. Boron carbide reduced the 28-day compressive strengths of the mortar mixtures by 8 to 17% compared to the control. However, the 3-day compressive strengths of the 20B, 40B, and 80B mixtures were approximately 9 to 26% higher than that of the control, while 7-day compressive strengths were comparable. The 3- and 7-day compressive strengths of the 4B and 11B were similar or marginally lower than those of the control. The boron carbide had a finer particle-size distribution than the silica sand, which may have improved particle packing and subsequent strength at higher fine aggregate replacement rates. However, this does not explain why strength did not substantially improve for mixtures with higher boron carbide content after 7 days. Although some measured strengths deviated from the control by up to 26%, the compressive strengths of the boron carbide and control mortars generally remained within a relatively narrow band. The workability of mixtures with high boron carbide dosages was poor, necessitating higher doses of PCE. Without sufficient PCE, mixtures were difficult to consolidate into molds. This behavior has previously been observed in a study that showed that the partial substitution of fine aggregates with boron carbide led to slight increases in the early-age compressive strengths of mortar cubes but reduced 28-day strengths, relative to the control mixture (Glinicki et al. 2018).

Table 7—CTE values

	Mixture ID	με/°C (με/°F)
Mortar	Control	16.6 (9.22)
	4B	15.1 (8.39)
	11B	15.4 (8.56)
	20B	14.7 (8.17)
	40B	13.4 (7.44)
	80B	12.6 (7.00)
	5P	15.6 (8.67)
	10P	17.6 (9.78)
	20P	20.3 (11.28)
	20B-5P	14.7 (8.17)
	20B-10P	16.6 (9.22)
	20B-20P	17.3 (9.61)
Concrete	RC	11.8 (6.56)

The addition of HDPE powders reduced compressive strength relative to the control with and without the presence of boron carbide powder, as shown in Fig. 5. The combination of lower binder content and the impact of HDPE on the microstructure of mortars likely caused this reduction in strength. Strength loss has been observed in cement-based systems when fine aggregates are partially replaced with plastic (Badache et al. 2018; Choi et al. 2009; Malkapur et al. 2017; Saikia and de Brito 2012). The smooth surface texture and spherical morphology of micronized plastic particles likely cause a weakened cementitious matrix due to poor plastic-cement paste bonding and interlocking (Rocco and Elices 2009; Siddique et al. 2008; Zhou et al. 2021). Moreover, HDPE-based aggregates are reported to increase matrix porosity in cement-based systems due to their innate hydrophobicity, leading to poor mechanical properties (Iucolano et al. 2013). Water repulsion near plastic surfaces has been suggested to impede cement hydration by preventing the uniform diffusion of ionic species, further increasing porosity and lowering strength (Saikia and de Brito 2012) while likely increasing the interfacial transition zone distance around plastic particles. The low modulus of elasticity of plastic polymers may also reduce the compressive strength of cementitious systems (Saikia and de Brito 2012). Moreover, boron carbide, at an addition rate of 20 kg ^{10}B per m^3 of mortar, did not appreciably alter strength

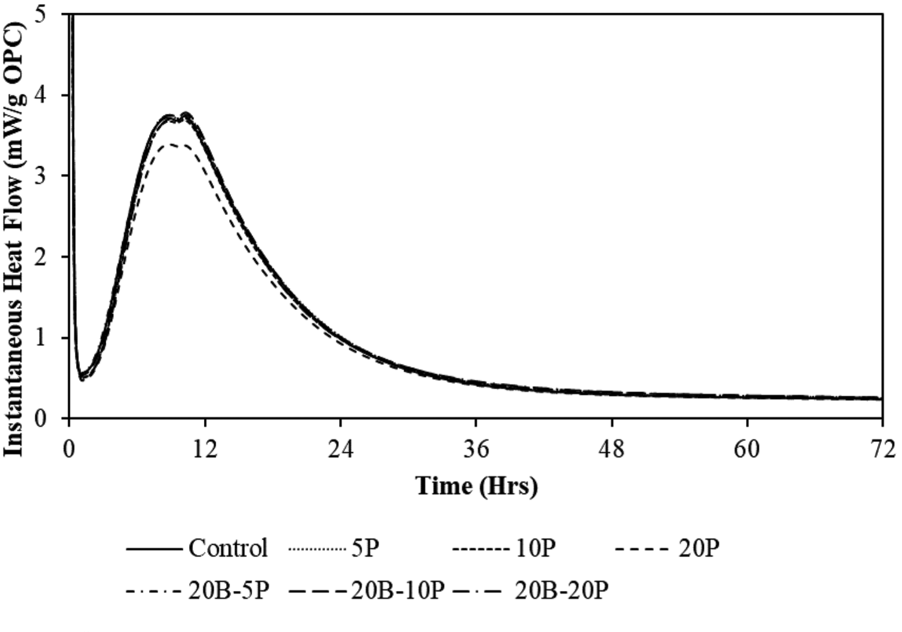

Fig. 3—Instantaneous heat flow curves for HDPE and boron carbide-amended pastes.

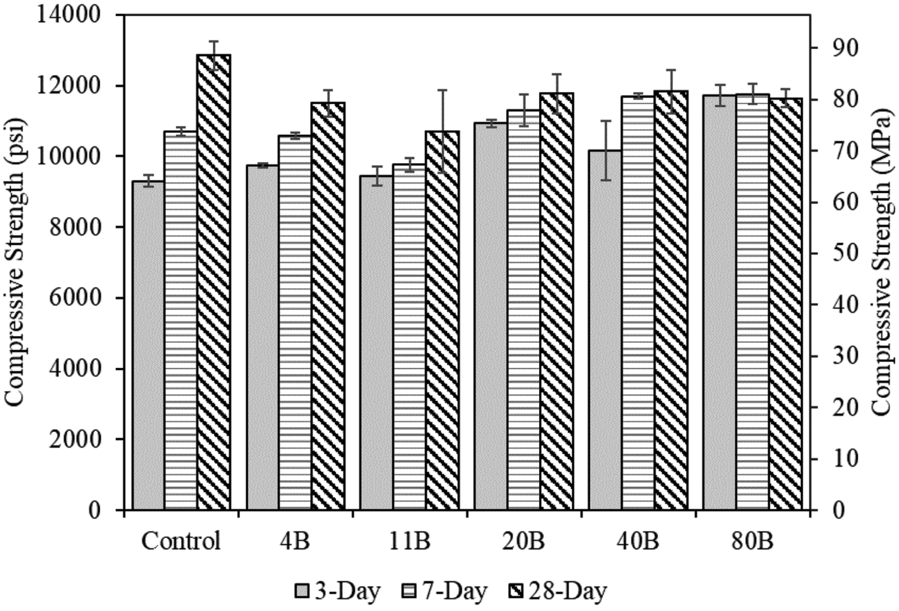

Fig. 4—Compressive strengths of mortars with boron carbide.

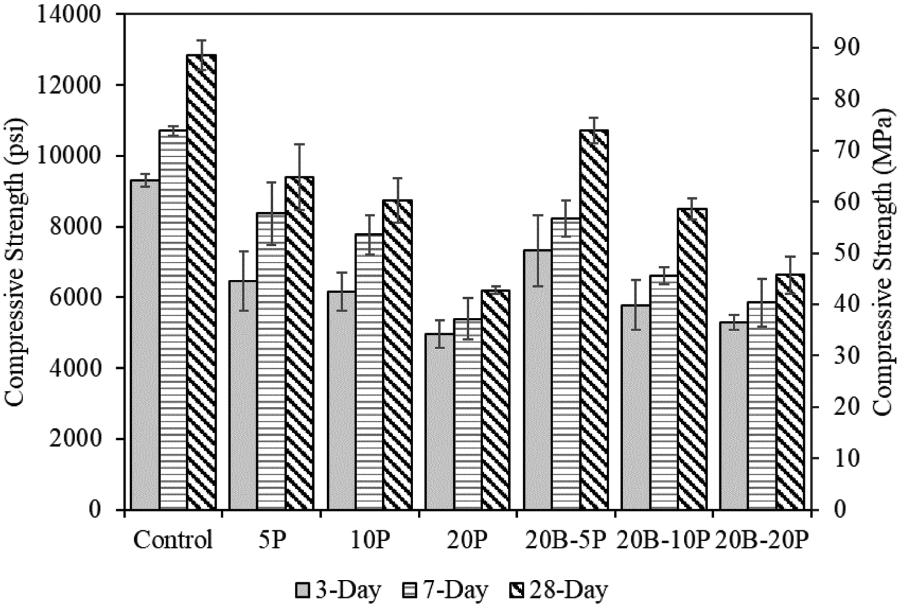

Fig. 5—Compressive strength of mortars with HDPE and boron carbide.

development in mortars with fine aggregates consisting of 10 or 20% HDPE by mass. Lower HDPE content likely allowed early-age cement hydration to proceed with less interruption, while the inclusion of fine boron carbide particles was able to more efficiently improve particle packing when sufficient PCE was used. Although HDPE lowers strength development in mortars when used as a partial fine aggregate replacement, the results indicate that HDPE-amended mortar mixtures generate sufficient strength for structural applications when appropriate mixture design parameters are selected and water-reducing admixtures are used.

Neutron attenuation of mortars under 1 Ci ^{239}Pu-Be neutron radiation field

The neutron attenuation of mortar panels made with boron carbide is compared to the control mortar and RC when exposed to a mixed energy spectrum in Fig. 6. As expected, increasing boron carbide content led to greater neutron-shielding performance under the mixed energy spectrum. There was a clear performance gap between mixtures with boron carbide and those without (control and RC) across all tested thicknesses, indicating that boron carbide had a greater effect on attenuation than specimen thickness. Furthermore, boron carbide-amended specimens required less thickness than either the control or RC mixture to achieve equivalent shielding performance. Mixture 4B exhibited better shielding performance at 30 mm than the control and RC specimens at 90 mm. Mixtures with higher boron carbide content than Mixture 4B required only 10 mm to achieve similar or better shielding performance than the 90 mm thick control and RC specimens.

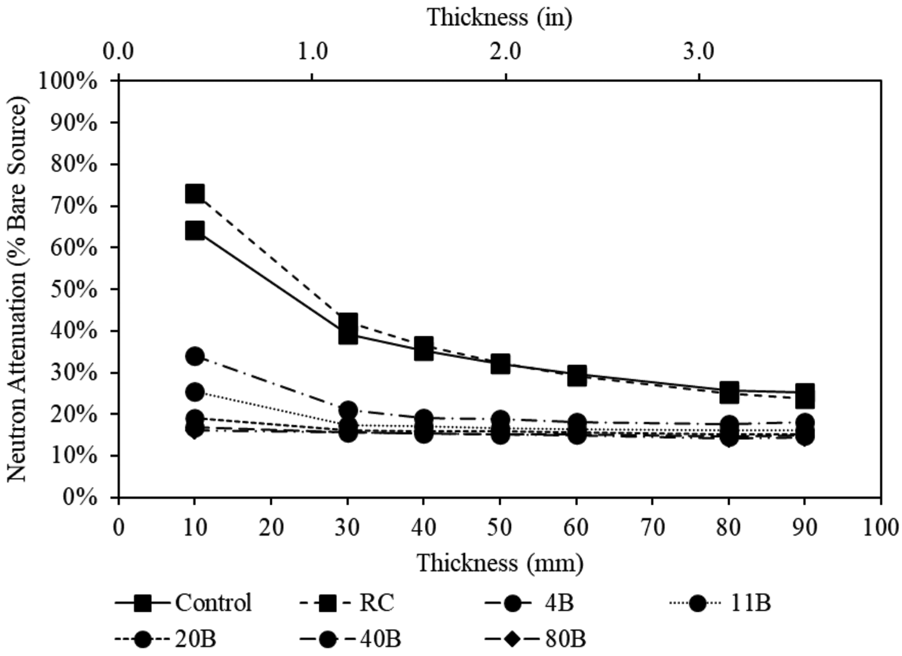

Fig. 6—Neutron attenuation of mortars with boron carbide under mixed energy spectrum (^{239}Pu-Be full spectrum). Lower neutron attenuation values indicate better shielding performance.

Higher boron content led to diminishing improvements in neutron shielding. Despite having more than twice the boron content of the 4B mixture, the 11B mixture improved shielding efficiency by approximately 25.2% at a thickness of 10 mm. The diminishing returns on boron content were more apparent when examining the shielding performances of mixtures 40B and 80B. The 40B and 80B mixtures improved thermal neutron shielding by 73.8% and 74.8%, respectively, compared to the control at 10 mm thickness. Although the 40B and 80B mixtures had 10 and 20 times the boron content as mixture 4B, respectively, neutron shielding only improved by slightly more than double at thicknesses of 10 mm. The marginal utility of boron further diminished as specimen thickness increased. At 50 mm, the 11B mixture enhanced shielding efficiency by approximately 11.2% compared to the 4B mixture. The diminishing returns are also a function of the 1 Ci neutron source; having a source with more neutron flux, longer irradiation times, different energy spectrums, and other factors would all change the resulting efficiency as a function of boron loading.

These results indicate that initial boron doses need to be carefully optimized in practice to meet the shielding requirements, such as physical size restrictions and allowable dose burdens. Although boron content has lower marginal returns on thermal neutron shielding at higher doses, retrofit applications of the composites may benefit from higher initial boron content. Boron and neutron-shielding efficiency are expected to progressively decay when subjected to neutron radiation; the rate of boron decay is dependent on the initial boron dose, neutron flux, and the neutron energy distribution. This is because ^{10}B transmutes to ^{7}Li, a stable lithium isotope with a relatively low absorption cross section, during neutron absorption. At high initial boron doses, a relatively large decrease in boron content would yield a low reduction in shielding efficiency, as evidenced by the difference in shielding efficiencies of mixtures 40B and 80B. Because dosing would be based on shielding efficiency, higher initial boron doses would exponentially extend the lifespan and serviceability of retrofit panels.

The normalized neutron counts are expected to stabilize near zero given sufficient specimen thickness and boron content. One potential reason this may not be happening is that high-energy neutrons moderated within the specimen but not absorbed are being detected. Though the ^{3}He detection chamber used in this study is highly efficient at detecting thermal neutrons, it still registers moderated higher-energy neutrons as counts. Furthermore, the cadmium annular sheet used to prevent uncollimated thermal neutrons from reaching the detector is not as efficient in filtering out neutrons that were moderated, but not thermalized, within the walls of the HDPE collimator. These moderated and uncollimated neutrons (that do not interact with the specimen) may be thermalized within the detector gas chamber and counted. Both factors are likely partially responsible for the observed higher-than-expected lower limits.

The addition of HDPE in mixtures without boron carbide improved shielding performance relative to the control and RC mixtures (Fig. 7), but not as strongly as boron carbide. Furthermore, the shielding performance between mixtures containing only HDPE and the control mixture converged as thicknesses increased. Although hydrogen isotopes are poor absorbers of neutrons relative to ^{10}B, they are strong neutron moderators. Neutrons that are moderated into the thermal energy range are more efficiently absorbed by hydrogen or other atomic nuclei within the mortar specimen. Previous work has shown that increasing hydrogen content, whether through bound water content (Prochon and Piotrowski 2020) or the use of hydrogenous polymers (Malkapur et al. 2017), incrementally improves the neutron-shielding efficiency of cement-based systems. Mixtures 20B-5P, 20B-10P, and

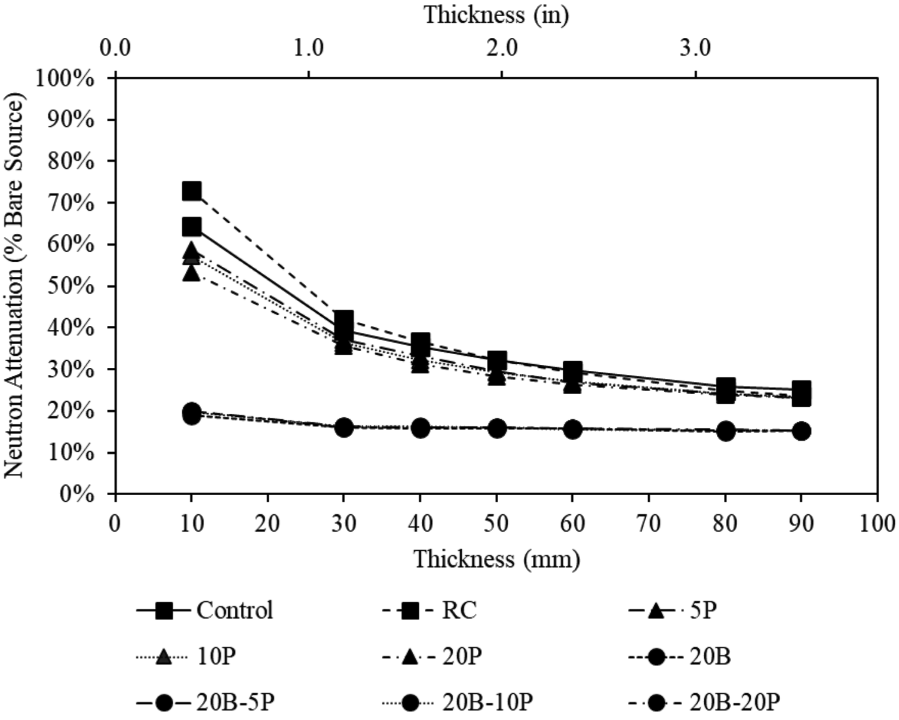

Fig. 7—Neutron efficiency of mortars with HDPE and boron carbide under mixed energy spectrum (^{239}Pu-Be full spectrum). Lower neutron attenuation values indicate better shielding performance.

20B-20P exhibited nearly identical attenuation to the 20B mixture. Despite increasing hydrogen content, shielding performance is dominated by the presence of boron carbide. The neutron detector used in this study was more sensitive to lower-energy neutrons. Neutrons in the higher-energy ranges that were moderated by HDPE could have been absorbed by boron carbide without detection.

Neutron attenuation under purely high-energy neutron spectrum

To investigate whether HDPE improves the efficiency of boron at high neutron energy ranges, evaluation of shielding under a purely fast-neutron spectrum was performed. It was posited that if this were correct, mixtures with only HDPE would produce more detectable neutrons than the baseline measurement, and mortars with both HDPE and boron would show no difference from just boron mortars. If this were the case, the hydrogen addition would thermalize neutrons for the boron to capture, effectively removing more neutrons from the system.

The neutron radiation field produced by the ^{239}Pu-Be neutron source was filtered to remove low-energy, or thermal, neutrons using a 0.08 mm thick cadmium sheet. The shielding performance of mortars modified with only boron carbide can be found in Fig. 8. The shielding performance of mortars subjected to a purely high-energy neutron flux was enhanced with increasing boron carbide content and specimen thickness; shielding efficiency of boron carbide-amended mixtures was not as high under the purely high-energy spectrum relative to performance under the mixed energy spectrum. This is because the neutron absorption cross section decreases as neutron energies increase. Neutron attenuation results indicated that mixtures with boron carbide required less thickness than the RC mixture to achieve equivalent shielding. The improvement in shielding was primarily a function of boron content because the hydrogen loads in the control and boron carbide-amended mortar mixtures were nearly equivalent.

When hydrogen was boosted using HDPE powder as partial fine aggregate replacement in mortar mixtures with no boron carbide, the normalized neutron counts increased under a purely high-energy neutron flux as anticipated (Fig. 9). This indicates that the additional hydrogen assisted in moderating the high-energy neutrons such that they were detectable by the ^{3}He gas proportional counter. Relative to the control mixture, the addition of hydrogen significantly improved neutron moderation. When boron carbide was incorporated into the HDPE-amended mortar mixtures, the mortar mixtures exhibited lower normalized neutron counts than the control or the mortar mixture containing only boron carbide. This shows that the synergistic blend of HDPE and boron can significantly enhance the neutron-shielding capacity of mortar shields by working to moderate and absorb neutrons across a wider energy spectrum than mixtures with only boron.

It is appropriate to discuss the life cycle of a shielding application of this type when discussing service-life extension. If used as a mechanically fastened panel, bond strength and compressive strength would not be critical design considerations; rather, degradation of the panel from radiation and reduction in shielding efficiency over time would be the most significant considerations. Based upon the work by Remec (2013), for a selected two-loop and three-loop NPP, the thermal neutron flux experienced at the surface of a CBS is approximately 4×10^9 n/cm^2·s and 1.9×10^9 n/cm^2·s, respectively. As the capture of a single neutron results

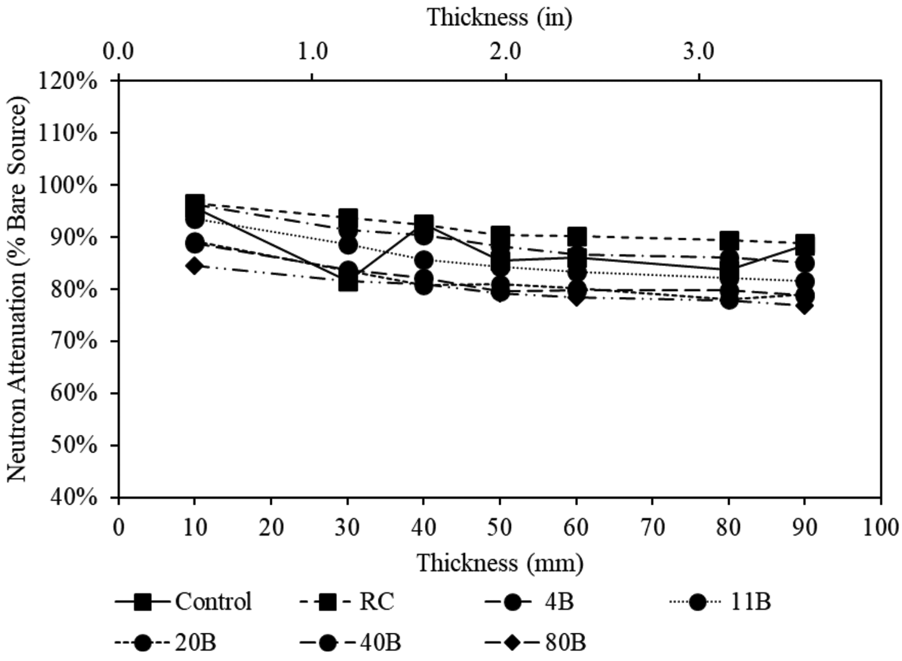

Fig. 8—Neutron attenuation of mortars with boron carbide under high-energy neutron spectrum (^{239}Pu-Be with cadmium filter). Lower neutron attenuation values indicate better shielding performance.

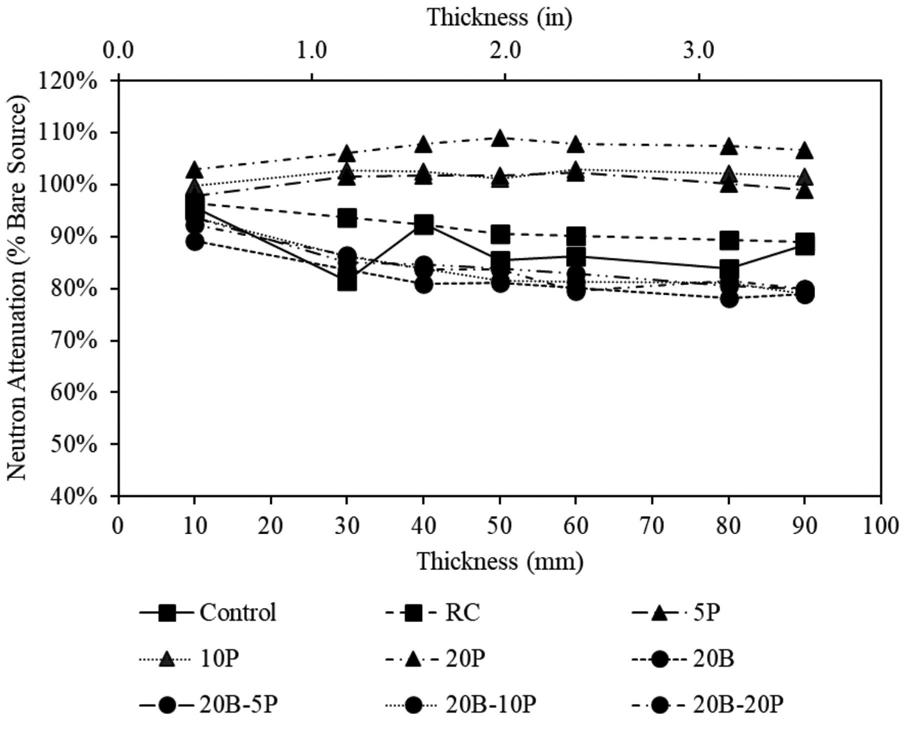

Fig. 9—Neutron attenuation of mortars with HDPE and boron carbide under high-energy neutron spectrum (^{239}Pu-Be with cadmium filter). Lower neutron attenuation values indicate better shielding performance.

in one ^{10}B atom transmuting into lithium and helium, the boron depletion can be calculated using boron dosage per m^3, thickness of shielding, neutron flux, and operating time. Using the work of Remec (2013) as a guide, a dosage of 4 kg ^{10}B/m^3 resulted in a concentration of 0.004 g/cm^3. For a 1 cm thick coating, this means 0.004 g ^{10}B per exposed cm^2; converting to number of atoms of ^{10}B using Avogadro's number results in 2.4×10^{20} ^{10}B atoms. Because one neutron is absorbed per atom, a neutron flux of 4×10^9 n/cm^2·s would result in complete depletion after approximately 2000 years, assuming perfect capture. As shown experimentally, this number is not accurate due to the self-shielding of particles, streaming effects, imperfect homogenization, neutron energy differences, and moderation, among other factors. As such, in future research, the researchers anticipate installing specimens into the University of Florida Training Reactor (UFTR) to subject specimens to extended neutron flux to investigate radiation damage that equates to more than 5 years of thermal neutron exposure in a three-loop NPP.

CONCLUSIONS

In this research, the combined effects of boron carbide and high-density polyethylene (HDPE) powders were evaluated for compatibility, structural and thermal properties, and neutron-shielding performance in cementitious systems. The hydration kinetics of cement paste mixtures amended with boron carbide and HDPE polymers were first evaluated to check for potential issues with setting. The coefficient of thermal expansion (CTE) and strength development of mortars amended with boron carbide and HPDE powders as partial fine aggregate replacements were then tested. Finally, the neutron-shielding efficiency of mortars was evaluated in relation to radiological concrete (RC) under purely high-energy and mixed-neutron energy spectrums. Based upon the results, the following conclusions were drawn:

1. The shielding mortars outperformed typical RC exposed to a mixed-neutron energy source. The same performance can be achieved with mortars amended with boron carbide, with a 90% reduction in thickness compared to the RC.
2. Using a purely fast neutron energy source, the shielding mortars outperformed traditional RC. The same performance can be achieved with mortars amended with boron carbide and HDPE, with a 90% reduction in thickness compared to the RC under the given test conditions.
3. The combination of boron carbide and HDPE powders do not substantially retard the hydration kinetics of cement.
4. HDPE powders substantially increased CTE values relative to the control mortar (up to 22%) and RC (up to 72%), which are representative of existing concrete biological shields (CBSs). Due to the high CTE of the HDPE-modified mortars, thermal cracking potential should be assessed under realistic thermal loading conditions in future research.
5. The control and boron carbide-amended mortars exhibited adequate compressive strength suitable for nonstructural and structural applications. However, retrofit panels would not be expected to be load-bearing during application. Compressive strength is used to demonstrate the ability to resist mechanical stress during exposure to radiation. Though not experimentally tested in this study, tensile strength under realistic thermal loading conditions in nuclear power plants (NPPs) will be examined in future research.
6. HDPE powder reduces compressive strength across all ages, but appropriate mixture designs can be used to achieve sufficient strength for most structural applications. Tensile strength may be impacted by HDPE powder, especially under thermal loading conditions reflective of NPPs, but further testing is required.

AUTHOR BIOS

Ashish D. Patel *is a Postdoctoral Research Associate in the Department of Civil and Coastal Engineering at the University of Florida, Gainesville, FL. He received his BA from the University of California, Berkeley, Berkeley, CA; his MS from California State University, Fullerton, Fullerton, CA; and his PhD from the University of Florida. His research interests include cement hydration kinetics, concrete biological shielding, and concrete durability.*

ACI member **Jerry M. Paris** *is a Research Civil Engineer at the U.S. Army Corps of Engineers Engineer Research and Development Center (ERDC). He received his BS, MS, and PhD from the University of Florida. He is a member of ACI Committees 207, Mass and Thermally Controlled Concrete, and 323, Low-Carbon Concrete Code. His research interests include concrete durability, nuclear shielding concrete, concrete sustainability, cement chemistry, and military construction.*

Christopher C. Ferraro, *FACI, is an Associate Professor in the Department of Civil and Coastal Engineering at the University of Florida, where he received his BS, MS, and PhD. He is Vice Chair of ACI Committee 323, Low-Carbon Concrete Code, and a member of the ACI Technical Activities Committee and 10 other ACI committees. His research interests include waste management, alternative materials, and durability of portland cement concrete.*

James E. Baciak *is a Professor in the Nuclear Engineering Program and the Department of Materials Science and Engineering at the University of Florida. He is also the Director of the Consortium for Nuclear Forensics and the Chair of the Reactor Safety Review Subcommittee for the University of Florida. He received his PhD in nuclear engineering from the University of Michigan, Ann Arbor, MI.*

Kyle A. Riding, *FACI, is a Professor and Head of the Department of Civil and Coastal Engineering at the University of Florida. He received his PhD in civil engineering from The University of Texas at Austin, Austin, TX. He is Chair of ACI Committee 231, Properties of Concrete at Early Ages, and a member of ACI Committees 201, Durability of Concrete; 207, Mass and Thermally Controlled Concrete; and 236, Material Science of Concrete; and ACI Subcommittee 318-A, General, Concrete, and Construction.*

ACI member **Eric R. Giannini** *is the Director of Product Standards and Technology for the American Cement Association. He received his PhD from The University of Texas at Austin. He is Secretary of ACI Committee 323, Low-Carbon Concrete Code, and a member of ACI Committees 123, Research and Current Developments, and 228, Nondestructive Testing of Concrete. His research interests include alkali-silica reaction, nondestructive testing, and sustainability.*

ACKNOWLEDGMENTS

The researchers would like to thank the United States Department of Energy (DOE) for funding this research under the Advanced Research Projects Agency – Energy program (ARPA-E) project No. DE-AR-000157 and program manager J. King. The researchers would also like to acknowledge C. McCall, who provided the mixture design and coarse aggregate for the production of radiological concrete, and R. Zeidan for assisting with laser particle-size analysis. Lastly, the authors would like to thank C. Nmai, Distinguished Engineer and Director of Concrete Sustainability at Master Builders Solutions for the provision of admixtures used for this research.

REFERENCES

AASHTO T 336-22, 2022, “Standard Method of Test for Coefficient of Thermal Expansion of Hydraulic Cement Concrete,” American Association of State Highway and Transportation Officials, 9 pp.

ASTM C33/C33M-18, 2018, “Standard Specification for Concrete Aggregates,” ASTM International, West Conshohocken, PA, 8 pp.

ASTM C109/C109M-21, 2021, “Standard Test Method for Compressive Strength of Hydraulic Cement Mortars (Using 2-in. or [50 mm] Cube Specimens),” ASTM International, West Conshohocken, PA, 12 pp.

ASTM C150/C150M-19, 2019, “Standard Specification for Portland Cement,” ASTM International, West Conshohocken, PA, 10 pp.

ASTM C192/C192M-19, 2019, “Standard Practice for Making and Curing Concrete Test Specimens in the Laboratory,” ASTM International, West Conshohocken, PA, 8 pp.

ASTM C305-20, 2020, “Standard Practice for Mechanical Mixing of Hydraulic Cement Pastes and Mortars of Plastic Consistency,” ASTM International, West Conshohocken, PA, 3 pp.

ASTM C511-19, 2019, “Standard Specification for Mixing Rooms, Moist Cabinets, Moist Rooms, and Water Storage Tanks Used in the Testing of Hydraulic Cements and Concretes,” ASTM International, West Conshohocken, PA, 3 pp.

ASTM C618-17, 2017, “Standard Specification for Coal Fly Ash and Raw or Calcined Natural Pozzolan for Use in Concrete,” ASTM International, West Conshohocken, PA, 5 pp.

ASTM C1202-19, 2019, “Standard Test Method for Electrical Indication of Concrete’s Ability to Resist Chloride Ion Penetration,” ASTM International, West Conshohocken, PA, 8 pp.

ASTM C1233-15(2021), 2021, "Standard Practice for Determining Equivalent Boron Contents of Nuclear Materials," ASTM International, West Conshohocken, PA, 3 pp.

ASTM C1679-17, 2017, "Standard Practice for Measuring Hydration Kinetics of Hydraulic Cementitious Mixtures Using Isothermal Calorimetry," ASTM International, West Conshohocken, PA, 15 pp.

ASTM C1702-17, 2017, "Standard Test Method for Measurement of Heat of Hydration of Hydraulic Cementitious Materials Using Isothermal Conduction Calorimetry," ASTM International, West Conshohocken, PA, 9 pp.

Ataie, F. F., 2019, "Influence of Cementitious System Composition on the Retarding Effects of Borax and Zinc Oxide," *Materials*, V. 12, No. 15, Aug., Article No. 2340. doi: 10.3390/ma12152340

Badache, A.; Benosman, A. S.; Senhadji, Y.; and Mouli, M., 2018, "Thermo-Physical and Mechanical Characteristics of Sand-Based Lightweight Composite Mortars with Recycled High-Density Polyethylene (HDPE)," *Construction and Building Materials*, V. 163, Feb., pp. 40-52. doi: 10.1016/j.conbuildmat.2017.12.069

Chidiac, S. E.; El-Samrah, M. G.; Reda, M. A.; and Abdel-Rahman, M. A. E., 2021, "Mechanical and Radiation Shielding Properties of Concrete Containing Commercial Boron Carbide Powder," *Construction and Building Materials*, V. 313, Dec., Article No. 125466. doi: 10.1016/j.conbuildmat.2021.125466

Choi, Y. W.; Moon, D. J.; Kim, Y. J.; and Lachemi, M., 2009, "Characteristics of Mortar and Concrete Containing Fine Aggregate Manufactured from Recycled Waste Polyethylene Terephthalate Bottles," *Construction and Building Materials*, V. 23, No. 8, Aug., pp. 2829-2835. doi: 10.1016/j.conbuildmat.2009.02.036

Davis, R. E., 1930, "A Summary of the Results of Investigations Having to Do with Volumetric Changes in Cements, Mortars, and Concretes, Due to Causes Other Than Stress," *ACI Journal Proceedings*, V. 26, No. 2, Feb., pp. 407-443.

Ferraro, C. C.; Tibbetts, C. M.; Perry, M. C.; Watts, B. E.; and Paris, J. M., 2015, "Effects of Coarse Aggregate on the Physical Properties of Florida Concrete Mixes," FDOT Contract No. BDV-31-977-08se, Florida Department of Transportation, Tallahassee, FL, 172 pp.

Field, K. G.; Remec, I.; and Le Pape, Y., 2015, "Radiation Effects in Concrete for Nuclear Power Plants – Part I: Quantification of Radiation Exposure and Radiation Effects," *Nuclear Engineering and Design*, V. 282, Feb., pp. 126-143. doi: 10.1016/j.nucengdes.2014.10.003

Fillmore, D. L., 2004, "Literature Review of the Effects of Radiation and Temperature on the Aging of Concrete," Report No. INEEL/EXT-04-02319, Idaho National Engineering and Environmental Laboratory, Idaho Falls, ID, Sept., 26 pp. doi: 10.2172/910954

Glinicki, M. A.; Antolik, A.; and Gawlicki, M., 2018, "Evaluation of Compatibility of Neutron-Shielding Boron Aggregates with Portland Cement in Mortar," *Construction and Building Materials*, V. 164, Mar., pp. 731-738. doi: 10.1016/j.conbuildmat.2017.12.228

Hei, D.; Jia, W.; Cheng, C.; Yao, Z.; Shan, Q.; Ling, Y.; and Gao, Y., 2021, "Feasibility Study of Fast Neutron-Induced Gamma Ray Imaging of Large Sample Based on D-T Neutron Generator," *Nuclear Instruments and Methods in Physics Research Section B: Beam Interactions with Materials and Atoms*, V. 492, Apr., pp. 7-14. doi: 10.1016/j.nimb.2021.01.014

Hilsdorf, H. K.; Kropp, J.; and Koch, H. J., 1978, "The Effects of Nuclear Radiation on the Mechanical Properties of Concrete," *Douglas McHenry International Symposium on Concrete and Concrete Structures*, SP-55, B. Bresler, ed., American Concrete Institute, Farmington Hills, MI, pp. 223-254.

Hsiao, Y.-H.; La Plante, E. C.; Krishnan, N. M. A.; Le Pape, Y.; Neithalath, N.; Bauchy, M.; and Sant, G., 2017, "Effects of Irradiation on Albite's Chemical Durability," *The Journal of Physical Chemistry A*, V. 121, No. 41, Oct., pp. 7835-7845. doi: 10.1021/acs.jpca.7b05098

Iucolano, F.; Liguori, B.; Caputo, D.; Colangelo, F.; and Cioffi, R., 2013, "Recycled Plastic Aggregate in Mortars Composition: Effect on Physical and Mechanical Properties," *Materials & Design (1980-2015)*, V. 52, Dec., pp. 916-922. doi: 10.1016/j.matdes.2013.06.025

Kharita, M. H.; Yousef, S.; and AlNassar, M., 2011, "Review on the Addition of Boron Compounds to Radiation Shielding Concrete," *Progress in Nuclear Energy*, V. 53, No. 2, Mar., pp. 207-211. doi: 10.1016/j.pnucene.2010.09.012

Kinchin, G. H., and Pease, R. S., 1955, "The Displacement of Atoms in Solids by Radiation," *Reports on Progress in Physics*, V. 18, No. 1, Jan., pp. 1-51. doi: 10.1088/0034-4885/18/1/301

Kumar, S.; Panda, A. K.; and Singh, R. K., 2011, "A Review on Tertiary Recycling of High-Density Polyethylene to Fuel," *Resources, Conservation and Recycling*, V. 55, No. 11, Sept., pp. 893-910. doi: 10.1016/j.resconrec.2011.05.005

Le Pape, Y.; Alsaid, M. H. F.; and Giorla, A. B., 2018, "Rock-Forming Minerals Radiation-Induced Volumetric Expansion – Revisiting Literature Data," *Journal of Advanced Concrete Technology*, V. 16, No. 5, pp. 191-209. doi: 10.3151/jact.16.191

Le Pape, Y.; Field, K. G.; and Remec, I., 2015, "Radiation Effects in Concrete for Nuclear Power Plants, Part II: Perspective from Micromechanical Modeling," *Nuclear Engineering and Design*, V. 282, Feb., pp. 144-157. doi: 10.1016/j.nucengdes.2014.10.014

Le Pape, Y.; Giorla, A.; and Sanahuja, J., 2016, "Combined Effects of Temperature and Irradiation on Concrete Damage," *Journal of Advanced Concrete Technology*, V. 14, No. 3, pp. 70-86. doi: 10.3151/jact.14.70

Li, Q.; Ma, H.; Tang, Y.; and Chen, W., 2021, "Combined Effect of $NaAlO_2$ and NaOH on the Early Age Hydration of Portland Cement with a High Concentration of Borate Solution," *Cement and Concrete Research*, V. 144, June, Article No. 106430. doi: 10.1016/j.cemconres.2021.106430

Malkapur, S. M.; Divakar, L.; Narasimhan, M. C.; Karkera, N. B.; Goverdhan, P.; Sathian, V.; and Prasad, N. K., 2017, "Neutron Radiation Shielding Properties of Polymer Incorporated Self Compacting Concrete Mixes," *Applied Radiation and Isotopes*, V. 125, July, pp. 86-93. doi: 10.1016/j.apradiso.2017.03.029

Malkapur, S. M.; Satdive, H.; Narasimhan, M. C.; Karkera, N. B.; Goverdhan, P.; and Sathian, V., 2015, "Effect of Mix Parameters and Hydrogen Loading on Neutron Radiation Shielding Characteristics of Latex Modified Concrete Mixes," *Progress in Nuclear Energy*, V. 83, Aug., pp. 8-12. doi: 10.1016/j.pnucene.2015.02.010

Maruyama, I.; Kontani, O.; Sawada, S.; Sato, O.; Igarashi, G.; and Takizawa, M., 2013, "Evaluation of Irradiation Effects on Concrete Structure: Background and Preparation of Neutron Irradiation Test," *Proceedings of ASME 2013 Power Conference (POWER2013)*, V. 2, Boston, MA, 9 pp. doi: 10.1115/POWER2013-98114

Mehta, P. K., and Monteiro, P. J. M., 2014, *Concrete: Microstructure, Properties, and Materials*, fourth edition, McGraw-Hill Education, New York.

Mondal, S.; Bykova, E.; Dey, S.; Ali, S. I.; Dubrovinskaia, N.; Dubrovinsky, L.; Parakhonskiy, G.; and van Smaalen, S., 2016, "Disorder and Defects Are Not Intrinsic to Boron Carbide," *Scientific Reports*, V. 6, No. 1, Article No. 19330. doi: 10.1038/srep19330

Moradllo, M. K.; Chung, C.-W.; Keys, M. H.; Choudhary, A.; Reese, S. R.; and Weiss, W. J., 2020, "Use of Borosilicate Glass Powder in Cementitious Materials: Pozzolanic Reactivity and Neutron Shielding Properties," *Cement and Concrete Composites*, V. 112, Sept., Article No. 103640. doi: 10.1016/j.cemconcomp.2020.103640

Pignatelli, I.; Kumar, A.; Field, K. G.; Wang, B.; Yu, Y.; Le Pape, Y.; Bauchy, M.; and Sant, G., 2016, "Direct Experimental Evidence for Differing Reactivity Alterations of Minerals following Irradiation: The Case of Calcite and Quartz," *Scientific Reports*, V. 6, No. 1, Article No. 20155. doi: 10.1038/srep20155

Primak, W., 1958, "Fast-Neutron-Induced Changes in Quartz and Vitreous Silica," *Physical Review*, V. 110, No. 6, June, pp. 1240-1254. doi: 10.1103/PhysRev.110.1240

Prochon, P., and Piotrowski, T., 2020, "The Effect of Cement and Aggregate Type and w/c Ratio on the Bound Water Content and Neutron Shielding Efficiency of Concretes," *Construction and Building Materials*, V. 264, Dec., Article No. 120210. doi: 10.1016/j.conbuildmat.2020.120210

Remec, I., 2013, "Radiation Environment in Concrete Biological Shields of Nuclear Power Plants," Light Water Reactor Sustainability Program, U.S. Department of Energy, Washington, DC.

Remec, I.; Rosseel, T. M.; Field, K. G.; and Le Pape, Y., 2017, "Characterization of Radiation Fields for Assessing Concrete Degradation in Biological Shields of NPPs," *EPJ Web of Conferences*, V. 153, Article No. 05009. doi: 10.1051/epjconf/201715305009

Remec, I.; Rosseel, T. M.; Field, K. G.; and Le Pape, Y., 2018, "Radiation-Induced Degradation of Concrete in NPPs," *Reactor Dosimetry: 16th International Symposium*, D. W. Vehar, K. R. DePriest, and M. H. Sparks, eds., Santa Fe, NM, pp. 201-211. doi: 10.1520/STP160820170059

Rocco, C. G., and Elices, M., 2009, "Effect of Aggregate Shape on the Mechanical Properties of a Simple Concrete," *Engineering Fracture Mechanics*, V. 76, No. 2, Jan., pp. 286-298. doi: 10.1016/j.engfracmech.2008.10.010

Rockwell, T. III, ed., 1956, "Reactor Shielding Design Manual," United States Atomic Energy Commission, Washington, DC, 480 pp. doi: 10.2172/4360248

Rosseel, T. M.; Maruyama, I.; Le Pape, Y.; Kontani, O.; Giorla, A. B.; Remec, I.; Wall, J. J.; Sircar, M.; Andrade, C.; and Ordonez, M., 2016, "Review of the Current State of Knowledge on the Effects of Radiation on Concrete," *Journal of Advanced Concrete Technology*, V. 14, No. 7, pp. 368-383. doi: 10.3151/jact.14.368

Saikia, N., and de Brito, J., 2012, "Use of Plastic Waste as Aggregate in Cement Mortar and Concrete Preparation: A Review," *Construction and Building Materials*, V. 34, Sept., pp. 385-401. doi: 10.1016/j.conbuildmat.2012.02.066

Shin, J. W.; Lee, J.-W.; Yu, S.; Baek, B. K.; Hong, J. P.; Seo, Y.; Kim, W. N.; Hong, S. M.; and Koo, C. M., 2014, “Polyethylene/Boron-Containing Composites for Radiation Shielding,” *Thermochimica Acta*, V. 585, June, pp. 5-9. doi: 10.1016/j.tca.2014.03.039

Siddique, R.; Khatib, J.; and Kaur, I., 2008, “Use of Recycled Plastic in Concrete: A Review,” *Waste Management*, V. 28, No. 10, pp. 1835-1852. doi: 10.1016/j.wasman.2007.09.011

Sindelar, R. L.; Dupont, M. E.; Iyer, N. C.; Lam, P. S.; Skidmore, T. E.; Utsch, F. R.; and Zapp, P. E., 2000, “Degradation and Failure Characteristics of NPP Containment Protective Coating Systems,” Report No. WSRC-TR-2000-00079, U.S. Nuclear Regulatory Commission, Washington, DC, 97 pp.

Sindelar, R. L.; Dupont, M. E.; Iyer, N. C.; Lam, P. S.; Skidmore, T. E.; Utsch, F. R.; and Zapp, P. E., 2001, “Degradation and Failure Characteristics of NPP Containment Protective Coating Systems,” Report No. WSRC-TR-2001-00067, U.S. Nuclear Regulatory Commission, Washington, DC, 106 pp.

Yakel, H. L., 1973, “Lattice Expansions of Two Boron Carbides between 12 and 940°C,” *Journal of Applied Crystallography*, V. 6, No. 6, Dec., pp. 471-473. doi: 10.1107/S0021889873009246

Zhou, X.; Xie, Y.; Long, G.; and Li, J., 2021, “Effect of Surface Characteristics of Aggregates on the Compressive Damage of High-Strength Concrete Based on 3D Discrete Element Method,” *Construction and Building Materials*, V. 301, Sept., Article No. 124101. doi: 10.1016/j.conbuildmat.2021.124101

ACI MATERIALS JOURNAL TECHNICAL PAPER

Title No. 122-M22

Evaluation of Different Migratory Corrosion Inhibitors as Repair Strategy for Reinforced Concrete

by Ashish Kumar Tiwari, Purnima Dogra, Shweta Goyal, and Vijay Luxami

This research establishes a systematic methodology for selecting a migratory corrosion inhibitor (M-CoI) as a repair strategy for reinforced concrete (RC) structures exposed to aggressive environments. Conducted in two phases, Phase 1 involves corrosion testing in pore solutions to evaluate inhibitor efficacy, while Phase 2 examines the percolation ability of M-CoIs in different concrete systems and performance of M-CoI in RC with corroded reinforcing bars. The findings reveal that the efficiency of the compounds as repair measures is significantly lower than their preventive performance, primarily due to the presence of corrosion products on the steel surface. Additionally, the effectiveness of the M-CoIs is influenced by their concentration and form at the reinforcing bar level; specifically, 4-Aminobenzoic acid (ABA) achieved maximum concentration in its purest form, whereas Salicylaldehyde (SA) and 2-Aminopyridine (AP) reached the reinforcing bar in lower concentrations. Importantly, the study highlights that compounds effective in pore solution may not perform well in concrete, underscoring the necessity of considering the intended application—preventive or repair—when selecting inhibitors. Thus, a comprehensive approach involving both pore solution testing and migration ability assessments is essential for optimal corrosion protection in reinforced concrete.

Keywords: carbonation; chloride; corrosion; corrosion inhibitors; fly ash-blended cement; repair strategy.

INTRODUCTION

In reinforced concrete (RC) structures, the protection of steel is ensured by the alkaline nature of the concrete pore solution, with pH ranging from 12.5 to 13.5. That allows the formation of a passive layer (γ-Fe_2O_3) around the reinforcing bar, acting as a barrier to metal dissolution.[1] The corrosion of reinforcing bars initiates when this protective shield is compromised by external aggressive agents, such as chloride ions (Cl^-) and carbon-dioxide (CO_2).[2] The severity of corrosion is most pronounced when both of these factors occur together, rather than individually,[3,4] as chloride-induced corrosion and the carbonation of concrete strongly influence each other.[5] In the authors' previous research, it was observed that the combined action of these two on the reinforcing bar surface increases the corrosion rate multiple times as compared to the individual environment. Both pitting and uniform corrosion occur on the bar surface simultaneously, making a more vulnerable situation for the reinforcing bars.[6,7] However, protection against such a condition is still a vacant region to explore.

Common repair strategies for corroded RC include cathodic protection, electrochemical chloride extraction, corrosion inhibitors, and electrochemical re-alkalization. Except for corrosion inhibitors, these methods are costly and require continuous electricity. Migratory corrosion inhibitors (M-CoIs) can be applied to the concrete surface, diffusing through the cover to protect reinforcing bars after corrosion initiation.[8] Most M-CoIs are proprietary, primarily designed for chloride-induced corrosion, but often misused in carbonated or combined environments, where they prove ineffective.[9] Even in chloride conditions, their claimed efficiency applies mainly to fresh RC with passive, corrosion-free reinforcing bars, while their molecular structure and mechanism remain undisclosed.

The inhibition mechanisms of various corrosion inhibitors, including green and synthetic compounds, have been extensively studied to reduce steel corrosion. Their efficiency depends on molecular structure (aliphatic or aromatic), functional groups (–NH_2, –COOH, –OH, SH, –CHO), number of functional groups in single compound, presence of additional hetero-atoms, and number of adsorption sites.[10,11] However, their performance is typically evaluated in simulated pore solutions replicating isolated corrosive environments, with limited progression to concrete applications.[12-14] This gap necessitates a systematic approach to assess their effectiveness in restoring steel passivation within concrete.

Studying M-CoIs in combined aggressive environments for actively corroding reinforcing bars is crucial. Instead of proprietary products, generic compounds with efficient functional groups and known structures should be explored. Aromatic compounds with varied functional groups and heteroatoms have shown excellent inhibition in harsh environments like chloride, carbonation, sulfuric acid, and so on.[15,16] Considering all these factors, this study investigates three such compounds—4-Aminobenzoic acid (ABA), 2-Aminopyridine (AP), and Salicylaldehyde (SA)—selected for their structural diversity and effectiveness in combined environments.[7,17] Preliminary findings suggest ABA and SA inhibit corrosion though chelation-based adsorption, with differences in inhibition mechanisms due to functional group positioning. AP, however, increases solution resistance and restricts anodic reactions, making these compounds promising candidates for RC repair applications.

In the presented study, the inhibition ability of these generic compounds against ongoing corrosion in RC is

---

ACI Materials Journal, V. 122, No. 4, July 2025.

MS No. M-2024-059.R5, doi: 10.14359/51746804, received January 30, 2025, and reviewed under Institute publication policies. Pertinent discussion including author's closure, if any, will be published ten months from this journal's date if the discussion is received within four months of the paper's print publication.

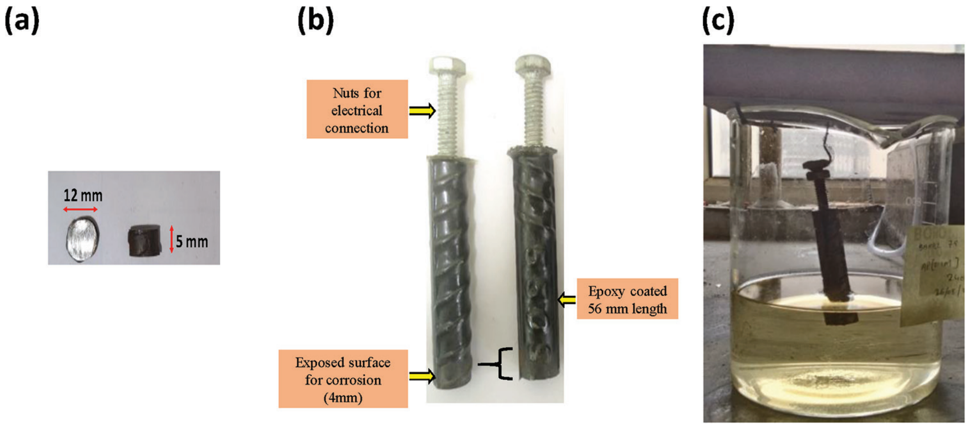

Fig. 1—(a) Steel coupons; (b) specimen for electrochemical test; and (c) specimen immersed in SCP solution.

explored by using various techniques. The work is executed on the corroded reinforcing bars in two phases: Phase 1, pore solution testing; and Phase 2, testing on concrete. During the first phase, potentiodynamic polarization curves were used to assess the inhibition behavior and surface analysis was carried out to understand the working mechanism of generic compounds; while, in the second phase (Phase 2), percolation capacity in concrete and inhibition efficiency of generic compounds on RC specimens was assessed. Based on the obtained results, the correct methodology to select a corrosion inhibitor and the inhibition mechanism of the selected compounds were developed.

RESEARCH SIGNIFICANCE

This research aims to establish a systematic methodology for selecting M-CoIs as a repair strategy for RC structures in aggressive environments. Conducted in two phases, the study first evaluates the efficacy of selected M-CoIs in simulated pore solutions and then assesses their performance within concrete systems. By investigating the influence of molecular structure and functional groups on inhibitor effectiveness, this work addresses limitations seen in existing proprietary products, which often lack transparency in terms of their percolation capacity and inhibition mechanisms in real-world conditions, which emphasize on-site results without providing detailed approaches or discussing the molecular structure of inhibitors, leading to limited understanding and transparency.[18-20] Furthermore, the systematic approach presented herein is largely absent in current literature, where inhibitor selection often lacks a consistent methodology. Findings from this research aim to advance effective repair strategies, enhancing the durability and longevity of RC structures.

EXPERIMENTAL INVESTIGATION AND PROCEDURE

The evaluation of the inhibitory effectiveness of organic compounds was carried out in two distinct phases: Phase 1 involved synthetic pore solution testing, while Phase 2 focused on concrete testing. In both the phases, the reinforcing bar specimens were subjected to accelerated corrosive environments before application of respective inhibitor. For reproducibility in data, all the tests were performed on triplicate specimens.

Phase 1: Corrosion testing in simulated concrete pore (SCP) solution

Material for Phase 1—Thermomechanically treated (TMT) steel cylindrical bars of 12 mm diameter made of grade Fe550D steel, which are extensively used in the construction industry, conforming to IS 1786-2008,[21] were used in this study. Two types of specimens were prepared from the bars: steel coupons of 5 mm height, and cylindrical specimens of 60 mm height (shown in Fig. 1(a) and (b)). The former was used to evaluate the corrosion initiation time and to perform the surface analysis tests, while the latter were used to perform electrochemical tests for evaluating corrosion inhibition performance of the selected organic compounds. Prior to the immersion in SCP solution, the steel coupons were abraded with emery papers of different grit sizes, and washed with distilled water and then hexane. The method for the preparation of steel specimens for electrochemical tests and the pore solution simulating concrete's interstitial fluid constituents (SCP) was reported by Tiwari et al.,[7] to which 0.1M NaCl admixed and 99% pure CO_2 (to reach pH~9) was bubbled to further simulate the combined aggressive environment. The obtained SCP solution is referred to as S1. M-CoIs were added to S1 after the initiation of corrosion on the reinforcing bar specimens.

ABA, AP, and SA were selected as M-CoIs due to their aromatic structures and functional groups that enhance chelation of ferrous ions and mitigate corrosion.[22] ABA comprises a benzene ring with carboxylic (–COOH) and amine (–NH2) groups. AP is a heterocyclic compound with an amine group linked to a pyridine ring containing nitrogen. SA features a benzene ring with adjacent aldehyde (–CHO) and hydroxyl (–OH) groups. The heteroatoms and double bonds in these compounds donate electron pairs to the d-orbitals of iron, forming coordinate complexes with ferrous ions. These properties validate their selection as effective M-CoIs. The authors' research demonstrated >90% inhibition efficiency of ABA, AP, and SA in combined aggressive environments through pore solution testing and RC specimen application as preventive techniques. All three M-CoIs have performed well with >90% inhibition efficiency.[6] Each M-CoI was individually mixed in synthetic pore solution at an optimal concentration of 0.1M, as established previously.

Table 1—Nomenclature and detail of respective solutions

Nomenclature	Inhibitor	Molecular structure	Molecular mass, g/mol	Solution composition
S1 (Base solution)	—	—	—	Carbonated pore solution + 0.1M NaCl
S1 + ABA	4-Aminobenzoic acid (ABA)	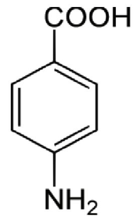	134.17	Base solution + 0.1M 4-Aminobenzoic acid
S1 + AP	2-Aminopyridine (AP)	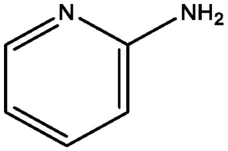	94	Base solution + 0.1M 2-Aminopyridine
S1 + SA	Salicylaldehyde (SA)	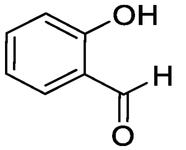	122.12	Base solution + 0.1M Salicylaldehyde

Details of the compounds and Phase 1 testing nomenclature are provided in Table 1.

Testing for Phase 1—The effectiveness of M-CoI was assessed by conducting electrochemical tests—that is, potentiodynamic polarization scanning on actively corroding cylindrical reinforcing bar specimens immersed in M-CoI-admixed pore solutions.

Surface analysis: Surface analysis techniques were applied to TMT steel coupons (12 mm diameter and 5 mm height) to examine the metal surface both with and without inhibitor after a 240-hour immersion period. For microscopy analysis, a digital microscope was used, and the surface morphology of the dried specimens was observed using scanning electron microscopy (SEM). The elements present on the surface were identified through energy-dispersive X-ray spectroscopy (EDX). An accelerating voltage of 10 kV was employed for both imaging and EDX analysis, and magnifications were set at 500×.

Electrochemical test: Using data from steel coupons, 12 mm diameter (as mentioned in the "Material for Phase 1" subsection) cylindrical specimens with height of 60 mm were placed in S1 for 10 hours to trigger corrosion initiation. After 240 hours, potentiodynamic polarization (PDP) scans were conducted to evaluate corrosion activity. The 240-hour period was chosen based on literature identifying it as optimal for representing inhibitor performance.[23,24] It has been explicitly noted that a testing duration of 240 hours is suitable for accurately representing the inhibitor's actual performance against corrosion. The test setup (shown as Fig. SD1 in the Appendix[*]) employed an instrument with a three-electrode system: TMT reinforcing bar as the working electrode, a saturated calomel electrode (SCE) as the reference, and a platinum electrode as the counter. PDP scans, performed at 0.5 mV/s over –250 mV to +1500 mV versus OCP, provided inhibition mechanisms and corrosion current density (i_{corr}) values to calculate inhibition efficiency (λ)

$$\lambda\ (\%) = ((i_{corr,0} - i_{corr,1})/i_{corr,0}) \times 100 \tag{1}$$

where $i_{corr,0}$ represents the corrosion current density after 240 hours in the absence of inhibitor, while $i_{corr,1}$ represents the corrosion current density after 240 hours in the presence of M-CoI.

Phase 2: Testing on reinforced concrete specimens

Material for Phase 2—Two distinct types of cement in the study—namely, portland cement (OPC) and fly-ash-based pozzolanic cement (PPC), in accordance with Indian standards IS 8112:2013[25] and IS 1489 (Part 1)-1991[26] (detailed composition presented in Table SD1). Fine aggregates were obtained from river sand, and coarse aggregates were in sizes of 20 and 10 mm following IS 383-2016.[27] The two aggregate sizes were combined in a 1:1 ratio (physical properties of all the aggregates are provided in Table SD2). The concrete mixture was formulated in accordance with IS 10262,[28] using a water-cement ratio (*w*/*c*) of 0.43, resulting in a final mixture proportion by weight of 1:1.39:2.91 (cement: fine aggregates: coarse aggregates). The detailed mixture design proportions by weight are provided in the Appendix as Table SD3.

Reinforcement in RC specimens consisted of 12 mm diameter TMT bars, like those employed in Phase 1. These bars were cut to a length of 360 mm and prepared in accordance with ASTM G109 guidelines.[29] Of this 360 mm length, the central 200 mm was intentionally exposed to corrosion. To achieve this, epoxy was initially applied over an 80 mm section on both ends of the bar, followed by the application of insulating tape. Subsequently, a neoprene rubber tube, 3 mm thick, was placed over the insulating tape. A representative prepared bar is depicted in Fig. 2(a). At one end of the

---

[*] The Appendix is available at **www.concrete.org/publications** in PDF format, appended to the online version of the published paper. It is also available in hard copy from ACI headquarters for a fee equal to the cost of reproduction plus handling at the time of the request.

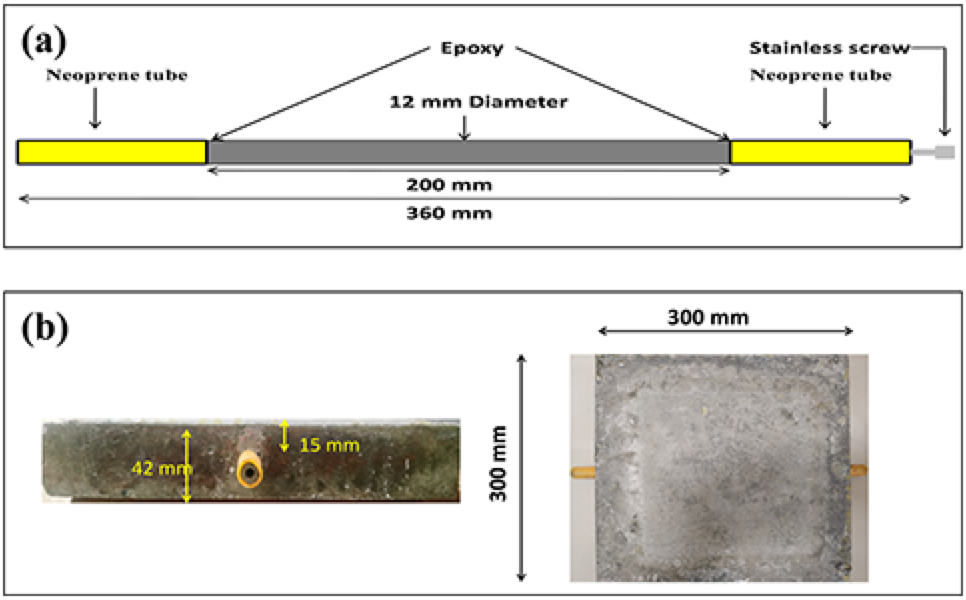

Fig. 2—Cross-sectional details of: (a) reinforcing bar; and (b) prism specimen.

Table 2—Labels and description of specimens

Inhibitor applied	Material used	Labels	Material used	Labels
—	OPC	OC	PPC	PC
4-Aminobenzoic acid		O-ABA-R		P-ABA-R
2-Aminopyridine		O-AP-R		P-AP-R
Salicyaldehyde		O-SA-R		P-SA-R

bar, a threaded hole was created to insert a screw, ensuring electrical connectivity.

RC specimen preparation and inhibitor application—Two types of concrete specimens were prepared: 100 mm cubes and 300 x 300 x 42 mm reinforced concrete prisms, with a single bar embedded at a 15 mm clear cover, as illustrated in Fig. 2(b). Special molds ensured correct bar cover. Cubes were used to study inhibitor percolation and chloride/carbonation profiles over time, while prisms were employed for electrochemical tests on corrosion. All tests used triplicate specimens for reliability. In total, 24 prisms (12 each for OPC and PPC concrete) and 72 cubes (both concrete types) were cast. Inhibitors were applied to prisms at the active corrosion stage to evaluate M-CoI efficacy as a repair strategy. A 1M solution (ABA, AP, or SA in deionized water) was applied in three coats at 500 mL/m^2, per commercial guidelines, with sufficient absorption time between coats. After application, surfaces cured for 15 days for optimal inhibitor performance, similar to methods in Tiwari et al.[6] and Kaur et al.[30] A description of each specimen set is provided in Table 2.

Exposure cycle—The RC specimens were exposed to 7-day cyclic exposure, which consists of 2 days of wetting and 5 days of drying. During the wetting period, RC specimens were subjected to 3.5% NaCl solution by forming an artificial reservoir (200 x 200 x 70 mm) on the top surface of the specimens. To prevent evaporation losses, the reservoir was securely covered with a plastic sheet. After 2 days of wetting followed by 2 days of drying, specimens were exposed to carbonation for the period of the next 2 days. The chamber was maintained at a temperature of 30 ± 2°C and a relative humidity of 60 to 70%, with a CO_2 concentration of 5% by volume. Following this carbonation phase, the specimens underwent 1 day of air drying. Finally, at the conclusion of the cyclic exposure period, electrochemical tests were conducted.

Testing of Phase 2—

Percolation ability: The percolation of a specific compound was assessed at an interval of 15, 30, 45, and 60 days following its application. This assessment was based on the concentration detected at a specific depth using the ultraviolet (UV)-vis spectroscopy technique. This quantitative method allows for the determination of concentration, even in the case of very low quantities. For the specific procedure, refer to the detail provided in Tiwari et al.[17]

Corrosion monitoring: The efficacy of the selected inhibitor against reinforcing bar corrosion was evaluated using electrochemical methods, widely regarded as suitable for corrosion monitoring in RC structures.[31] Linear polarization resistance (LPR) tests were conducted every second exposure cycle, and electrochemical impedance spectroscopy (EIS) at 0, 10, 30, and 50 cycles. Crack width was monitored, stopping at 50 cycles when it exceeded 0.3 mm, the durability threshold per IS 456. It is important to mention that the M-CoI was applied after i_{corr} values indicated active corrosion (that is, the 10th cycle in the present case). An additional reading was taken after 15 days of M-CoI application

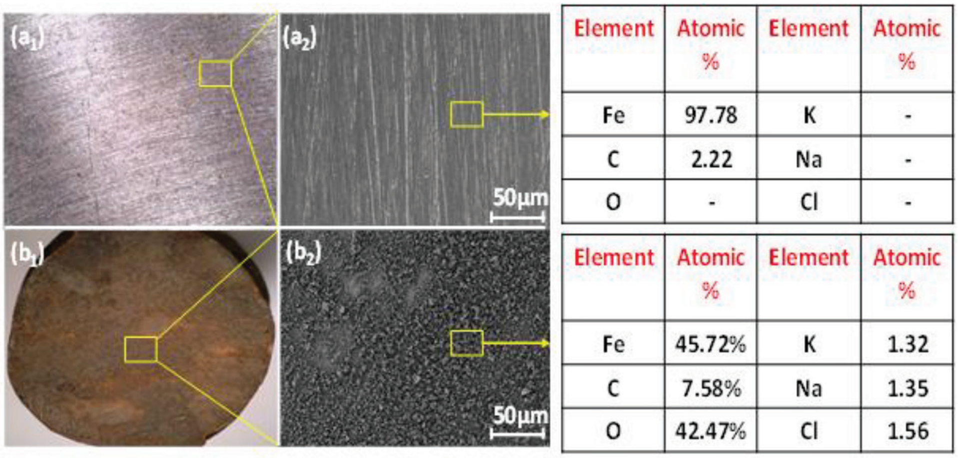

Element	Atomic %	Element	Atomic %
Fe	97.78	K	-
C	2.22	Na	-
O	-	Cl	-

Element	Atomic %	Element	Atomic %
Fe	45.72%	K	1.32
C	7.58%	Na	1.35
O	42.47%	Cl	1.56

Fig. 3—Surface inspection of steel coupons before and after 10 hours of immersion: (a) optical images; and (b) SEM-EDX.

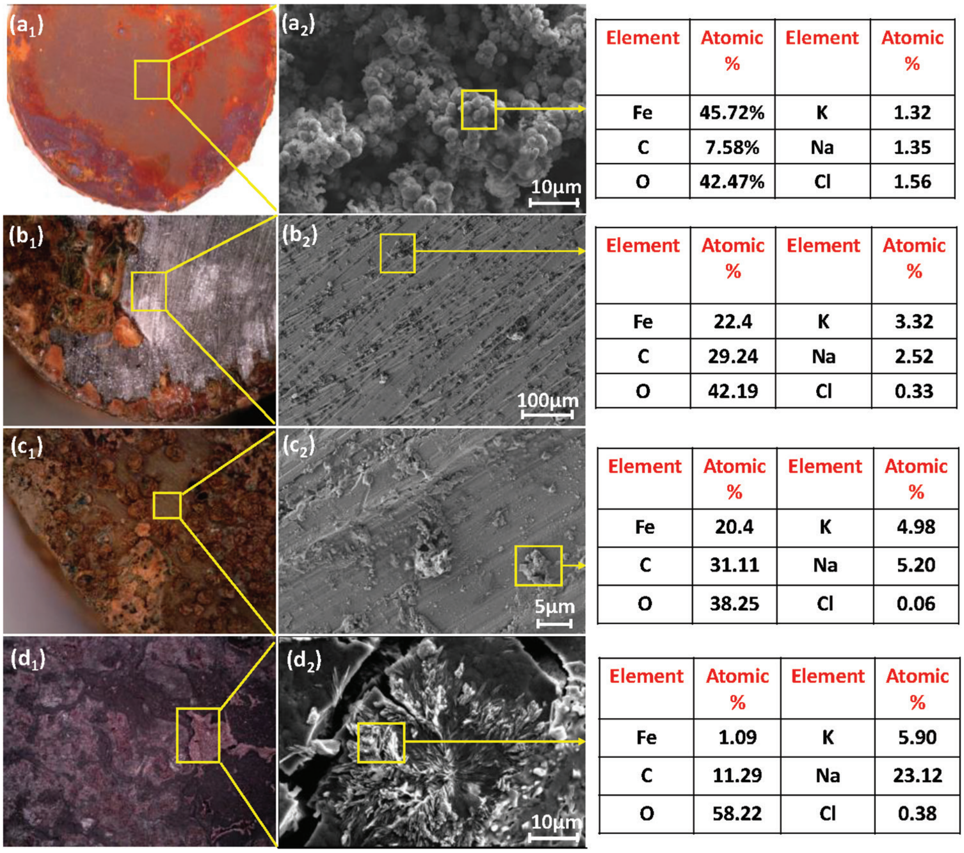

Element	Atomic %	Element	Atomic %
Fe	45.72%	K	1.32
C	7.58%	Na	1.35
O	42.47%	Cl	1.56

Element	Atomic %	Element	Atomic %
Fe	22.4	K	3.32
C	29.24	Na	2.52
O	42.19	Cl	0.33

Element	Atomic %	Element	Atomic %
Fe	20.4	K	4.98
C	31.11	Na	5.20
O	38.25	Cl	0.06

Element	Atomic %	Element	Atomic %
Fe	1.09	K	5.90
C	11.29	Na	23.12
O	58.22	Cl	0.38

Fig. 4—Optical microscopy images of: (a1) control (inhibitor-free); (b1) ABA; (c1) AP; and (d1) SA; and SEM images with EDX results of: (a2) control (inhibitor-free); (b2) ABA; (c2) AP; and (d2) SA admixed in pore solution.

to see any marked change in the electrochemical parameters. For electrochemical measurement, corrosion monitoring equipment with a guard ring was used.

Prior to commencing LPR tests, the testing surface was pre-wetted following ASTM C876.[32] The steel reinforcing bar (working electrode) was polarized ±25 mV from the equilibrium potential at a 10 mV/min scan rate. A wetted conducting sponge ensured contact with the guard ring, followed by the placement of the electrode assembly (reference, guard ring, and auxiliary, as shown in Fig. SD2).

EIS tests analyzed the concrete pore structure and corrosion mechanisms, including resistivity, dielectric properties, corrosion rate, and steel/concrete interface kinetics.[33] Sinusoidal voltage (25 mV) was applied across a 100 kHz to 1 mHz frequency range. Data was processed using EIS data analysis software for modeling.

RESULTS AND DISCUSSION

Phase 1 test results and discussion

Optical microscopy and SEM-EDX—

Corrosion initiation time: To get an idea of the corrosion initiation time, a set of steel coupons (three coupons) were immersed in S1 and monitored through optical microscopy after each hour. Once the occurrence of corrosion products/

pit embryo formation was witnessed, the samples were carefully taken out, dried, and subjected to SEM-EDX testing and the time to initiate corrosion was noted. The optical image of coupon before immersion and after formation of corrosion product is shown in Fig. 3(a1) and (b1). The initial surface was shiny and lustrous, whereas; after 10 hours of immersion some red brown products were visible over the entire surface. The morphological images of top surface (Fig. 3(a2) and (b2)) also indicated the development of hydroxides and oxides after 10 hours. The validity of the argument was further confirmed through EDX spectral analysis, which revealed a decrease in the concentration of iron (from 97.78 to 45.72%) and an increase in concentration of oxygen (from 0 to 42.47%) along with slight rise in C (from 2.22% to 7.58%). Therefore, a duration of 10 hours was considered to initiate corrosion on immersed reinforcing bars. After corrosion has been initiated, M-CoI's were added in S1 to assess their inhibition efficiencies on already corroded bars.

After the corrosion initiated, the compounds were added at 0.1M concentration in their respective solutions. The optical images and SEM-EDX results after 240 hours of immersion of steel coupons in M-CoI-free and M-CoI-admixed pore solution are presented in Fig. 4. As can be seen from Fig. 4(a1), the surface of the coupon immersed in M-CoI-free pore solution is severely corroded, with red-brown corrosion product accumulation all over the surface. The SEM image of the same sample (Fig. 4(a2)) displays the presence of globular loose products, which are confirmed as corrosion products by elemental analysis. With the addition of M-CoI, corrosion is seen to be reduced. For ABA and AP, the coupon surface exhibits a clear steel surface along with the presence of some product formation, whereas for SA, a black layer region and a few products' assemblage is observed from the optical images (Fig. 4(b1), (c1), and (d1)). From the SEM and EDX results, it is confirmed that maximum exposed area of the coupons was protected from corrosion in the presence of M-CoI. In M-CoI-admixed specimens, the concentration of Fe reduced from 45% to near 20% (for ABA and AP; while it reduced drastically to 1.09% for SA) with the corresponding increase in concentration of C (Fig. 4(b2), (c2), and (d2)). This indicates the presence of M-CoI molecules on the Fe surface due to some chelate formation, as organic molecules are the only source of C atoms in the pore solution.

Table 3—Corrosion current density and efficiency of generic compounds

	S0	S0+ABA	S0+AP	S0+SA
i_{corr}, µA/cm^2	92.57	44.05	52.85	15.62
Efficiency (%λ)—Repair	—	52.41	42.90	83.12
Efficiency (%λ)—Preventive[7,17]	—	99.97	99.97	99.9

These results suggest that the addition of aromatic multifunctional organic compounds has the potential to reduce the ongoing corrosion processes. To validate the inhibition efficiency of the selected M-CoIs by more reliable test methods, electrochemical testing was performed, and the results are discussed in the upcoming section.

Potentiodynamic polarization test (PDP)—Table 3 provides corrosion current densities (i_{corr}) and inhibition efficiencies. Though the tests were carried out in triplicate, only one (representative) measurement is included in the result due to consistent repeatability of the data.

From the obtained PDP curves and current density values, it can be seen that S1 shows a visible active zone of corrosion with high i_{corr} values (92.57 µA/cm^2), indicating severe corrosion; while, with the addition of organic compounds, a significant decrease in the i_{corr} values (44.05 µA/cm^2, 52.85 µA/cm^2, and 15.62 µA/cm^2 for ABA, AP, and SA, respectively) was witnessed. The decrease in i_{corr} indicates that the generic compounds can reduce the ongoing corrosion processes. Among the three M-CoIs, SA displayed the highest inhibition efficiency of 83.12%, followed by ABA and AP. The shift of the corrosion potential towards the noble side is also indicative of the protective nature of selected compounds. Hence, it can be stated that all the three organic compounds can act as potential M-CoIs as repair strategy in

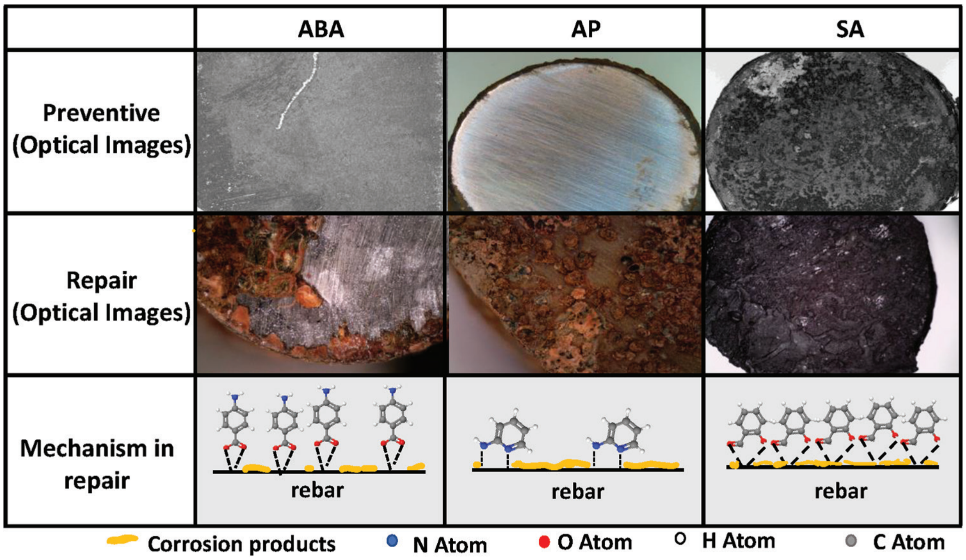

Fig. 5—Optical images of preventive versus repair strategy and inhibition mechanism in repair strategy.

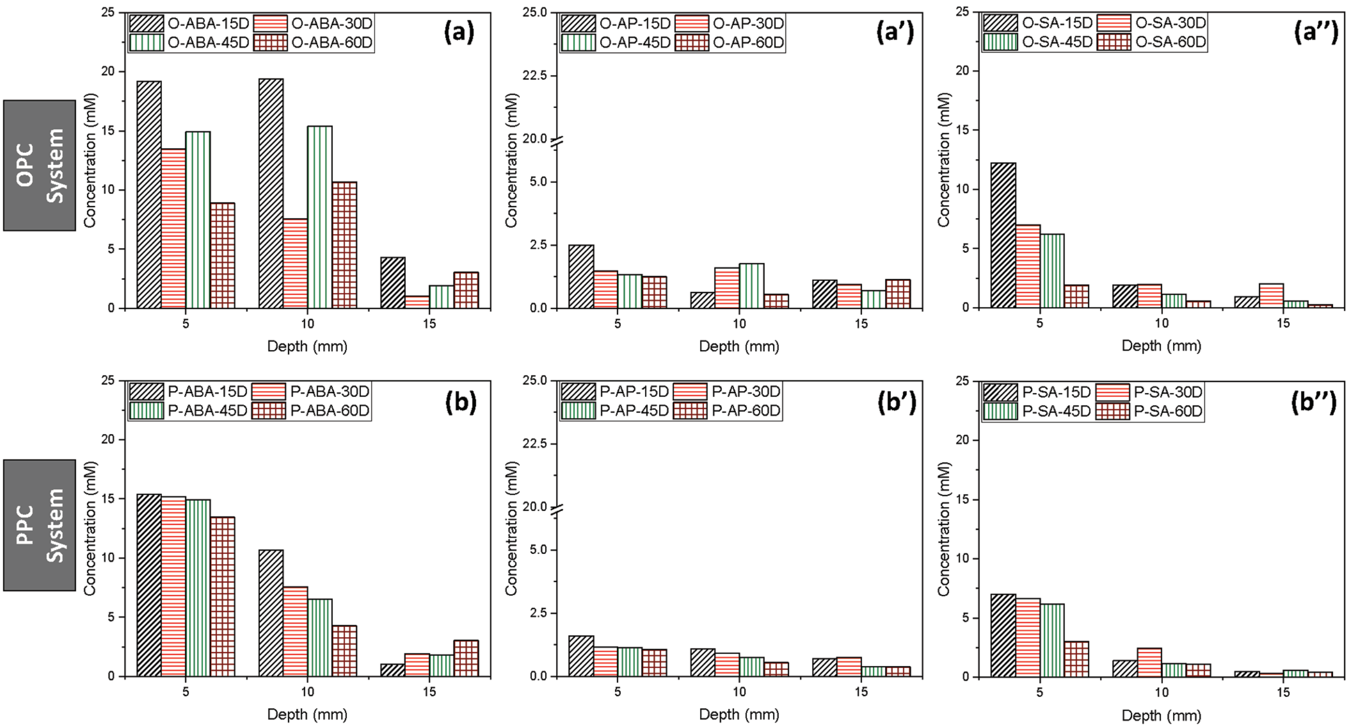

Fig. 6—Concentration of compound at different depths: (a), (a'), and (a") OPC-based system; and (b), (b'), and (b") PPC-based system.

combined corrosive environment. The results are in compliance with the surface analysis outcomes.

An important point to be noted is that the efficiency of ABA, AP, and SA was 99.9% when they were employed as M-CoI in preventive strategy—that is, when the inhibitors were added before corrosion initiated; however, in repair strategy, reductions of 47%, 57%, and 16.79% were observed in the performance of ABA, AP, and SA, respectively. The variance in the inhibition mechanism for repair, as outlined in this current study—in contrast to the preventive approach reported previously—can be attributed to the existence of corrosion products on the surface of the reinforcing bar prior to the introduction of the inhibitor.

Mechanism of inhibition (preventive versus repair)—The schematic representation of the mechanism is illustrated in Fig. 5. When the M-CoIs were added as preventive technique in corrosive pore solution, the adsorption sites of the M-CoIs were attracted electrostatically and chemically towards the metal surface. As the M-CoIs were added before corrosion initiation, the entire surface of the metal was available for interaction with the M-CoI molecules hence, the complete coverage by M-CoI which led to the high inhibition efficiency. On the other hand, in repair strategy, the accumulation of the corrosion products on the reinforcing bar before the addition of M-CoI acted as some sort of barrier for M-CoI molecules to interact with the Fe ions. As can be seen from the figure, the M-CoI molecules could only bind with Fe ions from the selective available sites. As the number of interaction sites reduced, so did the surface coverage by the M-CoI and hence, the decrease in inhibition efficiency was recorded during the PDP tests.

SA displayed the highest efficiency, followed by ABA and AP. SA gets converted into a negative ion when admixed in alkaline solution with negative charge on the O atom of alcohol functional group. –CHO (electron withdrawing group) and $–O^-$ both have negative charge density, which attracted Fe ions and formed a chelating ring, hindering the corrosion reaction. Also, when seen in preventive strategy, SA proved to be a very active compound which started performing from the time of addition. ABA also existed in its anionic form with $–COO^-$ acting as the reaction center for binding with Fe ions, but unlike SA, could not form a chelating ring as the other group ($–NH_2$) was placed away and could not participate in the interactions with metal surface. As a single functional group was involved in the inhibition mechanism, ABA displayed the second-highest efficiency. On the other hand, AP existed in its neutral form in solution; therefore, it had no negative charge accumulation which could attract the Fe ions. The only possibility for its interaction with the metal surface was the sharing of a lone pair of electrons, which could not happen as Fe ions were not free (as they got accumulated as Fe_2O_3 on the coupons). Additionally, AP took longer time than ABA and SA for stabilization when observed in preventive technique with chloride ions effect being very prominent even during the inhibition action. ABA and SA developed a physical as well as chemical bonding with Fe ions, making the interaction very strong as compared to only sharing of electrons in the case of AP. Hence, the order of efficiency: SA > ABA > AP.

Phase 2 test results and discussion

Concentration of inhibitors—The concentration of M-CoIs (1M) was applied on one surface of cube specimens in various concrete systems and measured after 15, 30, 45, and 60 days from depths of 5, 10, and 15 mm using UV-vis spectroscopy. The choice of a 1M concentration in this study was based on preliminary tests indicating optimal inhibition

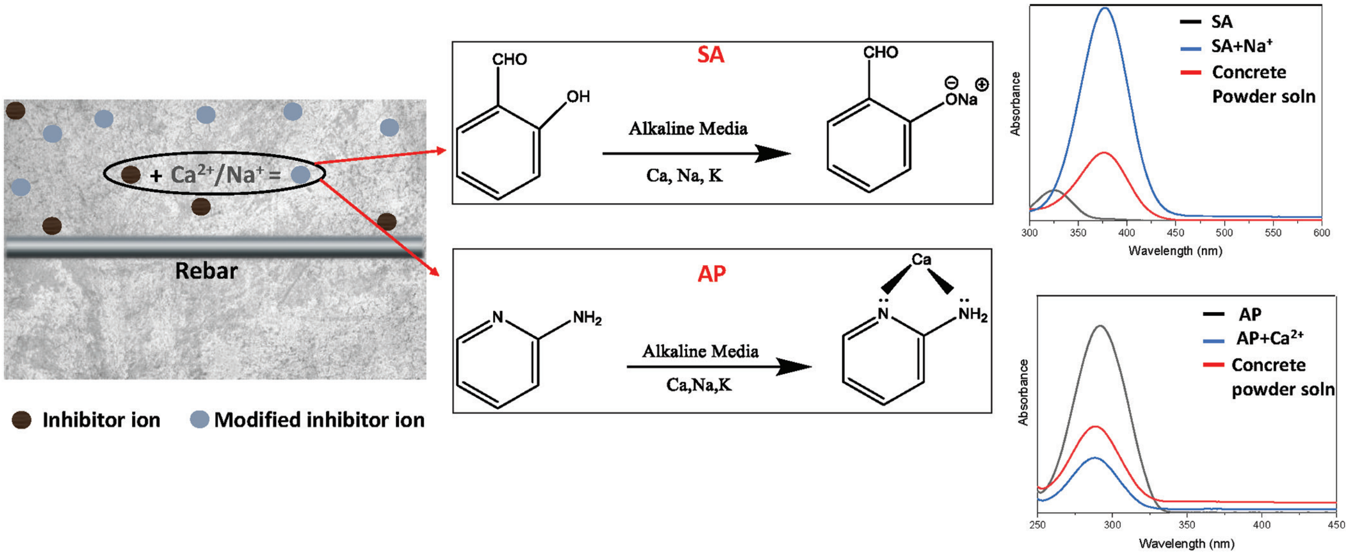

Fig. 7—Chemical interactions between: (a) AP and Ca^{2+} ions; and (b) SA and Na^+ ions.

efficiency for RC exposed to aggressive environments.[7,17] Although previous studies examined M-CoI's effectiveness across different corrosive conditions, none have specifically measured the exact concentration that reaches the reinforcing bar level. Measuring this precise concentration is critical, as it provides a clearer assessment of the true efficiency of the inhibitor.[34-36] The test results are presented in Fig. 6. Along with this, the wavelength of pure compound and the concrete powder specimen were analyzed to understand possible interaction of the compound with constituents of concrete. The bar graph data presented in Fig. 6 reveals that all M-CoIs successfully permeated both concrete systems within 15 days of application. Regardless of the cement type, the concentration order achieved was ABA > AP > SA. The maximum concentration reached at the reinforcing bar level (that is, 15 mm) is presented in Table SD4, showing 4 mM of ABA and 1 mM of AP and SA in OPC, whereas in PPC, 4 mM of ABA, 1 mM of AP, and 0.5 mM of SA were reached at different durations.

The ultimate concentration of each compound can be linked to a combination of factors, including the compound's molecular weight and its potential interaction with the concrete constituents. For instance, ABA exhibits the highest migration rate in both cement systems due to its highest molecular weight. However, the concentration of SA, despite its higher molecular weight (which is greater than AP), was the lowest. This is attributed to the electrostatic interaction of the hydroxyl functional group in SA with Na^+ ions present in concrete (as indicated in Fig. 7). This interaction is evident in the UV spectra, where the peak of concrete solution treated with SA as M-CoI aligns with the peak of SA + Na^+ ions. Similarly, the presence of amine group near the nitrogen atom within the pyridine ring of AP resulted in the formation of chelating ring with Ca^{2+} ions in the concrete, which slowed down its dispersion, as depicted Fig. 7. This could explain the lower concentration of AP at the cover depth. When comparing the impact of concrete matrixes, the primary distinction lies in the delayed dispersion of compounds in PPC as compared to OPC, primarily owing to PPC's denser pore structure. Such observations align with studies by Vedalakshmi et al.,[34] who found that inhibitor migration is influenced by concrete's pore structure, indicating that inhibitor efficiency is not only compound-dependent, but also matrix-dependent. Hence, it can be deduced that the generic compounds have the capability to percolate through concrete cover and the ability is dependent on the concrete type and structural properties of M-CoI.

Linear polarization resistance (LPR)—A test involving LPR was conducted to assess the change in corrosion current density (i_{corr}) of reinforcing steel bar embedded in concrete under specific cyclic exposure conditions, both with and without the application of M-CoI. The obtained results are shown in Fig. 8. Based on the i_{corr} values, the corrosion status of the reinforcing steel bars is categorized into four regions: R1—'Passive' ($i_{corr} < 0.1\ \mu A/cm^2$); R2—'Low corrosion level' (i_{corr} 0.1 to 0.5 $\mu A/cm^2$); R3—'Moderate corrosion condition' (i_{corr} 0.5 to 1 $\mu A/cm^2$); and R4—'High corrosion level' ($i_{corr} > 1\ \mu A/cm^2$).[37-39]

From the authors' previous study, it was observed that the combined corrosive environment creates a more vulnerable situation for the embedded reinforcing bar as both pitting and uniform corrosion occurs on the surface. The condition is more severe for PPC-based concrete systems due to changes in concrete microstructure during long-term carbonation. Hence, in this study, the comparative graph (Fig. 8(a)) is shown for reference only. A detailed explanation and the corrosion mechanism in a combined environment is already discussed in Tiwari et al.[6]

The M-CoI was applied to RC specimens following the completion of the 10th exposure cycle ($i_{corr} > 0.1\ \mu A/cm^2$). The recorded data for the i_{corr} is illustrated in Fig. 8(b) and (c). It is evident from the figure that ABA proved to be an effective repair strategy, effectively inhibiting the ongoing corrosion processes. In contrast, the other two M-CoI (AP and SA) were found to be less efficient. Notably, even after 50 exposure cycles, ABA exhibited significantly low CR, with i_{corr} values of 38.46% and 63.54%—lower than the

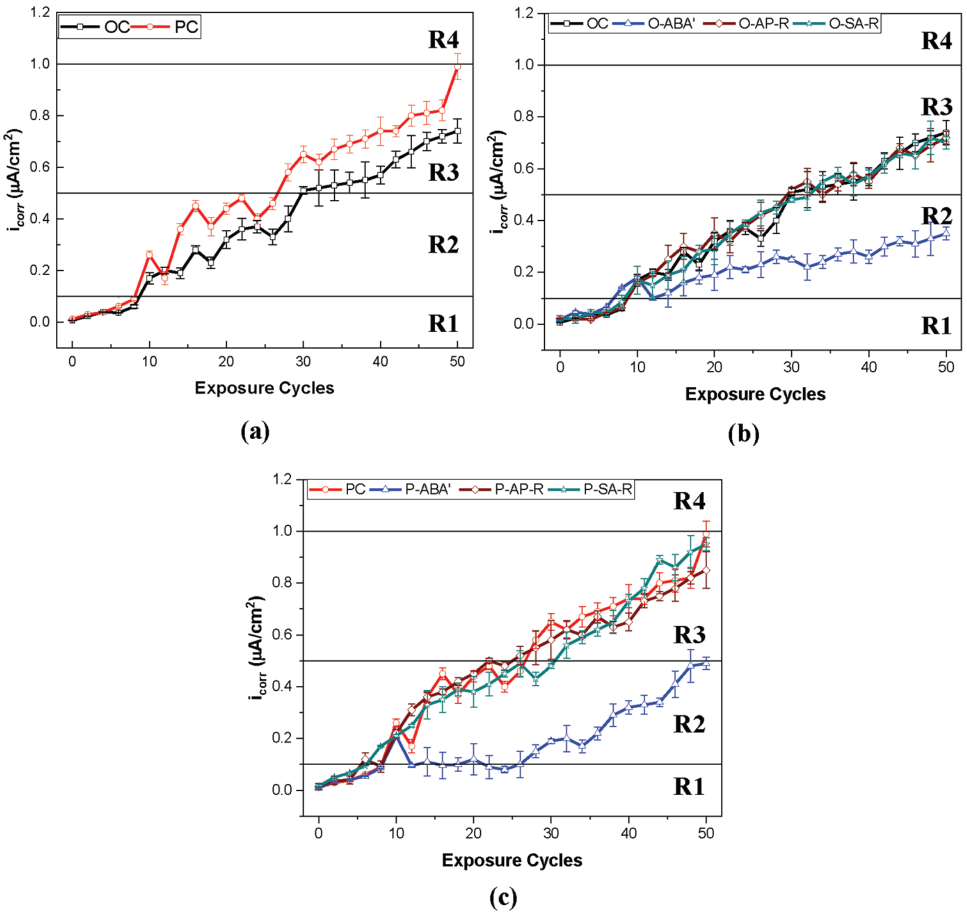

(a) (b)

(c)

Fig. 8—Corrosion current density values for: (a) control; (b) M-CoI applied in OPC-based specimens; and (c) M-CoI applied in PPC-based specimens.

control specimens—in OPC and PPC concrete, respectively. This indicates that ABA continued to perform efficiently throughout the entire test exposure period. On the other hand, specimens treated with AP and SA showed that i_{corr} increased at a similar rate as observed in control specimens.

In both concrete systems, the inhibition efficiency of AP is 12.16% in OPC and 14.14% in PPC, whereas SA exhibits limited efficiency, with 5.4% in OPC and 9.1% in PPC. Notably, the order of efficiency aligns with the concentration of inhibitors that penetrate to the reinforcing bar's depth within the concrete, but it differs from the results obtained through corrosion testing in pore solution. This suggests a direct correlation between inhibition efficiency and the concentration of M-CoI ions reaching the reinforcement in RC. Moreover, it highlights that synthetic pore solution testing alone is insufficient to determine the effectiveness of a compound as a successful M-CoI for protecting reinforcement in concrete.

Electrochemical impedance spectroscopy (EIS)—In addition to gathering information on reinforcing bar corrosion, it is essential to comprehend the evolving characteristics of the concrete pore structure and the interface between steel and concrete with exposure, especially when corrosion inhibitor is applied. To achieve this, EIS testing was conducted at different stages of exposure—specially at 0, 10, 30, and 50 exposure cycles—and the results were represented through Nyquist and Bode magnitude plots.

In the Nyquist plot, data is presented in the form of $Z = Z' + jZ''$ where Z' represents the real component, and Z'' represents the imaginary component, measured at various frequencies. The changes observed in the capacitive arc in the Nyquist plot and the impedance in Bode plot reflect the ongoing processes in concrete matrix and on the surface of the embedded reinforcing bar (as depicted in Fig. SD4). In the Nyquist plot, variations in the radii of the high-frequency (HF) arc indicates alteration within the concrete matrix, while changes in low-frequency (LF) arc describes the condition of reinforcing bar surface.[40,41]

Furthermore, the shift in the spectra relative to the x-axis reveals the dominant process, whether it is related to chloride ingress or carbonation. In the Bode magnitude plots, distinct regions can be categorized into three zones. Zone I corresponds to HF range (100 to 10 KHz), and changes in impedance in this region are indicative of alterations in the concrete matrix. Zone II pertains to the mid-frequency (MF) range (10 KHz to 10 Hz) and is associated with the change in the concrete microstructure and composition at steel-concrete interface. Zone III encompasses the LF region (10 Hz to 1 mH), which is linked to variations in the passivity of the steel.

When investigating the application of M-CoI, particular attention is given to the MF range, which is associated with the properties of the steel-concrete interface. This is crucial because inhibitors are anticipated to reach the reinforcing

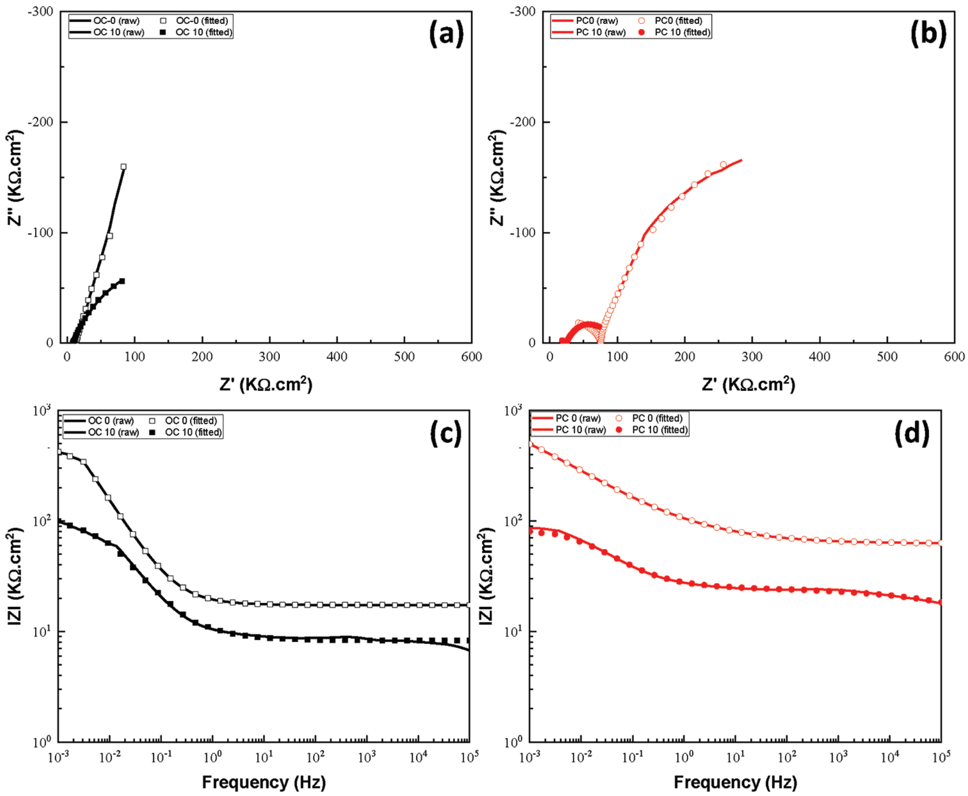

Fig. 9—EIS plots of OPC- and PPC-based specimens before subjected to combined exposure: (a) and (b) Nyquist plot; and (c) and (d) Bode plot.

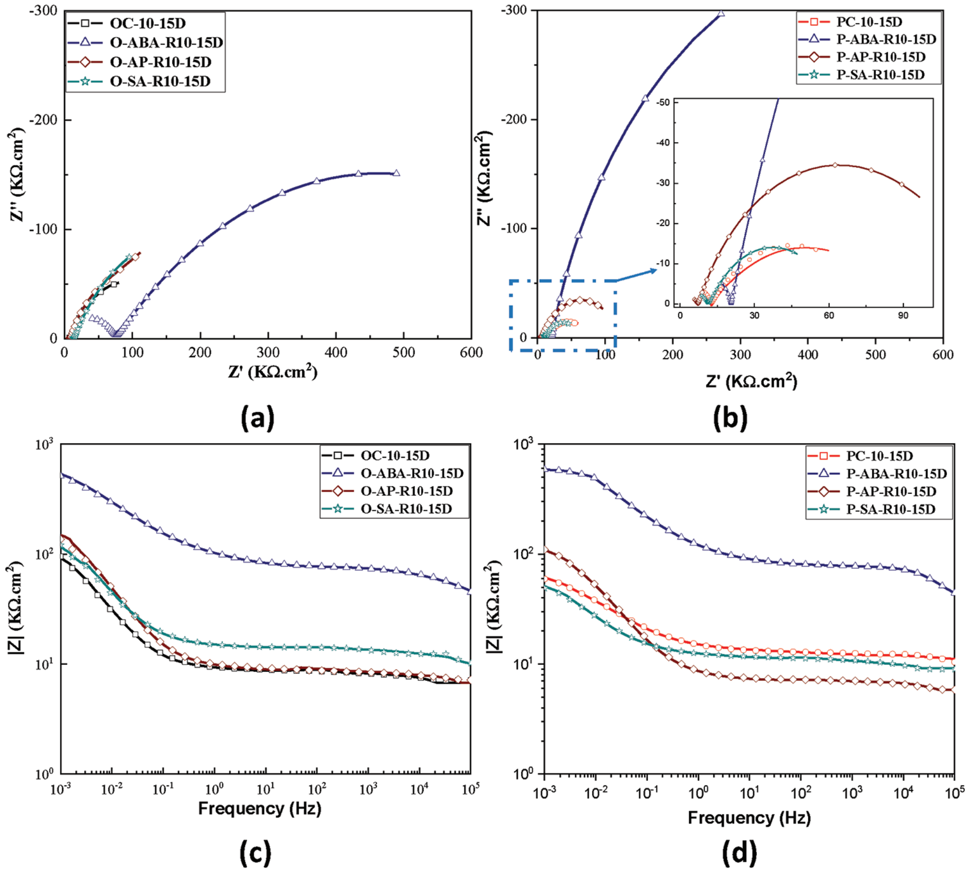

Fig. 10—EIS plots of OPC- and PPC-based specimens after 15 days of application: (a) and (b) Nyquist plot; and (c) and (d) Bode plot.

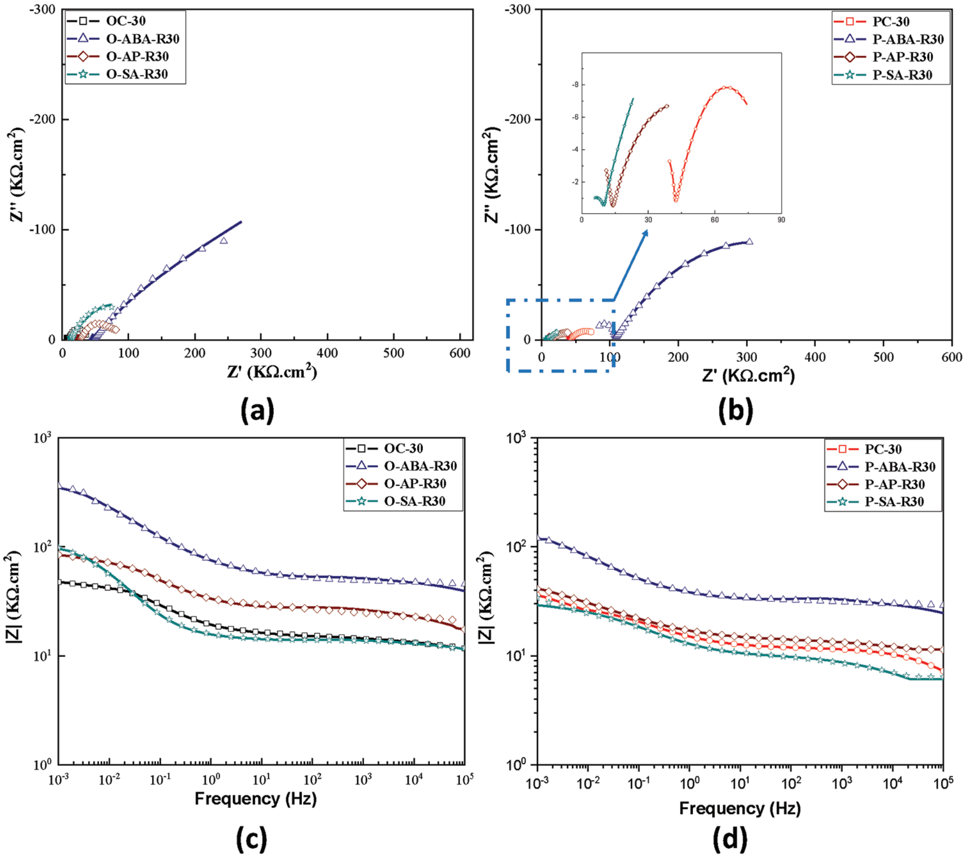

Fig. 11—EIS plots of OPC- and PPC-based specimens after 30th cycle: (a) and (b) Nyquist plot; and (c) and (d) Bode plot.

bar and create a protective layer that affects the interface between the steel and concrete.

Nyquist and Bode magnitude plots: From the LPR test, it was observed that corrosion was active after 10 cyclic exposures in both cement types. The Nyquist and Bode magnitude plots for the control specimens—namely OC and PC at the initial stage (0 cycles) and after 10 cycles (prior to the application of M-CoI)—are displayed in Fig. 9. From the initial cycle to the 10th cycle of exposure, there is a noticeable reduction in the diameter of the LF arc observed in both types of cement specimens. This reduction clearly indicates that the protective film on the reinforcing bar deteriorated rapidly, leading to corrosion starting in a shorter timeframe. Therefore, M-CoIs were applied after the 10th exposure cycle.

The Nyquist and Bode plots, generated after 15 days of inhibitor application, are displayed in Fig. 10. Analyzing the Nyquist plot, it can be observed that the diameter of the LF capacitive loop for O-AB and P-AB increased compared to control specimens (without M-CoI application). This increase clearly indicates the efficacy of ABA in penetrating the concrete cover and forming a more robust protective layer within just 15 days of application. Similarly, in line with the Nyquist plot, the rise in LF impedance for O-AB and P-AB indicates an enhancement in the surface characteristics of the steel due to the formation of more adherent layer in specimen treated with ABA. Conversely, there is only a slight increase in diameter of the LF arc and |*Z*| for O-AP, P-AP, O-SA, and P-SA. This may be attributed to the slower migration rate of these compounds, suggesting that AP and SA could not hinder the ongoing corrosion process with the same effectiveness as achieved by ABA.

Upon reaching the 30th exposure cycle, as shown in Fig. 11, it becomes evident that the diameter of the LF capacitive arc and the impedance value of the specimens (both control and M-CoI-applied) diminished due to the impact of aggressive ions on the reinforcing bar surface. This decline in arc diameter and impedance is continuous until the 50th exposure cycle, as illustrated in Fig. 12. Even as exposure to the corrosive environment persists, ABA managed to maintain some level of protection until the conclusion of testing. In contrast, AP and SA were unable to effectively halt the ongoing corrosion process, as evidenced by their significantly reduced LF arc diameter. The limited effectiveness of AP and SA can be attributed to the insufficient concentration reaching the bar level to perform inhibitory actions. Notably, an important conclusion drawn from the analysis of the LF Nyquist curve and impedance values in the case of ABA-treated specimens in both OPC and PPC is that the final |*Z*| values (after the 50th exposure cycle) for both concrete systems are comparable (65 KΩcm^2 for OPC and 50 KΩcm^2 for PPC). This finding is significant, as it indicates that PPC concrete, which was initially more susceptible to corrosion without inhibitor application, developed a strong inhibitive capability and can perform well in the face of combined aggressive environments involving chlorides and carbonation. Consequently, it is reasonable to expect that similar service life can be achieved for PPC concrete when inhibitors are employed in the presence of a combined corrosive environment.

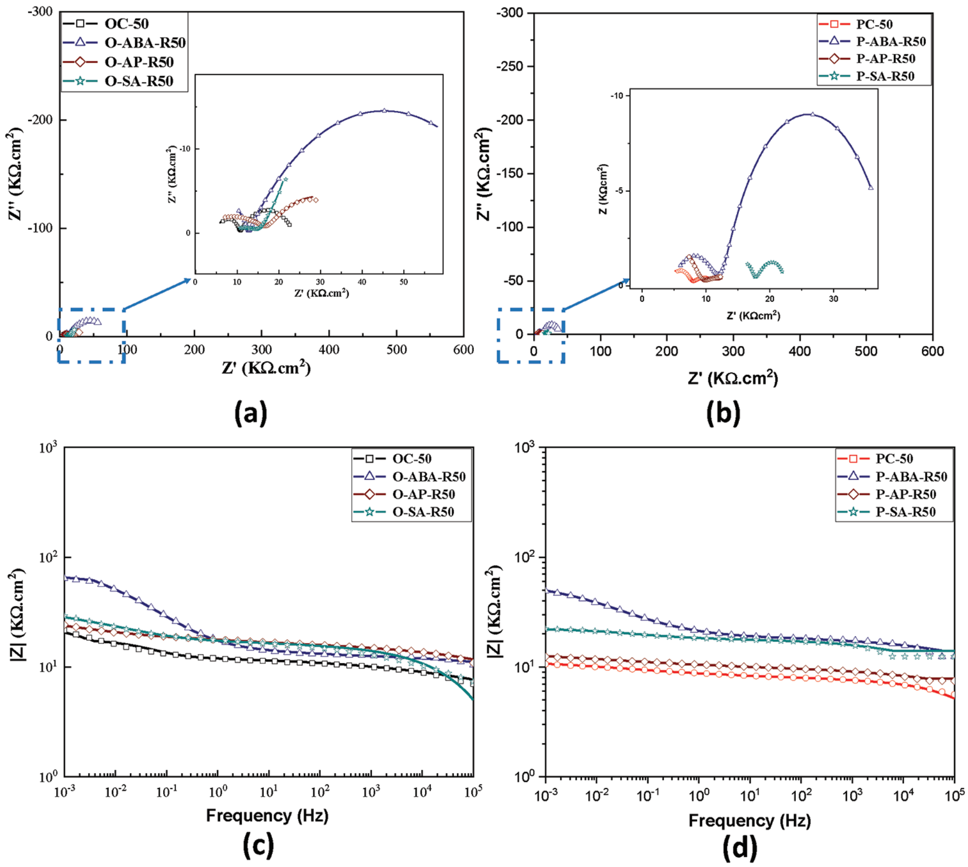

Fig. 12—EIS plots of OPC- and PPC-based specimens after 50th cycle: (a) and (b) Nyquist plot; and (c) and (d) Bode plot.

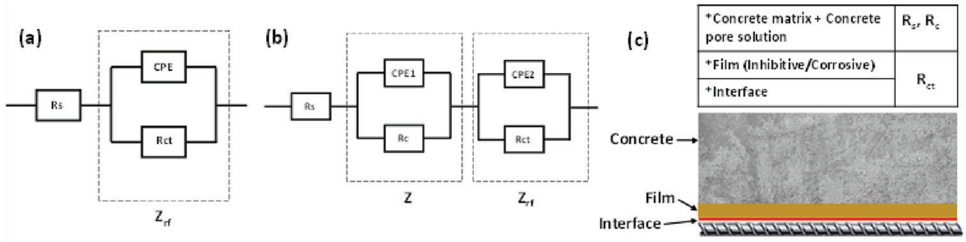

Fig. 13—Electrochemical equivalent circuits: (a) EEC1; (b) EEC2; and (c) schematic representation of steel-concrete interface.

Electrochemical parameters and equivalent circuits: Furthermore, the Nyquist and Bode magnitude plots obtained in the study were subjected to fitting using the EIS software. In this study, multiple models were explored to identify the most accurate electrochemical equivalent circuit (EEC), and the resulting circuit is depicted in Fig. 13. Two EEC models, denoted EEC1 and EEC2, were developed based on the fit to experimental data. EEC1 represents cases where only one impedance arc is observed in the Nyquist spectra, and it is applicable to OPC-based specimens during the 0 and 10th exposure cycles. EEC2, on the other hand, is applicable for all other cycles and corresponds to situations where both HF and LF arcs are obtained. Within the equivalent circuit, R_s stands for the resistance of the electrolytic pore solution resistance within concrete followed by a series of impedances (Z). EEC1 comprises a single impedance (Z_{rf}), while EEC2 includes two impedances, Z_c and Z_{rf}. Z_c represents the Faradaic process occurring within a concrete matrix, while Z_{rf} corresponds to the Faradaic process between the interfacial film and reinforcing bar. Z_c consists of two elements: the resistance (R_c) offered by the concrete matrix and constant phase element (CPE_c) that describes the process between solid/liquid phase in the concrete bulk. Similarly, Z_{rf} includes the resistance (R_{ct}) offered by the interfacial film at the steel-concrete interface (commonly known as charge transfer resistance), and a constant phase element (CPE_{dl}) that accounts for the interaction between the interfacial film and steel. In this circuit, a constant phase element (CPE) is employed instead of pure capacitor to fit a depressed semicircle. The depression in this semicircle is attributed to factors such as surface reactivity, inhomogeneity, porosity of concrete, roughness, and irregularities on reinforcing bar surface.[42,43] The impedance of the CPE is dependent on angular frequency and is determined by Eq. (2)

$$Z_{cpe} = 1/Q(j\omega)^{\alpha} \quad (2)$$

Table 4—Resistive parameters obtained from Nyquist spectra

Specimen description	Exposure duration, days	R_s	R_c	R_{ct}	Specimen description	Exposure duration, days	R_s	R_c	R_{ct}
		kΩ.cm^2					kΩ.cm^2		
OC	0	10.99	—	405.67	PC	0	62.87	354.2	353.46
	10	6.74	—	90.71		10	17.92	143.01	62.48
	10+15	8.12	—	87.65		10+15	10.41	92.69	48.95
	30	11.45	23.84	33.25		30	3.44	45.13	25.41
	50	7.69	10.95	10.29		50	5.17	3.43	5.26
O-ABA-R	10+15	44.73	35.43	467.16	P-PBA-R	10+15	54.16	95.21	542.84
	30	45.39	12.36	214.61		30	29.13	35.12	90.32
	50	10.41	7.22	43.7		50	12.41	18.57	36.79
O-AP-R	10+15	7.16	28.86	129.33	P-AP-R	10+15	5.87	106.64	103.77
	30	17.45	17.17	67.09		30	11.38	55.12	29.85
	50	7.36	8.49	17.75		50	7.49	18.578	4.92
O-SA-R	10+15	10.19	28.60	110.77	P-SA-R	10+15	8.96	48.12	103.74
	30	11.73	12.49	86.38		30	6.40	39.65	28.1
	50	12.41	9.56	16.43		50	14.07	17.92	8.22

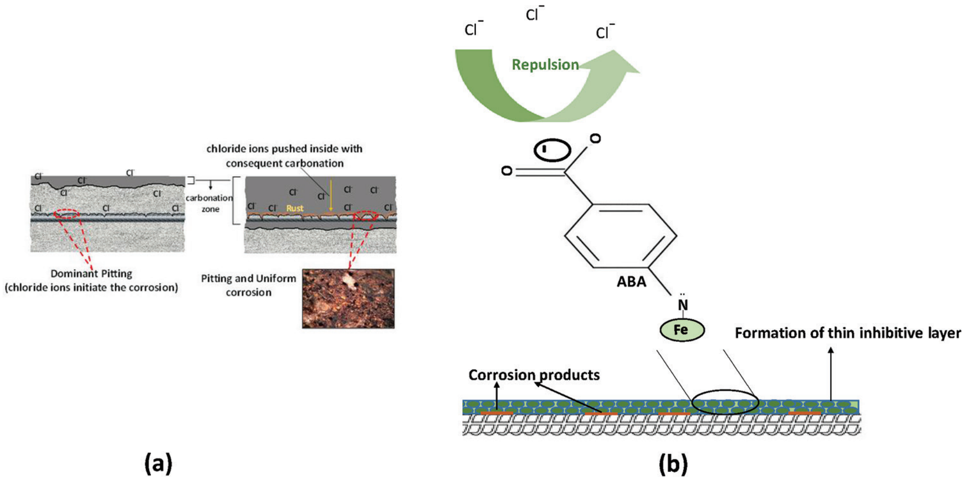

Fig. 14—(a) Degradation mechanism in combined chloride and carbonation environment; and (b) inhibition mechanism of ABA.

where Q represents the admittance; ω stands for angular frequency; and α denotes the exponent associated with the CPE, which accounts for the depressed semicircle. When α equals 1, CPE behaves like a pure capacitor, and when α equals 0, it acts like a pure resistor. The EIS fitted parameters for both control specimens and those treated with inhibitors are presented in Table 4.

It can be asserted that alterations occurring within the concrete's bulk are mirrored by change in R_s and R_c. The values of R_s and R_c, as shown in Table 4, decreased as the exposure period advanced in both control specimens (OC and PC). This decrease signifies an increase in the movement of ions within the concrete matrix. Notably, in some of the OC samples, R_c was absent as the HF arc (HFA) was not present in their respective Nyquist plots. Gu et al.[44] noted that the size of HFA, which represents the properties of concrete matrix, tends to decrease when the ion concentration in the concrete electrolyte or when the porosity of concrete system rises. Following the application of inhibitors, a noticeable increase in R_s value was observed only after ABA application, indicating potential modifications in the concrete pore solution during percolation. However, no substantial changes in R_c values were detected for any of the inhibitors, suggesting that the resistance provided by the concrete matrix remains unaltered upon inhibitor application. With continued exposure, both R_s and R_c progressively decreased the presence of highly conductive ions within various concrete matrixes, whether they were OPC- or PPC-based control specimens or those treated with inhibitors.

The resistive parameter obtained from the fitting of the LF (R_{ct}) reflects the processes occurring at the reinforcing bar level and is examined to understand alterations in the charge transfer mechanism for both control specimens and those treated with inhibitors. It is regarded as a critical parameter directly linked to the corrosion rate. A decrease in R_{ct} signifies an active corrosion state. As indicated in the table, for the control specimens, R_{ct} declined over time (from 405 to 10 kΩ.cm^2 for OC and from 353 to 5 kΩ.cm^2 for PC), clearly indicating an elevated corrosion rate. The application of M-CoI led to an increase in R_{ct} values for both the concrete systems, indicating the effectiveness of the applied generic compounds in serving as migratory inhibitors. For ABA, R_{ct} values increased to 467 kΩ.cm^2 in OPC and 542 kΩ.cm^2 in PPC. In the case of AP, the R_{ct} value reached 129 kΩ.cm^2 for OPC and 103 kΩ.cm^2 for PPC, while for SA, the values were 110 and 103 kΩ.cm^2 for OPC and PPC, respectively. The rise in R_{ct} value suggests that the inhibitors might create a resistive film on the reinforcing bar, likely through surface adsorption. When comparing the inhibitors, the ABA-applied specimens exhibited higher R_{ct} values for both OPC and PPC concrete, followed by AP and SA. This implies that ABA has a greater potential to inhibit corrosion in combined exposure condition, a conclusion supported by the corresponding i_{corr} values.

Discussion on degradation and inhibition mechanism in RC—The present study is focused on subsequent protection of RC structures by using M-CoIs. To simulate a combined aggressive environment, the RC samples underwent a dual exposure cycle involving both chloride and carbonation. The degradation mechanism was already explained in the previous published work[6] and shown in Fig. 14(a). The first stage (I) is characterized by dominant pitting corrosion, while the second stage (II) sees both uniform and pitting corrosion reaching their most severe levels. Therefore, in situations where both factors can be seen concurrently, chloride ions are responsible for initiating corrosion, but over time, carbonation exacerbates the degradation process. Additionally, it is worth noting that in combined corrosive environment, concrete based on PPC exhibits a higher level of corrosion severity as compared to OPC.

This observation contrasts with the general perception that fly ash improves concrete's durability by reducing its permeability to aggressive ions, thus slowing down corrosion initiation and propagation. Several studies have highlighted the positive effects of fly ash in enhancing the corrosion resistance of concrete, particularly in relation to chloride ion migration. Choi et al.[45] observed that the partial replacement of cement with fly ash resulted in improved corrosion resistance, attributed to a reduction in chloride ion permeability. This aligns with the authors' understanding that fly ash can enhance concrete's resistance to chloride ingress that has been observed during initial exposure cycles. Similarly, Zhao et al.[46] found that fly ash-containing concrete exhibited superior resistance to chloride ion migration, leading to better overall corrosion protection. However, the authors' findings reveal a more complex behavior when carbonation is considered. While fly ash reduces chloride ingress, it appears to be more susceptible to carbonation, likely due to the accelerated carbonation affecting the microstructure more rapidly in PPC. Beglarigale et al.[47] also noted that fly ash could promote carbonation, especially when the concrete cover is insufficient, which diminishes its corrosion resistance. Although fly ash showed positive effects in reducing chloride penetration, carbonation offset these benefits, as observed in the authors' research. These results suggest that PPC-based concrete demonstrates higher corrosion severity under combined chloride and carbonation exposure, emphasizing that the resistance to chloride ion migration may not be enough to overcome the detrimental effects of carbonation. In conclusion, while fly ash is widely recognized for improving chloride resistance in concrete, the compounded effects of chloride and carbonation in aggressive environments significantly influence its overall performance. These findings highlight the need for a balanced approach in using fly ash in concrete, taking into account its susceptibility to carbonation in addition to its chloride resistance capabilities.

When the organic compounds were applied as migratory M-CoI on the concrete surface after the accumulation of corrosion products, ABA performed well in suppressing the rate of ongoing corrosion by forming a layer over the reinforcing bar surface (as confirmed by the high-diameter arc in Nyquist plots). The schematic representation inhibition mechanism of ABA is shown in Fig. 14(b). This layer sustained itself even after the exposure to harsh corrosive environment, which explains the inhibitive nature of ABA molecules. On the other hand, the molecules of SA and AP were unable to perform as M-CoI in concrete due to the modification of their ions (as explained in Fig. 7) when applied as migratory M-CoI. This observation was opposed to the Phase 1 test results, where SA performed most efficiently. The reason is that in the pore solution, the reinforcing bar is readily available for the M-CoI ions to chelate Fe ions through their adsorption centers; however, in concrete, an intermediate step is to be fulfilled—that is, the percolation through concrete matrix. To validate this, the pore solution test was repeated with M-CoI concentrations as 4, 1, and 1 mM for ABA, AP, and SA, respectively, as these are the concentrations reaching the reinforcing bar level during the percolation ability test (discussed in the "Mechanism of inhibition (preventive versus repair)" subsection). The order of efficiency was ABA > AP ~ SA (i_{corr} values and polarization curve given in Fig. SD5). Hence, it can be stated that pore solution testing alone cannot determine the inhibition performance of any compound as corrosion inhibitor for protection of reinforcement in concrete, and the migration ability test is important to conduct to obtain the actual concentration of compound that could reach the reinforcing bar level.

CONCLUSIONS

The current research work presents the outcomes of the performance of three aromatic multifunctional compounds acting as migratory corrosion inhibitors (M-CoIs) for already corroded steel specimens in simulated concrete pore (SCP) solution and concrete. The following conclusions are so made:

1. The compounds were more effective as preventive measures than as repair strategies, highlighting the critical role of the steel surface condition in inhibitor performance (as seen in previous research work[7,17]).

2. Inhibition efficiency depends on the concentration and form of M-CoI at the reinforcing bar level. 4-Aminobenzoic acid (ABA), in its pure form, showed superior performance, while Salicylaldehyde (SA) and 2-Aminopyridine (AP)

reached the reinforcing bar in reduced concentrations and altered forms, resulting in lower efficiency.

3. Preventive and repair strategies require different considerations. In pore solution, M-CoIs directly chelate Fe ions, effectively inhibiting corrosion. In concrete, the need for percolation reduces efficiency, emphasizing that pore solution testing alone cannot fully predict inhibitor performance in concrete.

4. A robust methodology for corrosion inhibitor selection should include both pore solution testing and migration ability assessments in concrete to ensure effectiveness in preventive and repair applications under aggressive conditions.

AUTHOR BIOS

Ashish Kumar Tiwari *is a Research Associate at the Indian Institute of Technology (IIT) Roorkee, Roorkee, India. He received his master's degree in structural engineering and his PhD studies were in corrosion inhibitors and reinforced concrete (RC) durability. His research interests include RC corrosion and durability, inhibitors, condition assessment, and repair techniques.*

Purnima Dogra *is a Postdoctoral Researcher at IIT Madras, Chennai, India. Her PhD studies were in carbonation-induced corrosion and its repair using inhibitors. Her research interests include RC durability, supplementary cementitious materials, and steel substrate characterization.*

Shweta Goyal *is a Professor in Civil Engineering at Thapar Institute of Engineering & Technology, Patiala, India. Her research interests includes microbial concrete, RC corrosion protection, accelerated carbonation for precast concrete, and sustainable concrete research.*

Vijay Luxami *is a Professor in Chemistry at Thapar Institute of Engineering & Technology. Her research interests include organic and supramolecular chemistry, molecular recognition, molecular electronics, and organic materials.*

ACKNOWLEDGMENTS

The authors gratefully acknowledge the financial support provided by the Atomic Energy Regulatory Board under Committee for Safety Research Programs (Sanction No. AERB/CSRP/73/02/19) and Center of Excellence for Emerging Materials under TIET-VT (Thapar Institute of Engineering and Technology, Patiala – Virginia Tech, Sanction No.TIET/CEEMS/Regular/2021/20).

REFERENCES

1. Bolzoni, F.; Brenna, A.; and Ormellese, M., "Recent Advances in the Use of Inhibitors to Prevent Chloride-Induced Corrosion in Reinforced Concrete," *Cement and Concrete Research*, V. 154, 2022, p. 106719. doi: 10.1016/j.cemconres.2022.106719

2. Zhang, G.; Yang, Q.; Hou, D.; Zhou, P.; and Ding, Q., "Unraveling the Microstructural Properties of Cement-Slag Composite Pastes Incorporated with Smart Polymer-Based Corrosion Inhibitors: From Experiment to Molecular Dynamics," *Cement and Concrete Composites*, V. 125, 2022, p. 104298. doi: 10.1016/j.cemconcomp.2021.104298

3. Aguirre-Guerrero, A. M.; Mejía-De-Gutiérrez, R.; and Montês-Correia, M. J. R., "Corrosion Performance of Blended Concretes Exposed to Different Aggressive Environments," *Construction and Building Materials*, V. 121, 2016, pp. 704-716. doi: 10.1016/j.conbuildmat.2016.06.038

4. Zhang, D., and Shao, Y., "Effect of Early Carbonation Curing on Chloride Penetration and Weathering Carbonation in Concrete," *Construction and Building Materials*, V. 123, 2016, pp. 516-526. doi: 10.1016/j.conbuildmat.2016.07.041

5. Batis, G.; Routoulas, A.; and Rakanta, E., "Effects of Migrating Inhibitors on Corrosion of Reinforcing Steel Covered with Repair Mortar," *Cement and Concrete Composites*, V. 25, No. 1, 2003, pp. 109-115. doi: 10.1016/S0958-9465(01)00047-6

6. Tiwari, A. K.; Purnima; Goyal, S.; and Luxami, V., "Influence of Corrosion Inhibitors on Two Different Concrete Systems under Combined Chloride And Carbonated Environment," *Structures*, V. 48, 2023, pp. 717-735. doi: 10.1016/j.istruc.2022.12.093

7. Tiwari, A.; Goyal, S.; Luxami, V.; Chakraborty, M. K.; and Gundlapalli, P., "Evaluation of Inhibition Efficiency of Generic Compounds with Additional Heteroatom in Simulated Concrete Pore Solution and Migration Potential in Concrete," *Journal of Building Engineering*, V. 43, 2021, p. 102490. doi: 10.1016/j.jobe.2021.102490

8. Ormellese, M.; Bolzoni, F.; Goidanich, S.; Pedeferri, M. P.; and Brenna, A., "Corrosion Inhibitors in Reinforced Concrete Structures Part 3 – Migration of Inhibitors into Concrete," *Corrosion Engineering, Science and Technology*, V. 46, No. 4, 2011, pp. 334-339. doi: 10.1179/174327809X419230

9. Kaur, K.; Goyal, S.; Bhattacharjee, B.; and Kumar, M., "Efficiency of Migratory-Type Organic Corrosion Inhibitors in Carbonated Environment," *Journal of Advanced Concrete Technology*, V. 14, No. 9, 2016, pp. 548-558. doi: 10.3151/jact.14.548

10. Dariva, C. G., and Galio, A. F., "Corrosion Inhibitors - Principles Mechanisms and Applications," *Developments in Corrosion Protection*, 2014, pp. 365-379.

11. Osial, M., and Wiliński, D., "Organic Substances as Corrosion Inhibitors for Steel in Concrete – An Overview," *Journal of Building Chemistry*, V. 1, No. 1, 2016, pp. 42-53.

12. Purnima; Goyal, S.; and Luxami, V., "Exploring the Corrosion Inhibition Mechanism of Serine (Ser) and Cysteine (Cys) in Alkaline Concrete Pore Solution Simulating Carbonated Environment," *Construction and Building Materials*, V. 384, 2023, p. 131433. doi: 10.1016/j.conbuildmat.2023.131433

13. Mandal, S.; Singh, J. K.; Mallapur, S.; Lee, D.-E.; and Park, T., "Effect of Triethanolamine and Sodium Hexametaphosphate on Formation, Growth and Breakdown of Passive Layer in Concrete Pore Solution," *Journal of Building Engineering*, V. 59, 2022, p. 105113. doi: 10.1016/j.jobe.2022.105113

14. Hu, J.; Zhu, Y.; Hang, J.; Zhang, Z.; Ma, Y.; Huang, H.; Yu, Q.; and Wei, J., "The Effect of Organic Core–Shell Corrosion Inhibitors on Corrosion Performance of the Reinforcement in Simulated Concrete Pore Solution," *Construction and Building Materials*, V. 267, 2021, p. 121011. doi: 10.1016/j.conbuildmat.2020.121011

15. Verma, C.; Olasunkanmi, L. O.; Quadri, T. W.; Sherif, E.-S. M.; and Ebenso, E. E., "Gravimetric, Electrochemical, Surface Morphology, DFT, and Monte Carlo Simulation Studies on Three N-Substituted 2-Aminopyridine Derivatives as Corrosion Inhibitors of Mild Steel in Acidic Medium," *The Journal of Physical Chemistry. C, Nanomaterials and Interfaces*, V. 122, No. 22, 2018, pp. 11870-11882. doi: 10.1021/acs.jpcc.8b02740

16. Attar, T.; Nouali, F.; Kibou, Z.; Benchadli, A.; Messaoudi, B.; Choukchou-Braham, E.; and Choukchou-Braham, N., "Corrosion Inhibition, Adsorption and Thermodynamic Properties of 2-Aminopyridine Derivatives on the Corrosion of Carbon Steel in Sulfuric Acid Solution," *Journal of Chemical Sciences*, V. 133, No. 4, 2021, p. 109. doi: 10.1007/s12039-021-01971-w

17. Tiwari, A.; Goyal, S.; Luxami, V.; Chakraborty, M. K.; and Prabhakar, G., "Assessment of Corrosion Inhibition Efficiency of Generic Compounds Having Different Functional Groups in Carbonated Pore Solution with Chlorides and Migration Ability in Concrete," *Construction and Building Materials*, V. 290, 2021, p. 123275. doi: 10.1016/j.conbuildmat.2021.123275

18. Donadio, M.; Bakalli, M.; and Dan, Z., "Reinforced Concrete Corrosion Prevention/Reduction by Hydrophobic Impregnation," *MATEC Web of Conferences*, V. 289, 2019.

19. Seyhan, E. C.; Goodwin, F.; and Huang, I. W., "Corrosion Protection of Steel Reinforcement by Using Surface Applied Corrosion Inhibitors," *MATEC Web of Conferences*, V. 289, 2019.

20. Goyal, A.; Ganjian, E.; Pouya, H. S.; and Tyrer, M., "Inhibitor Efficiency of Migratory Corrosion Inhibitors to Reduce Corrosion in Reinforced Concrete Exposed to High Chloride Environment," *Construction and Building Materials*, V. 303, 2021, p. 124461. doi: 10.1016/j.conbuildmat.2021.124461

21. IS 1786:2008, "High Strength Deformed Steel Bars and Wires for Concretereinforcement— Specification," Bureau of Indian Standards, New Delhi, India, 2008, 12 pp.

22. Aslam, R.; Mobin, M.; Zehra, S.; and Aslam, J., "A Comprehensive Review of Corrosion Inhibitors Employed to Mitigate Stainless Steel Corrosion in Different Environments," *Journal of Molecular Liquids*, V. 364, 2022, p. 119992. doi: 10.1016/j.molliq.2022.119992

23. Poursaee, A., and Hansson, C. M., "Reinforcing Steel Passivation in Mortar and Pore Solution," *Cement and Concrete Research*, V. 37, No. 7, 2007, pp. 1127-1133. doi: 10.1016/j.cemconres.2007.04.005

24. Liu, R.; Jiang, L.; Xu, J.; Xiong, C.; and Song, Z., "Influence of Carbonation on Chloride-Induced Reinforcement Corrosion in Simulated Concrete Pore Solutions," *Construction and Building Materials*, V. 56, 2014, pp. 16-20. doi: 10.1016/j.conbuildmat.2014.01.030

25. IS 8112:2013, "Specification for 43 Grade Ordinary Portland Cement," Bureau of Indian Standards, New Delhi, India, 2013, 17 pp.

26. IS 1489-1:1991, "Portland-Pozzolana Cement-Specification," Bureau of Indian Standards, New Delhi, India, 1991.

27. IS 383:1970, "Specification for Coarse and Fine Aggregates From Natural Sources for Concrete," Bureau of Indian Standards, New Delhi, India, 1970, 24 pp.

28. IS 10262:2009, "Guidelines for Concrete Mix Design Proportioning," Bureau of Indian Standards, New Delhi, India, 2009.

29. ASTM G109-21, "Standard Test Method for Determining the Effects of Chemical Admixtures on the Corrosion of Embedded Steel Reinforcement in Concrete Exposed to Chloride Environments," ASTM International, West Conshohocken, PA, 2021, 6 pp.

30. Kaur, K.; Goyal, S.; Bhattacharjee, B.; and Kumar, M., "Electrochemical Impedance Spectroscopy to Study the Carbonation Behavior of Concrete Treated with Corrosion Inhibitors," *Journal of Advanced Concrete Technology*, V. 15, No. 12, 2017, pp. 738-748. doi: 10.3151/jact.15.738

31. Zaki, A.; Chai, H. K.; Aggelis, D. G.; and Alver, N., "Non-Destructive Evaluation for Corrosion Monitoring in Concrete: A Review and Capability of Acoustic Emission Technique," *Sensors*, V. 15, No. 8, 2015, pp. 19069-19101. doi: 10.3390/s150819069

32. ASTM C876-22b, "Standard Test Method for Corrosion Potentials of Uncoated Reinforcing Steel in Concrete," ASTM International, West Conshohocken, PA, 2022, 8 pp.

33. Rodrigues, R.; Gaboreau, S.; Gance, J.; Ignatiadis, I.; and Betelu, S., "Reinforced Concrete Structures: A Review of Corrosion Mechanisms and Advances in Electrical Methods for Corrosion Monitoring," *Construction and Building Materials*, V. 269, 2021, p. 121240. doi: 10.1016/j.conbuildmat.2020.121240

34. Vedalakshmi, R.; Rajagopal, K.; and Palaniswamy, N., "Determination of Migration Efficiency of Amino Alcohol Based Migrating Corrosion Inhibitor through Concrete," *Corrosion Engineering, Science and Technology*, V. 44, No. 1, 2009, pp. 20-31. doi: 10.1179/174327808X272405

35. Söylev, T. A.; McNally, C.; and Richardson, M., "Effectiveness of Amino Alcohol-Based Surface-Applied Corrosion Inhibitors in Chloride-Contaminated Concrete," *Cement and Concrete Research*, V. 37, No. 6, 2007, pp. 972-977. doi: 10.1016/j.cemconres.2007.03.010

36. Jamil, H. E.; Shriri, A.; Boulif, R.; Montemor, M. F.; and Ferreira, M. G. S., "Corrosion Behaviour of Reinforcing Steel Exposed to an Amino Alcohol Based Corrosion Inhibitor," *Cement and Concrete Composites*, V. 27, No. 6, 2005, pp. 671-678. doi: 10.1016/j.cemconcomp.2004.09.019

37. Kondratova, I. L.; Montes, P.; and Bremner, T. W., "Natural Marine Exposure Results for Reinforced Concrete Slabs with Corrosion Inhibitors," *Cement and Concrete Composites*, V. 25, No. 4-5, 2003, pp. 483-490. doi: 10.1016/S0958-9465(02)00088-4

38. Vyrides, I.; Rakanta, E.; Zafeiropoulou, T.; and Batis, G., "Efficiency of Amino Alcohols as Corrosion Inhibitors in Reinforced Concrete," *Open Journal of Civil Engineering*, V. 3, No. 2, 2013, pp. 1-8. doi: 10.4236/ojce.2013.32A001

39. Andrade, C., and Alonso, C., "Test Methods for On-Site Corrosion Rate Measurement of Steel Reinforcement in Concrete by Means of the Polarization Resistance Method," *Materials and Structures*, V. 37, No. 9, 2004, pp. 623-643. doi: 10.1007/BF02483292

40. Ford, S. J.; Shane, J. D.; and Mason, T. O., "Assignment of Features in Impedance Spectra of the Cement-Paste/Steel System," *Cement and Concrete Research*, V. 28, No. 12, 1998, pp. 1737-1751. doi: 10.1016/S0008-8846(98)00156-2

41. Dong, B.-Q.; Qiu, Q.-W.; Xiang, J.-Q.; Huang, C.-J.; Xing, F.; Han, N.-X.; and Lu, Y.-Y., "Electrochemical Impedance Measurement and Modeling Analysis of the Carbonation Behavior for Cementititous Materials," *Construction and Building Materials*, V. 54, 2014, pp. 558-565. doi: 10.1016/j.conbuildmat.2013.12.100

42. Bragança, M. O. G. P.; Portella, K. F.; Bonato, M. M.; and Marino, C. E. B., "Electrochemical Impedance Behavior of Mortar Subjected to a Sulfate Environment - A Comparison with Chloride Exposure Models," *Construction and Building Materials*, V. 68, 2014, pp. 650-658. doi: 10.1016/j.conbuildmat.2014.06.040

43. Criado, M.; Monticelli, C.; Fajardo, S.; Gelli, D.; Grassi, V.; and Bastidas, J. M., "Organic Corrosion Inhibitor Mixtures for Reinforcing Steel Embedded in Carbonated Alkali-Activated Fly Ash Mortar," *Construction and Building Materials*, V. 35, 2012, pp. 30-37. doi: 10.1016/j.conbuildmat.2012.02.078

44. Gu, P.; Elliott, S.; Hristova, R.; Beaudoin, J. J.; Brousseau, R.; and Baldock, B., "A Study of Corrosion Inhibitor Performance in Chloride Contaminated Concrete by Electrochemical Impedance Spectroscopy," *ACI Materials Journal*, V. 94, No. 5, Sept.-Oct. 1997, pp. 385-395.

45. Choi, Y. S.; Kim, J. G.; and Lee, K. M., "Corrosion Behavior of Steel Bar Embedded in Fly Ash Concrete," *Corrosion Science*, V. 48, No. 7, 2006, pp. 1733-1745. doi: 10.1016/j.corsci.2005.05.019

46. Zhao, R.; Jin, Z.; Feng, G.; and Li, J., "Chloride Diffusion and Induced Reinforcement Corrosion in Concrete with Fly Ash and Ground-Granulated Blast-Furnace Slag Exposed to Marine Submerged Zone1," *Advances in Materials Science and Engineering*, V. 2020, No. 1, 2020, pp. 1-17. doi: 10.1155/2020/8881446

47. Beglarigale, A.; Yiğiter, H.; and Yazıcı, H., "Corrosion Performance of Various Reinforced Concretes Subjected to a Systematic Wetting–Drying Cycle Regime in Real Marine Environment," *Journal of Materials in Civil Engineering*, ASCE, V. 35, No. 5, 2023, pp. 1-16. doi: 10.1061/(ASCE)MT.1943-5533.0004707

ACI MATERIALS JOURNAL TECHNICAL PAPER

Title No. 122-M23

Review of High-Volume Fly Ash Binder in Engineered Cementitious Composites

by Tianyu Xiao and Sen Du

Engineered cementitious composite (ECC), a prominent innovation in the realm of concrete materials in recent years, contains a substantial amount of cement in its composition, thereby resulting in a significant environmental impact. To enhance the environmental sustainability of ECC, it is plausible to substitute a large portion of cement in the composition with fly ash, a by-product of coal-fired power plants. Recent years have seen increased research in ECC containing high-volume fly ash (HVFA) binder and its wider application in construction practices. In this particular context, it becomes imperative to review the role of HVFA binder in ECC. This review first examines the effects of incorporating HVFA binder in ECC on the fiber dispersion and fiber-matrix interface behavior. Additionally, mechanical properties, including compressive strength, tensile behavior, and cracking behavior under loading, as well as durability performances of HVFA-based ECC under various exposure conditions, are explored. Last, this review summarizes the research needs pertaining to HVFA-based ECC, proving valuable guidance for future endeavors in this field.

Keywords: durability performance; engineered cementitious composite (ECC); fiber dispersion; fiber-matrix interface; high-volume fly ash (HVFA); mechanical properties.

INTRODUCTION

Engineered cementitious composite (ECC), characterized by its exceptional tensile strain and ductility, can exhibit a tensile strain capacity ranging from 3 to 5% under tensile loading, which is several hundred times greater than that of conventional concrete.[1] This remarkable tensile capacity enables ECC to withstand considerable deformation, thereby enhancing the structural reliability in the face of extreme loading events such as earthquakes, hurricanes, or blasts.[2] Additionally, ECC can effectively control crack width through the bridging effect of randomly distributed fibers, contributing to the reduced ingress of corrosive substances and significantly improved durability.[3] As a result, the application of ECC has witnessed substantial growth in structures exposed to harsh environments, such as bridge decks and airport runways, which are usually subjected to combined deterioration effects.[4]

Despite presenting obvious advantages as mentioned previously, the substantial amount of cement employed in the production of ECC manifests a significant environmental impact. Traditional cement-based ECC typically contains approximately 800 to 1200 kg/m^3 (50 to 75 lb/ft^3) of cement,[1,5] which equates to nearly three times the amount found in conventional concrete. Cement, one of the most carbon-intensive products manufactured by mankind, emits an average of 840 kg of CO$_2$ for every ton (1680 lb/ton) produced.[6] Considering the huge global consumption of cement, it is estimated that nearly 9% of annual anthropogenic CO$_2$ emissions can be attributed to cement production. Furthermore, cement-related CO$_2$ emissions account for about 70% of the total greenhouse gas emission derived from concrete.[7] Consequently, a higher cement content in ECC would directly translate to amplified greenhouse gas emission, thereby exacerbating the environmental footprint.

To diminish the embodied CO$_2$ of cement-based ECC, the partial replacement of cement with industry by-products has emerged as a highly effective approach.[8] Fly ash, a by-product resulting from coal combustion in coal-fired power plants, has been used as supplementary cementitious material (SCM) in concrete for decades due to its pozzolanic, morphological, and micro-aggregate effects.[9] Normally, fly ash is admixed into concrete in the range of 10 to 30% by mass of the binder, considering the instability of fly ash sources and its adverse effect on early-age strength.[10] In this range, the incorporation of fly ash can reduce the hydration heat, enhance the resistance to chemical attack, and improve the steel corrosion resistance.[11-13] With the objective of rendering concrete more sustainable and environmentally friendly, high-volume fly ash (HVFA) concrete has been formulated, with a fly ash replacement level for cement of 50% or higher.[14]

In an effort to reduce the embodied CO$_2$ emission and environmental impact of ECC, numerous researchers have employed HVFA binder in ECC production, aiming at attaining comparable or even superior tensile strain ductility in comparison to cement-based ECC.[5] A recent study demonstrated that despite a slight decrease in strength, ECC containing HVFA binder continued to exhibit quasi-brittle and ductile behaviors.[15] Furthermore, the incorporation of fly ash at a high volume enhances the durability performances of ECC when exposed to harsh environments.[16] Even the reduced strength of ECC due to the presence of HVFA binder can be compensated by using ultrafine fly ash, which still facilitates ECC to feature a lower embodied carbon footprint than cement-based ECC.

However, to the best of the authors' knowledge, there exists no comprehensive review that explores the role of HVFA binder in ECC. In light of this, there is a need to

---

ACI Materials Journal, V. 122, No. 4, July 2025.
MS No. M-2024-061.R6, doi: 10.14359/51746805, received March 26, 2025, and reviewed under Institute publication policies. Pertinent discussion including author's closure, if any, will be published ten months from this journal's date if the discussion is received within four months of the paper's print publication.

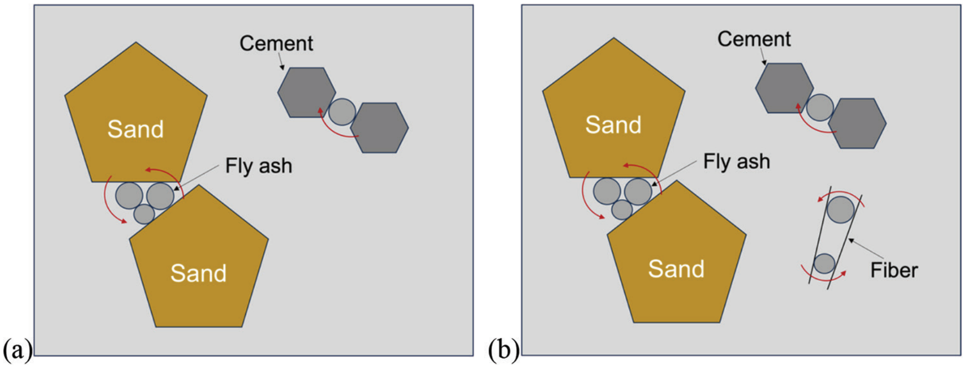

Fig. 1—Ball-bearing effect of fly ash in: (a) conventional concrete; and (b) ECC.

synthesize and review existing knowledge regarding HVFA-based ECC, particularly with respect to the effects of the incorporation of HVFA binder in ECC on fiber dispersion, fiber-matrix interface behavior, as well as mechanical properties and durability performances. To accomplish this goal, approximately 100 relevant publications from the past two decades were gathered from various databases and subsequently analyzed to provide a comprehensive overview.

RESEARCH SIGNIFICANCE

An examination of the significance of HVFA binder in ECC could offer a cutting-edge review of advancements in research on ECC using HVFA, thereby aiding in the endeavor of transition ECC into a more environmentally friendly material. Through focusing on the morphological and pozzolanic effects of fly ash as well as the interaction between fly ash and fiber, a comprehensive understanding of the correlation between material characteristics and properties of HVFA-based ECC can be established.

EFFECT OF HVFA BINDER ON FIBER IN ECC

Fiber dispersion

In cement-based ECC, the dispersion of fiber is significantly affected by the presence of sand and its morphological parameters. It was reported that the uniformity of fiber dispersion may be adversely affected by sand particles possessing a high degree of roundness and sphericity.[17] This, in turn, reduces the tensile strain capacity of ECC. Moreover, fiber clumping may occur in ECC if the sand particle size exceeds the average spacing between fibers. This leads to a reduction in the number of fibers present in the cracking area, thus compromising the tensile strain capacity of ECC. Fortunately, the incorporation of HVFA binder proves advantageous in eliminating or minimizing the detrimental effects of sand on fiber dispersion within ECC.[18]

The incorporation of fly ash at a high replacement level has been shown to enhance the dispersion of fibers during the mixing process of ECC.[19] By replacing 58 to 74% of cement with fly ash, a self-consolidating ECC with uniformly dispersed fibers throughout the matrix can be produced.[20] This finding is consistent with the conclusions drawn by Zhu et al.,[21] who observed that ECC containing 70% fly ash exhibited desirable deflection properties, which was attributed to the improved dispersion of fibers within the matrix facilitated by the presence of HVFA binder. Specifically, Tosun-Felekoğlu et al.[22] proposed that the efficiency of fiber dispersion in HVFA-based ECC can be enhanced due to the smooth, glassy, and spherical characteristics of fly ash particles, especially Class F fly ash. Conversely, the use of Class C fly ash, characterized by irregular shape and coarse particle size, may result in fiber clumping.

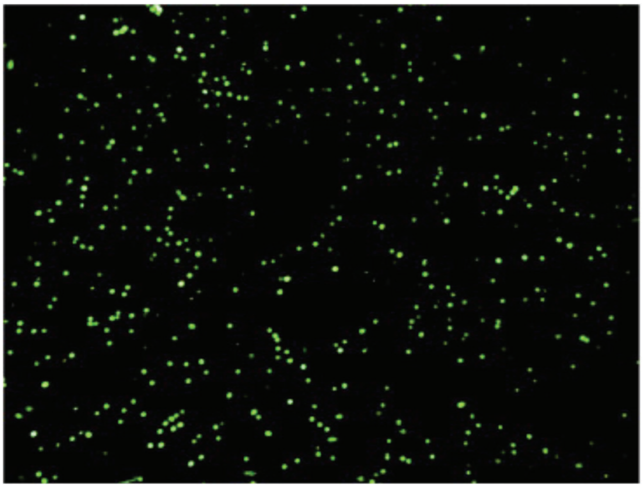

Fig. 2—Fluorescence image showing dispersion of PVA fiber in ECC containing 69% fly ash.[24] Green: fiber. Black: matrix. (Full-color PDF of this paper can be accessed at www.concrete.org.)

It is well known that Class F fly ash is the most commonly used type of fly ash in concrete, characterized by its predominantly smooth surface and spherical morphology. In this case, fly ash particles can function as ball bearings, facilitating the mitigation of internal friction among various grains[23] including cement and sand particles, as shown in Fig. 1(a). As a result, the incorporation of fly ash in concrete could improve its workability. It could be expected that the good dispersion of fibers in HVFA-based ECC benefits at least partially from the "ball-bearing" effect of fly ash. Figure 1(b) illustrates the positive effect of fly ash addition on the fiber dispersion in ECC.

In the research of ECC, the direct determination of fiber dispersion homogeneity in the matrix has been a seldom-explored domain due to the absence of suitable methodologies. Recently, a novel approach based on image analysis emerged to assess the uniformity of fiber dispersion,[24]

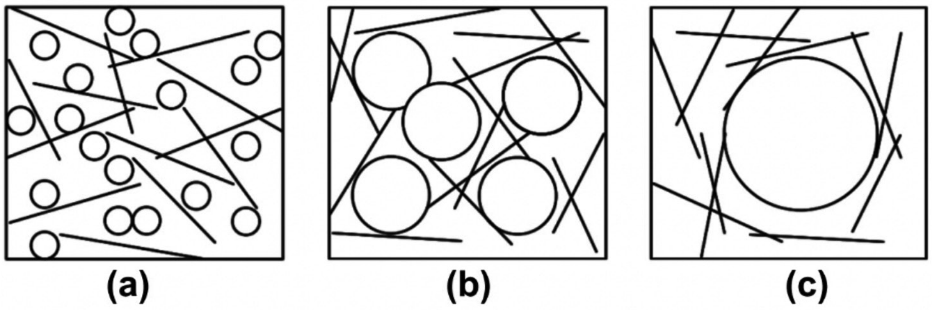

Fig. 3—Schematic diagram of fiber with average distance: (a) greater than; (b) similar to; and (c) smaller than aggregate size.[27]

especially polyvinyl alcohol (PVA) fibers, as presented in Fig. 2. In this figure, pixels highlighted in green denote the presence of PVA fibers, while those in black represent the matrix (full-color PDF of this paper is available at www.concrete.org). Through the image analysis, the fiber-dispersion coefficient can be obtained, wherein a coefficient of 1 indicates a state of completely homogenous dispersion while a value of 0 represents all fibers are clustered together.[25] When the replacement level of cement with fly ash was 55%, ECC mixtures exhibited a fiber-dispersion coefficient ranging from 0.5 to 0.9, suggesting excellent fiber dispersion and confirming the beneficial effect of HVFA binder on fiber dispersion in ECC.[26] It is postulated that the average distance between fibers should exceed the size of aggregate to facilitate proper fiber dispersion,[27] as depicted in Fig. 3. It is obvious that fibers in Fig. 3(a) exhibit a significantly improved fiber-dispersion homogeneity compared to those in Fig. 3(b) and (c), owing to the greater fiber spacing. The theoretical distance between fibers was calculated to be in a range of 205 to 307 μm using PVA fibers with diameter and volume fraction of 39 μm and 2%, respectively.[24]

It is obvious that nearly all the fine aggregates have a larger size than the theoretical fiber spacing, while the fly ash particles are smaller than this distance, confirming the favorable effect of HVFA binder on fiber dispersion in ECC. The typical particle size for fly ash used in concrete falls within the range of 0.2 to 100 μm,[28,29] while the fine aggregate may span from 70 to 5000 μm, as illustrated in Fig. 4. The lower and upper limits for the fiber spacing using the aforementioned PVA fiber factors are also present in this figure, which are clearly smaller than the majority of sand particles yet surpassing the particle size range of fly ash. As a result, the incorporation of HVFA binder in ECC could mitigate the fiber clumping caused by the presence of sand.

Fiber-matrix interface behavior

In the formulation of ECC, a variety of fibers can be used, including PVA, steel, polyethylene (PE), basalt, and hybrid fibers. Among them, PVA fiber, characterized by its high tensile strength and modulus of elasticity as well as its cost-effectiveness, has been the most widely used admixed fiber in ECC.[5,30] When admixed into the cement-based ECC mixtures, PVA fiber can undergo a chemical reaction with cement hydration products, thereby establishing a strong chemical bond between the fiber and the matrix.[31]

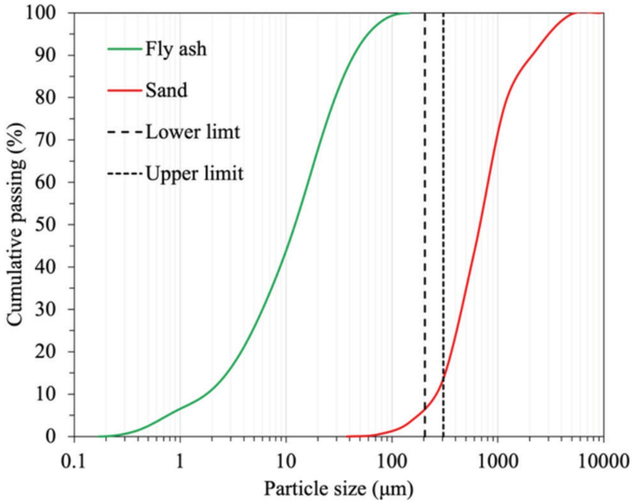

Fig. 4—Particle size distribution of fly ash and sand as well as limits of fiber spacing, based on data collected from references.[24,28,29]

Figure 5 presents the interfacial connections between PVA fiber and calcium silicate hydrate (C–S–H) as an example. As shown in Fig. 5, the hydrogen atoms in the molecular chains of PVA fiber react with Si–OH groups in C–S–H, resulting in the formation of the first type of H bond (indicated by the connection labeled as 1). Additionally, the second type of H bond, denoted by the label 2 in Fig. 5, is formed through the attraction between hydrogen atoms in C–S–H and C–OH groups from PVA fibers.[32] Therefore, the fiber-matrix interface bond is strengthened due to the chemical reaction between them, potentially leading to fiber rupture and a consequent reduction in the tensile strain capacity of ECC if the chemical bond surpasses the fiber bridging capacity.[33] In such scenarios, surface treatment on the fibers (for example, coating with oil) must be applied prior to admixing them in ECC.[34]

The incorporation of HVFA binder in ECC can also lead to a reduction in the bond between the fiber and the matrix. Peled et al.[35] conducted a study on the failure mode of fibers in ECC with varying fly ash contents and observed a shift from fiber fracture to fiber pullout as the fly ash content increased from 0 to 70%. It was proposed that a high replacement of cement by fly ash in ECC could increase the porosity of the matrix, leading to a deterioration in its properties and a decrease in the strength of the fiber-matrix interface bond

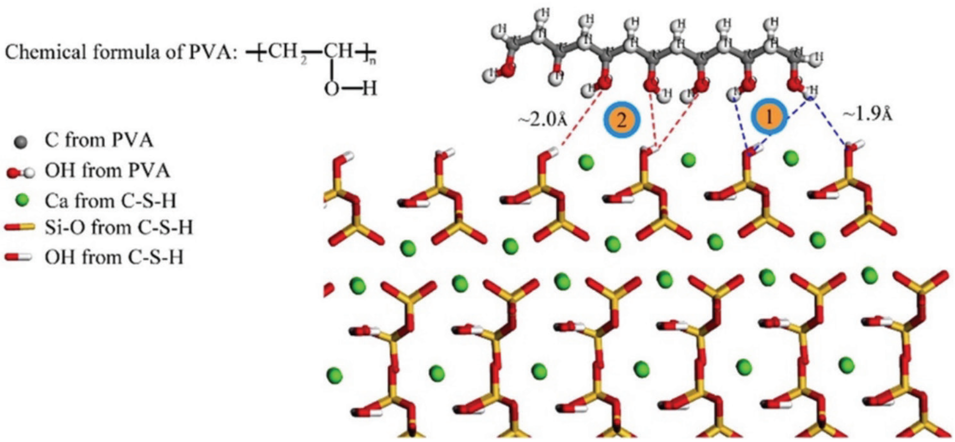

Fig. 5—Schematic illustration of interfacial connections between PVA and C–S–H.[32]

and thereby altering the fiber failure mode. As a result, at a given fiber bridging capacity, cement-based ECC without fly ash exhibited fiber rupture, whereas in HVFA-based ECC, the fiber would be pulled out from the matrix. This finding is similar with another study,[36] which demonstrated that the incorporation of 69% fly ash in the binder could reduce the matrix toughness, interface frictional stress, and interface chemical bond of ECC simultaneously. Therefore, the replacement of cement by fly ash at a high level is found to be beneficial for enhancing the tensile strain capacity of HVFA-based ECC, contributing to a superior strain-hardening behavior compared to cement-based ECC.

The reduced fiber-matrix chemical bond and interface frictional stress resulting from the incorporation of HVFA binder in ECC can be explained by two mechanisms. First, the presence of a high-volume fraction of fly ash in the matrix may dilute the concentration of cement hydration products, resulting in a reduced chemical reaction rate with PVA fiber and a subsequent reduction in the development of interface chemical bond.[37] Second, the residual carbon present in fly ash can act as a lubricant, facilitating easy fiber pullout and consequently reducing the interface fractional stress.

It is well known that almost all fly ashes contain unburnt carbon due to the incomplete combustion, and its content is typically indicated by the loss on ignition (LOI) of fly ash. Generally, the presence of unburnt carbon particles in fly ash has the capacity to absorb chemical admixtures,[38] compromising the workability of concrete containing such fly ash. However, owing to the spherical morphology of these carbon particles,[39] they are likely to demonstrate the ball-bearing effect similar to that of fly ash particles, thereby reducing the interfacial stress between the fiber and the matrix.

PROPERTIES AND PERFORMANCES OF ECC

It is well known that the incorporation of HVFA binder can have significant effects on the mechanical properties and durability performances of concrete, including ECC. This section provides a comprehensive overview of the compressive strength, tensile behavior, crack width, and durability performances of HVFA-based ECC.

Compressive strength

Typically, traditional cement-based ECC exhibits a high compressive strength owing to its high cement content. The primary concern when considering the incorporation of HVFA binder in ECC is the potential reduction in compressive strength. Studies have demonstrated that by using an ECC with 55% fly ash, the 7- and 28-day compressive strengths can reach 38 and 50 MPa (5511 and 7252 psi), respectively.[40-42] Furthermore, ECC has been shown to achieve a 28-day compressive strength exceeding 40 MPa with a substantial 70% replacement of cement by fly ash.[43] Even with a higher fly ash content of 74%, the 28-day compressive strength of HVFA-based ECC can still reach a value of 35 MPa (5076 psi), meeting the requirements of normal engineering applications.[5]

For cement-based ECC with appropriate water-binder ratios, the compressive strength typically falls within the 60 to 90 MPa (8702 to 13,053 psi) range.[44,45] It can be concluded that the incorporation of HVFA binder in ECC indeed leads to a reduction in the compressive strength, with the reduction increasing with the fly ash content. During the early ages, a significant portion of fly ash particles in the HVFA system remain unreacted, and the concentration of cement particles is diluted, resulting in the formation of fewer hydration products and thus a lower compressive strength of HVFA mixtures, including HVFA-based ECC.[46]

However, it should be noted that as the curing time increases—for example, from 28 to 90 days—the compressive strength of HVFA-based ECC demonstrates accelerated development compared to that at early ages.[47] With the prolonged curing age, the pozzolanic reaction of fly ash, occurring between the fly ash particle and the portlandite generated during cement hydration, leads to the generation of additional calcium aluminosilicate hydrate (C–A–S–H) gels and thereby the accelerated strength development of HVFA-based ECC.[48] In fact, at later-term ages, HVFA mixtures may develop a compressive strength comparable to that of cement-based materials.[49] At the curing time of 90 days, the compressive strength of HVFA-based ECC can reach a value in the range of 55 to 60 MPa,[50,51] or even higher than 60 MPa.[52] As a result, the compressive strength of HVFA-based ECC is usually represented by the strength at the curing time of 90 days.

Table 1—Maximum replacement level of fly ash in ECC

Property	Maximum fly ash replacement level	Effect of a further higher fly ash content	References
Compressive strength	70 to 75%	Fail to meet strength requirement	40-42, 55, 56
Tensile behavior	80%	Lower tensile strain being less than 2%	57-59
Crack width	70 to 75%	Limit self-healing of crack	53, 60-62

On the other hand, there exists an upper limit for fly ash replacement in ECC, approximately 70 to 75%, beyond which the compressive strength diminishes to a level inadequate for structural concrete requirements.[40] For instance, a study revealed that ECC with a 80% fly ash replacement only yielded a 28-day compressive strength of 24 MPa (4061 psi),[53] even in the condition of employing a water-binder ratio as low as 0.2.[54] Table 1 lists the maximum replacement level for fly ash in ECC concerning compressive strength, alongside additional properties that will be detailed in the following sections.

Tensile behavior

The tensile strain-hardening behavior is almost the focus of every study of HVFA-based ECC. Normally, HVFA-based ECC has demonstrated a tensile ductility that ranges between 2 and 4%.[5] It should be noted that the maximum permissible fly ash replacement in ECC to achieve a sufficient strain-hardening capacity (2%) is approximately 80%,[57] as included in Table 1. At a lower fly ash content of 70%, the tensile strain of ECC after 90 days of curing can exceed 2.5%.[43] ECC containing 50% fly ash has shown a tensile strain capacity ranging from 3 to 4%, with the tensile strength reaching as high as 4.5 MPa (652 psi).[50]

The high tensile strain capacity of HVFA-based ECC is believed to stem from reductions in three key properties: the chemical bond at the fiber-matrix interface, the frictional stress at the fiber-matrix interface, and the matrix toughness.[36] Additionally, the reduced cement content in ECC can also account for its diminished matrix toughness.[58] As a result, the pullout of fiber, rather than the rupture, would be observed as a consequence of the reduced adhesion between the fiber and the matrix. On the other hand, the decrease in matrix toughness facilitates the development of multiple cracks in the matrix prior to the stress reaching the fiber bridging capacity. Both effects will contribute to the exhibition of strain-hardening behavior of HVFA-based ECC under tension, characterized by the formation of multiple cracks with an average width of approximately 60 μm and a spacing of 1 to 2 mm when subjected to large deformation.[40]

Besides the high tensile strain capacity of HVFA-based ECC, it can also be concluded that the tensile strain capacity of HVFA-based ECC decreases with increasing the replacement level of fly ash. Table 2 presents the effect of fly ash content on the tensile strain of HVFA-based ECC. It should be noted that the tensile strain capacity listed in this table is based on the data obtained at the curing time of 28 days, as the predominant focus of studies lays on the tensile behavior of HVFA-based ECC at this specific age. As the fly ash content in HVFA-based ECC increases, the reduction in tensile strain capacity may be due to the tightened crack width under tensile loading, which will be detailed later.

Table 2—Effect of fly ash content on tensile strain of HVFA-based ECC

Fly ash replacement level	Tensile strain capacity	References
50%	3 to 4%	50
55%	3%	16, 41, 42
60%	3%	51
70%	2.5%	36, 43
80%	2%	57

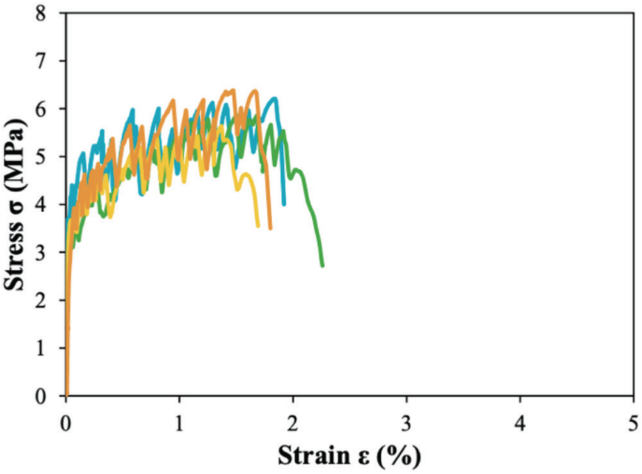

Fig. 6—Tensile stress-train curves of ECC containing 69% fly ash.[59] Curves with different colors mean replication specimens for same ECC mixture. (Full-color PDF of this paper can be accessed at www.concrete.org.)

Figure 6 illustrates typical tensile stress-strain curves for ECC containing 69% fly ash after 28 days of curing. Obviously, the strain-hardening behavior is observed in ECC, with the strain capacity reaching approximate 2%. It can also be inferred from Fig. 7 that the strain capacity of HVFA-based ECC is attributed to the presence of multiple cracks rather than a single crack. Specifically, both the increases in crack width and the increase in crack number contributed to the increase of strain up to 1% at the initial stage of tensile loading, while the later stage development of strain is mainly due to the increase in crack number.[59]

Crack width

The width of crack is a crucial parameter for assessing the tensile properties of ECC in relation to its strain-hardening behavior.[61] As the cement replacement level with fly ash in ECC rises from 0 to over 50%, the crack width in

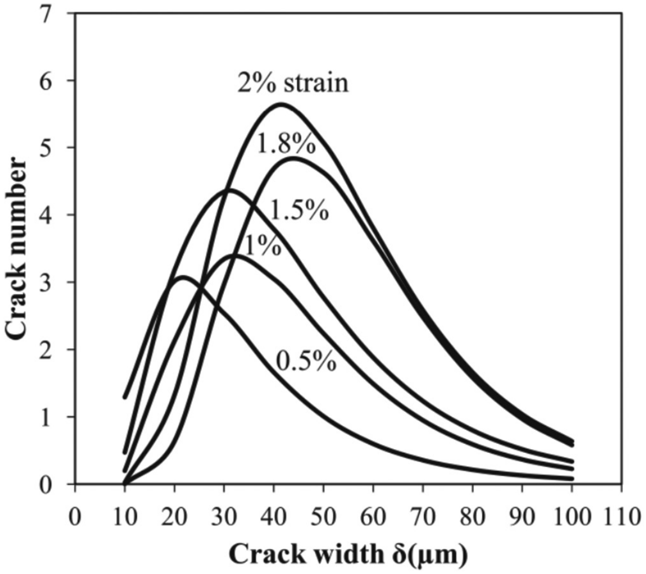

Fig. 7—Representative lognormal crack width distribution for ECC containing 69% fly ash at different imposed strain levels.[59]

ECC at the 60 μm level can be reduced to the range of 10 to 30 μm.[5,40,55] In ECC containing 55 to 78% fly ash, a further reduction in crack width is evident (as present in Fig. 8).[5] As the strain capacity is linked to the increase in crack width, the tensile strain capacity of HVFA-based ECC would also decrease as the fly ash content increases.

It is well acknowledged that the incorporation of fly ash in ECC could reduce the matrix toughness, fiber-matrix interface frictional stress, and fiber-matrix interface chemical bond simultaneously.[36] As a result, an increased fly ash content leads to a greater number of fibers being partially pulled out from the matrix in HVFA-based ECC, resulting in a constricting effect on crack propagation. This explains the tightened crack width of HVFA-based ECC containing a higher content of fly ash, consequently leading to a diminished tensile strain capacity in such ECC.

On the other hand, the reduction in crack width in HVFA-based ECC is beneficial for the long-term durability of ECC in aggressive environments, as it results in the limited ingress of deteriorative substances into ECC. However, the crack width would increase with increasing strain levels imposed on the HVFA-based ECC. The distribution of crack width for ECC containing 69% fly ash at different strain levels is shown in Fig. 7. It should be noted that as the strain level increases, the crack distribution transforms from a tight pattern to a loose pattern, wherein more cracks with larger width are observed.[59]

The width of cracks in ECC holds significant importance as it has been identified as a critical factor affecting in the self-healing ability of concrete. Self-healing refers to the ability of a crack to diminish in width autogenously over time. A tight crack width facilitates the easy and complete healing of a crack.[61] In fact, for ECC to exhibit effective self-healing behavior, the crack widths must be less than 150 μm, preferably lower than 50 μm.[63] Therefore, HVFA-based ECC featuring tight crack widths are expected to enhance the self-healing properties. For instance, Kan et al.[62] observed a highly robust self-healing in ECC containing 55% fly ash, where the crack width was less than 50 μm. Meanwhile, with a higher fly ash replacement level of 69%, Sahmaran et al.[61] found that cracks ranging from 30 to 50 μm in width could be healed. With the same fly ash replacement, Fan and Li[60] concluded that the self-healing behavior in HVFA-based ECC varied along the depth of cracks, emphasizing the importance of using crack volume rather than surface crack area for accurate self-healing characterization.

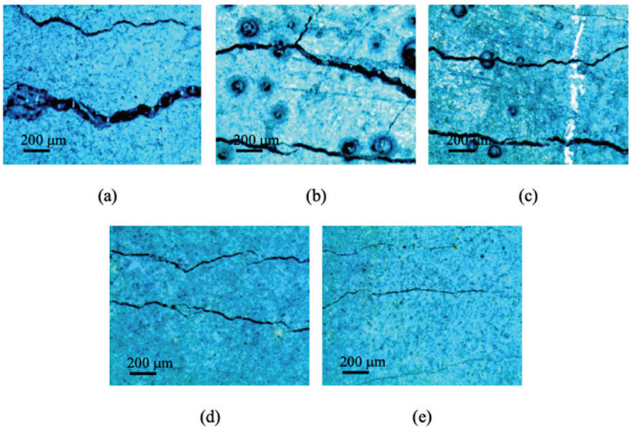

Fig. 8—Residual crack width of ECC after 3 days of quasi-static loading where fly ash content is: (a) 55%; (b) 62%; (c) 67%; (d) 74%; and (e) 78%, respectively.[5]

Generally, the formation of additional hydration products due to the pozzolanic reaction between fly ash and portlandite is responsible for the healing of cracks occurring in ECC during the pre-loading or exposure to various deteriorations.[47] Given the presence of more unhydrated cementitious materials in HVFA systems, it is expected that HVFA-based ECC possesses a greater capacity for self-healing cracks. Figure 9 shows the filling of a crack by newly formed C–S–H gels, which indicates the occurrence of crack self-healing.[56] The observed recovery in transport and mechanical properties in pre-cracked ECC further confirms the self-healing process.[64] It should be noted that there exists an upper limit for fly ash replacement level in ECC (normally 70 to 75%, as summarized in Table 1), beyond which increasing the fly ash content would no longer be beneficial for crack self-healing.[53] This is due to the insufficient supply of self-healing products at such high fly ash contents in ECC, where limited portlandite availability hinders the pozzolanic reaction of fly ash.

Durability

Generally, HVFA-based ECC has demonstrated excellent durability when subjected to various deterioration conditions. In fact, a series of studies investigating the durability performances of ECC containing 55% fly ash revealed its lower risk of capillary water transport,[65] reduced penetration of chloride ions,[56,66] enhanced resistance to freezing-and-thawing cycles with or without deicing salts,[55,67] absence of expansion due to alkali-silica reaction,[41] improved resistance to reinforcing bar corrosion,[42] higher residual tensile ductility in hot and humid environments,[68] and enhanced fire resistance in terms of residual mechanical properties and explosive spalling.[69]

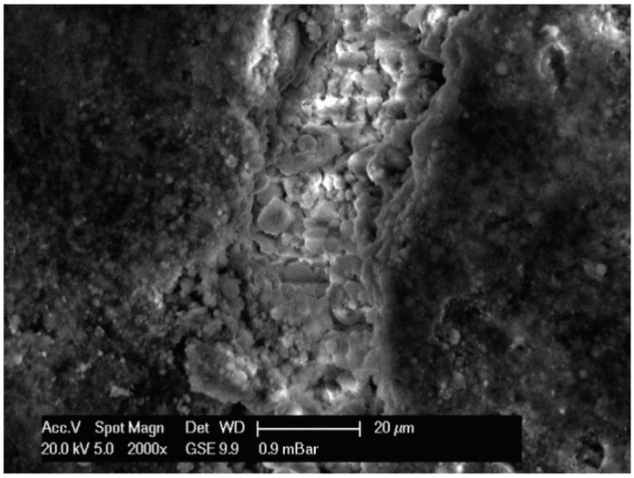

Fig. 9—Micrograph of pozzolanic reaction products present in crack in ECC containing 69% fly ash.[53]

Fire resistance—Generally, the fire resistance of HVFA-based ECC is good until the elevated temperatures compromise the fiber bridging effect. For ECC with 78% fly ash replacement level, the average fatigue life may exhibit a modest enhancement under cyclic loading conditions at elevated temperatures below 200°C (392°F).[70] At such a high temperature—for example, 100°C (212°F)—the number of microcracks increases rapidly in the initial stage of fatigue loading and then reaches a stable expansion stage, contributing to its improved fire resistance. When using as a repair material for structures impaired by elevated temperatures, ECC containing 55% fly ash demonstrates superior bonding properties, guaranteeing the structural integrity.[71] With a similar fly ash content, ECC exhibits enhanced residual compressive strength, reduced mass loss, and delayed decomposition of hydration products when subjected to high temperatures below 200°C (392°F).[72,73] A similar conclusion can be drawn from ECC containing 50% fly ash, in which the compressive strength and tensile ductility are mostly retained under elevated temperature exposures up to 200°C (392°F).[74]

Note that the tensile capacity of HVFA-based ECC may diminish at elevated temperatures exceeding 150 to 200°C (302 to 392°F), as the reinforcing PVA fibers begin to melt.[75] At such high temperatures, both the fiber strength and the fiber-matrix strength are compromised, resulting in the loss of strain-hardening characteristic of ECC,[76] as illustrated by the crack patterns shown in Fig. 10. It is also evident from this figure that the mass losses in matrix material become significant when the exposure temperature exceeds 200°C (392°F).

Freezing-and-thawing resistance—Normally, the freezing-and-thawing resistance of HVFA concrete is inferior to that of its cement counterpart with an equivalent water-binder ratio.[77] This is because of the absorption effect of the air-entraining admixture by the unburnt carbon particles in the fly ash, which compromises the air-void characteristic, such as the spacing factor, and consequently, the freezing-and-thawing durability of HVFA concrete.[78] With an proper air void system, the freezing-and-thawing resistance of air-entrained HVFA concrete can be exceptional, showing a durability factor exceeding 95% upon completion of the rapid freezing-and-thawing cycling test.[79]

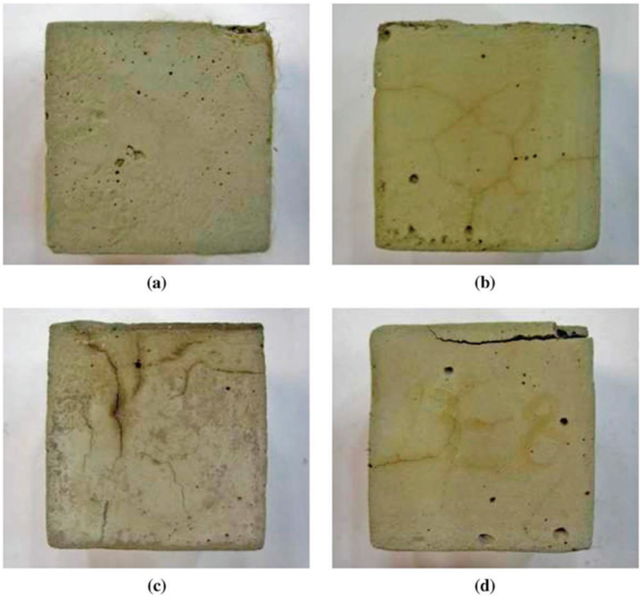

Fig. 10—Crack patterns on surface of HVFA-based ECC after exposure to high temperatures: (a) 200°C (392°F); (b) 400°C (752°F); (c) 600°C (1112°F); and (d) 800°C (1472°F).[69]

However, HVFA-based ECC features good freezing-and-thawing resistance in terms of the tensile strain capacity after specific freezing-and-thawing cycles. Specifically, HVFA-based ECC exhibits remarkable tensile strain capacity, surpassing 2%, even after 300 freezing-and-thawing cycles.[67] Moreover, ECC containing 64% fly ash demonstrates excellent resistance to combined effects of sulfate attack and freezing-and-thawing cycles.[4] Similar findings were reported in a study conducted by Liu et al.,[80] where it was observed that the ductility of ECC containing 50% fly ash could even increase after being subjected to freezing-and-thawing cycles in water or sodium chloride solution, as depicted in Fig. 11.

It can be seen from Fig. 11(a) that prior to the freezing-and-thawing cycles, the first cracking load and maximum deflection of the ECC were 284 N (63.8 lb) and 7.59 mm (0.30 in.), respectively. After 200 freezing-and-thawing cycles in tap water, the counterparts changed to 192 N (43.2 lb) and 18.50 mm (0.73 in.), respectively. It should be noted that the maximum deflection of the ECC was more than two times compared to its state before freezing-and-thawing cycles. Even after 200 freezing-and-thawing cycles in NaCl solution, the maximum deflection of the ECC containing 50% fly ash still reached a higher value of 16.51 mm (0.65 in.) (as shown in Fig. 11(b)).

This increased ductility of HVFA-based ECC during freezing-and-thawing cycles has mainly resulted from the self-healing capacity induced by the incorporation of HVFA binder. A similar conclusion was drawn in a study on preloaded HVFA-based ECC under freezing-and-thawing cycles, in which the recovery in the mechanical and transport properties was attributed to the self-healing behavior.[81] The

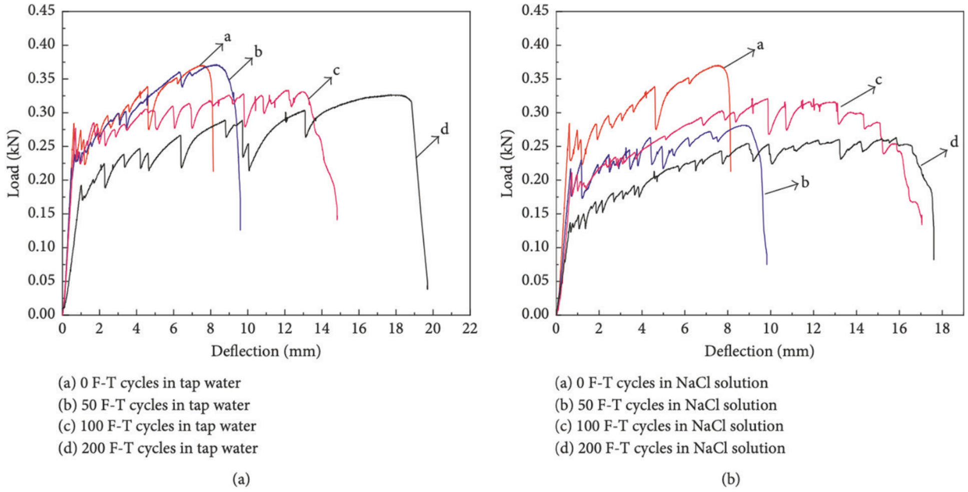

(a) 0 F-T cycles in tap water
(b) 50 F-T cycles in tap water
(c) 100 F-T cycles in tap water
(d) 200 F-T cycles in tap water

(a)

(a) 0 F-T cycles in NaCl solution
(b) 50 F-T cycles in NaCl solution
(c) 100 F-T cycles in NaCl solution
(d) 200 F-T cycles in NaCl solution

(b)

Fig. 11—Load-defection curves of ECC containing 50% fly ash subjected to different freezing-and-thawing cycles: (a) in tap water; and (b) in NaCl solution.[80]

generation of additional C–A–S–H gels from the pozzolanic reaction between fly ash particles and calcium hydroxide during the self-healing process would benefit the refinement of the pore structure, which contributes to the strength enhancement and transport properties.[82,83] Given the close connection between the freezing-and-thawing resistance of HVFA-based mixture and its strength and transport properties, HVFA-based ECC could feature an improved tensile ductility due to the self-healing effect of HVFA binder after specific freezing-and-thawing cycles. Table 3 summarizes the mechanisms contributing to the enhanced durability performances of HVFA-based ECC.

Transport properties—Generally, the incorporation of HVFA binder in cement-based materials can induce pore and grain refinement, resulting in enhanced transport properties of HVFA mixtures. These improvements include reduced water permeability, water sorptivity, gas permeability, and chloride ion penetration.[88-90] For HVFA-based ECC, it typically exhibits further lower water permeability, even in the presence of multiple microcracks under tensile strain of up to 3.0%.[84] A similar conclusion was drawn by Liu et al.,[59] who assessed the water permeability of cracked ECC containing 69% fly ash and attributed the reduced water permeability to the tight crack width of HVFA-based ECC. On the other hand, even when subjected to a severe marine environment with 3% NaCl for up to 90 days, ECC incorporating 55% fly ash retains a robust tensile ductility despite a reduction in tensile strength.[66]

The improved resistance to water permeability and chloride-ion penetration in HVFA-based ECC is attributed to the slow pozzolanic reaction of fly ash, which fills pores and reduces the porosity of ECC.[47] It has been observed that the incorporation of HVFA binder typically leads to a diminished quantity of capillary pores.[91] Moreover, the presence of HVFA binder can also increase the tortuosity of the capillary network and reduce pore interconnectivity.[92] Both effects could contribute to the reduced capillary absorption and water sorptivity.

Furthermore, the chemical reaction between the Al-rich phase in fly ash and chloride ions leads to the formation of stable complexes such as AFt/AFm and Friedel's salt, endowing HVFA-based ECC with a greater chloride binding capacity.[93-95] The reduction in crack width resulting from the increase in the fly ash content in ECC also contributes to its resistance to water permeability and chloride-ion permeation.[94] Tight crack widths in ECC have been shown to impede the ingress of moisture, gas, and harmful ions from external environments, thereby improving its durability.[95]

Chemical attack—The deterioration of concrete by chemicals primarily arises from the erosion and expansion of the paste induced by the reactions of chemical ions with portlandite and other hydration products. For normal HVFA concrete, the resistances to sulfate, lactic acid, acetic acid, and hydrochloric acid have been reported to be superior to that of ordinary portland cement concrete.[96] This can be explained by the reduction in the content of calcium hydroxide and the compact microstructure of HVFA concrete, resulting from the pozzolanic reaction of fly ash.

Regarding HVFA-based ECC, it demonstrates desirable durability when subjected to chemical attack. Liu et al.[97] investigated the resistance of ECC to aggressive solutions (5% Na_2SO_4 + 3% NaCl) and found that ECC containing 69% fly ash maintained a tensile ductility of over 2% after 200 days of exposure to this solution. In addition, under the same conditions, the self-healing of microcracks was observed in preloaded ECC.[85] Gao et al.,[86] in their study on the corrosion resistance of ECC containing 53% fly ash under the combined actions of 5% Na_2SO_4 solution and wetting-and-drying cycles, reported that HVFA-based ECC exhibited desirable performance after 120 corrosion cycles. This finding is consistent with recent studies[98,99] in which ECC with 55 to 69% fly ash demonstrated high resistance to the combined effects of sulfate corrosion, sulfuric acid attack, and wetting-and-drying cycles.

The pozzolanic and filling effects of fly ash particles were considered the key contributors to the corrosion resistance of HVFA-based ECC. Notably, a recent study indicated that even when exposed to simulated sewer environments encompassing sulfuric acid, sodium sulfate solution, wetting-and-drying cycles, and surface erosion, ECC containing 78% fly

Table 3—Improvement mechanism of incorporation of HVFA binder on durability of ECC

Property	Improvement mechanism	References
Freezing-and-thawing resistance	Benefit from self-healing behavior	67, 80, 81
Transport property	Slow pozzolanic reaction of fly ash, chemical reaction between fly ash and chloride ion, and tight crack width	47, 59, 66, 84
Chemical attack	Self-healing of microcracks, pozzolanic effect, and filling effect of fly ash particle	85-87

ash retained a tensile ductility of over 2% while maintaining self-healing ability.[87]

RESEARCH NEEDS

Numerous investigations have validated the feasibility of incorporating a substantial proportion of fly ash in ECC, typically ranging from 55 to 75% of the total binder. However, the huge demand for fly ash in concrete production has led to a diminishing supply of conventional fly ash.[19] Furthermore, in certain regions, the availability of conventional fly ash is diminishing because of the transition in fuel sources at electricity generation facilities (for example, from coal to natural gas). In this context, unconventional types of fly ash, such as biomass ash, have been used in the production of ECC.[19] Given the distinct physical and chemical characteristics of these unconventional ashes including fineness, crystallinity, LOI, and chemical composition, it has become increasingly imperative to explore the effect of employing these unconventional ashes on ECC properties. This exploration includes rheological properties, fiber dispersion, tensile behavior, and composite microstructure.[26]

A typical ECC mixture comprises cement, fly ash, sand, water, chemical admixtures, and fibers, predominantly oil-coated PVA. Currently, the oil-coated PVA fiber is primarily manufactured by a company located in Japan and commands a premium in the market. As a result, ECC is constrained to specific structures, such as bridge deck link slabs, bridge deck overlays, dam repairs, and coupling beams in high-rise buildings. Economic considerations present a significant hurdle to the widespread application of ECC into large-scale practical engineering. Moreover, despite the prevalent assertion of the superiority of HVFA-based ECC over cement-based ECC in terms of carbon footprint and sustainability, there is a lack of understanding regarding the life cycle assessment and cost-effectiveness of HVFA-based ECC. To facilitate the broader adoption of ECC in large-scale applications, there is an urgent imperative to develop cost-effective ECC using local materials while maintaining exceptional strain-hardening performance and to conduct a comprehensive life cycle analysis of the resultant ECC.

CONCLUSIONS

This work reviews the effect of incorporating high-volume fly ash (HVFA) binder on engineered cementitious composite (ECC) mixtures, including fiber dispersion, fiber-matrix interface behavior, as well as mechanical properties and durability performances of ECC. The following conclusions can be drawn.

1. The addition of HVFA binder in ECC can enhance the fiber dispersion efficiency due to the smooth surface and spherical morphology of fly ash particles, which act like ball bearings, facilitating the exhibition of the high tensile strain capacity of HVFA-based ECC.

2. The presence of HVFA binder in ECC has been found to reduce both the frictional stress at the fiber-matrix interface and the interface chemical bond. Unburnt carbon particles present in fly ash can serve as a lubricating agent, reducing the interface frictional stress. Fly ash at a high replacement level dilutes the concentration of cement hydration products, lowering the development of the interface chemical bond between the hydration products and fiber.

3. With the fly ash replacement levels laying in the normal range, HVFA-based ECC can exhibit a sufficient compressive strength for normal engineering applications. As the curing time increases, the strength development of HVFA-based ECC accelerates due to the pozzolanic reaction of fly ash.

4. There exists a maximum fly ash content for ECC to achieve a sufficient strain-hardening capacity, beyond which the tensile strain capacity of HVFA-based ECC begins to decrease, resulting from the fact that a greater number of fibers have been partially pulled out from the matrix. In this case, a constricting effect on crack propagation can be observed, which leads to a diminished tensile strain capacity.

5. The reduction in crack width has been widely observed in HVFA-based ECC, which can be attributed to the self-healing behavior of cracks by the pozzolanic reaction of fly ash. An upper limit for fly ash content exists in ECC, beyond which increasing the fly ash content would no longer be beneficial for crack self-healing due to the limited supply of portlandite.

6. HVFA-based ECC containing polyvinyl alcohol (PVA) fiber can demonstrate excellent resistances to damage by elevated temperatures, water transport and chloride ion penetration, freezing-and-thawing cycles, and chemical attack, in terms of the residual strength and tensile ductility.

7. Due to the limited supply of the conventional fly ash and the high expense of the raw materials (mainly oil-coated PVA fiber), future research should focus on the feasibility of using unconventional ashes (such as biomass ash) in ECC, the design of ECC using local materials, as well as conducting life cycle analysis and assessing the cost-effectiveness of HVFA-based ECC.

AUTHOR BIOS

Tianyu Xiao *is a Master's Student in civil engineering at the School of Civil Engineering and Mechanics, Yanshan University, Qinhuangdao, China. He received his BS in civil engineering from Hebei University of Science and Technology, Shijiazhuang, China. His research interests include the use of fly ash in concrete.*

Sen Du *is a Scientist at Hebei Province Engineering Research Center for Harmless Synergistic Treatment and Recycling of Municipal Solid Waste, and an Assistant Professor at Hebei Key Laboratory of Green Construction and Intelligent Maintenance for Civil Engineering, Yanshan University. He received his PhD from Washington State University, Pullman, WA. His research interests include high-volume fly ash concrete and pozzolanic reaction of supplementary cementitious materials.*

ACKNOWLEDGMENTS

The authors acknowledge the financial support from the Hebei Natural Science Foundation of China under Grants No. E2024203092 and E2021203214.

DECLARATION OF COMPETING INTEREST

The authors declare that they have no known competing financial interests or personal relationship that could have influenced the work reported in this paper.

REFERENCES

1. Li, V. C., "On Engineered Cementitious Composites (ECC) A Review of the Material and Its Applications," *Journal of Advanced Concrete Technology*, V. 1, No. 3, 2003, pp. 215-230. doi: 10.3151/jact.1.215

2. Yu, J.; Lin, J.; Zhang, Z.; and Li, V. C., "Mechanical Performance of ECC with High-Volume Fly Ash after Sub-Elevated Temperatures," *Construction and Building Materials*, V. 99, 2015, pp. 82-89. doi: 10.1016/j.conbuildmat.2015.09.002

3. Paul, S. C., and Babafemi, A. J., "A Review of the Mechanical and Durability Properties of Strain Hardening Cement-Based Composite (SHCC)," *Journal of Sustainable Cement-Based Materials*, V. 7, No. 1, 2018, pp. 57-78. doi: 10.1080/21650373.2017.1394236

4. Zhao, N.; Wang, S.; Wang, C.; Quan, X.; Yan, Q.; and Li, B., "Study on the Durability of Engineered Cementitious Composites (Eccs) Containing High-Volume Fly Ash and Bentonite Against the Combined Attack of Sulfate and Freezing-Thawing (F-T)," *Construction and Building Materials*, V. 233, 2020, p. 117313. doi: 10.1016/j.conbuildmat.2019.117313

5. Yang, E.-H.; Yang, Y.; and Li, V. C., "Use of High Volumes of Fly Ash to Improve ECC Mechanical Properties and Material Greenness," *ACI Materials Journal*, V. 104, No. 6, Nov.-Dec. 2007, pp. 303-311.

6. Gunasekara, C.; Sandanayake, M.; Zhou, Z.; Law, D.; and Setunge, S., "Effect of Nano-Silica Addition into High Volume Fly Ash–Hydrated Lime Blended Concrete," *Construction and Building Materials*, V. 253, 2020, p. 119205. doi: 10.1016/j.conbuildmat.2020.119205

7. Adanagouda; Somasekharaiah, H. M.; Shobha, M. S.; and Mallikarjuna, H. M., "Mechanical Properties and Acid Attack Test of Hybrid Fiber Reinforced High Performance Concrete for Fly Ash Based Mineral Admixture," *Materials Today: Proceedings*, V. 51, 2022, pp. 742-749. doi: 10.1016/j.matpr.2021.06.220

8. Teixeira, E. R.; Mateus, R.; Camões, A.; and Branco, F. G., "Quality and Durability Properties and Life-Cycle Assessment of High Volume Biomass Fly Ash Mortar," *Construction and Building Materials*, V. 197, 2019, pp. 195-207. doi: 10.1016/j.conbuildmat.2018.11.173

9. Hemalatha, T., and Ramaswamy, A., "A Review on Fly Ash Characteristics – Towards Promoting High Volume Utilization in Developing Sustainable Concrete," *Journal of Cleaner Production*, V. 147, 2017, pp. 546-559. doi: 10.1016/j.jclepro.2017.01.114

10. Huseien, G. F., and Shah, K. W., "Durability and Life Cycle Evaluation of Self-Compacting Concrete Containing Fly Ash as GBFS Replacement with Alkali Activation," *Construction and Building Materials*, V. 235, 2020, p. 117458. doi: 10.1016/j.conbuildmat.2019.117458

11. Franco-Luján, V. A.; Maldonado-García, M. A.; Mendoza-Rangel, J. M.; and Montes-García, P., "Effect of Cl−Induced Corrosion on the Mechanical Properties of Reinforcing Steel Embedded in Ternary Concretes Containing FA and UtSCBA," *Construction and Building Materials*, V. 339, 2022, p. 127655. doi: 10.1016/j.conbuildmat.2022.127655

12. Baltazar-Zamora, M. A., and Bastidas, M., "Effect of Silica Fume and Fly Ash Admixtures on the Corrosion Behavior of AISI 304 Embedded in Concrete Exposed in 3.5% NaCl Solution," *Materials*, V. 12, No. 23, 2019, p. 4007. doi: 10.3390/ma12234007

13. Lopez-Calvo, H. Z.; Montes-García, P.; Jiménez-Quero, V. G.; Gómez-Barranco, H.; Bremner, T. W.; and Thomas, M. D. A., "Influence of Crack Width, Cover Depth and Concrete Quality on Corrosion of Steel in HPC Containing Corrosion Inhibiting Admixtures and Fly Ash," *Cement and Concrete Composites*, V. 88, 2018, pp. 200-210. doi: 10.1016/j.cemconcomp.2018.01.016

14. Malhotra, V. M., "High-Performance High-Volume Fly Ash Concrete," *Concrete International*, V. 24, No. 7, July 2002, pp. 30-34.

15. Shabakhty, N.; Karimi, H. R.; and Bakhtiary, A. Y., "Statistical Evaluation of Fracture and Mechanical Performance of Engineered Cementitious Composites (ECC), Containing Different Percentages of Glass, Polypropylene, Polyvinyl-Alcohol Fibers, and Fly Ash," *Construction and Building Materials*, V. 417, 2024, p. 135247. doi: 10.1016/j.conbuildmat.2024.135247

16. Baloch, W. L.; Siad, H.; Lachemi, M.; and Sahmaran, M., "The Role of Supplementary Cementitious Materials and Fiber Reinforcements in Enhancing the Sulfate Attack Resistance of Scc/Ecc Composite Systems," *Construction and Building Materials*, V. 423, 2024, p. 135821. doi: 10.1016/j.conbuildmat.2024.135821

17. Wu, H.-L.; Yu, J.; Zhang, D.; Zheng, J.-X.; and Li, V. C., "Effect of Morphological Parameters of Natural Sand on Mechanical Properties of Engineered Cementitious Composites," *Cement and Concrete Composites*, V. 100, 2019, pp. 108-119. doi: 10.1016/j.cemconcomp.2019.04.007

18. Şahmaran, M.; Lachemi, M.; Hossain, K. M. A.; Ranade, R.; and Li, V. C., "Influence of Aggregate Type and Size on Ductility and Mechanical Properties of Engineered Cementitious Composites," *ACI Materials Journal*, V. 106, No. 3, May-June 2009, pp. 308-316.

19. Zhang, Z.; Yang, F.; Liu, J.-C.; and Wang, S., "Eco-Friendly High Strength, High Ductility Engineered Cementitious Composites (ECC) with Substitution of Fly Ash by Rice Husk Ash," *Cement and Concrete Research*, V. 137, 2020, p. 106200. doi: 10.1016/j.cemconres.2020.106200

20. Yang, E.-H.; Şahmaran, M.; Yang, Y.; and Li, V. C., "Rheological Control in Production of Engineered Cementitious Composites," *ACI Materials Journal*, V. 106, No. 4, July-Aug. 2009, pp. 357-366.

21. Zhu, Y.; Zhang, Z.; Yang, Y.; and Yao, Y., "Measurement and Correlation of Ductility and Compressive Strength for Engineered Cementitious Composites (ECC) Produced by Binary and Ternary Systems of Binder Materials: Fly Ash, Slag, Silica Fume and Cement," *Construction and Building Materials*, V. 68, 2014, pp. 192-198. doi: 10.1016/j.conbuildmat.2014.06.080

22. Tosun-Felekoğlu, K.; Gödek, E.; Keskinateş, M.; and Felekoğlu, B., "Utilization and Selection of Proper Fly Ash in Cost Effective Green HTPP-ECC Design," *Journal of Cleaner Production*, V. 149, 2017, pp. 557-568. doi: 10.1016/j.jclepro.2017.02.117

23. Yang, T.; Zhu, H.; Zhang, Z.; Gao, X.; Zhang, C.; and Wu, Q., "Effect of Fly Ash Microsphere on the Rheology and Microstructure of Alkali-Activated Fly Ash/Slag Pastes," *Cement and Concrete Research*, V. 109, 2018, pp. 198-207. doi: 10.1016/j.cemconres.2018.04.008

24. Huang, X.; Ranade, R.; Ni, W.; and Li, V. C., "Development of Green Engineered Cementitious Composites Using Iron Ore Tailings as Aggregates," *Construction and Building Materials*, V. 44, 2013, pp. 757-764. doi: 10.1016/j.conbuildmat.2013.03.088

25. Lee, B. Y.; Kim, J.-K.; Kim, J.-S.; and Kim, Y. Y., "Quantitative Evaluation Technique of Polyvinyl Alcohol (PVA) Fiber Dispersion in Engineered Cementitious Composites," *Cement and Concrete Composites*, V. 31, No. 6, 2009, pp. 408-417. doi: 10.1016/j.cemconcomp.2009.04.002

26. Li, M., and Li, V. C., "Rheology, Fiber Dispersion, and Robust Properties of Engineered Cementitious Composites," *Materials and Structures*, V. 46, No. 3, 2013, pp. 405-420. doi: 10.1617/s11527-012-9909-z

27. de Koker, D., and van Zijl, G., "Extrusion of Engineered Cement-Based Composite Material," *6th International RILEM Symposium on Fibre Reinforced Concretes*, 2004, pp. 1301-1310.

28. Sua-iam, G., and Makul, N., "Incorporation of High-Volume Fly Ash Waste and High-Volume Recycled Alumina Waste in the Production of Self-Consolidating Concrete," *Journal of Cleaner Production*, V. 159, 2017, pp. 194-206. doi: 10.1016/j.jclepro.2017.05.075

29. Yu, J.; Lu, C.; Leung, C. K. Y.; and Li, G., "Mechanical Properties of Green Structural Concrete with Ultrahigh-Volume Fly Ash," *Construction and Building Materials*, V. 147, 2017, pp. 510-518. doi: 10.1016/j.conbuildmat.2017.04.188

30. Wang, Q.; Yi, Y.; Ma, G.; and Luo, H., "Hybrid Effects of Steel Fibers, Basalt Fibers and Calcium Sulfate on Mechanical Performance of PVA-ECC Containing High-Volume Fly Ash," *Cement and Concrete Composites*, V. 97, 2019, pp. 357-368. doi: 10.1016/j.cemconcomp.2019.01.009

31. Li, V. C.; Wu, C.; Wang, S.; Ogawa, A.; and Saito, T., "Interface Tailoring for Strain-Hardening Polyvinyl Alcohol-Engineered Cementitious Composite (PVA-ECC)," *ACI Materials Journal*, V. 99, No. 5, Sept.-Oct. 2002, pp. 463-472.

32. Zhou, Y.; Huang, J.; Yang, X.; Dong, Y.; Feng, T.; and Liu, J., "Enhancing the PVA Fiber-Matrix Interface Properties in Ultra High Performance Concrete: An Experimental and Molecular Dynamics Study," *Construction and Building Materials*, V. 285, 2021, p. 122862. doi: 10.1016/j.conbuildmat.2021.122862

33. Kanda, T., and Li, V. C., "Interface Property and Apparent Strength of High-Strength Hydrophilic Fiber in Cement Matrix," *Journal of Materials in Civil Engineering*, ASCE, V. 10, No. 1, 1998, pp. 5-13. doi: 10.1061/(ASCE)0899-1561(1998)10:1(5)

34. Redon, C.; Li, V. C.; Wu, C.; Hoshiro, H.; Saito, T.; and Ogawa, A., "Measuring and Modifying Interface Properties of PVA Fibers in ECC Matrix," *Journal of Materials in Civil Engineering*, ASCE, V. 13, No. 6, 2001, pp. 399-406. doi: 10.1061/(ASCE)0899-1561(2001)13:6(399)

35. Peled, A.; Cyr, M. F.; and Shah, S. P., "High Content of Fly Ash (Class F) in Extruded Cementitious Composites," *ACI Materials Journal*, V. 97, No. 5, Sept.-Oct. 2000, pp. 509-517.

36. Wang, S., and Li, V. C., "Engineered Cementitious Composites with High-Volume Fly Ash," *ACI Materials Journal*, V. 104, No. 3, May-June 2007, pp. 233-241.

37. Gülgün, M. A.; Kriven, W. M.; Tan, L. S.; and McHugh, A. J., "Evolution of Mechano-Chemistry and Microstructure of a Calcium Aluminate-Polymer Composite: Part I. Mixing Time Effects," *Journal of Materials Research*, V. 10, No. 7, 1995, pp. 1746-1755. doi: 10.1557/JMR.1995.1746

38. Lin, L.; Hui, Z.; Jie, Y.; Yinghua, C.; Haisheng, L.; Siwei, C.; and Lei, X., "Rapid Detection of Loss on Ignition for Unburned Carbon Powder in Fly Ash Triboelectric Separation Based on Image Recognition and Machine Learning," *Advanced Powder Technology*, V. 35, No. 4, 2024, p. 104422. doi: 10.1016/j.apt.2024.104422

39. Iwan, M. A.; Günthel, M.; Kaminski, T. S.; Franus, W.; and Drewniak, Ł., "Biotransformation of Coal Fly Ash With High Carbon Content; Behavior and Release Patterns of Coal Fly Ash Constituents Under the Influence of Pseudomonas Stutzer MT1," *Journal of Cleaner Production*, V. 420, 2023, p. 138358. doi: 10.1016/j.jclepro.2023.138358

40. Şahmaran, M., and Li, V. C., "Durability Properties of Micro-Cracked ECC Containing High Volumes Fly Ash," *Cement and Concrete Research*, V. 39, No. 11, 2009, pp. 1033-1043. doi: 10.1016/j.cemconres.2009.07.009

41. Şahmaran, M., and Li, V. C., "Durability of Mechanically Loaded Engineered Cementitious Composites Under Highly Alkaline Environments," *Cement and Concrete Composites*, V. 30, No. 2, 2008, pp. 72-81. doi: 10.1016/j.cemconcomp.2007.09.004

42. Şahmaran, M., "Corrosion Resistance Performance of Steel-Reinforced Engineered Cementitious Composite Beams," *ACI Materials Journal*, V. 105, No. 3, May-June 2008, pp. 243-250.

43. Zhu, Y.; Yang, Y.; and Yao, Y., "Use of Slag to Improve Mechanical Properties of Engineered Cementitious Composites (ECCs) With High Volumes of Fly Ash," *Construction and Building Materials*, V. 36, 2012, pp. 1076-1081. doi: 10.1016/j.conbuildmat.2012.04.031

44. Sheta, A.; Ma, X.; Zhuge, Y.; ElGawady, M.; Mills, J. E.; and Abd-Elaal, E., "Axial Compressive Behaviour of Thin-Walled Composite Columns Comprise High-Strength Cold-Formed Steel and PE-ECC," *Thin-walled Structures*, V. 184, 2023, p. 110471. doi: 10.1016/j.tws.2022.110471

45. Zhang, Z.; Li, Z.; He, J.; Qian, S.; and Shi, X., "Recycled Mask Polypropylene Microfibers Benefit Tensile Properties and Prevent Thermally Induced Spalling of High-Strength Engineered Cementitious Composite (HS-ECC)," *Journal of Cleaner Production*, V. 457, 2024, p. 142476. doi: 10.1016/j.jclepro.2024.142476

46. Liu, M.; Tan, H.; and He, X., "Effects of Nano-SiO_2 on Early Strength and Microstructure of Steam-Cured High Volume Fly Ash Cement System," *Construction and Building Materials*, V. 194, 2019, pp. 350-359. doi: 10.1016/j.conbuildmat.2018.10.214

47. Ammasi, A. K., and Ragul, "Strength and Durability of High Volume Fly Ash in Engineered Cementitious Composites," *Materials Today: Proceedings*, V. 5, No. 11, 2018, pp. 24050-24058. doi: 10.1016/j.matpr.2018.10.198

48. Thangaraj, R., and Thenmozhi, R., "Industrial and Environmental Application of High Volume Fly Ash in Concrete Production," *Nature Environment and Pollution Technology*, V. 12, No. 2, 2013, p. 315-320.

49. Du, S.; Zhao, Q.; and Shi, X., "High-Volume Fly Ash-Based Cementitious Composites as Sustainable Materials: An Overview of Recent Advances," *Advances in Civil Engineering*, V. 2021, No. 1, 2021, pp. 1-22. doi: 10.1155/2021/4976169

50. Gu, D.; Xu, H.; Huang, Y.; Zhu, Y.; Pan, J.; and Luković, M., "Shear Crack Kinematics in Reinforced Engineered Cementitious Composite (ECC) Beams," *Case Studies in Construction Materials*, V. 21, 2024, p. e03587. doi: 10.1016/j.cscm.2024.e03587

51. Fernández, F.; Jarabo, R.; Asensio, E.; and Guerrero, A., "Study of Self-Healing at Large Ages for a 3D Printable ECC Material," *Materials Today: Proceedings*, 2023. doi: 10.1016/j.matpr.2023.05.087

52. Wei, J.; Ke, L.; Wang, P.; Li, W.; and Leung, C. K. Y., "Microstructure, Mechanical Properties and Interaction Mechanism of Seawater Sea-Sand Engineered Cementitious Composite (SS-ECC) With Glass Fiber Reinforced Polymer (GFRP) Bar," *Composite Structures*, V. 343, 2024, p. 118302. doi: 10.1016/j.compstruct.2024.118302

53. Zhang, Z.; Qian, S.; and Ma, H., "Investigating Mechanical Properties and Self-Healing Behavior of Micro-Cracked ECC With Different Volume of Fly Ash," *Construction and Building Materials*, V. 52, 2014, pp. 17-23. doi: 10.1016/j.conbuildmat.2013.11.001

54. Yu, J., and Leung, C. K. Y., "Strength Improvement of Strain-Hardening Cementitious Composites with Ultrahigh-Volume Fly Ash," *Journal of Materials in Civil Engineering*, ASCE, V. 29, No. 9, 2017, p. 05017003. doi: 10.1061/(ASCE)MT.1943-5533.0001987

55. Şahmaran, M., and Li, V. C., "De-icing Salt Scaling Resistance of Mechanically Loaded Engineered Cementitious Composites," *Cement and Concrete Research*, V. 37, No. 7, 2007, pp. 1035-1046. doi: 10.1016/j.cemconres.2007.04.001

56. Şahmaran, M.; Li, M.; and Li, V. C., "Transport Properties of Engineered Cementitious Composites under Chloride Exposure," *ACI Materials Journal*, V. 104, No. 6, Nov.-Dec. 2007, pp. 604-611.

57. Lin, C.; Kayali, O.; Morozov, E. V.; and Sharp, D. J., "Development of Self-Compacting Strain-Hardening Cementitious Composites by Varying Fly Ash Content," *Construction and Building Materials*, V. 149, 2017, pp. 103-110. doi: 10.1016/j.conbuildmat.2017.05.051

58. Turk, K., and Nehdi, M. L., "Coupled Effects of Limestone Powder and High-Volume Fly Ash on Mechanical Properties of ECC," *Construction and Building Materials*, V. 164, 2018, pp. 185-192. doi: 10.1016/j.conbuildmat.2017.12.186

59. Liu, H.; Zhang, Q.; Gu, C.; Su, H.; and Li, V. C., "Influence of Micro-Cracking on the Permeability of Engineered Cementitious Composites," *Cement and Concrete Composites*, V. 72, 2016, pp. 104-113. doi: 10.1016/j.cemconcomp.2016.05.016

60. Fan, S., and Li, M., "X-ray Computed Microtomography of Three-Dimensional Microcracks and Self-Healing in Engineered Cementitious Composites," *Smart Materials and Structures*, V. 24, No. 1, 2015, p. 015021. doi: 10.1088/0964-1726/24/1/015021

61. Sahmaran, M.; Yildirim, G.; and Erdem, T. K., "Self-Healing Capability of Cementitious Composites Incorporating Different Supplementary Cementitious Materials," *Cement and Concrete Composites*, V. 35, No. 1, 2013, pp. 89-101. doi: 10.1016/j.cemconcomp.2012.08.013

62. Kan, L.-L.; Shi, H.-S.; Sakulich, A. R.; and Li, V. C., "Self-Healing Characterization of Engineered Cementitious Composite Materials," *ACI Materials Journal*, V. 107, No. 6, 2010, pp. 617-624.

63. Yang, Y.; Lepech, M. D.; Yang, E.-H.; and Li, V. C., "Autogenous Healing of Engineered Cementitious Composites Under Wet–Dry Cycles," *Cement and Concrete Research*, V. 39, No. 5, 2009, pp. 382-390. doi: 10.1016/j.cemconres.2009.01.013

64. Yıldırım, G.; Keskin, Ö. K.; Keskin, S. B.; Şahmaran, M.; and Lachemi, M., "A Review of Intrinsic Self-Healing Capability of Engineered Cementitious Composites: Recovery of Transport and Mechanical Properties," *Construction and Building Materials*, V. 101, 2015, pp. 10-21. doi: 10.1016/j.conbuildmat.2015.10.018

65. Şahmaran, M., and Li, V. C., "Influence of Microcracking on Water Absorption and Sorptivity of ECC," *Materials and Structures*, V. 42, No. 5, 2009, pp. 593-603. doi: 10.1617/s11527-008-9406-6

66. Li, M., and Li, V. C., "Cracking and Healing of Engineered Cementitious Composites under Chloride Environment," *ACI Materials Journal*, V. 108, No. 3, May-June 2011, pp. 333-340.

67. Şahmaran, M.; Özbay, E.; Yücel, H. E.; Lachemi, M.; and Li, V. C., "Frost Resistance and Microstructure of Engineered Cementitious Composites: Influence of Fly Ash and Micro Poly-Vinyl-Alcohol Fiber," *Cement and Concrete Composites*, V. 34, No. 2, 2012, pp. 156-165. doi: 10.1016/j.cemconcomp.2011.10.002

68. Li, V. C.; Horikoshi, T.; Ogawa, A.; Torigos, S.; and Saito, T., "Micromechanics-Based Durability Study of Polyvinyl Alcohol-Engineered Cementitious Composite," *ACI Materials Journal*, V. 101, No. 3, May-June 2004, pp. 242-248.

69. Şahmaran, M.; Özbay, E.; Yücel, H. E.; Lachemi, M.; and Li, V. C., "Effect of Fly Ash and PVA Fiber on Microstructural Damage and Residual Properties of Engineered Cementitious Composites Exposed to High Temperatures," *Journal of Materials in Civil Engineering*, ASCE, V. 23, No. 12, 2011, pp. 1735-1745. doi: 10.1061/(ASCE)MT.1943-5533.0000335

70. Gao, S., and Sun, Z., "Experimental Study and Theoretical Analysis of ECC Type I Fatigue Fracture After Subjected to Sub-High Temperature," *Theoretical and Applied Fracture Mechanics*, V. 131, 2024, p. 104391. doi: 10.1016/j.tafmec.2024.104391

71. Gao, S.; Zhao, X.; Qiao, J.; Guo, Y.; and Hu, G., "Study on the Bonding Properties of Engineered Cementitious Composites (ECC) and Existing Concrete Exposed to High Temperature," *Construction and Building Materials*, V. 196, 2019, pp. 330-344. doi: 10.1016/j.conbuildmat.2018.11.136

72. Wang, Q.; Zhou, Y.; Lai, M.; Gu, M.; and Ho, J. C. M., "Carbon Fiber to Improve the Resistance of High Strength PVA-ECC to Elevated Temperatures," *Journal of Building Engineering*, V. 71, 2023, p. 106475. doi: 10.1016/j.jobe.2023.106475

73. Ouyang, J.; Guo, R.; Wang, X.-Y.; Fu, C.; Wan, F.; and Pan, T., "Effects of Interface Agent and Cooling Methods on the Interfacial Bonding Performance of Engineered Cementitious Composites (ECC) and Existing

Concrete Exposed to High Temperature," *Construction and Building Materials*, V. 376, 2023, p. 131054. doi: 10.1016/j.conbuildmat.2023.131054

74. Wu, H.; Zhang, D.; Ellis, B. R.; and Li, V. C., "Mechanical Behavior of Carbonated Mgo-Based Engineered Cementitious Composite (ECC) After High Temperatures Exposure," *Cement and Concrete Composites*, V. 124, 2021, p. 104255. doi: 10.1016/j.cemconcomp.2021.104255

75. Bhat, P. S.; Chang, V.; and Li, M., "Effect of Elevated Temperature on Strain-Hardening Engineered Cementitious Composites," *Construction and Building Materials*, V. 69, 2014, pp. 370-380. doi: 10.1016/j.conbuildmat.2014.07.052

76. Liu, J.-C.; Tan, K. H.; and Fan, S., "Residual Mechanical Properties and Spalling Resistance of Strain-Hardening Cementitious Composite With Class C Fly Ash," *Construction and Building Materials*, V. 181, 2018, pp. 253-265. doi: 10.1016/j.conbuildmat.2018.06.009

77. Du, S.; Ge, Y.; and Shi, X., "A Targeted Approach of Employing Nano-Materials in High-Volume Fly Ash Concrete," *Cement and Concrete Composites*, V. 104, 2019, p. 103390. doi: 10.1016/j.cemconcomp.2019.103390

78. Li, Y.; Wang, R.; Li, S.; Zhao, Y.; and Qin, Y., "Resistance of Recycled Aggregate Concrete Containing Low- and High-Volume Fly Ash Against the Combined Action of Freeze–Thaw Cycles and Sulfate Attack," *Construction and Building Materials*, V. 166, 2018, pp. 23-34. doi: 10.1016/j.conbuildmat.2018.01.084

79. Pang, B.; Zhou, Z.; Cheng, X.; Du, P.; and Xu, H., "ITZ Properties of Concrete with Carbonated Steel Slag Aggregate in Salty Freeze-Thaw Environment," *Construction and Building Materials*, V. 114, 2016, pp. 162-171. doi: 10.1016/j.conbuildmat.2016.03.168

80. Liu, Y.; Zhou, X.; Lv, C.; Yang, Y.; and Liu, T., "Use of Silica Fume and GGBS to Improve Frost Resistance of ECC with High-Volume Fly Ash," *Advances in Civil Engineering*, V. 2018, No. 1, 2018, pp. 1-11. doi: 10.1155/2018/7987589

81. Zhu, Y.; Yang, Y.; and Yao, Y., "Autogenous Self-Healing of Engineered Cementitious Composites Under Freeze–Thaw Cycles," *Construction and Building Materials*, V. 34, 2012, pp. 522-530. doi: 10.1016/j.conbuildmat.2012.03.001

82. Zhu, H.; Wang, T.; Wang, Y.; Hu, W.-H.; and Li, V. C., "Feasibility of Structural Retrofit Concrete Pipelines Using Limestone Calcined Clay Cement Engineered Cementitious Composites (LC3 ECC)," *Engineering Structures*, V. 289, 2023, p. 116305. doi: 10.1016/j.engstruct.2023.116305

83. Zhu, H.; Hu, W.-H.; Mehthel, M.; Villette, T.; Vidal, O. S.; Nasser, W. N.; and Li, V. C., "Engineered Cementitious Composites (ECC) with a High Volume of Volcanic Ash: Rheological, Mechanical, and Micro Performance," *Cement and Concrete Composites*, V. 139, 2023, p. 105051. doi: 10.1016/j.cemconcomp.2023.105051

84. Lepech, M. D., and Li, V. C., "Water Permeability of Engineered Cementitious Composites," *Cement and Concrete Composites*, V. 31, No. 10, 2009, pp. 744-753. doi: 10.1016/j.cemconcomp.2009.07.002

85. Liu, H.; Zhang, Q.; Gu, C.; Su, H.; and Li, V., "Self-Healing of Microcracks in Engineered Cementitious Composites Under Sulfate and Chloride Environment," *Construction and Building Materials*, V. 153, 2017, pp. 948-956. doi: 10.1016/j.conbuildmat.2017.07.126

86. Gao, S.; Jin, J.; Hu, G.; and Qi, L., "Experimental Investigation of the Interface Bond Properties Between SHCC and Concrete Under Sulfate Attack," *Construction and Building Materials*, V. 217, 2019, pp. 651-663. doi: 10.1016/j.conbuildmat.2019.05.121

87. Wang, T.; Zhang, D.; Zhu, H.; Ma, B.; and Li, V. C., "Durability and Self-Healing of Engineered Cementitious Composites Exposed to Simulated Sewage Environments," *Cement and Concrete Composites*, V. 129, 2022, p. 104500. doi: 10.1016/j.cemconcomp.2022.104500

88. Du, S.; Zhao, H.; Ge, Y.; Yang, Z.; and Shi, X., "Laboratory Investigation into the Modification of Transport Properties of High-Volume Fly Ash Mortar by Chemical Admixtures," *Journal of Materials in Civil Engineering*, ASCE, V. 29, No. 10, 2017, p. 04017184. doi: 10.1061/(ASCE)MT.1943-5533.0002025

89. Moffatt, E. G.; Thomas, M. D. A.; and Fahim, A., "Performance of High-Volume Fly Ash Concrete in Marine Environment," *Cement and Concrete Research*, V. 102, 2017, pp. 127-135. doi: 10.1016/j.cemconres.2017.09.008

90. Shaikh, F. U. A., and Supit, S. W. M., "Mechanical and Durability Properties of High Volume Fly Ash (HVFA) Concrete Containing Calcium Carbonate (CaCO3) Nanoparticles," *Construction and Building Materials*, V. 70, 2014, pp. 309-321. doi: 10.1016/j.conbuildmat.2014.07.099

91. Gesoğlu, M.; Güneyisi, E.; and Özbay, E., "Properties of Self-Compacting Concretes Made with Binary, Ternary, and Quaternary Cementitious Blends of Fly Ash, Blast Furnace Slag, and Silica Fume," *Construction and Building Materials*, V. 23, No. 5, 2009, pp. 1847-1854. doi: 10.1016/j.conbuildmat.2008.09.015

92. Filho, J. H.; Medeiros, M. H. F.; Pereira, E.; Helene, P.; and Isaia, G. C., "High-Volume Fly Ash Concrete with and without Hydrated Lime: Chloride Diffusion Coefficient from Accelerated Test," *Journal of Materials in Civil Engineering*, ASCE, V. 25, No. 3, 2013, pp. 411-418. doi: 10.1061/(ASCE)MT.1943-5533.0000596

93. Sun, R.; Hu, X.; Ling, Y.; Zuo, Z.; Zhuang, P.; and Wang, F., "Chloride Diffusion Behavior of Engineered Cementitious Composite Under Dry-Wet Cycles," *Construction and Building Materials*, V. 260, 2020, p. 119943. doi: 10.1016/j.conbuildmat.2020.119943

94. Su, P.; Dai, Q.; and Kane, E. S., "Predicting Chloride Ingression in Concrete Containing Different Scms Based on Chloride Binding and Electrical Resistivity," *Construction and Building Materials*, V. 414, 2024, p. 134928. doi: 10.1016/j.conbuildmat.2024.134928

95. Franco-Luján, V. A.; Mendoza-Rangel, J. M.; Jiménez-Quero, V. G.; and Montes-García, P., "Chloride-Binding Capacity of Ternary Concretes Containing Fly Ash and Untreated Sugarcane Bagasse Ash," *Cement and Concrete Composites*, V. 120, 2021, p. 104040. doi: 10.1016/j.cemconcomp.2021.104040

96. Dakhane, A.; Tweedley, S.; Kailas, S.; Marzke, R.; and Neithalath, N., "Mechanical and Microstructural Characterization of Alkali Sulfate Activated High Volume Fly Ash Binders," *Materials and Design*, V. 122, 2017, pp. 236-246. doi: 10.1016/j.matdes.2017.03.021

97. Liu, H.; Zhang, Q.; Li, V.; Su, H.; and Gu, C., "Durability Study on Engineered Cementitious Composites (ECC) Under Sulfate and Chloride Environment," *Construction and Building Materials*, V. 133, 2017, pp. 171-181. doi: 10.1016/j.conbuildmat.2016.12.074

98. Quan, X.; Wang, S.; Liu, K.; Zhao, N.; Xu, J.; Xu, F.; and Zhou, J., "The Corrosion Resistance of Engineered Cementitious Composite (ECC) Containing High-Volume Fly Ash and Low-Volume Bentonite Against the Combined Action of Sulfate Attack and Dry-Wet Cycles," *Construction and Building Materials*, V. 303, 2021, p. 124599. doi: 10.1016/j.conbuildmat.2021.124599

99. Wu, H.-L.; Zhang, D.; Du, Y.-J.; and Li, V. C., "Durability of Engineered Cementitious Composite Exposed to Acid Mine Drainage," *Cement and Concrete Composites*, V. 108, 2020, p. 103550. doi: 10.1016/j.cemconcomp.2020.103550

ACI MATERIALS JOURNAL TECHNICAL PAPER

Title No. 122-M24

Role of Intercrystallite Phosphorus on Properties of α-Hemihydrate Gypsum

by Dongmei Liu, Xinyu Li, Wanqing Zhou, Gang Xu, and Yi Qin

Phosphogypsum (PG) is often used to produce α-hemihydrate gypsum (α-HH), but the impurities in PG, including intercrystalline phosphorus (IP), limit its reuse. The objective of this paper is to study the effect of IP on the morphology, hydration, and hardening properties of α-HH, using X-ray diffraction (XRD); X-ray photoelectron spectroscopy (XPS); scanning electron microscopy (SEM); Fourier-transform infrared spectroscopy (FTIR); and testing of setting time, hydration, heat, and strength. The results revealed that IP dissolved out from dihydrate gypsum (DH) and entered the lattice of α-HH during the preparation of α-HH, while there was little difference in the morphology of α-HH. When α-HH hydrated, IP dissolved and converted into $Ca_3(PO_4)_2$ absorbed on the surface of DH. 0.04% IP had no effect on the hydration, setting time, and strength of α-HH, with 0.1% or more IP significantly prolonging the hydration of α-HH and deteriorating microstructure of hardened paste, thus reducing strength. Based on the results, IP content in PG should be controlled to less than 0.04%.

Keywords: α-hemihydrate gypsum; hydration; intercrystalline phosphorus; microstructure; morphology; setting time; strength.

INTRODUCTION

As an industrial by-product produced in the wet phosphoric acid process,[1-3] phosphogypsum (PG) is mainly composed of $CaSO_4 \cdot 2H_2O$ (abbreviated as DH). In addition, it contains various harmful impurities such as soluble phosphorus and fluorine compounds, insoluble phosphorus and fluorine compounds, and intercrystalline phosphorus (IP) compound.[4,5] With the rapid development of the phosphate fertilizer industry in China, the average annual yield of PG has exceeded 75 million tons, and the accumulated stockpiling has reached more than 600 million tons.[6,7] However, the current use rate of PG is only 40% according to China Phosphate and Compound Fertilizer Industry Association, and massive amounts of PG have piled up in stacking fields, which led to the occupation of land and enormous environmental pressure.[8,9]

α-hemihydrate gypsum (α-HH) is known as a high-strength gypsum, has good working environmental and biological performances, and has been widely used in precision casting, high-end building materials, arts and crafts, medical, and other fields.[10] Because the DH content in PG is very high, PG can be used as raw material to produce α-HH by an autoclaved method, and the strength is mostly between 30 and 40 MPa.[11-13] This use is an effective way to realize high value-added application and sustainable development of PG, but the impurities, especially the phosphorus, deteriorate the properties of gypsum plaster and restrict the use of PG in the plaster industry.[4,14-18] Until now, the effects and mechanism of soluble phosphorus—including H_3PO_4, H_2PO^{4-}, and HPO_4^{2-}—on the hydration, properties, and pore structure of α-HH have been clarified. However, the research about the effect of IP on properties of α-HH was relatively weak. Liu et al.[19] studied the state and evolution of phosphorus included in calcium sulfate, which was sampled in a hemihydrate-dihydrate phosphoric acid plant. The results showed that the content of IP wrapped into hemihydrate gypsum is significantly reduced when the hemihydrate gypsum dissolved and recrystallized into dihydrate gypsum. Peng et al.,[20] Li et al.,[21] and Song et al.[22] separately prepared the dihydrate gypsum samples containing different contents of IP; then the samples were calcined to β-hemihydrate gypsum (β-HH). The results indicated that the IP in the lattice of dihydrate gypsum did not change in the process of calcination but was retained in the lattice of β-HH. When β-HH hydrated, the IP released from the lattice and led to the retardation of setting time and decrease in strength. Note that α-HH is prepared by dihydrate gypsum in the presence of water or saturated steam, while β-HH is prepared by roasting dihydrate gypsum. There is a big difference between α-HH and β-HH in the specific surface area, crystal size, imperfection, and surface topography.[23-25] Therefore, the effect and mechanism of IP on the composition, morphology, hydration, and strength of α-HH is different from that of β-HH.

Recently, there have been many studies on removing harmful impurities such as phosphorus and fluorine from PG. The results indicated that water-soluble phosphorus and fluorine in PG can be removed by lime water washing or neutralization, but the insoluble phosphorus including IP only is decreased by acid washing, such as sulfuric acid, citric acid, and muriatic acid.[26-29] In fact, the PG system is complex and changeable; the pretreatment methods need to be adjusted appropriately for the different PG systems. Clarifying the influence and mechanism of IP on the properties of α-HH is necessary for selecting the pretreatment method of PG when it is used as raw material to produce α-HH by the autoclaving method.

This paper first studied the effect of IP on the composition and morphology of α-HH. Then, the experimental results of setting time, the rise of hydration temperatures, and anion

---

ACI Materials Journal, V. 122, No. 4, July 2025.

MS No. M-2024-152.R3, doi: 10.14359/51746806, received January 3, 2025, and reviewed under Institute publication policies. Pertinent discussion including author's closure, if any, will be published ten months from this journal's date if the discussion is received within four months of the paper's print publication.

Table 1—Chemical composition of NG (%, in mass)

SO_3	CaO	SiO_2	Fe_2O_3	K_2O	SrO	BaO	TiO_2	Ag_2O	CuO
55.14	34.51	8.60	0.57	0.52	0.35	0.17	0.12	0.01	0.01

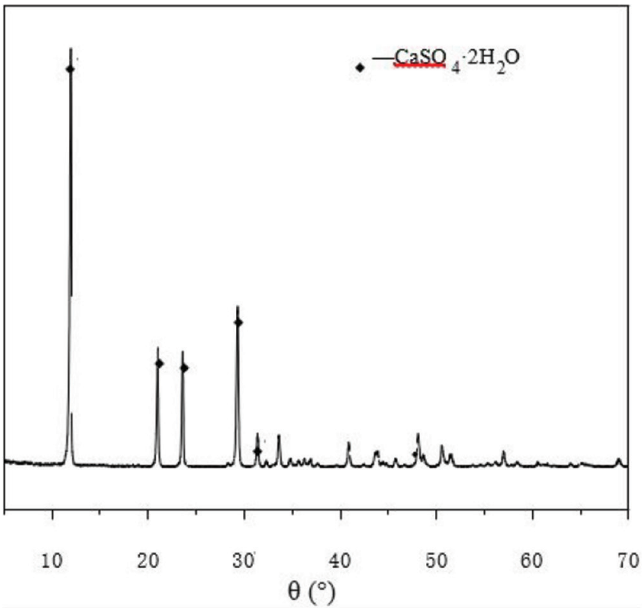

Fig. 1—XRD spectrum of NG.

concentration in the liquid phase of α-HH were tested. On these bases, the effect of IP on the hydration properties of α-HH was discussed. In addition, the effect of IP on strength and microstructure of α-HH-hardened pastes was investigated. Based on the results and analysis, the influencing mechanism of IP on the properties of α-HH was revealed and the control range of IP in PG used to produce α-HH was given.

RESEARCH SIGNIFICANCE

This paper prepared α-HH with the autoclaving method; studied the effect of IP on the composition, morphology, hydration, and hardened properties of α-HH; and revealed the influence mechanism through the study of a simplified system. The results provide the necessary theoretical and practical basis for selecting the appropriate pretreatment method of PG and promoting the efficient application of PG in α-HH.

EXPERIMENTAL INVESTIGATION

Raw materials

Natural gypsum (NG) is a creamy yellow lump. NG was ground for 20 minutes in a ball mill, dried at 110 ± 5°C for 24 hours, and finally screened by a 0.125 mm square-hole sieve for later use. The main chemical composition, X-ray diffraction (XRD), and microscopic morphology of NG are shown in Table 1 and Fig. 1 and 2. The main component of NG was DH; the NG consisted of lumpy crystals and fine grains.

All chemical reagents used in the test were analytical reagents. Succinic acid, phosphoric acid (H_3PO_4), DH, and calcium phosphate dihydrate ($CaHPO_4 \cdot 2H_2O$) were used.

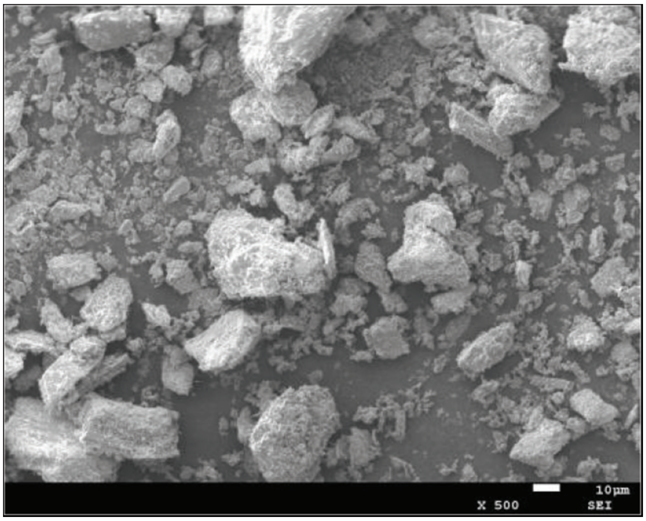

Fig. 2—SEM picture of NG.

Sample preparation and mixture proportions

The IP sample was prepared by referring to the existing references.[21] First, 10 mL of H_3PO_4 was diluted 10 times and heated to 80°C. Then, 4 g of $CaHPO_4 \cdot 2H_2O$ and 2 g of DH powder were added successively and stirred until dissolved well. Subsequently, 11 g of $Ca(OH)_2$ were quickly added to make a neutral solution, which was placed until $CaHPO_4 \cdot 2H_2O$ and DH were co-crystallized. Finally, the DH containing 8% IP ($Ca(SO_4,HPO_4) \cdot 2H_2O$) was obtained by filtrating the solution, then washed by deionized water twice and dried at 60°C for 24 hours.

The IP sample was added into NG and mixed well, making the NG contain different contents of IP, which were 0, 0.04%, 0.1%, 0.4%, and 0.6% by weight, respectively. Then, the NG was used to produce α-HH by the autoclaving method at the mass ratio of water to NG of 0.3. The slurry, which was made by stirring the NG and deionized water having 0.06% succinic acid by weight, was autoclaved at 144°C for 6 hours to produce α-HH. After autoclaving, α-HH was dried at 110 ± 5°C for 24 hours and then ground for 15 minutes to pass 0.125 mm square hole sieve for later use.

Test methods

The phase composition of α-HH was tested by XRD with Cu Kα radiation at a scanning rate of 10 deg/min and 2θ range of 5 to 90 degrees. The X-ray photoelectron spectroscopy (XPS) was used to test the interaction between IP and the α-HH surfaces. Besides, α-HH was analyzed by scanning electron microscopy (SEM) for the observation of the morphology.

A normal consistency of α-HH was obtained according to the Chinese standard JC/T 2038-2010,[30] where a gypsum standard consistency tester was used. Setting time of α-HH was obtained according to the Chinese standard GB/T 17669.4-1999,[31] where Vicat needle penetration tests were used.

A temperature recorder was used to monitor the hydration temperature rise of α-HH paste. Before testing, α-HH and deionized water were equilibrated separately for 24 hours at 20°C. In the case of standard consistency, 200 g of α-HH and deionized water were poured into a plastic bottle and stirred manually for 30 seconds to ensure homogeneity. Afterwards, the bottle was sealed and placed into the vacuum cup, which was covered after inserting the thermocouple. The temperature data was automatically recorded every 10 seconds.

To make clear the migration of IP in phosphorus gypsum, Fourier-transform infrared spectroscopy (FTIR), with wavenumber ranging from 600 to 4000 cm^{-1}, was used to test the IP in different samples, including NG with 0.6% IP, corresponding autoclaved product (α-HH), and corresponding hydration product (DH).

The anion concentration evolution in the liquid phase during the hydration of α-HH was measured by an ion chromatograph. The mass ratio of deionized water to α-HH in the test was 5:1. The α-HH was added under stirring to deionized water in a 250 mL conical flask at 25°C. At specific time intervals, the measured suspensions were withdrawn and immediately centrifuged at 5000 rpm for 15 seconds. The supernatant solution was collected by pressing through a polytetrafluoroethylene (PTFE) syringe filter (pore diameter <0.22 μm), quickly diluted by 250 times with distilled water, then injected into the ion chromatograph. Thereafter, the phosphate and sulfate ion concentrations in the diluent were tested.

Strength and microstructure of α-HH were tested as follows: in the case of standard consistency, the α-HH was blended with tap water in a mixer at a high speed for 30 seconds. The fresh plasters were cast into molds sized 40 x 40 x 160 mm with vibration for 15 seconds and cured at 23 ± 2°C and 50 ± 5% relative humidity, then demolded after final setting. One group of these specimens were tested for 2 hours for flexural strength; the other group of specimens were continually cured for 24 hours at 20 ± 2°C and 90 ± 5% relative humidity, then dried in an oven to a constant mass at 40 ± 1°C for testing the dry compressive strength.[31] After testing the dry strength, the samples were fractured and collected for the microstructure of α-HH by SEM.

RESULTS AND DISCUSSION

Characterization of α-HH in absence or presence of IP

It is known that calcium sulfate hemihydrate exists in three forms: monoclinic, hexagonal, and orthorhombic.[32,33] Figure 3 shows the XRD spectra of α-HH in absence or presence of IP. In Fig. 3, the XRD spectra of all samples presented similar patterns with similar peaks, which also existed in the monoclinic and hexagonal pattern of hemihydrates (as shown in PDF#83-0438 and PDF#14-0453). In the presence of IP, the intensity of dominant peaks of α-HH obviously increased, but the diffraction angles corresponding to different dominant peaks changed slightly and the characteristic diffraction peaks of other substances did not appear. Thus, the authors concluded that all NG had changed into hemihydrates, which had the monoclinic and hexagonal structure. Due to the small amount of IP, the characteristic peaks of phosphate crystal were not observed.

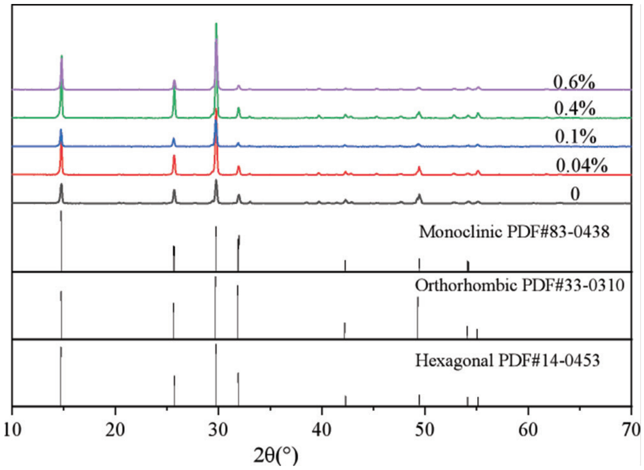

Fig. 3—XRD spectra of α-HH in absence or presence of IP.

Figure 4(a) shows the full XPS spectra of α-HH in absence or presence of IP. For the blank sample, the full spectra only exhibited the spectrums of Ca, S, C, and O elements. When 0.6% IP was added, the characteristic spectrum of P element could be observed. The C 1 second peak in the spectra at 284.8 eV was due to the contamination of the samples.[34] Figures 4(b) and (c) indicate that the binding energies of Ca 2p and S 2p for α-HH in presence of 0.6% IP were lower than those of the blank α-HH, and the decreased binding energies demonstrated that there existed a new electronic reaction between P element and the α-HH surface. Ca and S on the surface of α-HH captured some electrons from the P species on the α-HH surface. The peak of P 2p at 133.5 eV in Fig. 4(d) confirmed the presence of phosphate on the crystal surface. Based on the values published by Franke et al.,[35] it is possible that a $Ca_3(PO_4)_2$ compound, which shows a binding energy of 133.1 for the P 2p level, formed on the crystal surface. In the research of Feng et al.,[36] the peak of P 2p 3/2 and P 2p 1/2 for the α-HH, which contained 2.5% IP and was formed by the reaction of concentrated H_2SO_4 and $Ca(H_2PO_4)_2$ solution at 80°C, respectively corresponded to $CaHPO_4{\cdot}2H_2O$ and $H_3PO_4{\cdot}0.5H_2O$. The authors thought the absence of the peak corresponding to $CaHPO_4{\cdot}2H_2O$ in this paper was due to the small content of 0.6% IP and a different preparation method. They believe that as IP in DH dissovled during the preparation of α-HH, part of it reacted with Ca element to form $Ca_3(PO_4)_2$, and part entered the lattice of α-HH.

Figure 5 shows the SEM pictures of α-HH in absence or presence of IP. Whether adding the IP or not, the well-crystallized α-HH crystals presented monoclinic and hexagonal columnar structures, which were consistent with the XRD analysis. In the blank sample, more crystals developed well and showed short columnar shape, and some crystals were big and irregular polyhedrons. With an increasing IP content from 0.04 to 0.4%, the irregular polyhedrons and fine grains increased slightly, and the length-width ratio of well-crystallized α-HH crystals also presented little difference. While the content of IP reached 0.6%, the content of irregular polyhedrons and fine grains and the length-width

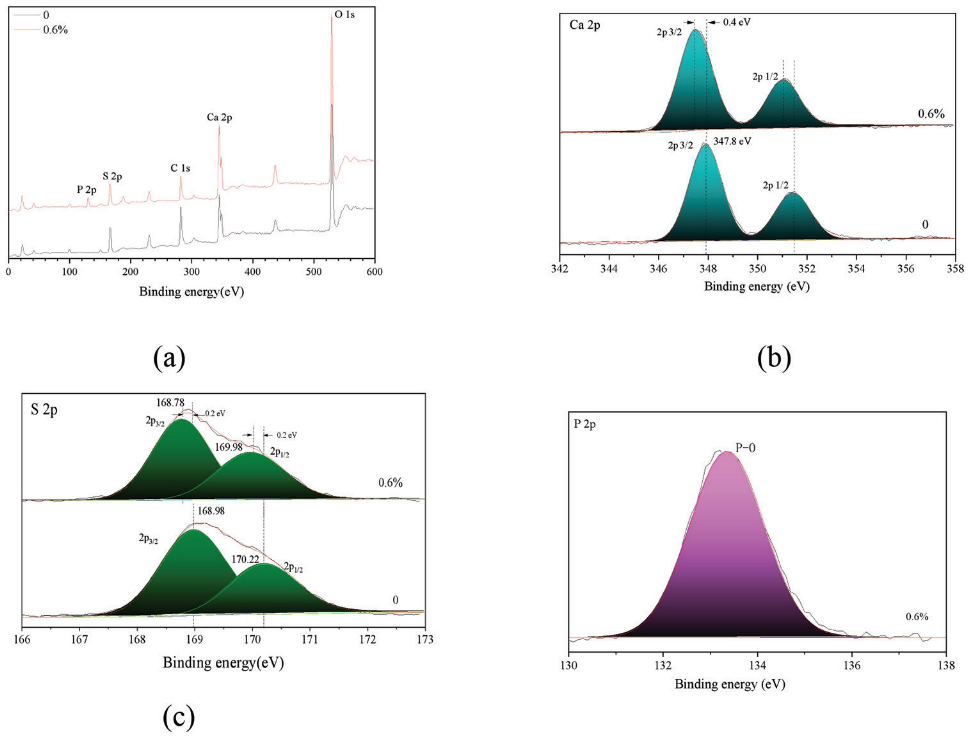

(a)

(b)

(c)

(d)

Fig. 4—XPS spectra of α-HH in absence or presence of IP: (a) full spectra; (b) P 2p spectrum; (c) Ca 2p spectra; and (d) S 2p spectra.

ratio obviously increased. The phosphate formed on the surface of α-HH crystals should be responsible for its morphology change. In the case of 0.04 to 0.4% IP, there was less phosphate and it had less effect on the crystal morphology. However, on addition of 0.6% IP, more phosphates were produced and effectively blocked access of the SO_4^{2-} growth units to the crystal surface and hence, crystal morphology deteriorated.

Effect of IP on setting time of α-HH paste

The setting times of α-HH paste were indicated in Fig. 6. When the content of IP is 0.04%, the initial and final setting time seemed the same to the blank group. However, when the addition of IP was ≥ 0.1%, the initial and final setting times of α-HH were retarded significantly, and the retarding effect increased as IP increased. In the case of 0.6% IP, the initial and final setting times were 168 and 226 minutes longer than those of the blank group, respectively. The effect of IP on the setting time of α-HH paste was same as the IP in β-HH.[20,21] The setting time of α-HH paste was closely related to the amount of hydration product, and the increase of the setting time was mainly due to the decrease of DH crystals.

Effect of IP on hydration temperature rise of α-HH

The temperature changes during the hydration of α-HH appear to be an effective method for characterizing the kinetic stages of α-HH hydration. Figure 7 shows the hydration temperatures evolution of α-HH. It was well known that the hydration mechanism of α-HH to DH is first the dissolution of α-HH followed by the precipitation of DH, including nucleation and following growth of DH. According to the dissolution-nucleation-growth mechanism, the hydration process of α-HH plaster could be divided into four stages: an initial dissolution stage (I), an induction stage (II), an acceleration stage (III), and a stable stage (IV).[37,38] The main reactions at each stage are presented in Fig. 7(a).

The IP had no obvious influence on stage I, and stage I for all samples was short. When the content of IP was within range of 0 to 0.1%, the induction stage (II) was not observed, but obviously prolonged in the case of 0.4 or 0.6% IP. The addition of 0.04% IP did not affect the acceleration stages. When the content of IP was ≥0.1%, as the IP content increased, the acceleration stage was markedly prolonged and the growth rate of DH markedly reduced; meanwhile, the time for maximum rise in temperature was greatly delayed. It was suggested that in the presence of IP, the normal growth kinetics of α-HH changed, and the degree of change was related to the content of eutectic. In addition, the α-HH pastes arrived at the initial setting soon after the start of the acceleration stage, and the final setting reached just before the appearance of the highest temperature. Therefore, these findings well agreed with the results about the setting time of α-HH pastes.

Migration of IP during preparation and hydration of α-HH

Ölmez and Yilmaz[39] confirmed that the infrared absorption peak around 835 cm^{-1} corresponded to the vibration of IP. The paper tested IP in the different samples by FTIR, including NG with 0.6% IP, the corresponding autoclaved product (α-HH), and the hydration product (DH). The FTIR spectra of different samples is shown in Fig. 8. The results

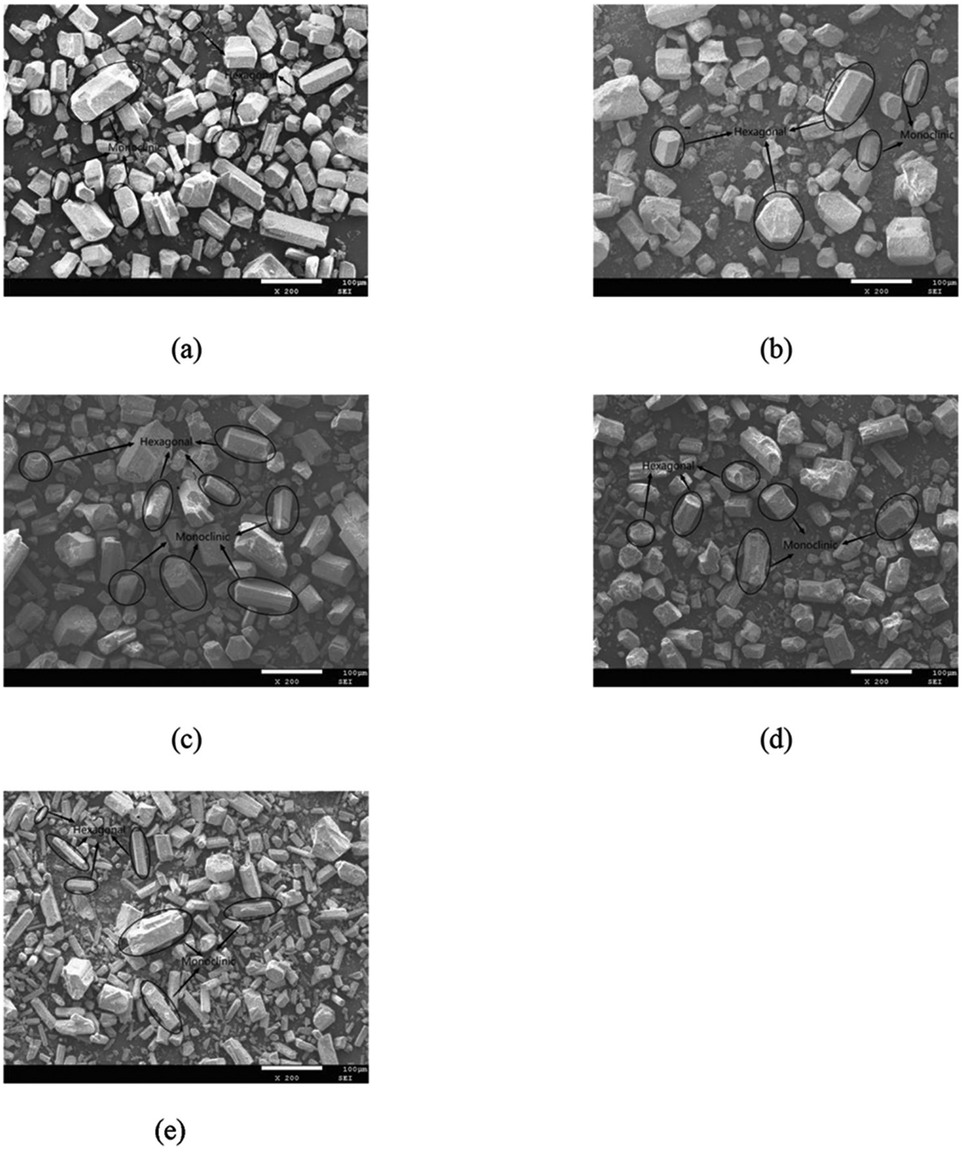

(a)

(b)

(c)

(d)

(e)

Fig. 5—SEM pictures of α-HH in absence or presence of IP: (a) 0; (b) 0.04%; (c) 0.1%; (d) 0.4%; and (e) 0.6%.

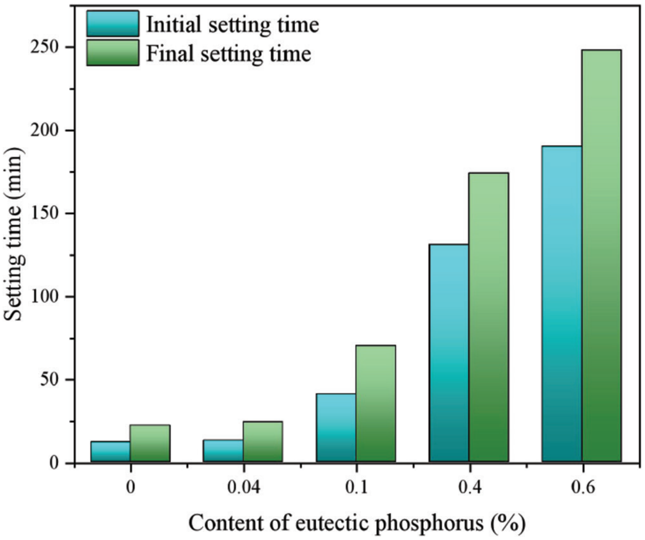

Fig. 6—Setting time of α-HH plasters in absence or presence of IP.

indicated that there existed a distinct infrared absorption peak at 838 cm^{-1} for NG with 0.6% IP, but the peak for α-HH obviously decreased. After the hydration of α-HH, the peak at 838 cm^{-1} for the hydration product disappeared. The research of Liu et al.[19] verified the dissolution of IP from hemihydrate gypsum when the hemihydrate gypsum hydrated to form DH. The IP in the lattice of $CaSO_4 \cdot 2H_2O$ dissolved out during preparation of α-HH and converted into the soluble HPO_4^{2-}. Part of the HPO_4^{2-} ionized into the H^+ and PO_4^{3-}, and then the PO_4^{3-} reacted with Ca^{2+} to form insoluble $Ca_3(PO_4)_2$ absorbed on the surface of α-HH. Part of the HPO_4^{2-} entered the lattice of $CaSO_4 \cdot 1/2H_2O$ to form $Ca(SO_4,HPO_4) \cdot 1/2H_2O$ solid solution, but the mechanism was not clear. The possible reason is that both HPO_4^{2-} and SO_4^{2-} are tetrahedral and carry two negative charges, so part of HPO_4^{2-} can substitute SO_4^{2-} in the structure of $CaSO_4 \cdot 1/2H_2O$ to form $Ca(SO_4,HPO_4) \cdot 1/2H_2O$ solid solution.[40,41] The XPS results in Fig. 4 confirmed the existence of $Ca_3(PO_4)_2$ on the surface of α-HH crystals and the IP in the lattice of α-HH. When α-HH hydrated, the IP in the lattice of α-HH all dissolved out.

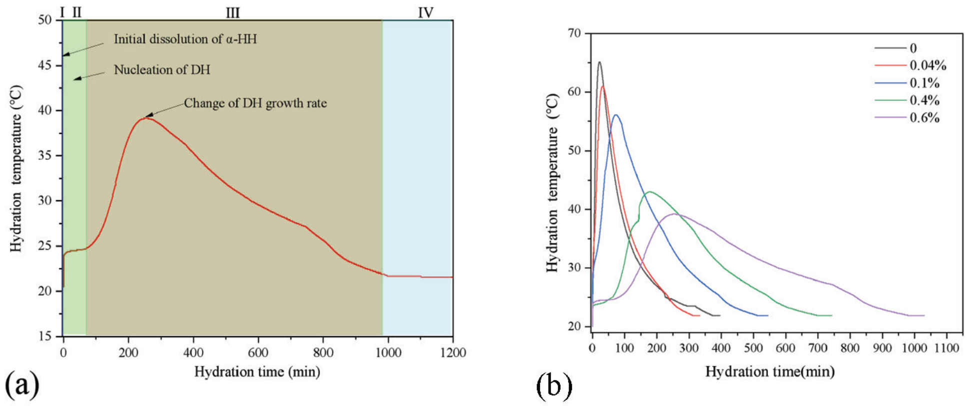

Fig. 7—Hydration temperature evolution of α-HH in absence or presence of IP: (a) stages in hydration temperature evolution curve; and (b) hydration temperature evolution curves.

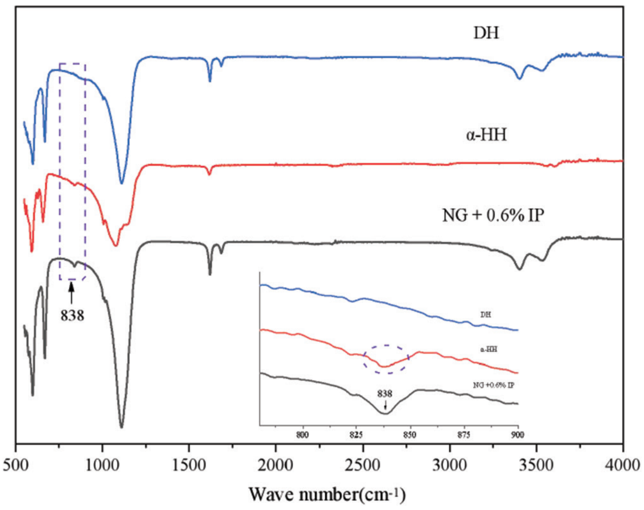

Fig. 8—FTIR spectra of NG, α-HH, and DH in presence of 0.6% IP.

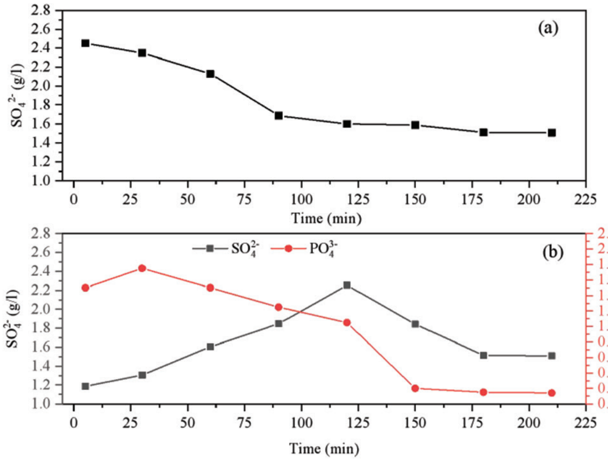

Fig. 9—Evolution of anion concentration during hydration of α-HH in absence or presence IP: (a) 0; and (b) 0.6%.

The migration of IP from the lattice of α-HH is a dynamic process; therefore, the evolution of SO_4^{2-} and PO_4^{3-} ion concentration was tested during the hydration of α-HH in presence of 0.6% IP, and the results are indicated in Fig. 9.

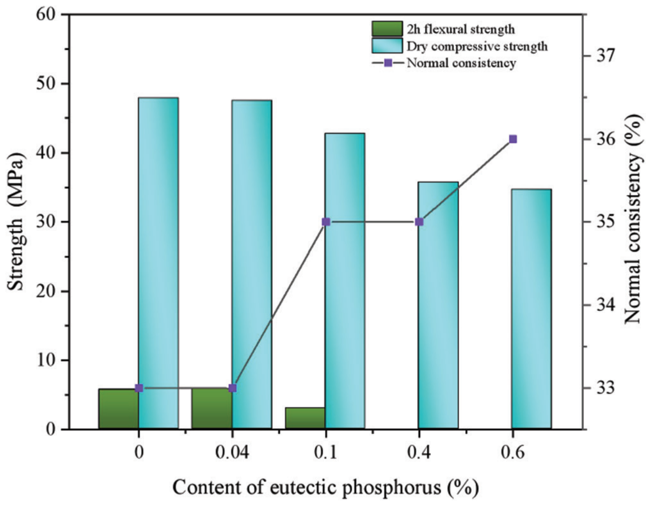

Fig. 10—Strength and normal consistency of α-HH in absence or presence of IP.

When α-HH without IP was mixed with water, the SO_4^{2-} concentration immediately increased to the maximum and then decreased gradually to a constant value. For α-HH in the presence of 0.6% IP, the SO_4^{2-} concentration at 5 minutes was far lower than that of blank α-HH, achieved the maximum at 120 minutes, and then began to decline to a constant value. In addition, the PO_4^{3-} ion appeared in the liquid and the concentration first increased and then decreased gradually. Combing the results of FTIR spectra and XPS, the $Ca_3(PO_4)_2$ absorbed on the surface of α-HH markedly inhibited the dissolution of α-HH and the nucleation of DH. Meanwhile, the IP in α-HH dissolved out and ionized into PO_4^{3-} ion during the hydration, which reacted with Ca^{2+} in the solution to form insoluble $Ca_3(PO_4)_2$ absorbed on the surface of α-HH and DH crystals. Consequently, the dissolution of α-HH and the nucleation and growth of DH was further slowed.

Effect of IP on strength and microstructure of α-HH hardened paste

Figure 10 indicated the normal consistency and strength of α-HH in absence or presence of IP. The influence of IP on the normal consistency was relatively small, which slightly increased with the addition of IP ≥0.1%. It was attributed to

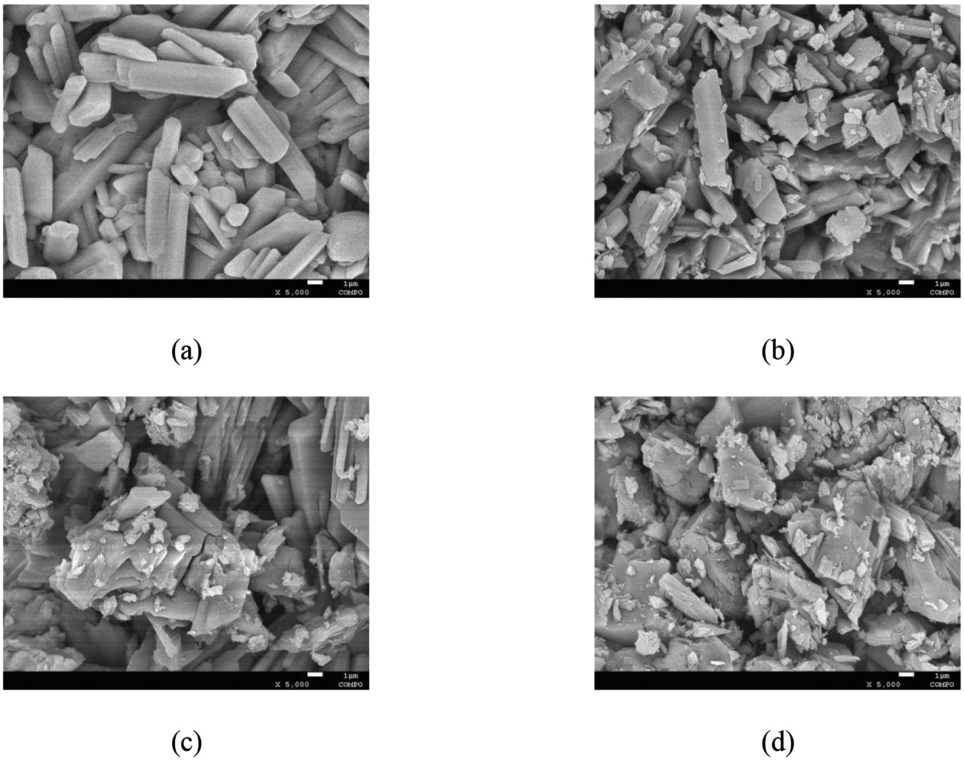

(a) (b)

(c) (d)

Fig. 11—SEM pictures of hydrated α-HH in absence or presence of IP:(a) 0; (b) 0.04%; (c) 0.1%; and (d) 0.6%.

the slight increase in the number of fine and irregular α-HH crystals, which had a larger specific surface area. It showed the flexural and compressive strength of α-HH in the absence of IP, respectively, reached 5.72 and 47.86 MPa. In the case of 0.04% IP, the flexural and compressive strength of α-HH was same to that of blank α-HH. However, the strength decreased with the continuing increase of IP, especially the 2-hour flexural strength. When the content of IP was ≥0.4%, the final setting time of α-HH paste was later than 120 minutes (as shown as Fig. 6), so 2-hour flexural strength could not be tested. The influence of IP on the strength of α-HH was the same as the IP in β-HH.[20,21]

The hardened paste of α-HH presented a porous network structure formed by the cross-linking of DH crystals. On the one hand, the strength of α-HH hardened paste is related to an interlocking structure and adhesion force between DH crystals.[42,43] On the other hand, the porosity and pore size distribution of hardened paste also plays an important role in the strength. SEM images of α-HH hardened pastes in the absence and presence of IP were shown in Fig. 11. In the absence of IP, most DH crystals presented long and rod-like or columnar and had a high degree of interlocking. The effect of IP on morphologies of DH crystals was closely related to its content. In the case of 0.04% IP, the growing habit of DH crystals was not modified, which results in little changes of morphology and numbers. Therefore, the strength of α-HH was almost the same as blank α-HH. With the increase of IP, the nucleation and growth time of DH crystals were inhibited significantly (as shown as Fig. 7(b)); consequently, the number of DH crystals decreased, and DH crystals were mainly composed of large, plate-like DH crystals and fine particles. The weak overlap between large and plate-like DH crystals and the increasing normal consistency of α-HH all led to the higher porosity, and the decreasing DH crystals reduced the adhesion force between DH crystals. The combined effect of the higher porosity and the decreased adhesion force between DH crystals reduced the strength of the hardened paste. Under the action of IP, the coarsening of DH crystals and the reduction in overlap between crystals in α-HH paste were similar to that in β-HH paste.[20,21]

Effect mechanism of IP during preparation and hydration of α-HH

Through the previously mentioned study, the effect mechanism of IP during the preparation and hydration of α-HH was found out. In the paper, the preparation and hydration of α-HH all follow the dissolution-crystallization mechanism. During the preparation of α-HH, first, the NG and $Ca(SO_4,HPO_4)\cdot 2H_2O$ all dissolved in the liquid. When the concentration of α-HH in the solution reached saturation point, α-HH fast crystallized to form the large and dense crystals. Part of the dissolved IP would ionize into H+ and PO_4^{3-}, the latter reacting with Ca^{2+} in the liquid to form the $Ca_3(PO_4)_2$ absorbed on the surface of α-HH. However, part of the IP entered the lattice of α-HH. The effect of IP on the microstructure of α-HH was not significant, though.

During the hydration of α-HH, the α-HH first dissolved in the liquid, and then the nuclei of DH produced in the supersaturated solution. The nuclei of DH continuously absorbed the energies to become stable and finally grew into the large DH crystals. The $Ca_3(PO_4)_2$ on the surface of α-HH inhibited the dissolution of α-HH and the nucleation of DH. In addition, the IP in the lattice of α-HH also dissolved in the liquid and ionized into H+ and PO_4^{3-}, then the PO_4^{3-} also reacted with Ca^{2+} to form the insoluble $Ca_3(PO_4)_2$ absorbed on the surface of α-HH and DH crystals. As a result, the dissolution of α-HH and the nucleation and growth of DH were further inhibited. The higher the amount of IP, the more significant the inhibition in the dissolution of α-HH crystals and the nucleation of DH. The decreasing nuclei and the extension of growth time all made DH crystals coarser and larger. With an increasing IP content, the setting time of α-HH pastes was prolonged due to the decreasing DH amount, and the strength of α-HH hardened paste was decreased due to the coarsening DH crystals, weak overlap, and decreased adhesion force between DH crystals.

CONCLUSIONS

To effectively reuse phosphogypsum (PG) to prepare α-hemihydrate gypsum (α-HH), this study systematically investigated the influence of intercrystalline phosphorus (IP) on the properties of α-HH using multiple techniques. Based on the results, the following conclusions can be drawn.

The X-ray diffraction (XRD), X-ray photoelectron spectrometer (XPS), and scanning electron microscopy (SEM) tests of α-HH indicated the IP in the lattice of $CaSO_4{\cdot}2H_2O$ dissolved and entered the lattice of α-HH during the preparation of α-HH. The IP in range of 0.04 to 0.4% had no obvious effect on the morphology of α-HH crystals. When the content of IP reached 0.6%, the content of irregular polyhedrons and fine grains and the length-width ratio increased obviously.

When α-HH hydrated, the IP in the lattice of α-HH dissolved and converted into $Ca_3(PO_4)_2$, which absorbed on the surface of α-HH and inhibited the further hydration of α-HH. However, the effect of 0.04% IP on the hydration, setting time, strength, and microstructure of α-HH was not obvious.

When the content of IP was $\geq$0.1%, as the IP content increased, the hydration process of α-HH was markedly prolonged, the setting time increased, the DH crystals in hardened paste became coarse and large, and then the strength decreased.

When PG was used to prepare α-HH by the autoclaving method, PG should be pretreated with the appropriate method to control the content of IP to less than 0.04%.

AUTHOR BIOS

ACI member **Dongmei Liu** *is an Associate Professor in the College of Civil Engineering and Architecture at China Three Gorges University, Yichang, Hubei, China. She received her PhD in hydraulic structure engineering from Wuhan University, Wuhan, Hubei, China, in 2007. Her research interests include cement, concrete, and gypsum materials, with an interest in the reuse of industrial wastes in building materials.*

ACI member **Xinyu Li** *is a Graduate in the College of Civil Engineering and Architecture at China Three Gorges University. His research interests include the reuse of industrial wastes in gypsum materials.*

ACI member **Wanqing Zhou** *is an Associate Professor in the College of Civil Engineering and Architecture at China Three Gorges University. He received his PhD in civil engineering from South China University of Technology, Guangzhou, China, in 2007. His research interests include concrete materials for infrastructure applications, with an interest in the reuse of industrial wastes in building materials.*

ACI member **Gang Xu** *is a Professor in the College of Civil Engineering and Architecture at China Three Gorges University. He received his PhD in civil engineering from the Huazhong University of Science and Technology, Wuhan, China, in 2007. His research interests include the durability of reinforced concrete structures, with an interest in the reuse of industrial wastes in building materials.*

ACI member **Yi Qin** *is a Lecturer at Guangxi Eco-engineering Vocational and Technological College, Liuzhou City, China. She received her MS from the College of Civil Engineering and Architecture at China Three Gorges University in 2022. Her research interests include the reuse of industrial waste in gypsum material.*

ACKNOWLEDGMENTS

This work was supported by the Programme of National Natural Science Youth Foundation (No. 52308266) for the detailed laboratory work.

REFERENCES

1. Pinto, S. R.; Luz, C. A. D.; Munhoz, G. S.; and Medeiros-Junior, R. A., “Durability of Phosphogypsum-Based Supersulfated Cement Mortar Against External Attack by Sodium and Magnesium Sulfate,” *Cement and Concrete Research*, V. 136, No. 1, 2020, p. 106172. doi: 10.1016/j.cemconres.2020.106172

2. Jiang, G. Z.; Wu, A. X.; Wang, Y. M.; and Lan, W. T., “Low Cost and High Efficiency Utilization of Hemihydrate Phosphogypsum: Used as Binder to Prepare Filling Material,” *Construction and Building Materials*, V. 167, 2018, pp. 263-270. doi: 10.1016/j.conbuildmat.2018.02.022

3. Taher, M. A., “Influence of Thermally Treated Phosphogypsum on the Properties of Portland Slag Cement,” *Resources, Conservation and Recycling*, V. 52, No. 1, 2007, pp. 28-38. doi: 10.1016/j.resconrec.2007.01.008

4. Singh, M., “Effect of Phosphatic and Fluoride Impurities of Phosphogypsum on the Properties of Selenite Plaster,” *Cement and Concrete Research*, V. 33, No. 9, 2003, pp. 1363-1369. doi: 10.1016/S0008-8846(03)00068-1

5. Hentati, O.; Abrantes, N.; Caetano, A. L.; Bouguerra, S.; Gonçalves, F.; Rombke, J.; and Pereira, R., “Phosphogypsum as a Soil Fertilizer: Ecotoxicity of Amended Soil and Elutriates to Bacteria, Invertebrates, Algae And Plants,” *Journal of Hazardous Materials*, V. 294, 2015, pp. 80-89. doi: 10.1016/j.jhazmat.2015.03.034

6. Yang, L.; Zhang, Y.; and Yan, Y., “Utilization of Original Phosphogypsum as Raw Material for the Preparation of Self-Leveling Mortar,” *Journal of Cleaner Production*, V. 127, 2016, pp. 204-213. doi: 10.1016/j.jclepro.2016.04.054

7. Zhang, J.; Tan, H.; He, X.; Yang, W.; Deng, X.; Su, Y.; and Yang, J., “Compressive Strength and Hydration Process of Ground Granulated Blast Furnace Slag-Waste Gypsum System Managed by Wet Grinding,” *Construction and Building Materials*, V. 228, 2019, p. 116777. doi: 10.1016/j.conbuildmat.2019.116777

8. Zhang J.W.; Wang X.; Jin B.; Liu C.G.; Zhang X.T.; and Li Z.X., “Effect of Soluble P_2O_5 Form on the Hydration and Hardening of Hemihydrate Phosphogypsum,” *Advances in Materials Science and Engineering*, V. 5, 2022, pp. 1-8.

9. Luo, X. H.; Zhang, S. J.; Guo, R. X.; Jia, J. P.; Ma, F. Y.; and Kong, C. Y., “Effect of Carbide Slag Instead of Cement as Alkali Activator on Properties and Microstructure of Excess-Sulphate Phosphogypsum Cementitious Material,” *Materials Review*, V. 37, 2023.

10. Jiang, G.; Wang, H.; Chen, Q.; Zhang, X.; Wu, Z.; and Guan, B., “Preparation of Alpha-Calcium Sulfate Hemihydrate from FGD Gypsum in Chloride-Free $Ca(NO_3)_2$ Solution Under Mild Conditions,” *Fuel*, V. 174, 2016, pp. 235-241. doi: 10.1016/j.fuel.2016.01.073

11. Liu, J. F., “Preparation of Industrial Phosphogypsum-Based α-Hemihydrate Gypsum and Regulation of its Paste Properties,” Southwest University of Science and Technology, 2019.

12. Yang, L.; Zhang, B.; Zhou, J.; and Cao, J., “Preparation of α-high Strength Gypsum Using Phosphogypsum and Transformation of Phosphogypsum to α-High Strength Gypsum,” *Jianzhu Cailiao Xuebao*, V. 17, No. 1, 2019

13. Liu D.M.; Wang Q.; Xu G.; Peng Y.Z.; Huang T.Q.; and Yu X., “Effect of Modifiers on Crystalizing Habit and Mechanical Strength of α-Hemihydrate Gypsum Prepared from PG by an Autoclaved Method,” *Construction and Building Materials*, V. 366, 2023.

14. Singh, M., “Role of Phosphogypsum Impurities on Strength and Microstructure of Selenite Plaster,” *Construction and Building Materials*, V. 19, No. 6, 2005, pp. 480-486. doi: 10.1016/j.conbuildmat.2004.07.010

15. Kubota, N., and Mullin, J. W., “A Kinetic Model for Crystal Growth from Aqueous Solution in the Presence of Impurity,” *Journal of Crystal Growth*, V. 152, No. 3, 1995, pp. 203-208. doi: 10.1016/0022-0248(95)00128-X

16. Wang, L. S.; Li, X. B.; Du, W. F.; and Gao, W. X., “Effect of Soluble Phosphorus on the Mechanical Properties of α-Hemihydrate Gypsum,” *Journal of the Minerals Metals & Materials Society*, V. 75, No. 4, 2023, pp. 1128-1136. doi: 10.1007/s11837-023-05709-6

17. Nilles, V., and Plank, J., “Study of the Retarding Mechanism of Linear Sodium Polyphosphates on α-Calcium Sulfate Hemihydrate,”

Cement and Concrete Research, V. 42, No. 5, 2012, pp. 736-744. doi: 10.1016/j.cemconres.2012.02.008

18. Ru, X. H.; Li, H. T.; Zhang, X. A.; Ma, B. G.; and Lu, S. W., "Effect of Soluble Phosphorus on High-Strength α-Hemihydrate Gypsum Prepared by Atmospheric Hydrothermal Method," *CIESC Journal*, V. 66, No. 5, 2015, pp. 1983-1988.

19. Liu, Y.; Hu, Y.; and Zhang, L. H., "State and Evolution of Calcium Sulfate Filter Residue and its Inclusion Phosphorus in a Semihydrate-Dihydrate Phosphoric Acid Plant," *Phosphat & Compound Fertilizer*, V. 36, No. 11, 2021, pp. 32-35.

20. Peng, J. H.; Wan, T. Z.; Tang, L.; and Zhang, J. X., "Organic Matters and P2O5 in Crystal Lattice and Their Influence on Properties of Phosphogypsum," *Jianzhu Cailiao Xuebao*, V. 6, No. 3, 2003, pp. 221-226.

21. Li, M.; Peng, J. H.; and Zhang, H., "Influence of P2O5 in Crystal Lattice on Gypsum Properties and its Mechanisms," *Journal of Sichuan University: Engineering Science Edition*, V. 44, No. 3, 2012, pp. 200-204.

22. Song, J. B.; Mei, Y.; Xia, J. P.; and Zhou, Q. B., "Study on Influence of Phosphorus and Fluorine Impurities on Properties of Building-Purpose Gypsum," *Modern Chemical Industry*, V. 44, No. 10, 2024, pp. 137-143.

23. Singh, N. B., and Middendorf, B., "Calcium Sulphate Hemihydrate Hydration Leading to Gypsum Crystallization," *Progress in Crystal Growth and Characterization of Materials*, V. 53, No. 1, 2007, pp. 57-77. doi: 10.1016/j.pcrysgrow.2007.01.002

24. Kuzel, H. J., and Hauner, M., "Chemical and Crystallographic Properties of Calcium Sulphate Hemihydrate and Anhydrite III," *Zement-Kalk-Gips*, V. 40, 1987, p. 628-632

25. Follner, S.; Wolter, A.; and Preusser, A., "The Setting Behavior of α and β-$CaSO_4 \cdot 0.5H_2O$ as a Function of Crystal Structure and Morphology," *Crystal Research and Technology*, V. 37, No. 10, 2002, pp. 1075-1087. doi: 10.1002/1521-4079(200210)37:10<1075::AID-CRAT1075>3.0.CO;2-X

26. Chen, X.; Gao, J.; Liu, C.; and Zhao, Y., "Effect of Neutralization on the Setting and Hardening Characters of Hemihydrate Phosphogypsum Plaster," *Construction and Building Materials*, V. 190, 2018, pp. 53-64. doi: 10.1016/j.conbuildmat.2018.09.095

27. Singh, M., "Treating Waste Phosphogypsum for Cement and Plaster Manufacture," *Cement and Concrete Research*, V. 32, No. 7, 2002, pp. 1033-1038. doi: 10.1016/S0008-8846(02)00723-8

28. Potgieter, J. H.; Potgieter, S. S.; McCrindle, R. I.; and Strydom, C. A., "An Investigation into the Effect of Various Chemical and Physical Treatments of a South African Phosphogypsum to Render it Suitable as a Set Retarder for Cement," *Cement and Concrete Research*, V. 33, No. 8, 2003, pp. 1223-1227. doi: 10.1016/S0008-8846(03)00036-X

29. Guan, Q.; Sui, Y.; and Yu, W., "Deep Removal of Phosphorus and Synchronous Preparation of High-Strength Gypsum from Phosphogypsum by Crystal Modification in Nacl-Hcl Solutions," *Separation and Purification Technology*, V. 298, October 2022, p. 121592.

30. JC/T 2038-2010, "α-High Strength Gypsum Plaster," Ministry of Industry and Information Technology, Beijing, China.

31. GB/T 17669.4-1999, "Gypsum Plasters Determination of Physical Properties of Pure Paste," State Bureau of Quality and Technical Supervision, Beijing, China, 1999.

32. Ballirano, P.; Maras, A.; Meloni, S.; and Caminiti, R., "The Monoclinic I2 Structure of Bassanite, Calcium Sulphate Hemihydrate ($CaSO_4 \cdot 0.5H_2O$)," *European Journal of Mineralogy*, V. 13, No. 5, 2001, pp. 985-993. doi: 10.1127/0935-1221/2001/0013/0985

33. Goto, M.; Molony, B.; Ridge, M. J.; and West, G. W., "The Forms of Calcium Sulphate Hemihydrate," *Australian Journal of Chemistry*, V. 19, No. 2, 1966, pp. 313-316. doi: 10.1071/CH9660313

34. Mielczarski, J. A.; Cases, J. M.; Alnot, M.; and Ehrhardt, J. J., "XPS Characterization of Chalcopyrite, Tetrahedrite, and Tennantite Surface Products After Different Conditioning. 1. Aqueous Solution at pH 10," *Langmuir*, V. 12, No. 10, 1996, pp. 2519-2530. doi: 10.1021/la9505881

35. Franke, R.; Chasse, T.; Streubel, P.; and Meisel, A., "Auger Parameters Sand Relaxation Energies of Phosphorus in Solid Compounds," *Journal of Electron Spectroscopy and Related Phenomena*, V. 56, 1991, p. 381. doi: 10.1016/0368-2048(91)85035-R

36. Feng, B. Q.; Jing, Y. Z.; Xie, C.; Li, G. B.; and Na, P., "Surfactant Regulation of Co-Crystallized Phosphorus Content and Morphology of α-Calcium Sulfate Hemihydrate," *Chemical Industry and Engineering*, V. 1, 2024, p. 23

37. Jia, R. Q.; Wang, Q.; and Luo, T., "Reuse of Phosphogypsum as Hemihydrate Gypsum: The Negative Effect and Content Control of H3PO4," *Resources, Conservation and Recycling*, V. 174, 2021, pp. 12-26. doi: 10.1016/j.resconrec.2021.105830

38. Chen, X.; Gao, J.; and Zhao, Y., "Investigation on the Hydration of Hemihydrate Phosphogypsum After Post Treatment," *Construction and Building Materials*, V. 229, 2019, pp.116864.1-116864.9.

39. Ölmez, H., and Yilmaz, V. T., "Infrared Study on the Refinement of Phosphogypsum for Cements," *Cement and Concrete Research*, V. 18, No. 3, 1988, pp. 449-454. doi: 10.1016/0008-8846(88)90079-8

40. Rinaudo, A. M.; Lanfranco, M.; and Franchini, A., "The System $CaHPO_4 \cdot 2H_2O$-$CaSO_4 \cdot 2H_2O$: Crystallizations from Calcium Phosphate Solutions in the Presence of SO_4^{2-}," *Journal of Crystal Growth*, V. 142, No. 1-2, 1994, pp. 184-192. doi: 10.1016/0022-0248(94)90287-9

41. Rinaudo, C.; Lanfranco, A. M.; and Boistelle, R., "The Gypsum-Brushite System-Crystallization from Solutions Poisoned by Phosphate Ions," *Journal of Crystal Growth*, V. 158, No. 3, 1996, pp. 316-321. doi: 10.1016/0022-0248(95)00444-0

42. Finot, E.; Goudonnet, J.-P.; Mutin, J. C.; and Lesniewska, E., "Correlation Between Surface Forces and Surface Reactivity in the Setting of Plaster by Atomic Force Microscopy," *Applied Surface Science*, V. 161, No. 3-4, 2000, pp. 316-322. doi: 10.1016/S0169-4332(00)00030-1

43. Finot, E.; Lesniewska, E.; Goudonnet, J.-P.; Mutin, J.-C.; Domenech, M.; and Kadi, A. A., "Correlating Surface Forces with Surface Reactivity of Gypsum Crystals by Atomic Force Microscopy. Comparison with Rheological Properties of Plaster," *Solid State Ionics*, V. 141-142, 2001, pp. 39-46. doi: 10.1016/S0167-2738(01)00718-4

JOIN AN ACI Chapter!

The American Concrete Institute has Chapters and Student Chapters located throughout the world. Participation in a local chapter can be extremely rewarding in terms of gaining greater technical knowledge and networking with leaders in the concrete community.

Because chapters are distinct and independent legal entities, membership includes both ACI members and non-ACI members and is made up of a diverse blend of architects, engineers, consultants, contractors, educators, material suppliers, equipment suppliers, owners, and students—basically anyone interested in concrete. Many active ACI members initially became involved in ACI through their local chapter. In addition to technical programs and publications, many chapters sponsor ACI Certification programs, ACI educational seminars, project award recognition programs, and social events with the goal of advancing concrete knowledge.

To find a chapter near you, go to: https://www.concrete.org/getinvolved/chapters.aspx

---

Student Chapters

Join or form an ACI Student Chapter to maximize your influence, knowledge sharing, and camaraderie! ACI has 240+ student chapters located throughout the world, each providing opportunities for students to:

- Connect with their peers and participate in concrete-related activities such as: student competitions, ACI Conventions, ACI Certification Programs, ACI Educational Seminars, local chapter meetings, social events, and community service projects;
- Network with members of local chapters, many of whom have been in the industry for decades and can help to develop professional relationships and offer career advice;
- Win recognition for their universities through the University Award; and
- Learn about the many scholarships and fellowships offered by the ACI Foundation and by ACI's local chapters.

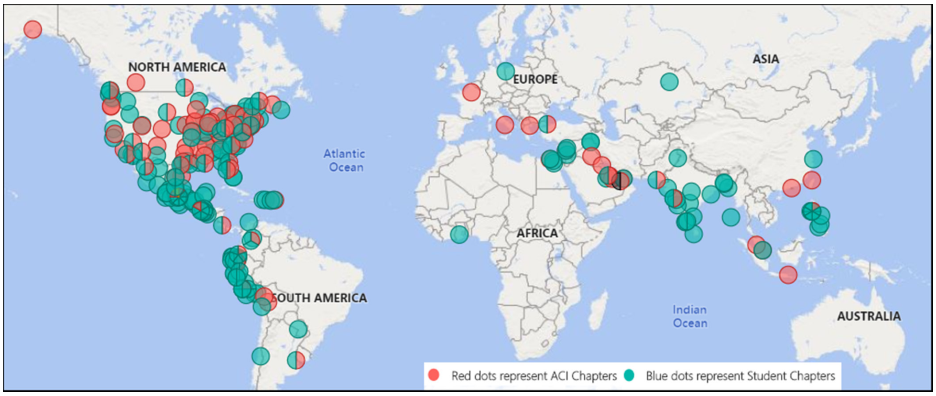

American Concrete Institute

www.concrete.org/getinvolved/chapters.aspx

ACI MATERIALS JOURNAL TECHNICAL PAPER

Title No. 122-M25

Phase-Change Material for Enhancing Frost Resistance of Cementitious Materials

by Zhiyong Liu, Jinyang Jiang, Yang Li, Yuncheng Wang, Xi Jin, and Zeyu Lu

A capsule phase-change material (CPCM) was synthesized using n-tetradecane as the core, expanded graphite as the shell, and ethyl cellulose as the coating material through a controlled assembly process. The results demonstrate that the infiltration of n-tetradecane significantly enhances the density of the expanded graphite, while the ethyl cellulose coating effectively prevents the desorption and leakage of the liquid phase-change material during phase transitions. As a result, the CPCM exhibits a compact structure, chemical stability, and excellent thermal stability. The incorporation of this CPCM into cement-based materials endows the material with an autonomous heat-release capability at temperatures below 5°C. When the CPCM content reaches 20%, the thermal conductivity of the cementitious matrix increases by 24.66%. Moreover, the CPCM significantly improves the freezing-and-thawing resistance of the cement-based materials, reducing the compressive strength loss by 96% and the flexural strength loss by 65% after freezing-and-thawing cycles. This CPCM fundamentally enhances the frost resistance of cement-based materials, addressing the issue of freezing-and-thawing damage in concrete structures in cold regions.

Keywords: capsule phase-change material (CPCM); cement-based materials; expanded graphite; frost resistance; n-tetradecane.

INTRODUCTION

Freezing-and-thawing environments readily cause damage, deterioration, and structural degradation of concrete. Deicing salts can achieve the effect of melting ice and snow by reducing the freezing point of the concrete pore solution.[1] However, deicing salts mainly composed of chloride salts in the later stage will lead to severe erosion of concrete, and their failure rate is much faster than that caused by ordinary freezing-and-thawing environments, thereby seriously affecting the service life of concrete structures.[2] Considering the harm of freezing-and-thawing cycles to concrete structures, the main measures currently taken to improve the frost resistance of concrete include adding air-entraining agents,[3-5] mineral admixtures,[6-8] fibers,[9,10] porous aggregate,[11,12] and surface coatings.[13-15] Although these measures have to some extent improved the frost resistance of concrete, they have not fundamentally solved the problem by using passive methods to improve concrete.

The physical state of phase-change materials undergoes transformation in tandem with the fluctuation of external temperature, during which the absorption and release of energy occur concomitantly.[16,17] Phase-change energy storage materials have found extensive use within the domain of concrete.[18-20] The integration of phase-change materials with cement-based materials holds the potential to efficaciously curtail building energy consumption and address the issue of energy mismatches in both temporal and spatial dimensions.[21,22] N-tetradecane has a suitable phase transition temperature range (approximately 20 to 30°C) and a high latent heat value (approximately 163 J/g), which gives it excellent heat-storage capacity and makes it suitable for thermal energy regulation in building materials.[23] Pilehvar et al.[12] delved into the impact of incorporating micro-encapsulated phase-change materials on the interfacial transition zone as well as the setting time of portland cement and geopolymer. The findings revealed that the addition of micro-encapsulated phase-change materials endows the composites with remarkable resistance to freezing-and-thawing cycles, albeit accompanied by a reduction in compressive strength. Rodríguez et al.[24] probed into the influence of phase-change materials on the frost resistance of cement-based materials. It was ascertained that as the content of phase-change materials augments, the frost resistance of cement-based materials initially ascends and subsequently declines, with the threshold being correlated to the volume of the cement paste. Notwithstanding the extensive research efforts dedicated by domestic and international scholars to phase-change frost-resistant concrete, the preponderant majority of investigations remain centered around the performance analysis of phase-change concrete, falling short of delving into the underlying mechanism of action and optimization strategies of phase-change materials.

Moreover, the practical application of phase-change materials is currently confronted with an issue of utmost urgency. Namely, the thermal conductivity of the main phase-change materials currently available is often quite low.[25] The thermal conductivity of a phase-change system not only epitomizes its heat-transfer capacity, but also bears a close-knit relationship with the response rate of the phase-change system upon the variation of external environmental temperature. The relatively low thermal conductivity renders it arduous for the phase-change system to furnish immediate positive feedback when confronted with temperature alterations in the external environment, which has emerged as a bottleneck impeding the further expansion of the application scope of organic phase-change materials. The higher the thermal conductivity, the swifter the response rate of the phase-change

---

ACI Materials Journal, V. 122, No. 4, July 2025.

MS No. M-2024-168.R5, doi: 10.14359/51746807, received May, 4, 2025, and reviewed under Institute publication policies. Pertinent discussion including author's closure, if any, will be published ten months from this journal's date if the discussion is received within four months of the paper's print publication.

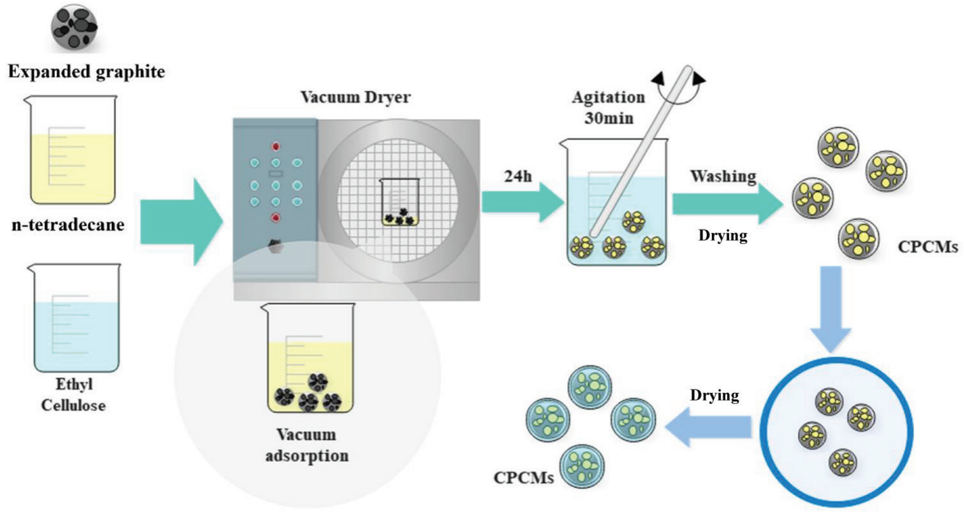

Fig. 1—CPCM preparation process.

system to temperature fluctuations, the greater the energy discharge efficiency, and the more diminutive the temperature regulation hysteresis of the phase-change system.[26] Expanded graphite has excellent thermal conductivity, which can effectively improve the overall thermal conductivity of cement-based materials and promote uniform distribution of heat.[27] It is imperative to develop zero-energy-consumption phase-change concrete capable of autonomous heat release from the freezing point, predicated on the principle of phase-change heat storage and release. In so doing, the concrete structure can spontaneously release heat to modulate the surface temperature of the structure, thereby fulfilling the ultra-stringent requirements for the frost resistance of concrete materials in complex, harsh environments as well as in unmanned regions.

In this study, ethyl cellulose was used as a coating material to coat n-tetradecane (core material) and expanded graphite (shell) in cement-based materials. The change mechanism of frost resistance of cement composites before and after adding n-tetradecane/expanded graphite core-shell capsule phase-change material (CPCM) was systematically studied. The effects of the content of CPCMs on the mechanical properties, thermal conductivity, and frost resistance were investigated. The developed CPCMs are capable of effectively mitigating the damage to cement-based materials under severe cold environments. By reducing maintenance costs arising from cement matrix cracking, degradation, and other structural problems, CPCMs hold tremendous application potential in frigid regions.

RESEARCH SIGNIFICANCE

This research introduces an innovative CPCM made by encapsulating n-tetradecane in expanded graphite and coating it with ethyl cellulose. This construction results in a highly compact and stable material with superior thermal properties. The incorporation of CPCMs into cement-based materials enhances thermal conductivity by 24.66% when used at a 20% content, while considerably improving freezing-and-thawing durability, with compressive strength loss reduced by 96% and flexural strength loss by 65%. This advancement offers a solution to mitigate freezing-and-thawing damage in concrete structures situated in cold environments, significantly enhancing the longevity and resilience of cement-based materials.

MATERIALS AND METHODS

Materials

The used n-tetradecane is produced by a company in Guangdong, China, with a purity of 99%, a molecular formula of $C_{14}H_{30}$, a melting point near 6°C, and a density of 0.763 g/cm^3. The expanded graphite used is produced by a company in Shandong, China, presenting a loose and porous wormlike structure with a carbon content of 99.5%, a particle size of 80 mesh, a purity of 99%, and an expansion factor of 200 to 300 times. The cement used is P·O 42.5 cement produced by a company in Jiangsu, China.

Preparation of CPCMs

As shown in Fig. 1, the n-tetradecane/expanded graphite core-shell CPCM were prepared by the macro encapsulation microcapsule method. First, the expanded graphite was dried in a 60°C oven for 24 hours to fully remove moisture from the material. Then the dried expanded graphite was mixed with a proper amount of n-tetradecane evenly and placed in a –0.01 MPa vacuum dish for vacuum immersion for 24 hours to fully immerse n-tetradecane into the interlayer structure of expanded graphite. Ethyl cellulose, as an important encapsulation material between phase-change materials (n-tetradecane) and carriers (expanded graphite), plays a crucial role in the performance of CPCMs. Finally, the n-tetradecane/expanded graphite composite was fully mixed with an ethyl cellulose/absolute ethanol solution of 2% (No. 1), 3% (No. 2), and 4% (No. 3) concentration, stirred for 30 minutes, filtered out, and dried to obtain CPCMs.

Macroscopic performance testing

To study the effect of CPCMs on the mechanical properties and thermal conductivity of cement-based materials, CPCMs were added to cement materials in mass ratios of 10, 15, and 20%; refer to Table 1 for details. The water-cement

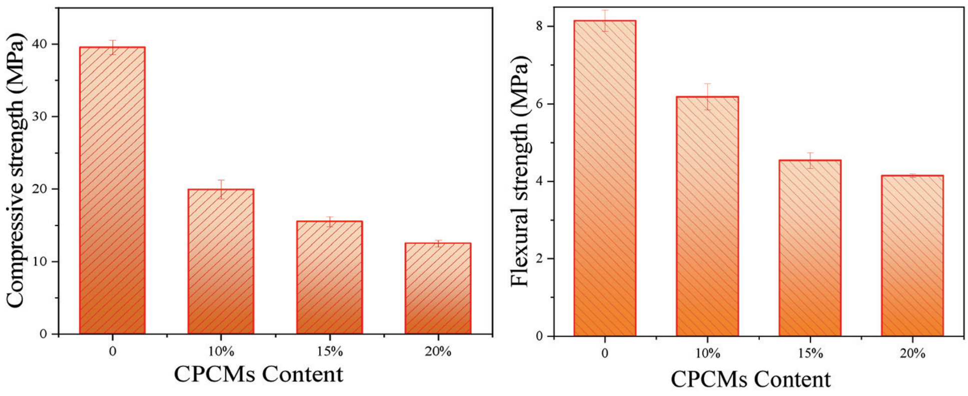

(a) Compressive strength (b) Flexural strength

Fig. 2—Strength of samples mixed with varying CPCMs contents.

Table 1—Mortar mixture proportion

Sample	Cement, g	CPCM, g	Sand, g	Water, g
0%	450	0	1350	180
10%	405	45	1350	180
15%	382.5	67.5	1350	180
20%	360	90	1350	180

ratio (*w*/*c*) was 0.4, and the standard curing was 14 days. The size of the thermal conductivity sample was 50 x 50 x 20 mm, and the size of the strength sample was 40 x 40 x 160 mm. Three samples were formed for each test conducted for each set of ratios. A thermal conductivity tester was used to test the thermal conductivity of samples. A fully automatic cement strength testing machine was used to test the compressive strength and flexural strength of samples.

To study the effect of CPCMs on the frost resistance of cement-based materials, experiments were conducted in accordance with specification GB/T50081-2019. N-tetradecane/expanded graphite core-shell CPCMs were mixed into cement at a mass ratio of 20%, and a reinforced cement-based material with a *w*/*c* of 0.4 and a size of 40 x 40 x 160 mm was prepared. After 24 days of standard curing, it was soaked in water for 4 days, and the water surface was at least 20 mm higher than the top surface of the test piece during soaking. After 4 days, one set of samples was removed and the surface moisture was wiped off. After weighing, it was placed in a concrete slow freezing-and-thawing testing machine, with a spacing of no less than 20 mm between the test blocks and the inner wall of the test box. The instrument used in the experiment is a fully automatic low-temperature freezing-and-thawing testing machine with a freezing temperature of –15°C and a melting temperature of 15°C. The freezing and melting time was not less than 4 hours, and the weight was measured every two cycles. After 30 cycles, its mechanical strength was tested.

Microscopic characterization

To study the influence of CPCMs on the microstructure of cement-based materials, a scanning electron microscope (SEM) was used to characterize the micro morphology of expanded graphite and CPCMs; a specific surface area analyzer was used to characterize the specific surface area and pore size distribution of CPCMs; X-ray diffraction (XRD), a Fourier-transform infrared spectrometer (FTIR), and laser spectrometer were used to analyze the composition, structure, and chemical stability of expanded graphite and CPCMs (among them, XRD reveals the crystal structure and phase transition characteristics of the material, FTIR is used to investigate the vibration of chemical bonds to evaluate the interactions of organic components, and Raman spectroscopy provides in-depth information about the degree of disorder and carbon-based structure of the material); a differential scanning calorimeter (DSC) was used to measure the phase-change temperature, latent enthalpy, and cyclic stability of CPCMs; and a synchronous thermal analyzer (STA) was used to characterize the thermal stability of CPCMs.

RESULTS AND DISCUSSION

Mechanical properties

Figure 2 illustrates the compressive and flexural strength of the samples blended with CPCMs. When the content of the CPCMs reached 10%, the compressive strength experienced a reduction of 49.6%, while the flexural strength witnessed a decrease of 24.1%. In the case where the content amounts to 15%, the compressive strength diminished by 60.7% and the flexural strength declined by 44.3%. When the content ascended to 20%, the compressive strength dropped by 68.4% and the flexural strength decreased by 49.1%. The incorporation of the CPCMs triggered a substantial loss in the strength of the cement matrix. Moreover, the reduction in compressive strength was more pronounced than that in flexural strength. This phenomenon can be attributed to the fact that expanded graphite is a loose and porous worm-like material, which is capable of playing a role analogous to crack-resistant fibers within the cement matrix. Consequently, its influence on flexural strength was less significant compared to its impact on compressive strength.

In general, the addition of CPCMs gave rise to a deterioration in the mechanical properties of the cement matrix. The greater the quantity of the added CPCMs, the more substantial the adverse effect on the mechanical properties. This is primarily due to the poor compatibility between CPCMs and cement substrates. This incompatibility can lead to the

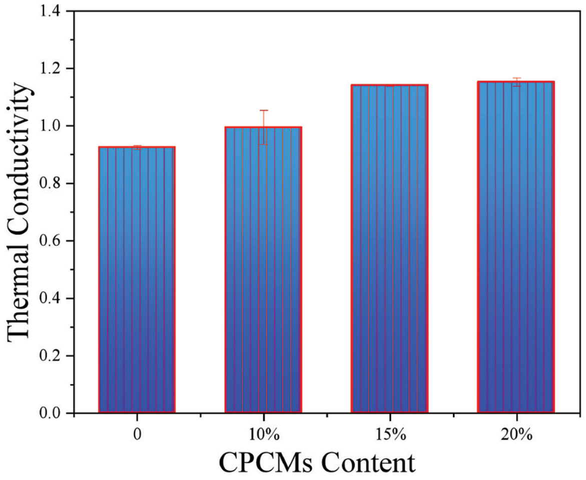

Fig. 3—Thermal conductivity of samples with varying CPCMs contents.

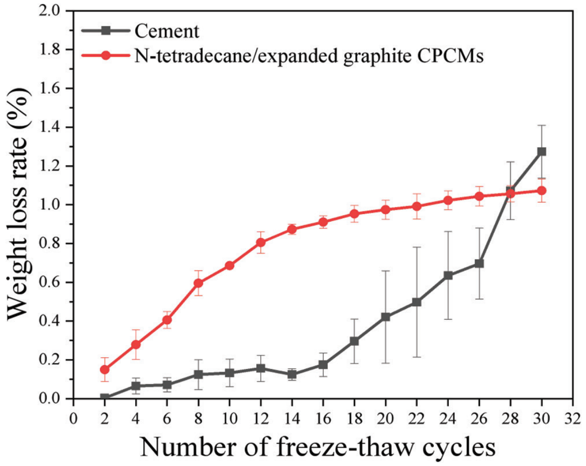

Fig. 4—Weight loss rate of samples after 30 freezing-and-thawing cycles.

formation of defects and weaknesses in cement-based materials, which can interfere with the surrounding microstructure and affect the overall strength. In addition, as a carrier, expanded graphite itself is a loose and porous material, and its strength is relatively low compared to the cement matrix. This strength difference exacerbates the fragility of the surrounding area of the capsule material, forming stress concentration points and making it more prone to cracking.

Thermal conductivity

Figure 3 shows the thermal conductivity of phase-change samples when the CPCM content was 0, 10, 15, and 20%. The addition of CPCMs increased the thermal conductivity of samples. When the CPCM content increased to 20%, the thermal conductivity of cement-based materials increased by 24.66%. This is because the thermal conductivity of expanded graphite is excellent, and its thermal conductivity is much higher than that of cement. When conducting heat, transfers along the expanded graphite with strong thermal conductivity, which is known as the thermal bridge effect.[28] For phase-change systems, higher thermal conductivity means stronger heat-transfer ability and faster phase-change efficiency.[29] Therefore, from the perspective of phase-change rate, the introduction of expanded graphite can not only fix and support phase-change materials, but also improve the thermal conductivity of CPCMs. When the temperature drops, the CPCMs can give faster positive feedback. By quickly initiating the solidification and heat-release program, the temperature of the cement matrix is maintained stable, solving the problem of low energy charging and discharging rate caused by the low thermal conductivity of phase-change materials.

Frost resistance

Figure 4 shows the change in mass loss of pure cement samples and cement-based samples mixed with CPCMs during freezing-and-thawing cycles. It can be seen from Fig. 4 that after 30 freezing-and-thawing cycles, the mass loss rate of pure cement samples and cement-based samples of CPCMs was 1.273% and 1.073%, respectively. The early mass loss of cement-based samples of CPCMs is greater than that of pure cement samples, and it is not lower than the mass loss rate of pure cement samples until 28 freezing-and-thawing cycles. The reason lies in the following two points: first, expanded graphite is wormlike, with a loose structure, porous and curved, extremely loose texture, and poor interfacial bonding performance; and second, the latent heat of phase-change of expanded graphite is extremely high. When the ambient temperature decreases, the n-tetradecane phase-change will release a lot of heat to maintain the internal temperature of the samples at a level higher than the external temperature. As a result, a large temperature difference will be generated inside and outside the samples, which will lead to temperature cracks, resulting in a large weight loss rate of cement-based samples of CPCMs.

Figures 5(a) and (b) show the compressive and flexural strength of pure cement samples and cement-based samples mixed with CPCMs before and after 30 freezing-and-thawing cycles, respectively. After 30 freezing-and-thawing cycles, the change rate of compressive strength of pure cement samples and cement-based samples of CPCMs was –16.82% and –0.74%, respectively; the change rates of flexural strength were –22.74% and –8.03%, respectively. Compared with previous research results,[20] the compressive strength loss rate after freezing and thawing decreased from 32.71 to 0.74%, and the flexural strength loss rate decreased from 16.82 to 8.03%, achieving new breakthroughs. It can be seen from the analysis data that the addition of CPCMs reduces the compressive strength loss rate of the cement matrix by 96% and the flexural strength loss rate by 65%. The results indicate that the addition of CPCMs effectively reduces the strength loss of cementitious materials during freezing-and-thawing cycles. Combining Fig. 2 and 5, it is found that although CPCMs reduce the early strength of cement-based materials, they significantly improve their strength retention in freezing-and-thawing environments. This greatly improves the service life of cement-based materials in freezing-and-thawing environments, proving that CPCMs have great application value in cold regions.

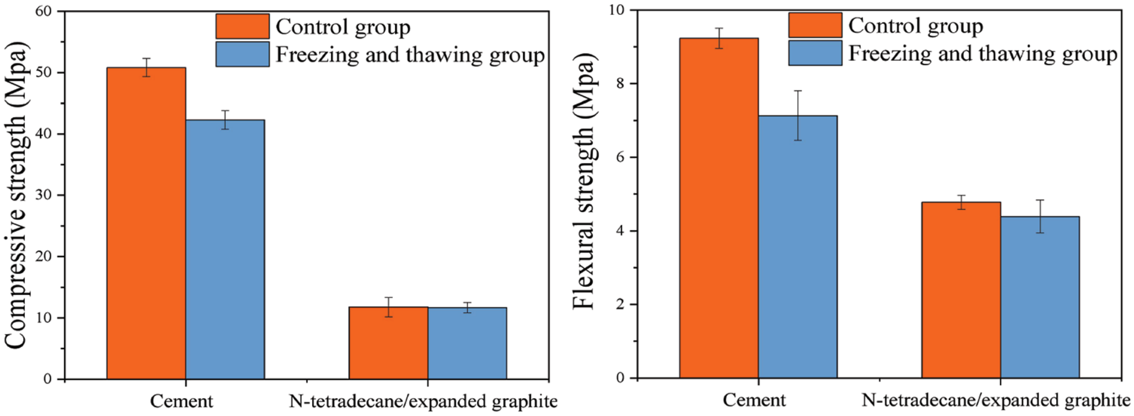

(a) Compressive strength (b) Flexural strength

Fig. 5—Strength of samples after 30 freezing-and-thawing cycles.

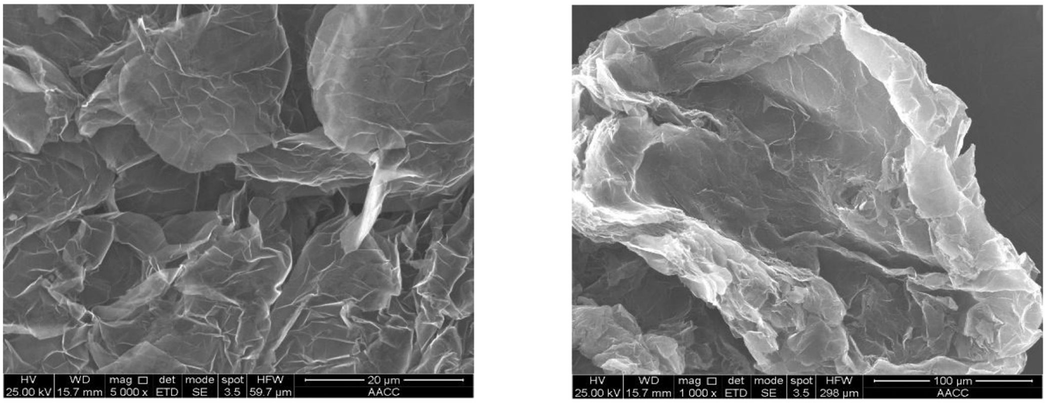

(a) Expanded graphite (b) #1

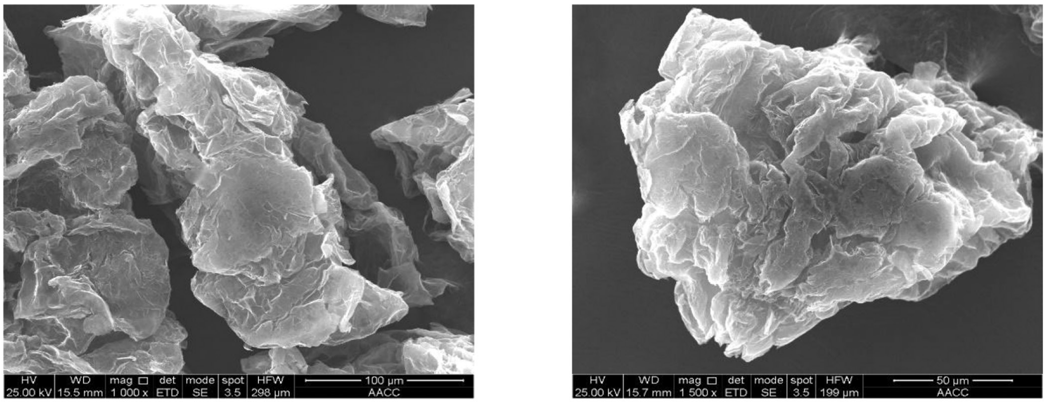

(c) #2 (d) #3

Fig. 6—SEM of expanded graphite and n-tetradecane/expanded graphite CPCMs.

Mechanism analysis

Micromorphology—The microscopic morphology of expanded graphite and CPCMs is shown in Fig. 6. From Fig. 6(a), it can be seen that the interlayer structure of expanded graphite is loose, curved, and worm-like, with rich pore structures and a large specific surface area. Figures 6(b) to (d) are SEM morphology of CPCMs with ethyl cellulose solution concentration of 2% (No. 1), 3% (No. 2), and 4% (No. 3). It can be seen from Fig. 6 that the texture of expanded graphite adsorbed with n-tetradecane becomes relatively tight. Ethyl cellulose forms a smooth and dense film on the surface of n-tetradecane/expanded graphite composite, covering the surface of expanded graphite. Moreover, the higher the concentration of ethyl cellulose, the greater the film coverage rate, the fewer interlayer pore structures can be observed, and the denser the composite material structure. This indicates that ethyl cellulose film can effectively prevent the desorption and leakage of liquid phase-change materials during the phase-change process.

XRD—The XRD analysis of expanded graphite, ethyl cellulose and CPCMs is shown in Fig. 7. Because n-tetradecane is amorphous and has no characteristic

Table 2—Characteristic absorption peaks of FTIR spectra of n-tetradecane, expanded graphite, ethyl cellulose, and n-tetradecane/expanded graphite CPCMs

Materials	Peak value of characteristic peak, cm^{-1}
N-tetradecane	3435, 2958, 2925, 2855, 1638, 1463, 1377, 1303, 1082, 1048, 883, 721
Expanded graphite	3691, 3487, 3466, 3418, 3282, 3230, 3066, 1733, 1638, 1559, 1389, 1363, 1145, 908, 848, 752, 696, 625, 528, 477, 461, 444, 431, 417, 3680, 3439, 3308, 2979, 2877, 2809, 2722, 2611, 1980
Ethyl cellulose	1739, 1582, 1486, 1453, 1381, 1314, 1280, 1111, 1055, 917, 879, 813, 706, 667, 580, 523
No. 1	3677, 3279, 2958, 2924, 2854, 1719, 1559, 1467, 1378, 1305, 890, 721
No. 2	3690, 2958, 2924, 2854, 2731, 2673, 1716, 1612, 1467, 1378, 1303, 889, 721
No. 3	3683, 2958, 2924, 2854, 1726, 1564, 1467, 1378, 889, 721, 552, 444

diffraction peak in the XRD pattern, it was not analyzed by XRD. The main characteristic peak of expanded graphite is at 26.57 degrees, with high diffraction peak intensity and a sharp and symmetrical peak shape. This indicates that expanded graphite has a high degree of crystallization and regular arrangement of internal particles. Ethyl cellulose has two main characteristic diffraction peaks, located at 7.87 and 19.98 degrees, respectively. The diffraction peak shape of CPCMs is similar to that of expanded graphite. The characteristic peak diffraction angle areas of the three different membrane solution concentrations of CPCMs are roughly the same, which are composed of the characteristic diffraction peaks of ethyl cellulose and expanded graphite. Although the characteristic peak of n-tetradecane could not be observed, no new characteristic peak appeared in the XRD curve of the CPCM. This shows that n-tetradecane and expanded graphite are simply mixed physically without chemical reaction, and the chemical properties of the CPCMs are stable.

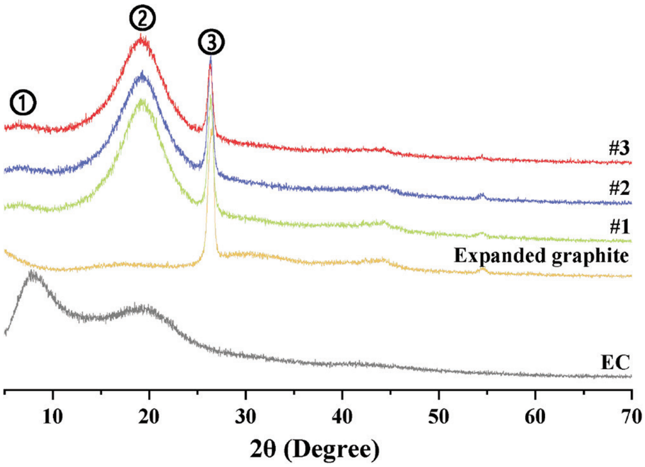

Fig. 7—XRD results of expanded graphite, ethyl cellulose, and n-tetradecane/expanded graphite CPCMs.

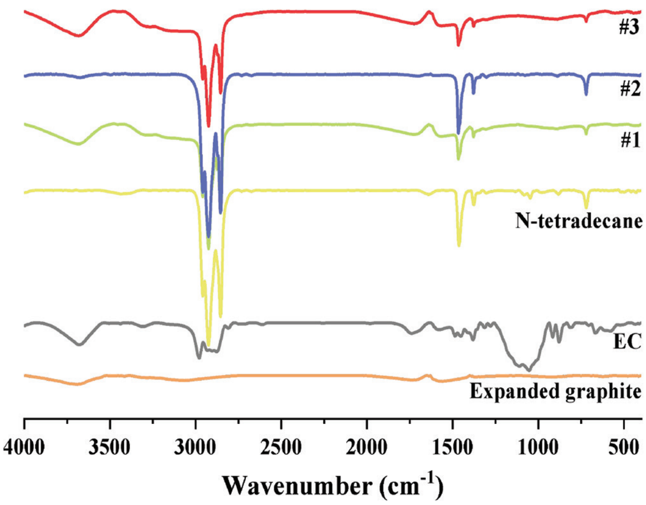

Fig. 8—FTIR results of n-tetradecane, expanded graphite, ethyl cellulose, and n-tetradecane/expanded graphite CPCMs.

FTIR—The FTIR spectra of expanded graphite, n-tetradecane, ethyl cellulose, and CPCMs are shown in Fig. 8. Figure 8 shows the peak value of the characteristic peak of expanded graphite, n-tetradecane, ethyl cellulose, and CPCMs; refer to Table 2 for details. Due to the thin nature of the ethyl cellulose film, its characteristic diffraction peaks are submerged in the characteristic diffraction peaks of the substrate material, so the characteristic peaks of the ethyl cellulose film cannot be observed in Fig. 8. The characteristic peak of n-tetradecane at 721 cm^{-1} is the in-plane rotation vibration absorption peak of methylene, the characteristic peaks at 1463 and 1377 cm^{-1} are the C-H bond absorption peaks of methylene bridge weight, and the characteristic peaks at 2925 and 2855 cm^{-1} are the expansion vibration of n-alkane C-H bond. The infrared spectrum analysis results show that the characteristic peak positions of three different membrane liquid concentrations of n-tetradecane/expanded graphite capsule materials are very close. Compared with the raw material, no new characteristic peaks were found in the infrared spectrum, and the positions of the characteristic peaks were a superposition of the peaks of n-tetradecane and expanded graphite. This indicates that n-tetradecane was successfully impregnated into the interlayer structure of expanded graphite. The prepared CPCM has stable chemical properties, and no new substances are generated in the phase-change composite materials with different membrane concentrations; only physical interactions (capillary and surface tension) exist.

Raman spectra—Figure 9 shows the Raman spectra of raw materials and CPCMs. It can be seen from Fig. 9 that the characteristic peak and peak positions of n-tetradecane, expanded graphite, and CPCMs are shown in Table 3. N-tetradecane belongs to normal alkanes. Its spectral peak at 1302.30 cm^{-1} represents CH_2 torsional vibration, and the peak at 1133.34 cm^{-1} corresponds to C-C antisymmetric vibration. The peak of expanded graphite at 1349.58 cm^{-1} is a D-mode, originating from the vibration of the carbon crystal edge of the graphite, which is caused by defects and reflects the disorder and incompleteness of the graphite; the peak at 1581.95 cm^{-1} correspond to G-mode, which is a

Table 3—Characteristic absorption peaks of Raman spectra of n-tetradecane, expanded graphite, ethyl cellulose, and n-tetradecane/expanded graphite CPCMs

Materials	Peak value of characteristic peak, cm^{-1}
N-tetradecane	1079.89, 1133.34, 1302.30, 1441.02, 2729.09, 2852.66, 2890.02
Expanded graphite	1349.58, 1581.95, 2454.88, 2716.81, 3246.60, 4295.52
Ethyl cellulose	1125.50, 1203.00, 1457.50, 1485.00, 1550.00, 1650.50, 1756.50, 1874.00, 1995.00
No. 1	1582.10, 2445.52, 2719.47, 2853.45, 3247.79, 4292.79
No. 2	1351.67, 1581.35, 2450.20, 2719.06, 3246.79, 4300.72
No. 3	1072.73, 1305.01, 1365.72, 1443.92, 1582.68, 2035.15, 2074.07, 2327.23, 2445.67, 2719.83, 2855.28, 2893.39, 3246.18, 4299.70

typical sp2 structure Raman peak of bulk crystalline graphite and the basic vibration mode of graphite crystal, reflecting the symmetry and crystallinity of graphite; 2454.88 cm^{-1} belongs to the G+A2u combination frequency; 2719.47 cm^{-1} is the second-order mode D* of the D-mode; 32,426.60 cm^{-1} belongs to E2g; and 4295.52 cm^{-1} belongs to the G+D* combination frequency. Ethyl cellulose does not exhibit significant Raman scattering peaks. Compared with normal tetradecane and expanded graphite, the Raman characteristic peak of CPCMs is slower. This is caused by the immersion of n-tetradecane in the interlayer structure of expanded graphite. There is no chemical reaction between n-tetradecane and expanded graphite, and the chemical properties of the phase-change composites are stable. This is mutually confirmed by the XRD and FTIR test results.

DSC—To test the phase-change temperature and latent heat value of CPCMs, a thermal cycle test was carried out, and the results are shown in Fig. 10. During the test, the cycle temperature range was –30 to 30°C, the temperature rise and fall rate was 5°C/min, and the cycle test was conducted three times. It can be seen from Fig. 10 that the initial phase-change temperature of CPCMs was approximately 5.0°C, and the final phase-change temperature was approximately –1.9°C. When the temperature dropped, the n-tetradecane in the CPCM solidified and emitted heat. The peak temperature of phase change was 1.73°C, and the latent heat values were 163.02, 163.24, and 162.59 J/g, respectively. When the temperature rose, the n-tetradecane in the phase-change material was liquefied and endothermic. The peak temperature of phase change was 7.81°C, and the latent heat values were 164.12, 164.04, and 164.10 J/g, respectively. The thermal performance parameters, such as phase-change temperature and latent heat value of the CPCM, after three thermal cycles were basically consistent. The extremely low change rate indicates that the thermal performance of CPCMs is stable. The heat released by a cubic meter of samples with 10% of CPCMs was approximately 28.6 MJ, which is equal to the heat released by the combustion of 1 kg of commercial coal. When the ambient temperature drops to 5°C or lower, under the action of CPCMs, the concrete structure can release heat autonomously, avoiding internal pore water freezing and structural surface covering with ice and snow. This is of great significance for improving the frost resistance of concrete structures and enhancing the durability of concrete engineering.

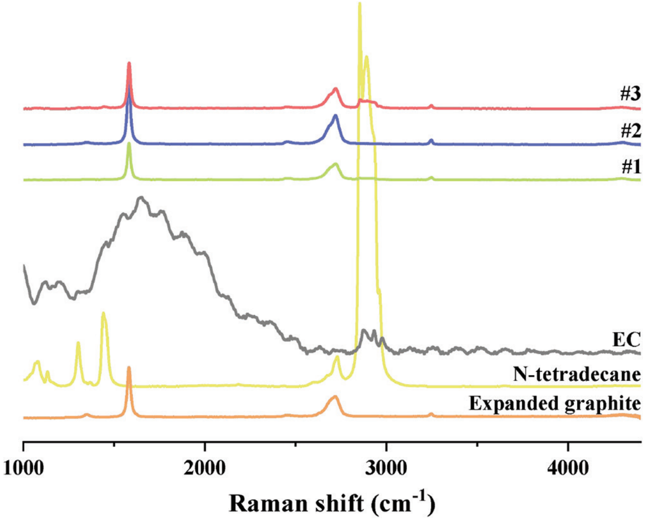

Fig. 9—Raman results of n-tetradecane, expanded graphite, ethyl cellulose, and n-tetradecane/expanded graphite CPCMs.

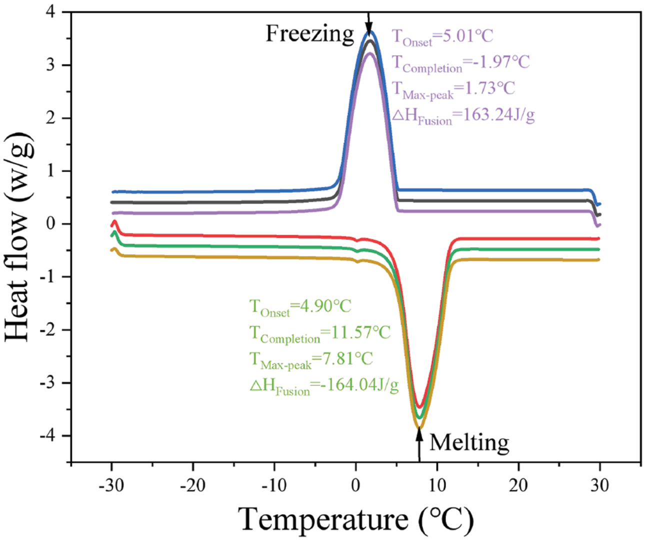

Fig. 10—DSC results of No. 3 n-tetradecane/expanded graphite.

Thermogravimetric—The test results of thermal stability of n-tetradecane, expanded graphite, ethyl cellulose, and CPCMs with 4% solution concentration are shown in Fig. 11. It can be seen from Fig. 11 that the mass of n-tetradecane began to decline at 72.06°C and stabilizes at 152.70°C. The weight loss rate of this process was 98.89%, which is due to the thermal evaporation of n-tetradecane. The weight loss rate of expanded graphite from room temperature to 800°C was only 5.06%, indicating good thermal stability of expanded graphite. Ethyl cellulose began to undergo thermal decomposition within the range of 344.9 to 372.0°C, resulting in a rapid loss of mass and a weight loss rate of 91.81%. The mass loss of CPCMs was 85.84% when it was heated from 82.06 to 206.98°C, corresponding to the

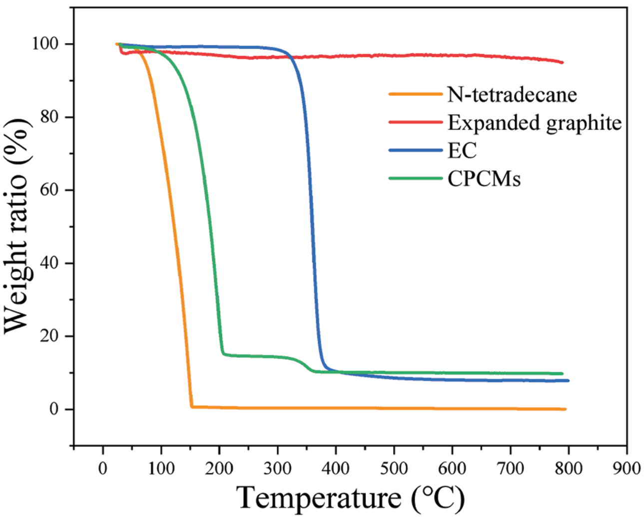

Fig. 11—TG results of n-tetradecane, expanded graphite, ethyl cellulose, and n-tetradecane/expanded graphite CPCMs.

thermal volatilization of n-tetradecane; within the range of 320 to 365°C, a mass loss of 4.4% corresponds to the thermal decomposition of ethyl cellulose. Due to the rich pore structure of expanded graphite, n-tetradecane accounts for a large proportion in the CPCM, so the weight loss rate during the first mass loss is large. The reason for the second mass loss is the high-temperature decomposition of ethyl cellulose, which has a relatively low mass ratio in CPCMs, resulting in a relatively low weight loss rate. The thermogravimetric characteristics of CPCMs are consistent with the thermogravimetric characteristics of the three raw materials. And below 80°C, CPCMs have good thermal stability.

CONCLUSIONS

In this study, n-tetradecane was used as the phase-change core material, and expanded graphite with high thermal conductivity was used as the carrier material. The two were physically matched by negative pressure adsorption, and then the ethyl cellulose film was assembled on its surface to prepare n-tetradecane/expanded graphite core-shell capsule phase-change materials (CPCMs). The physical and chemical properties and application effects of CPCMs are characterized comprehensively and from multiple angles through modern characterization methods. The specific conclusions are as follows:

1. The addition of CPCMs will enhance the thermal conductivity of the cement matrix. When the CPCM content reaches 20%, the thermal conductivity of cement-based materials increases by 24.66%.

2. The addition of CPCMs reduces the initial strength of cement-based materials. When the content increases to 20%, the compressive strength decreases by 68.4% and the flexural strength decreases by 49.1%.

3. CPCMs significantly improve the frost resistance of cement-based materials. The addition of CPCMs reduced the compressive strength loss rate of cement-based materials by 96% and the flexural strength loss rate by 65%. CPCMs are suitable for infrastructure subjected to severe freezing-and-thawing conditions.

4. Based on microscopic analysis, it was found that expanded graphite has a rich interlayer structure and is an ideal container for phase-change materials. The encapsulation effect of ethyl cellulose film is good. The chemical properties of CPCMs are stable. Their thermal cycling stability is good, with a latent heat value of 163 J/g. In addition, CPCMs can withstand high temperatures of 80°C, meeting practical application requirements.

5. Although CPCMs have shown significant advantages in enhancing thermal conductivity and improving the frost resistance of cement-based materials, it is still recommended to conduct further testing under simulated long-term freezing-and-thawing cycle conditions in the real world. This will help evaluate the long-term performance and stability of CPCMs in more complex and dynamic environments.

AUTHOR BIOS

Zhiyong Liu *is a Professor at Southeast University, Nanjing, Jiangsu Province, China, where he received his doctoral degree in 2013. His research interests include the durability of structural concrete.*

Jinyang Jiang *is a Professor at Southeast University, where he received his doctoral degree in 2008. His research interests include civil engineering materials.*

Yang Li *is a Doctoral Student at Southeast University. He received his doctoral degree from Anhui Jianzhu University, Hefei, China, in 2020. His research interests include measures to improve the durability performance of concrete.*

Yuncheng Wang *is a Doctoral Student at Southeast University. He received his master's degree from China University of Mining and Technology, Xuzhou, China, in 2020. His research interests include simulating the durability of concrete.*

Xi Jin *is a Master's Student at Southeast University, where she received her master's degree in 2024. Her research interests include the frost resistance of phase-change materials.*

Zeyu Lu *is a Professor at Southeast University. He received his doctoral degree from the Hong Kong University of Science and Technology, Hong Kong, in 2016. His research interests include the durability of structural concrete.*

ACKNOWLEDGMENTS

The authors gratefully acknowledge the financial support from Distinguished Young Scholars of Jiangsu Province (BK20220071), the National Science Foundation for Distinguished Young Scholars of China (51925903), the National Natural Science Foundation of China (52525901, U21A20150), and the Fundamental Research Funds for the Central Universities (RF1028623199).

REFERENCES

1. Besheli, A. E.; Samimi, K.; Nejad, F. M.; and Darivshan, E., "Improving Concrete Pavement Performance in Relation to Combined Effects of Freeze-Thaw Cycles and De-Icing Salt," *Construction and Building Materials*, V. 277, 2021, p. 122273. doi: 10.1016/j.conbuildmat.2021.122273

2. Kessler, S.; Thiel, C.; Grosse, C. U.; and Gehlen, C., "Effect of Freeze-Thaw Damage on Chloride Ingress Into Concrete," *Materials and Structures*, V. 50, No. 2, 2017, pp. 1-13. doi: 10.1617/s11527-016-0984-4

3. Chatterji, S., "Freezing of Air-Entrained Cement-Based Materials and Specific Actions of Air-Entraining Agents," *Cement and Concrete Composites*, V. 25, No. 7, 2003, pp. 759-765. doi: 10.1016/S0958-9465(02)00099-9

4. Xu, Y.; Yuan, Q.; Dai, X.; and Xiang, G., "Improving the Freeze-Thaw Resistance of Mortar by a Combined use of Superabsorbent Polymer and Air Entraining Agent," *Journal of Building Engineering*, V. 52, 2022, p. 104471. doi: 10.1016/j.jobe.2022.104471

5. Mardani, A., and Emin, A., "Utilization of High-Range Water Reducing Admixture Having Air-Entraining Agents in Cementitious

Systems," *Journal of Building Engineering*, V. 64, 2023. doi: 10.1016/j.jobe.2022.105565

6. Wang, D.; Zhou, X.; Meng, Y.; and Chen, Z., "Durability of Concrete Containing Fly Ash and Silica Fume Against Combined Freezing-Thawing and Sulfate Attack," *Construction and Building Materials*, V. 147, 2017, pp. 398-406. doi: 10.1016/j.conbuildmat.2017.04.172

7. Jin, S.; Zheng, G.; and Yu, J., "A Micro Freeze-Thaw Damage Model of Concrete with Fractal Dimension," *Construction and Building Materials*, V. 257, 2020, p. 119434. doi: 10.1016/j.conbuildmat.2020.119434

8. Chen, B.; Chen, J.; Chen, X.; Qiang, S.; and Zheng, Y., "Experimental Study on Compressive Strength and Frost Resistance of Steam Cured Concrete with Mineral Admixtures," *Construction and Building Materials*, V. 325, 2022, p. 126725. doi: 10.1016/j.conbuildmat.2022.126725

9. Dong, F.; Wang, H.; Yu, J.; Liu, K.; Guo, Z.; Duan, X.; and Qiong, X., "Effect of Freeze-Thaw Cycling on Mechanical Properties of Polyethylene Fiber and Steel Fiber Reinforced Concrete," *Construction and Building Materials*, V. 295, 2021, p. 123427. doi: 10.1016/j.conbuildmat.2021.123427

10. Affan, M., and Ali, M., "Experimental Investigation on Mechanical Properties of Jute Fiber Reinforced Concrete under Freeze-Thaw Conditions for Pavement Applications," *Construction and Building Materials*, V. 323, 2022, p. 126599. doi: 10.1016/j.conbuildmat.2022.126599

11. Meshgin, P., and Xi, Y., "Effect of Phase-Change Materials on Properties of Concrete," *ACI Materials Journal*, V. 109, No. 1, Jan.-Feb. 2012, pp. 71-80.

13. Pan, X.; Shi, Z.; Shi, C.; Ling, T.-C.; and Li, N., "A Review on Surface Treatment for Concrete–Part 2: Performance," *Construction and Building Materials*, V. 133, 2017, pp. 81-90. doi: 10.1016/j.conbuildmat.2016.11.128

14. Song, J.; Zhao, D.; Han, Z.; Xu, W.; Lu, Y.; Liu, X.; Liu, B.; Carmalt, C. J.; Deng, X.; and Parkin, I. P., "Super-Robust Superhydrophobic Concrete," *Journal of Materials Chemistry. A, Materials for Energy and Sustainability*, V. 5, No. 28, 2017, pp. 14542-14550. doi: 10.1039/C7TA03526H

15. Guo, T., and Weng, X., "Evaluation of the Freeze-Thaw Durability of Surface-Treated Airport Pavement Concrete under Adverse Conditions," *Construction and Building Materials*, V. 206, 2019, pp. 519-530. doi: 10.1016/j.conbuildmat.2019.02.085

16. Ling, T. C., and Poon, C. S., "Use of Phase Change Materials for Thermal Energy Storage in Concrete: An Overview," *Construction and Building Materials*, V. 46, 2013, pp. 55-62. doi: 10.1016/j.conbuildmat.2013.04.031

17. Ren, M.; Wen, X.; Gao, X.; and Liu, Y., "Thermal and Mechanical Properties of Ultra-High Performance Concrete Incorporated with Microencapsulated Phase Change Material," *Construction and Building Materials*, V. 273, 2021, p. 121714. doi: 10.1016/j.conbuildmat.2020.121714

18. Liu, Z.; Jiang, J.; Jin, X.; Wang, Y.; and Zhang, Y., "Experimental and Numerical Investigations on the Inhibition of Freeze-Thaw Damage of Cement-Based Materials by a Methyl Laurate/Diatomite Microcapsule Phase Change Material," *Journal of Energy Storage*, V. 68, 2023, p. 107665. doi: 10.1016/j.est.2023.107665

19. Memon, S. A.; Cui, H. Z.; Zhang, H.; and Xing, F., "Utilization of Macro Encapsulated Phase Change Materials for the Development of Thermal Energy Storage and Structural Lightweight Aggregate Concrete," *Applied Energy*, V. 139, 2015, pp. 43-55. doi: 10.1016/j.apenergy.2014.11.022

20. Liu, Z.; Jiang, J.; Liu, C.; Tang, A.; Hu, D.; Qian, R.; Zhang, Y.; and Jin, X., "Microstructure and Thermal Conductivity of Paraffin@Burning Garbage Ash Phase Change Energy Storage Materials Embedded in Hydraulic Cementitious Composites: Experiments and Numerical Simulation," *Journal of Cleaner Production*, V. 369, 2022, p. 133202. doi: 10.1016/j.jclepro.2022.133202

21. Farid, M. M.; Khudhair, A. M.; Razack, S A K.; and Al-Hallaj, S., "A Review on Phase Change Energy Storage: Materials and Applications," *Energy Conversion and Management*, V. 45, No. 9-10, 2004, pp. 1597-1615. doi: 10.1016/j.enconman.2003.09.015

22. Kong, X.; Lu, S.; Li, Y.; Huang, J.; and Liu, S., "Numerical Study on the Thermal Performance of Building Wall and Roof Incorporating Phase Change Material Panel for Passive Cooling Application," *Energy and Building*, V. 81, 2014, pp. 404-415. doi: 10.1016/j.enbuild.2014.06.044

23. Ismail, A.; Wang, J.; Salami, B. A.; Oydele, L. O.; and Otukogbe, G. K., "Microencapsulated Phase Change Materials for Enhanced Thermal Energy Storage Performance in Construction Materials: A Critical Review," *Construction and Building Materials*, V. 401, 2023, p. 132877. doi: 10.1016/j.conbuildmat.2023.132877

12. Pilehvar, S.; Szczotok, A. M.; Rodríguez, J. F.; Valentini, L.; Lanzón, M.; Pamies, R.; and Kjøniksen, A.-L., "Effect of Freeze-Thaw Cycles on the Mechanical Behavior of Geopolymer Concrete and Portland Cement Concrete Containing Micro-Encapsulated Phase Change Materials," *Construction and Building Materials*, V. 200, 2019, pp. 94-103. doi: 10.1016/j.conbuildmat.2018.12.057

24. Rodríguez, C. R.; de Mendonça Filho, F. F.; and Figueiredo, S. C., "Fundamental Investigation on the Frost Resistance of Mortar with Microencapsulated Phase Change Materials," *Cement and Concrete Composites*, V. 113, 2020, p. 103705. doi: 10.1016/j.cemconcomp.2020.103705

25. Bentz, D. P., and Turpin, R., "Potential Applications of Phase Change Materials in Concrete Technology," *Cement and Concrete Composites*, V. 29, No. 7, 2007, pp. 527-532. doi: 10.1016/j.cemconcomp.2007.04.007

26. Mills, A.; Farid, M.; Selman, J. R.; and Al-Hallaj, S., "Thermal Conductivity Enhancement of Phase Change Materials Using a Graphite Matrix," *Applied Thermal Engineering*, V. 26, No. 14-15, 2006, pp. 1652-1661. doi: 10.1016/j.applthermaleng.2005.11.022

27. Wu, H.; Li, D.; Yang, W.; Wang, S.; Wang, W.; Zhu, Z.; Tan, S.; Wu, J.; and Ding, Q., "Construction of New Conductive Networks for Expandable Graphite-Based Cement Composites Via a Facile Heat Treatment Process," *Cement and Concrete Composites*, V. 141, 2023, p. 105142. doi: 10.1016/j.cemconcomp.2023.105142

28. Cai, W.; Yang, W.; Jiang, Z.; He, F.; Zhang, K.; He, R.; Wu, J.; and Fan, J., "Numerical and Experimental Study of Paraffin/Expanded Graphite Phase Change Materials with an Anisotropic Model," *Solar Energy Materials and Solar Cells*, V. 194, 2019, pp. 111-120. doi: 10.1016/j.solmat.2019.02.006

29. Fan, L. W.; Fang, X.; Wang, X.; Zeng, Y.; Xiao, Y.-Q.; Yu, Z.-T.; Xu, X.; Hu, Y.-C.; and Cen, K.-F., "Effects of Various Carbon Nanofillers on the Thermal Conductivity and Energy Storage Properties of Paraffin-Based Nanocomposite Phase Change Materials," *Applied Energy*, V. 110, No. 5, 2013, pp. 163-172. doi: 10.1016/j.apenergy.2013.04.043

aci Foundation

Building the Future

We’re Building the Future

OUR MISSION

We make strategic investments in ideas, research, and people to create the future of the concrete industry.

Through its councils and programs, the ACI Foundation helps to keep the concrete industry at the forefront of advances in material composition, design, and construction.

OUR FOCUS

Identifying technologies and innovations which provide needed solutions for the concrete industry

Seeking concrete research projects that further the knowledge and sustainability of concrete materials, construction, and structures

Supporting our future concrete innovators and leaders by administering fellowships and scholarships

Helping honorably discharged veterans with our Veterans Rebate for ACI Certification program

www.acifoundation.org

ACI MATERIALS JOURNAL TECHNICAL PAPER

Title No. 122-M26

Corrosion Resistance of Continuously Galvanized Reinforcement

by Pooya Vosough Grayli, Matthew O'Reilly, and David Darwin

While many studies have evaluated the corrosion performance of hot-dip galvanized reinforcement (ASTM A767), few have evaluated that of the newer continuously galvanized reinforcement (ASTM A1094). This study compared the corrosion resistance of ASTM A767 and A1094 reinforcement, along with uncoated reinforcement, using the Southern Exposure (SE) and cracked beam (CB) tests. The galvanized reinforcement was tested both with and without damage to the coating, as well as after bending the bars. Both ASTM A767 and A1094 reinforcement exhibited better corrosion resistance than uncoated reinforcement, but corrosion rates on both types of galvanized reinforcement increased when the bars were bent. ASTM A767 and A1094 reinforcement exhibited similar corrosion resistance and can be used interchangeably.

Keywords: ASTM A767; ASTM A1094; continuously galvanized reinforcement; corrosion; hot-dip galvanized reinforcement.

INTRODUCTION

The cost of corrosion has been a large and growing problem in the U.S. highway system for decades. Nearly 20 years ago, the direct annual cost of corrosion damage in bridges was estimated to be $8.3 billion (Koch et al. 2002), a number that has continued to grow. Indirect costs are estimated to be more than 10 times this value (Koch et al. 2002). This cost justifies a significant investment in corrosion control, either by preventing or slowing the penetration of water, oxygen, carbon dioxide, and salt into the concrete or by using reinforcement that is more resistant to corrosion, including galvanized reinforcement.

Galvanized (zinc) coatings can sacrificially protect steel reinforcing bars because zinc is thermodynamically more active than iron. The zinc coating also acts as a barrier to moisture and chlorides. Galvanized coatings are more damage-resistant than epoxy coatings and continue to provide sacrificial protection to the underlying steel even if damaged. To date, however, galvanized reinforcement remains far less commonly used than epoxy-coated reinforcement as a corrosion protection system.

Hot-dip galvanizing, covered under ASTM A767/A767M-19 (2019), is the most common galvanizing method for reinforcing steel. Hot-dip galvanized reinforcement has been widely used for over 50 years (Yeomans 2016). The process involves immersing chromate-treated steel in a bath of molten zinc at a temperature of 824 to 860°F (440 to 460°C), where metallurgical reactions occur between the steel and the zinc. The coating that remains on the steel after it cools has an external bright layer of pure zinc and internal layers of iron-zinc alloys linked to the base steel. These iron-zinc compounds are brittle and may crack when bending.

Studies of the corrosion performance of ASTM A767 reinforcing bars show mixed results. Darwin et al. (2009) found that the average critical chloride corrosion threshold for ASTM A767 reinforcement was approximately 1.6 times the threshold of conventional steel, but that ASTM A767 reinforcement also exhibited a much larger range in performance, with some ASTM A767 specimens behaving similarly to conventional bars. A study by Treadaway and Davies (1989) examined conventional and ASTM A767 reinforcement and found that slabs cast with ASTM A767 reinforcement exhibited significantly more cracking than slabs cast with conventional steel. Other researchers have found that ASTM A767 reinforcement is effective in the presence of carbonation and that it may be used in structures exposed to carbonation or mild contamination with chlorides, such as cladding panels and coastal buildings (Andrade and Macias 1988; Broomfield 2003; Darwin et al. 2009; Bertolini et al. 2014; Poursaee 2016).

An alternate method, known as continuous galvanizing, has recently been introduced and is covered under ASTM A1094/A1094M-20 (2020). Continuous galvanizing is marketed as producing a more flexible coating that allows the bars to be bent after fabrication without damaging the corrosion protection provided to the underlying steel (Yeomans 2018). The coating on ASTM A1094 bars is mostly zinc and does not exhibit the intermetallic iron-zinc layers found on ASTM A767 reinforcement. Limited research on ASTM A1094 coatings is available. A recent study by Ogunsanya and Hansson (2018) found that an early prototype of ASTM A1094 bars, with an uneven coating thickness, exhibited higher corrosion rates than ASTM A767 bars.

RESEARCH SIGNIFICANCE

Studies examining the effectiveness of galvanized reinforcement in preventing corrosion have shown mixed results over the years. Continuous galvanization for reinforcement is a new development that facilitates the production of galvanized bars with a thinner zinc coating, which can decrease production costs. Only a prototype version of continuously galvanized reinforcement has been studied to date. As such, it is of great interest to determine the corrosion resistance

---

ACI Materials Journal, V. 122, No. 4, July 2025.

MS No. M-2024-213.R1, doi: 10.14359/51746808, received November 26, 2024, and reviewed under Institute publication policies. Pertinent discussion including author's closure, if any, will be published ten months from this journal's date if the discussion is received within four months of the paper's print publication.

Table 1—Mixture proportions for lab specimens based on SSD aggregate

Cement, lb/yd^3 (kg/m^3)	Water, lb/yd^3 (kg/m^3)	Coarse aggregate, lb/yd^3 (kg/m^3)	Fine aggregate, lb/yd^3 (kg/m^3)	Air-entraining agent, oz./yd^3 (mL/m^3)
598 (355)	269 (160)	1484 (880)	1435 (851)	8.5 to 9.5 (329 to 367)

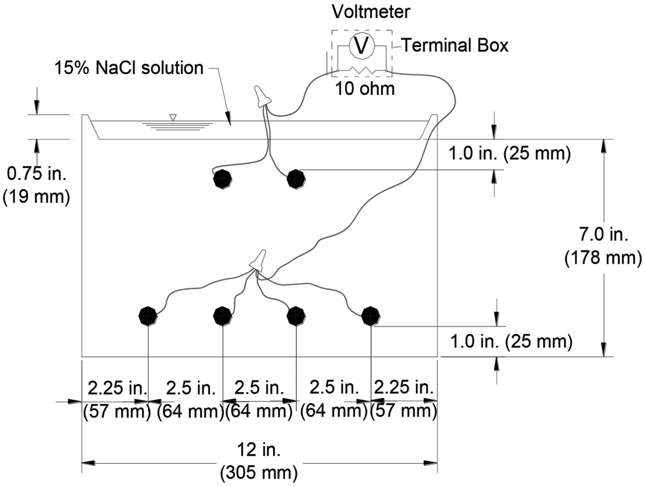

Fig. 1—End view of SE specimen.

of ASTM A1094 reinforcement in relation to ASTM A767 reinforcement.

EXPERIMENTAL WORK

Materials

Tests were performed on No. 5 (5/8 in. [16 mm]) ASTM A767 and A1094 galvanized bars; two heats of ASTM A615/A615M-20 (2020) conventional reinforcement were also evaluated. Identified as Conv-I and II, the conventional bars were used to produce the ASTM A767 and A1094 reinforcing bars, respectively.

Concrete

The concrete mixture proportions used in this study are shown in Table 1 and are representative of mixtures used in bridge decks. The concrete had a 0.45 water-cement ratio (w/c) and a target air content of 6 ± 1%.

The materials used in the concrete mixtures were Type I/II portland cement; municipal water from Lawrence, KS; fine aggregate (Kansas River sand) with a bulk specific gravity (SSD) = 2.62, absorption (dry) = 0.8%, and fineness modulus = 2.51; coarse aggregate (crushed limestone) with nominal maximum size = 0.75 in. (19 mm), SSD = 2.58, absorption = 2.3%, and unit weight = 95.9 lb/ft^3 (1534 kg/m^3); and saponified rosin-based air-entraining agent.

Test methods

Southern Exposure (SE) and cracked beam (CB) tests were used to evaluate the corrosion of reinforcing steel in uncracked and cracked concrete, respectively. The specimens were subjected to alternative cycles of wetting (exposure to a 15% by weight salt solution: 6.04 molal ion) and drying. The SE specimens (Fig. 1) consisted of 12 x 12 x 7 in. (305 x 305 x 178 mm) blocks. Twelve in. (305 mm) long No. 5 (5/8 in. [16 mm]) reinforcing bars were cast in the specimen in two mats. The top and bottom mats consisted of two and four bars, respectively, each with 1 in. (25 mm) clear cover to the horizontal surfaces. The bars in the top and bottom mats were electrically connected through a terminal box across a 10 Ω resistor to allow for macrocell corrosion rate measurements, where the term macrocell describes corrosion that results from current flow between two widely separated bars. A 0.75 in. (19 mm) deep concrete dam was integrally cast with the specimen to contain a ponded salt solution. A modified SE specimen was also used to allow for bent bars to be tested (Fig. 2). Bending a bar generally does not affect the performance of an uncoated bar (O'Reilly et al. 2011), but it can cause damage to the coating on a coated bar if the coating is brittle.

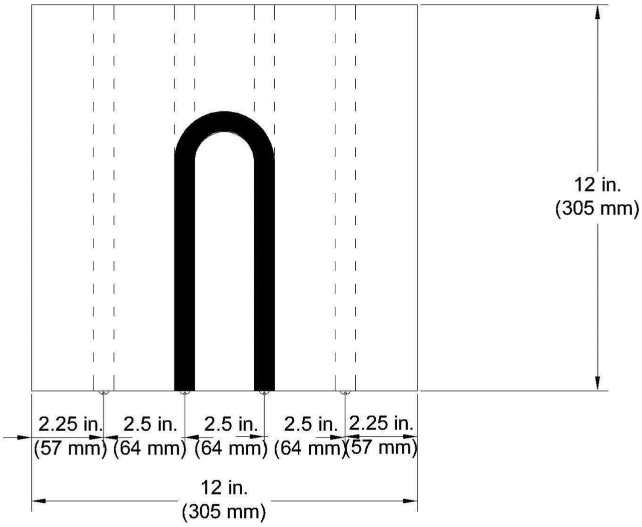

Fig. 2—Top view of SE specimen with bent anode bar.

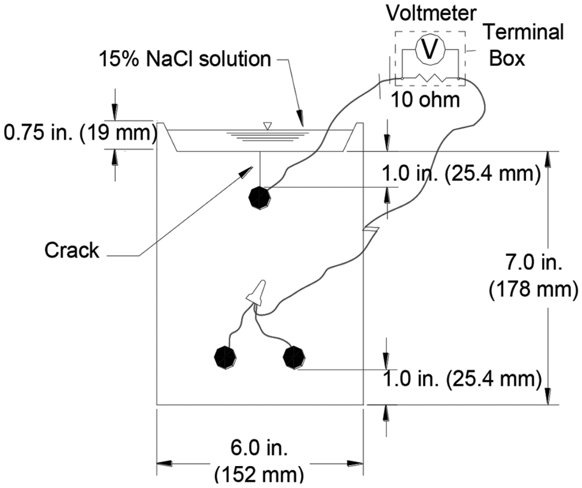

Fig. 3—End view of CB specimen.

The CB specimens (Fig. 3) were half the width of the SE specimens, measuring 12 x 6 x 7 in. (305 x 152 x 178 mm). The top mat consisted of a single No. 5 (5/8 in. [16 mm]) bar; the bottom mat consisted of two No. 5 bars. Before fabrication, a 12 mil (0.3 mm) thick by 6 in. (152 mm) long stainless steel shim was placed in the mold in direct contact with the top reinforcing bar. The shim was removed 12 to 24 hours after casting. This resulted in the direct infiltration of chlorides at the beginning of the test.

The SE and CB tests lasted 96 weeks. Galvanized bars were evaluated both with the zinc intact and penetrated by ten 1/8 in. (3 mm) diameter holes to simulate defects or damage; undamaged bars were also evaluated after being bent using SE specimens.

Fabrication

Specimen fabrication for the SE and CB specimens consisted of the following steps:

1. Reinforcing bars were cut to 12 in. (305 mm) with a band saw. Bars that were to be bent were cut to a length of 15 in. (381 mm).
2. Both ends of each bar were drilled and tapped to a 3/8 in. (10 mm) depth with 10-24 threading.
3. For reinforcing bars with intentional damage, the coating was penetrated with a 0.125 in. (3 mm) diameter four-flute drill bit using a milling machine. Five holes were placed on each side of the bar, approximately 2 in. (50 mm) apart. The coating was not penetrated on bent bars.
4. Bars were soaked in acetone for a minimum of 2 hours and cleaned to remove any oil.
5. The forms were assembled, and the reinforcement was attached. Reinforcing bars with penetrations in the coating were aligned so that the holes faced the top and bottom of the specimen. Forms and reinforcement were held in place using 10-24 threaded stainless steel machine screws.
6. Specimens were cast in an inverted position in two layers, with each layer consolidated using a 0.75 in. (19 mm) diameter vibrator. The free surface of the concrete (the bottom of the specimen, as they were cast upside down) was finished with a trowel. This procedure allowed for a level and consistent top surface of the specimen.
7. Specimens were cured for 24 hours at room temperature. A plastic cover was used to minimize evaporation. The stainless steel shims were removed from the CB specimens after 12 to 24 hours, when the concrete had set.
8. Formwork was removed after 24 hours.
9. Specimens were cured for an additional 2 days in a plastic bag containing deionized water, then air-cured for 25 days.
10. Before test initiation, wire leads were connected to the test bars using 10-24 x 3/8 in. (10 mm) stainless steel screws. A waterproofing epoxy coating was applied to the vertical sides of the specimens and the top surface of the dams, while the top and bottom surfaces of the specimens were left uncoated.
11. The two mats of steel were connected to the terminal box. Specimens were left connected across the 10 Ω resistor, except when corrosion potential readings were taken. Specimens were placed on 1.5 x 1.5 in. (38 x 38 mm) studs to allow airflow under the specimens. Tests began 28 days after casting.

Test procedure

The SE and CB tests were subjected to alternate cycles of ponding and drying. The test began with 12 weeks of ponding and drying, followed by 12 weeks of ponding, for a total of 24 weeks. This exposure regime was then repeated for the duration of the test. The tests concluded after 96 weeks. The procedures are described as follows.

Ponding and drying cycles—A 15% NaCl solution was ponded on the surface of the specimens. The temperature was maintained at 72 ± 3°F (22 ± 2°C). The SE specimens received 600 mL of the solution; the CB specimens received 300 mL. The specimens were covered with plastic sheeting during ponding to minimize evaporation. Readings were taken on day 4. After the readings were completed, the specimens were vacuumed to remove the salt solution, and a heating tent was placed over the specimens. The tent maintained the specimens at 100 ± 3°F (38 ± 2°C) for 3 days. The tent was then removed, and the specimens were again ponded with the NaCl solution to start the second week of testing. Ponding and drying cycles continued for 12 weeks.

Ponding cycle—After 12 weeks of ponding and drying, specimens were ponded for 12 weeks with the 15% NaCl solution and covered with plastic sheeting. The NaCl solution remained on the specimens throughout the 12 weeks. Readings continued to be taken every week. Deionized water was added to maintain the desired solution depth on the specimens during this time. After 12 weeks, the specimens were again subjected to the weekly ponding and drying cycles.

Corrosion rate and corrosion potential measurements were taken weekly. The current density on the anode was recorded and used to calculate the corrosion rate using Faraday's equation as follows

$$\text{Rate} = K\frac{Vm}{nFDRA} \tag{1}$$

where the rate is given in μm/yr; K is the conversion factor = 31.5×10^4 amp·μm·s/μA·cm·yr; V is the measured voltage drop across the resistor, millivolts; m is the atomic weight of the metal (for iron, $m = 55.8$ g/mol; for zinc, $m = 65.4$ g/mol); n is the number of ion equivalents exchanged (for iron and zinc, $n = 2$ equivalents); F is Faraday's constant = 96,485 coulombs (C)/equivalent; D is the density of the metal, g/cm^3 (for iron, $D = 7.87$ g/cm^3; for zinc, $D = 7.14$ g/cm^3); R is the resistance of the resistor, ohms (= 10 Ω for the test); and A is the surface area of the anode exposed to solution.

$$\text{For iron, Rate} = 11.6i \tag{2}$$

$$\text{For zinc, Rate} = 15.0i \tag{3}$$

In some cases, the corrosion rate may appear to be negative. This negative corrosion rate does not indicate negative corrosion; rather, it is caused at low corrosion rates by minor differences in the oxidation rate between the anode and cathode bars.

Following the measurement of the voltage drop, the electrical connection was interrupted to measure corrosion potentials. Linear polarization resistance (LPR) measurements were taken every 4 weeks. LPR is used to calculate the total corrosion loss, including localized corrosion, by measuring a metal's response to an applied voltage. Localized corrosion loss is not captured in the macrocell corrosion rate from the voltage drop readings through wire leads alone.

The specimens remained disconnected for a minimum of 2 hours before measuring corrosion potentials and taking the LPR readings. Potentials were measured with respect to a silver-silver chloride electrode and converted to an equivalent copper-copper sulfate electrode (CSE) value for presentation. All specimens were autopsied and photographed upon completion of the test.

Test program

The test program in this study consists of 48 SE and 33 CB specimens, as shown in Table 2. Six specimens were cast for each type of bar and surface preparation (undamaged, damaged, and bent), with the exception of Conv-II, for which only three CB specimens were cast due to the limited availability of that heat of steel. Conventional reinforcement was not tested in the bent condition.

RESULTS

Corrosion rates

Figures 4 and 5 show the average macrocell corrosion rates based on the total area of the top mat of reinforcement in contact with concrete for ASTM A767 and A1094 galvanized reinforcement, as well as the conventional reinforcement used to produce them, in the SE and CB tests, respectively.

In the SE test (Fig. 4), no difference in behavior was noted between damaged and undamaged galvanized specimens. ASTM A767 (A767, A767-ND, A767-Bent) reinforcement exhibited some corrosion activity at the beginning of the test, with average corrosion rates in the range of 1 to 2.5 μm/yr. The corrosion rates of damaged ASTM A767, peaking just below 2.5 μm/yr, were near zero during most of the testing period. Undamaged ASTM A767 exhibited corrosion rates similar to those of damaged ASTM A767 during the first 30 weeks. The corrosion rates of A767-Bent increased to 4 μm/yr by week 12 and remained between 2.5 and 4 μm/yr for approximately 12 weeks before dropping. By week 30, the average corrosion rates of all ASTM A767 galvanized specimens dropped to near zero or became negative, which was likely due to corrosion activity on both the bottom and top bars (the zinc coating on the bars can corrode in the high alkalinity of concrete regardless of exposure to chlorides). Undamaged and bent ASTM A767 reinforcement began exhibiting positive corrosion rates again around week 54, fluctuating and peaking at 4 μm/yr.

ASTM A1094 (A1094, A1094-ND, A1094-Bent) reinforcement exhibited some corrosion activity at the beginning of the test, with average corrosion rates in the range of zero to 2.5 μm/yr. Like ASTM A767 reinforcement, by week 30, the average corrosion rates of ASTM A1094 galvanized specimens dropped to near zero or became negative. The corrosion rates of ASTM A1094 reinforcement returned to near zero by week 48. Afterward, the corrosion rates remained lower than 1 μm/yr and near zero, except for another drop to negative rates at approximately week 70.

The corrosion rates for all galvanized bars after week 20 were much lower than those of conventional reinforcement.

Table 2—Test program

Reinforcement	Test program	
	SE	CB
A767	6	6
A767-ND	6	6
A767-Bent	6	—
A1094	6	6
A1094-ND	6	6
A1094-Bent	6	—
Conv-I	6	6[*]
Conv-II	6	3

[*] Four specimens were terminated before 96 weeks due to excessive cracking from corrosion.

Note: ND is not damaged.

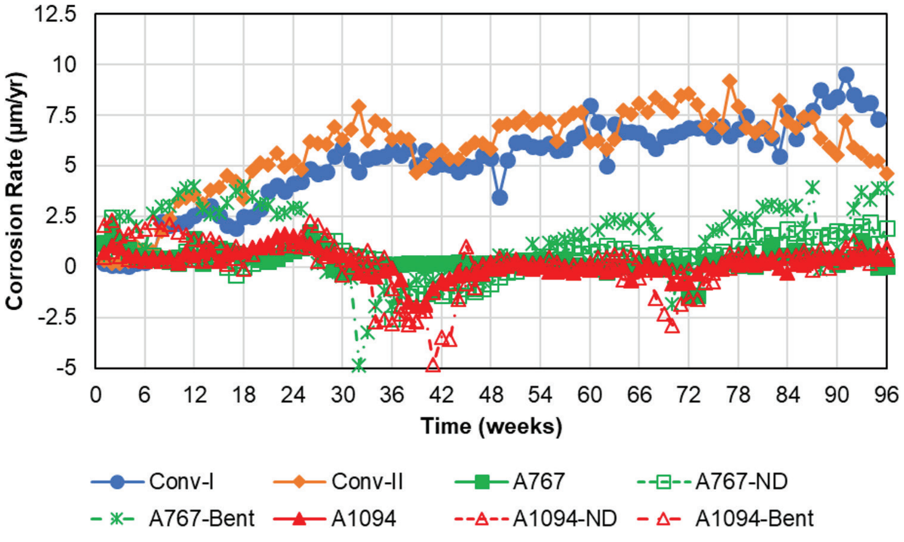

Fig. 4—SE test: average macrocell corrosion rate versus time. Corrosion rate based on total bar area of conventional, ASTM A767, and ASTM A1094 reinforcement.

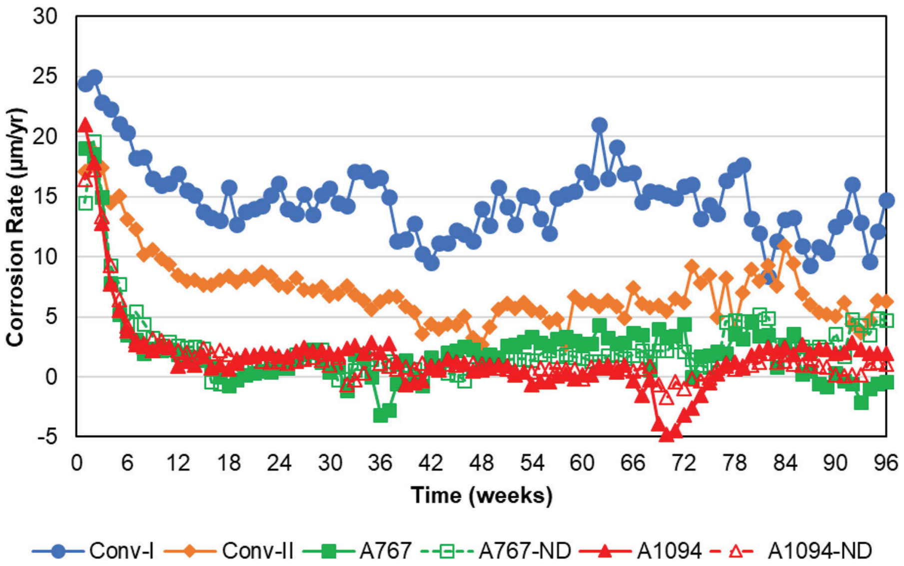

Fig. 5—CB test: average macrocell corrosion rate versus time. Corrosion rate based on total bar area of conventional, ASTM A767, and ASTM A1094 reinforcement.

The corrosion rate of specimens with Conv-I increased gradually throughout the test from approximately zero to approximately 9.5 μm/yr. The corrosion rate of specimens with Conv-II increased gradually throughout the test from approximately zero to approximately 9 μm/yr by week 91 and, afterward, decreased to approximately 7.5 μm/yr at the end of the test.

In the CB test (Fig. 5), all specimens exhibited very high corrosion rates, between 15 and 25 μm/yr, during the first few weeks of testing. The corrosion rates for the galvanized bars dropped rapidly to values less than 4 μm/yr by week 10 and gradually decreased to 1 to 2 μm/yr by week 18. The corrosion rates for damaged and undamaged ASTM A767 began to increase after week 18, reaching 5 μm/yr, with the corrosion rates of damaged ASTM A767 gradually decreasing to zero during the last 24 weeks of testing. Average corrosion rates for ASTM A1094 reinforcement increased after a drop to negative rates at week 70 but remained lower than 3 μm/yr.

The CB test directly exposes the top reinforcement to chlorides from the beginning of testing, initiating corrosion sooner than SE testing. CB specimens with uncoated and coated reinforcement showed a drop in the macrocell corrosion rates after a few weeks, as the accumulation of corrosion products in the crack inhibited the ingress of water and oxygen and slowed the corrosion process. The reduction in the corrosion rate may also be attributed to the corrosion activity in the bottom bars, bars designated as the cathode. As previously mentioned, the zinc coating can exhibit corrosion when exposed to the high alkalinity of concrete, even without exposure to chlorides.

The corrosion rates for galvanized bars were one-third to one-fourth that of conventional reinforcement, except at the beginning of the test. Conv-I and Conv-II had corrosion rates of approximately 25 and 20 μm/yr, respectively, at the beginning of the test; these corrosion rates decreased to approximately 15 and 5 μm/yr at the end of the test. It should be noted, however, that Conv-I reinforcement was used to produce the ASTM A767 reinforcement, and Conv-II reinforcement was used to produce the ASTM A1094 reinforcement. Therefore, the differences in the behavior between the two types of galvanized reinforcement may not be solely due to differences in the coating; differences in the corrosion performance of the conventional core may have affected the results, particularly for the damaged bars where the underlying steel was exposed.

Figures 6 and 7 show the average corrosion potentials versus CSE for ASTM A767 and A1094 reinforcement, as well as the conventional reinforcement used to produce them in the SE and CB tests, respectively. At the beginning of the SE test (Fig. 6), damaged, bent, and undamaged ASTM A767 had an average potential of approximately –0.50 V. The potentials for damaged ASTM A767 gradually became more positive over the first 12 weeks, reaching –0.40 V, before fluctuating until week 30. After week 30, the corrosion potentials of damaged ASTM A767 remained between –0.30 and –0.40 V until week 72, with some fluctuations. After week 72, they dropped to approximately –0.50 V, except for some spikes. The corrosion potentials of undamaged ASTM A767 exhibited similar behavior over most of the test.

At the beginning of the test, damaged, undamaged, and bent ASTM A1094 had an average potential close to –0.70 V; the corrosion potential of these bars gradually became more positive and reached –0.50 V at week 30. Afterward, the corrosion potentials of ASTM A1094 remained at approximately –0.50 V, with spikes to approximately –0.40 V.

Conv-I and Conv-II had corrosion potentials near –0.20V at the beginning of the test, which was more positive than those of the galvanized reinforcement. The corrosion potentials of Conv-I and Conv-II gradually became more negative during the test, reaching approximately –0.60 V, which was more negative than those of the galvanized reinforcement.

At the beginning of the CB test (Fig. 7), the damaged and undamaged ASTM A767 had an average potential of approximately –0.80 V, while the damaged and undamaged ASTM A1094 had an average potential of approximately –1.0 V. Over the first 18 weeks of the test, the potentials of

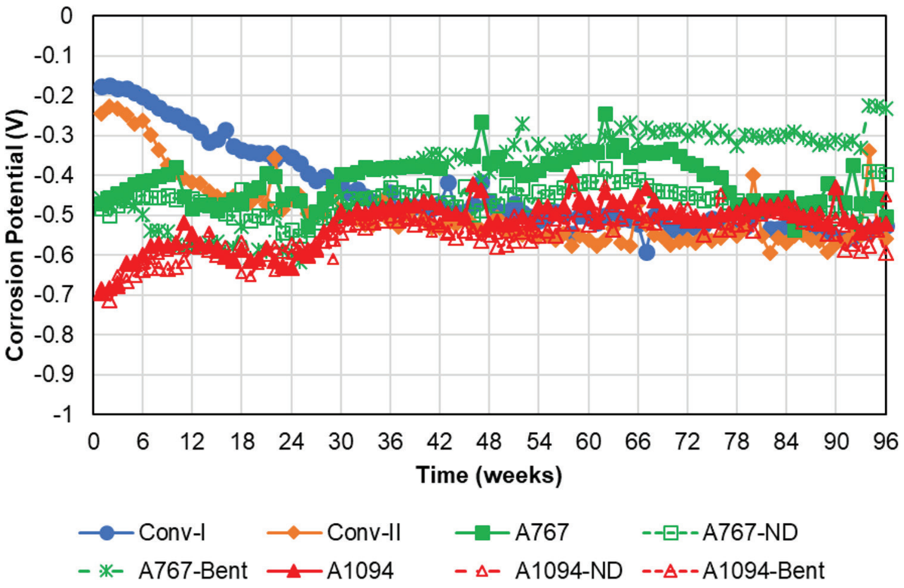

Fig. 6—SE test: average corrosion potentials (versus CSE) of conventional, ASTM A767, and ASTM A1094 reinforcement versus time.

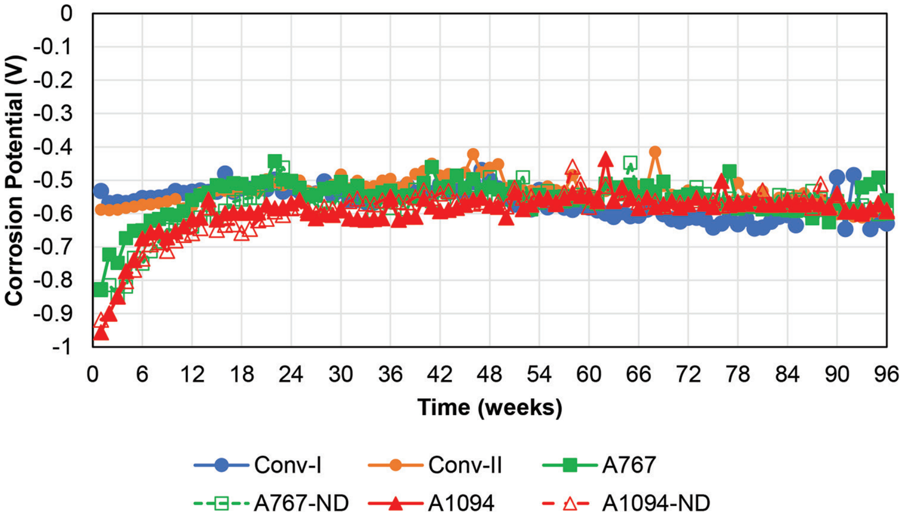

Fig. 7—CB test: average corrosion potentials (versus CSE) of conventional, ASTM A767, and ASTM A1094 reinforcement versus time.

the ASTM A767 and A1094 steel gradually became more positive, reaching values between –0.50 and –0.60 V, and then remained approximately constant for the remainder of the test.

During the first half of testing, Conv-I exhibited corrosion potentials between –0.50 and –0.60 V, dropping to values between –0.60 and –0.70 V in the second half. At the beginning of testing, Conv-II showed corrosion potentials near –0.60 V, which gradually reached near –0.40 V in the first half before tapering off to near –0.60 V again by week 96. Conv-I and Conv-II showed occasional spikes in corrosion potentials.

Corrosion loss

Table 3 shows the macrocell corrosion losses (based on voltage drop) for specimens in the SE test. Corrosion losses were obtained by integrating the weekly corrosion rate measurements over time. To determine the statistical significance of the differences in corrosion losses between corrosion protection systems, a two-tailed Student's *t*-test (Student 1908) was used, assuming equal variances. Student's *t*-test is a method of statistical analysis that compares the means and variances of two data sets to determine the probability, *p*, that any differences between the two data sets could have arisen by chance; that is, differences in the mean values are due to the natural variability of the test program, not differences in the effectiveness of the corrosion protection systems. In this study, a value of 0.20 was used as the threshold for statistical significance.

In the SE test, Conv-I and II exhibited similar average losses at 96 weeks: 10.55 and 10.62 μm, respectively; this difference is not statistically significant ($p = 0.98$). Among the specimens with galvanized reinforcement, a wide variation in losses was observed. As previously described, the corrosion activity of both the top and bottom mats of reinforcement resulted in significant fluctuations in macrocell

Table 3—SE test: macrocell corrosion loss based on total area at end of testing

Reinforcement	Corrosion loss, μm: total area						Average loss	Standard deviation
	1	2	3	4	5	6		
Conv-I	10.50	17.84	5.44	12.53	13.73	3.28	10.55	5.40
Conv-II	9.90	10.10	13.52	10.14	12.20	7.88	10.62	1.97
A767	–0.11	–0.46	1.31	0.60	–0.01	0.89	0.37	0.67
A767-ND	2.11	0.40	1.27	–0.60	1.12	1.55	0.98	0.95
A767-Bent	1.90	–0.76	–0.08	4.01	3.68	6.56	2.55	2.75
A1094	–0.57	0.31	0.32	–0.76	–0.23	1.02	0.02	0.66
A1094-ND	0.50	–1.83	0.84	0.27	0.84	1.13	0.29	1.08
A1094-Bent	2.21	–4.78	–1.41	2.28	1.42	1.88	0.27	2.83

Table 4—CB test: macrocell corrosion loss based on total area at end of testing

Reinforcement	Corrosion loss, μm: total area						Average loss	Standard deviation
	1	2	3	4	5	6		
Conv-I	9.69	27.43	*	*	*	*	18.56	12.55
Conv-II	9.21	15.20	14.36	—	—	—	12.93	3.24
A767	0.64	4.21	2.71	–1.18	9.35	8.18	3.99	4.15
A767-ND	1.32	8.81	2.20	6.98	6.51	2.29	4.69	3.13
A1094	3.60	6.12	3.10	–2.65	3.71	4.04	2.99	2.95
A1094-ND	2.78	4.59	2.36	1.99	2.02	4.00	2.96	1.09

*Terminated before 96 weeks due to excessive cracking from corrosion.

Note: — means no specimen.

corrosion rates. Specimens with bent ASTM A767 bars exhibited losses an order of magnitude greater than the other A767 specimens and all ASTM A1094 specimens, with a difference that is statistically significant ($p < 0.20$), except between A767-Bent and A767-ND ($p = 0.21$).

Table 4 shows the macrocell corrosion losses (based on voltage drop) for specimens in the CB test. In the CB test, four specimens with Conv-I reinforcement cracked due to excessive corrosion losses, preventing the test from continuing (Fig. 8); these specimens were removed from testing at weeks 49, 67, 77, and 83. Results from these specimens are not included in the average corrosion loss for Conv-I in Table 4. Conv-II exhibited lower average losses (12.9 μm) than Conv-I at 96 weeks (18.6 μm), though this difference is not statistically significant ($p = 0.48$). Among individual specimens with galvanized reinforcement, a wide variation of losses was observed, as occurred for the SE specimens. The ASTM A767 specimens exhibited slightly greater losses than the ASTM A1094 specimens, although these differences are not statistically significant ($p \geq 0.23$).

Table 5 shows the total corrosion losses (based on LPR) for specimens in the SE test. As mentioned, LPR determines the total corrosion rate of a metal, including localized corrosion activity that would be missed through corrosion rate measurements based on the voltage drop across the 10 Ω resistor. The trends are similar to those observed for these specimens for the macrocell corrosion losses based on voltage drop, although, as expected, the total losses are higher than the macrocell losses. Conv-II exhibited greater total losses (16.16 μm) than Conv-I (15.57 μm), although this difference is not statistically significant ($p = 0.87$). Among galvanized specimens, there was generally no statistically significant difference between the ASTM A767 and A1094 specimens when comparing specimens of the same type ($p \geq 0.56$). For both types of galvanized bar, however, bent bars did exhibit higher total losses than straight bars, with statistically significant differences ($p \leq 0.15$). These observations suggest potential issues with damage to the coating during bending and the need to patch or repair any damage that may occur.

Table 6 shows the total corrosion losses (based on LPR) for specimens in the CB test. As was the case for the SE specimens, trends generally match those observed for the macrocell corrosion losses, with total losses being higher than macrocell losses. For conventional reinforcement, Conv-I had the highest losses (41.99 μm), with Conv-II exhibiting total losses of 27.42 μm; the difference in losses between Conv-I and Conv-II was found to be statistically significant ($p = 0.15$). Among galvanized specimens, there was no statistically significant difference between ASTM A767 and A1094 specimens of the same type ($p > 0.53$), with losses for all types of galvanized bars equal to approximately 20 μm.

Autopsy results

Figure 9 shows the bars from SE specimen A767-3 after 96 weeks of testing and is representative of the ASTM A767 reinforcement in the SE test. The top mat of steel exhibited moderate amounts of corrosion (heavy in places), with both zinc corrosion products (white) and steel corrosion products

Table 5—SE test: LPR corrosion loss based on total area at end of testing

Reinforcement	Corrosion loss, μm: total area						Average loss	Standard deviation
	1	2	3	4	5	6		
Conv-I	11.84	17.76	11.69	15.79	20.79	16.78	15.57	3.91
Conv-II	18.54	15.79	19.63	16.34	19.12	7.55	16.16	4.49
A767	19.69	4.11	8.70	5.68	2.72	13.45	9.06	6.46
A767-ND	5.41	5.08	5.84	2.50	10.34	8.02	6.20	2.69
A767-Bent	16.34	9.19	4.66	16.12	30.06	19.96	16.05	8.81
A1094	15.40	6.13	5.17	3.11	2.72	14.19	7.79	5.59
A1094-ND	6.45	7.44	3.43	2.01	17.46	7.17	7.33	5.42
A1094-Bent	18.34	4.13	5.50	15.51	19.02	17.52	13.34	6.72

Table 6—CB test: LPR corrosion loss based on total area at end of testing

Reinforcement	Corrosion loss, μm: total area						Average loss	Standard deviation
	1	2	3	4	5	6		
Conv-I	39.90	44.08	*	*	*	*	41.99	2.95
Conv-II	22.55	38.94	20.79	—	—	—	27.42	10.01
A767	15.23	23.40	28.27	8.74	18.17	33.95	21.29	9.14
A767-ND	19.84	21.40	6.28	21.80	27.40	24.20	20.15	7.29
A1094	14.22	33.50	12.72	13.01	19.10	26.88	19.91	8.55
A1094-ND	17.61	19.50	14.34	12.64	25.03	18.32	17.91	4.34

*Terminated before 96 weeks due to excessive cracking from corrosion.

Note: — means no specimen.

Fig. 8—CB test: cracking of concrete in specimen Conv-I-3.

(orange-brown) visible. Corrosion was uneven, with the coating intact in several places but the underlying intermetallic layers visible in others. On several ASTM A767 specimens, corrosion was also present on the bottom bars (Fig. 10), explaining the "negative" corrosion loss observed on some ASTM A767 specimens.

Fig. 9—SE test: specimen A767-3 after 96 weeks of testing. Top mat (top) and bottom mat (bottom).

Figure 11 shows the bars from CB specimen A767-3 after 96 weeks of testing and is representative of the ASTM A767 reinforcement in the CB test. As observed for the SE specimens, the top mat of steel exhibited moderate amounts of corrosion (heavy in places), with both zinc corrosion products (white) and steel corrosion products (orange-brown) visible. Fewer white zinc corrosion products were visible on the bottom bars, with isolated areas of steel corrosion products visible.

Figure 12 shows the bars from SE specimen A1094-4 after 96 weeks of testing and is representative of the ASTM A1094 reinforcement in the SE test. The top mat of steel exhibited moderate to heavy corrosion, with both zinc corrosion products (white) and steel corrosion products (orange-brown) visible. As for the ASTM A767 specimens, corrosion was uneven, with undisturbed zinc adjacent to exposed underlying intermetallic layers. As observed on the ASTM A767 specimens, corrosion was also present on the bottom mat on some specimens, explaining the "negative" corrosion losses observed on these specimens.

Figure 13 shows the bars from CB specimen A1094-6 after 96 weeks of testing and is representative of the ASTM

Fig. 10—SE test: specimen A767-2 after 96 weeks of testing. Top mat (top) and bottom mat (bottom).

Fig. 11—CB test: specimen A767-3 after 96 weeks of testing. Top mat (top) and bottom mat (bottom).

Fig. 12—SE test: specimen A1094-4 after 96 weeks of testing. Top mat (top) and bottom mat (bottom).

Fig. 13—CB test: specimen A1094-6 after 96 weeks of testing. Top mat (top) and bottom mat (bottom).

Fig. 14—SE test: specimen A767-b-2 after 96 weeks of testing. Top mat (top) and bottom mat (bottom).

Fig. 15—SE test: specimen A1094-b-2 after 96 weeks of testing. Top mat (top) and bottom mat (bottom).

A1094 reinforcement in the CB test. The top mat of steel exhibited moderate amounts of corrosion, with both zinc corrosion products (white) and steel corrosion products (orange-brown) visible. Again, limited amounts of zinc corrosion products were observed on the bottom mat.

Figures 14 and 15 show bent ASTM A767 and A1094 bars, respectively, representative of all bent ASTM A767 and A1094 reinforcing bars in the SE test. For both types of bar, corrosion products were observed on the top of the bar, both at and away from the bend. As discussed, based on total corrosion losses, the presence of the bend resulted in a statistically significant increase in corrosion compared to straight bars.

Figure 16 shows the bars from the SE specimen Conv-II-1 after 96 weeks of testing and is representative of all conventional reinforcement in the SE test. As shown in the photo, moderate amounts of corrosion were visible on both bars from the top mat of steel, although corrosion did not cover the entirety of both bars. This corrosion was frequent enough to cause staining on the surface of the specimen (Fig. 17). No corrosion products were visible on the bars from the bottom mat of steel.

Figure 18 shows the bars from CB specimen Conv-I-1 after 96 weeks of testing and is representative of all conventional reinforcement in the CB test. Heavy corrosion was visible on the top mat of steel, with some pitting and deeper localized corrosion occurring, particularly in the region directly under the 6 in. (152 mm) simulated crack. As was the case with SE specimens, most CB specimens with conventional reinforcement exhibited staining on the surface (Fig. 19); this was not

Fig. 16—SE test: specimen Conv-II-1 after 96 weeks of testing. Top mat (top) and bottom mat (bottom).

Fig. 17—SE test: surface staining on specimen with conventional reinforcement.

the case for specimens with galvanized reinforcement. Some corrosion products were visible on the bars from the bottom mat of steel.

DISCUSSION

Generally, the differences between similar types of galvanized specimens with ASTM A767 and A1094 reinforcement were not found to be statistically significant. The CB and SE tests demonstrated that both ASTM A767 and A1094 reinforcement exhibited macrocell corrosion losses of at least an order of magnitude less than conventional reinforcement, with a difference that is statistically significant when comparing the corrosion losses of ASTM A767 and A1094 specimens with those of specimens with conventional reinforcement ($p < 0.05$). Also, with the exception of the specimens with bent bars, the ASTM A767 and A1094 specimens had approximately one-half the total corrosion losses of the specimens with conventional reinforcement based on the LPR measurements. Lower corrosion losses based on macrocell corrosion rates are expected as the zinc coating on bars designated as the cathode may exhibit corrosion in the high alkalinity of concrete even without exposure to chlorides; this would decrease the current between the top (anode exposed to chlorides) and bottom (cathode) mats, decreasing the macrocell corrosion rates and losses.

Fig. 18—CB test: specimen Conv-I-1 after 96 weeks of testing. Top mat (top) and bottom mat (bottom).

Fig. 19—CB test: surface staining on specimen with conventional reinforcement.

CONCLUSIONS AND RECOMMENDATIONS

The following conclusions and recommendations are based on the results and analyses presented in this paper:

1. Corrosion losses in ASTM A767 and A1094 reinforcement were generally less than those of conventional reinforcement, both with and without damage to the coating; however, corrosion losses increased when the bars were bent.
2. ASTM A767 and A1094 reinforcement exhibit similar corrosion resistance and can be used interchangeably.
3. If bends are shown to consistently reduce the corrosion performance of either ASTM A767 or A1094 bars, additional research is needed on the effect of bends on the corrosion performance of both types of galvanized reinforcement and methods of repair.

AUTHOR BIOS

Pooya Vosough Grayli *is a Civil Engineer at Burns & McDonnell. He received his BS from Ferdowsi University of Mashhad, Mashhad, Iran; his MS from Sharif University of Technology, Tehran, Iran; and his PhD from The University of Kansas, Lawrence, KS, all in civil engineering.*

ACI member **Matthew O'Reilly** *is the L. William and Margaret B. Zahner Chair's Council Associate Professor of Civil, Environmental, and Architectural Engineering at The University of Kansas. He received his BS in mechanical engineering from the University of Rochester, Rochester, NY, and his MS and PhD in civil engineering from The University of Kansas. He is a member of ACI Committees S802, Teaching Methods and Educational Materials; 123, Research and Current Developments; and 222, Corrosion of Metals in Concrete; and Joint ACI-ASCE Committee 408, Bond and Development of Steel Reinforcement.*

ACI Honorary Member **David Darwin** *is the Deane E. Ackers Distinguished Professor of Civil, Environmental, and Architectural Engineering at The University of Kansas and an ACI Past President. He is a member*

of ACI Committees 222, Corrosion of Metals in Concrete; 224, Cracking; and 318, Structural Concrete Building Code; and Joint ACI-ASCE Committees 408, Bond and Development of Steel Reinforcement; 445, Shear and Torsion; and 446, Fracture Mechanics of Concrete.

ACKNOWLEDGMENTS

This study was supported by the Oklahoma Department of Transportation (ODOT SP&R Item Number 2281). Material support was provided by Commercial Metals Company; the Concrete Reinforcing Steel Institute; Midwest Concrete Materials, Inc.; Cement Chemistry Systems, LP; and Xypex Chemical Corporation. Additional support was provided by the Structural Engineering and Materials Laboratory of the Infrastructure Research Institute at The University of Kansas.

REFERENCES

Andrade, M. C., and Macias, A., 1988, “Galvanized Reinforcements in Concrete,” *Surface Coatings—2*, A. D. Wilson, J. W. Nicholson, and H. J. Prosser, eds., Springer, Dordrecht, the Netherlands, pp. 137-182.

ASTM A615/A615M-20, 2020, “Standard Specification for Deformed and Plain Carbon-Steel Bars for Concrete Reinforcement,” ASTM International, West Conshohocken, PA, 8 pp.

ASTM A767/A767M-19, 2019, “Standard Specification for Zinc-Coated (Galvanized) Steel Bars for Concrete Reinforcement,” ASTM International, West Conshohocken, PA, 6 pp.

ASTM A1094/A1094M-20, 2020, “Standard Specification for Continuous Hot-Dip Galvanized Steel Bars for Concrete Reinforcement,” ASTM International, West Conshohocken, PA, 5 pp.

Bertolini, L.; Elsener, B.; Pedeferri, P.; Redaelli, E.; and Polder, R. B., 2014, *Corrosion of Steel in Concrete: Prevention, Diagnosis, Repair*, second edition, Wiley-VCH Verlag GmbH & Co. KGaA, Weinheim, Germany, 434 pp.

Broomfield, J. P., 2003, *Corrosion of Steel in Concrete: Understanding, Investigation and Repair*, second edition, Taylor & Francis, Abingdon, UK, 296 pp.

Darwin, D.; Browning, J.; O’Reilly, M.; Xing, L.; and Ji, J., 2009, “Critical Chloride Corrosion Threshold of Galvanized Reinforcing Bars,” *ACI Materials Journal*, V. 106, No. 2, Mar.-Apr., pp. 176-183.

Koch, G. H.; Brongers, M. P. H.; Thompson, N. G.; Virmani, Y. P.; and Payer, J. H., 2002, “Corrosion Cost and Preventive Strategies in the United States,” Report No. FHWA-RD-01-156, Federal Highway Administration, Turner-Fairbank Highway Research Center, McLean, VA, 786 pp.

O’Reilly, M.; Darwin, D.; Browning, J.; and Locke, C. E. Jr., 2011, “Evaluation of Multiple Corrosion Protection Systems for Reinforced Concrete Bridge Decks,” SM Report No. 100, The University of Kansas Center for Research, Inc., Lawrence, KS, 535 pp.

Ogunsanya, I. G., and Hansson, C. M., 2018, “The Influence of Coating Thickness and Composition on the Corrosion Propagation Rates of Galvanized Rebar in Cracked Concrete,” *CORROSION*, V. 74, No. 1, Jan., pp. 134-143. doi: 10.5006/2370

Poursaee, A., ed., 2016, *Corrosion of Steel in Concrete Structures*, Woodhead Publishing, Sawston, UK, 312 pp.

Student, 1908, “The Probable Error of a Mean,” *Biometrika*, V. 6, No. 1, Mar., pp. 1-25.

Treadaway, K. W. J., and Davies, H., 1989, “Performance of Fusion-Bonded Epoxy-Coated Steel Reinforcement,” *The Structural Engineer*, V. 67, No. 6, pp. 99-108.

Yeomans, S. R., 2016, “Galvanized Steel Reinforcement,” *Corrosion of Steel in Concrete Structures*, A. Poursaee, ed., Woodhead Publishing, Sawston, UK, pp. 111-129.

Yeomans, S. R., 2018, “Galvanized Steel Reinforcement: Recent Developments and New Opportunities,” *Better, Smarter, Stronger: Proceedings of the 5th International* fib *Congress*, S. Foster, R. I. Gilbert, P. Mendis, R. Al-Mahaidi, and D. Millar, eds., Melbourne, VIC, Australia, Oct., 17 pp.

ACI Faculty Network

Why Join the Faculty Network?

The Faculty Network is a support group for educators interested in ACI and the concrete industry. Members receive notifications about classroom resources, fellowships and scholarships, funding for research, online learning, and calls for papers and presenters.

Free 1-Year Educator Membership

ACI offers complimentary membership to teaching professionals who have not been an ACI member within the past 5 years.

Free Desk Copies

Faculty Network members can request a complimentary print or PDF copy of:

- ACI 318 PLUS (includes digital access to ACI CODE-318, ACI Reinforced Concrete Design Handbook, and ACI Detailing Manual)
- ACI CODE-318-25: Building Code for Structural Concrete—Code Requirements and Commentary (includes a free subscription to ACI 318 PLUS)
- ACI/PCI CODE-319-25: Structural Precast Concrete—Code Requirements and Commentary
- ACI/PTI CODE-320-25: Post-Tensioned Structural Concrete—Code Requirements and Commentary
- ACI CODE-323-24: Low-Carbon Concrete—Code Requirements and Commentary
- ACI CODE-562-25: Assessment, Repair, and Rehabilitation of Existing Concrete Structures—Code Requirements and Commentary
- ACI MNL-3(20): Guide to the Code for Assessment, Repair, and Rehabilitation of Existing Concrete Structures
- ACI MNL-5(19): Contractor's Guide to Quality Concrete Construction, 4th Edition
- ACI MNL-17(21): ACI Reinforced Concrete Design Handbook (available digitally with ACI 318 PLUS subscription)
- ACI SP-4: Formwork for Concrete

Networking

ACI hosts a Faculty Network Reception twice a year during the ACI Concrete Conventions, giving an opportunity to exchange ideas and network.

aci 318PLUS Faculty Network members receive a complimentary annual subscription that provides users with convenient digital interactive access to ACI CODE-318-25, ACI CODE-318-19, the ACI Detailing Manual, and the numerous design examples in the ACI Reinforced Concrete Design Handbook. The platform allows professors to create custom user notes that can be distributed to the students to view alongside the Code. Student members are provided 1-year access to ACI 318 PLUS when they purchase their printed copy of ACI 318-25 or ACI 318-19 at the student price of $105 (plus shipping).

aci Professors' Workshop
Materials | Pavements | Structures
Sponsor: aci Foundation

The Professors' Workshop is designed to provide instructors in civil engineering, architecture, architectural engineering, materials science, and construction management programs the tools to engage students in the latest developments in concrete design, construction, and materials.

aci Foundation
Building the Future

The Concrete Research Council (CRC) seeks concrete research projects that further the knowledge and sustainability of concrete materials, construction, and structures in coordination with ACI Committees. Annual Request for Proposals (RFP) are received annually between August 1 and December 1.

aci®
American Concrete Institute
Always advancing

ADVANCE YOUR CLASSROOM WITH ACI
JOIN OR RENEW TODAY! concrete.org/educatorsandresearchers

ACI MATERIALS JOURNAL TECHNICAL PAPER

Title No. 122-M27

Biochar to Enhance Curing and Rheology of Mortars without Formwork

by Devid Falliano, Luciana Restuccia, Jean-Marc Tulliani, and Giuseppe Andrea Ferro

Biochar properties—in particular, its fineness and ability to absorb water—can be exploited to modify the rheological behavior of cementitious conglomerates and improve the hydration of cement paste under adverse curing conditions, such as those related to three-dimensional (3-D) concrete printing. Regarding the fresh-state properties, the study of rheological properties, conducted on cementitious pastes for different biochar additions (by weight of cement: 0, 1.5, 2, and 3%), highlights that the biochar induces an increase in yield stress and plastic viscosity. The investigation of mechanical properties—in particular, flexural and compressive strength—performed on mortars evidences the internal curing effect promoted by biochar additions (by weight of cement: 0, 3, and 7.7%). In fact, compared to the corresponding specimens cured for the first 48 hours in the formwork, specimens with biochar addition cured directly in air are characterized by a drastically lower reduction in compressive strength than the reference specimens—that is, approximately 36% and 48%, respectively. This interesting result can also be exploited in traditional construction techniques where faster demolding is needed.

Keywords: biochar; internal curing agent; mechanical properties; rheological properties; three-dimensional (3-D) concrete printing.

INTRODUCTION

Concrete is a primary cause of carbon dioxide emissions into the atmosphere, as 8 to 9% of greenhouse gas emissions are attributed to its production.[1] Several studies have focused on finding solutions to replace part of the cement with materials from industrial waste to achieve a lower environmental impact while maintaining or even improving mechanical performance. However, in the macro field of studies aimed at reducing the environmental impact of the construction sector and the exploitation of raw resources, interest in cutting-edge construction technologies, such as three-dimensional (3-D) printing, can also be considered.[2]

Three-dimensional concrete printing has attracted increasing interest in the construction field due to its flexibility, the possibility of manufacturing elements on-site that would otherwise be difficult to transport, and countless opportunities for further development, including saving raw materials and optimizing their use.[3,4] In addition, other distinguishing features of this technology are the advantages related to the optimization of production cycles and the increased architectural and design versatility of the works,[5] as well as greater efficiency and safety of workers.[6]

The study of cementitious mixtures for use in automated processes such as 3-D printing can not only concern the evaluation of properties in the hardened state but must also deal with the rheological characteristics in the fresh state.[7,8]

Interest in 3-D concrete printing has also led to the investigation of special concrete mixtures, such as those characterized by low density, both in terms of mechanical properties in the hardened state and rheological properties in the fresh state.[9-12] Three-dimensional printing would have a substantial impact on the different cost distribution of structures. In fact, costs can currently be classified into four macro areas: 7% concrete labor, 10% formwork materials, 30% concrete materials, and 53% formwork labor.[13] More than 50% of the total costs can be attributed to labor and formwork, costs that would be reduced by 3-D printing. This consideration is linked to a challenge: the absence of formwork, with the risk of premature evaporation of the mixture water and poor hydration of the cement paste. Structural concrete elements have historically required formwork to maintain their shape and provide good conditions for proper hydration. The effect of the presence of formwork has become a relevant factor over time, so much so that various technologies have been developed both on the construction site and in the field of precasting—for example, flexible formwork, controlled-permeability formwork, and pneumatic formwork, which involve innovative aspects and effects on the concrete mixture.[14] Proper curing results in a better microstructure of the cementitious conglomerate, characterized by lower porosity and thus greater durability of the structure with a reduced CO_2 penetration rate.[15] Therefore, the effect of curing in formwork on the performance and durability of structures is considerable.

In contrast, 3-D concrete printing does not involve formwork, and the concrete mixture exposed directly to air, not being adequately protected from water evaporation, may have reduced performance.

There are several commonly used solutions to limit the negative effects of inadequate curing. The most common method is to constantly spray water on the surface of the concrete element. Another solution is referred to as external curing, which consists of waterproofing by means of a curing compound, a film-forming additive, with the aim of preventing evaporation of the mixture water. A third solution is called internal curing. It consists of the addition of a superabsorbent additive that gradually releases water over time to optimize the curing process.[16] Superabsorbent additives

---

ACI Materials Journal, V. 122, No. 4, July 2025.

MS No. M-2024-214.R2, doi: 10.14359/51746809, received March 5, 2025, and reviewed under Institute publication policies. Pertinent discussion including author's closure, if any, will be published ten months from this journal's date if the discussion is received within four months of the paper's print publication.

create water pockets that provide a water reserve, resulting in better hydration.

Regarding the internal curing strategy, this work aims to highlight the beneficial effects of using biochar in the production of cementitious conglomerates to be applied through 3-D printing. In fact, given its ability to absorb water due to its porous nature, biochar could have a beneficial internal curing effect.[17] Biochar is an industrial by-product obtained from pyrolysis and gasification processes and could be exploited to produce more environmentally sustainable concretes.[18] Biochar can provide a significant contribution to reducing the environmental impact of the construction sector, sequestering, depending on the raw material and pyrolysis conditions, between 2.0 and 2.6 tons of CO_2-eq per ton of biochar.[19] Therefore, biochar could be used to make a carbon-neutral or carbon-negative concrete.[20] Moreover, as stated in the relevant literature, biochar is chemically stable over time and should not alter when mixed with concrete.[21] Furthermore, the addition of a small amount of biochar can improve the mechanical strength and increase the fracture energy of concrete, while the addition of an excessive amount of biochar negatively affects the mechanical properties of cementitious conglomerates.[22-24] It can also contribute positively to the production of concrete mixtures characterized by excellent dimensional stability in the fresh state.[25] This can lead to the use of biochar as a dual-purpose resource in the development of concrete mixtures to be applied through 3-D printing: viscosity-modifying agent and internal curing agent.

RESEARCH SIGNIFICANCE

This study focuses on the possibility of improving the mechanical performance of cementitious conglomerates exposed to the curing that characterizes 3-D-printed products through the addition of biochar. In fact, in addition to the investigation of rheological properties, the effect of biochar addition on the reduction of mechanical performance of mortars cured in formwork for the first 48 hours or directly in air is presented in comparison with reference samples without biochar. The further effect on the same properties due to different water-cement ratios (*w/c*) is also highlighted. The results obtained may pave the way for new uses of this by-product as an effective resource in the concrete field while reducing environmental impact.

EXPERIMENTAL INVESTIGATION

The experimental campaign aims to highlight the possibility of using biochar as a viscosity-enhancing agent and an internal curing agent to reduce the negative effect of inadequate curing conditions on the mechanical properties of cementitious mixtures.

To this end, rheological tests and mechanical tests were performed. Based on preliminary studies, some of which have been published,[25] the effect of biochar on internal curing was carried out on mortars characterized by an addition of biochar equal to 7.7% by weight of cement, with three different *w/c*: 0.28, 0.31, and 0.35. For the highest *w/c*—that is, 0.35—the impact of biochar on internal curing was also studied in the case of lower biochar additions—that is, 3% by weight of cement. This shows how internal curing is affected not only by varying the *w/c*, but also by the amount of biochar in the cementitious mixture. As detailed in the subsection "Specimen preparation and curing conditions," internal curing is assessed by comparing the mechanical properties of specimens cured directly in air (a condition typical of 3-D-printed elements and when faster demolding is required) with those of specimens left in the formwork for the first 48 hours to avoid premature dehydration of the specimens. The study of rheological properties is carried out on cement pastes cast using the same raw materials. In fact, as evidenced in the relevant literature, it is possible to understand the behavior of viscosity-modifying agents by simply comparing the rheological behavior of cement pastes, neglecting the effect of aggregates.[17] A *w/c* of 0.35 was considered for the rheological study. The rheological study was conducted considering three different biochar contents: 1.5%, 2%, and 3%. It was not possible to extend the study to the case of 7.7% biochar addition due to the too-high consistency of the resulting pastes, which was not compatible with the specified measuring range of the rheometer used. Due to the impossibility of assessing the rheological properties in this case, biochar additions of 1.5% and 2% were chosen in addition to 3%. This approach allowed a more detailed evaluation of the impact of biochar on the rheological behavior of mixtures. Furthermore, as high-range water-reducing admixture (HRWRA) has a significant impact on the rheological properties of cementitious composites, to specifically assess the effect of biochar on the rheological properties in the fresh state, the study of rheological properties was conducted without the use of HRWRA. This approach was chosen to isolate the influence of biochar, avoiding potential interactions with other factors that could contaminate the results.

Materials

Portland cement CEM I 52.5 R, in accordance with UNI EN 197-1, was used for the preparation of the conglomerates. The physical and mechanical properties of the cement used are given in Table 1.

Tap water was employed; the *w/c* used ranged from 0.28 to 0.35. Basalt sand with a maximum diameter of 3 mm was used. This choice is motivated by the aim of developing mixtures that can be usefully employed in automated processes where the maximum diameter of the aggregate particles is limited to avoid occlusions when the material exits the printhead nozzle; the latter is characterized by diameters between 15 and 50 mm.[26]

A polycarboxylate ether-based HRWRA was used to enhance the mixing process and improve the workability of the material, especially in view of the low *w/c* adopted.

The mixtures were prepared by adding biochar produced from wood chips by gasification at a temperature of approximately 700°C.

Nitrogen adsorption and desorption isotherms were determined with a physisorption instrument at a temperature of –196°C. Prior to measurements, the sample was degassed under vacuum at 150°C for 8 hours. Moreover, the Brunauer-Emmett-Teller (BET) model was applied to

Table 1—Physical and mechanical properties of cement, as declared by producer

Cement type	Initial setting time, h	Specific gravity, g/cm^3	Blaine fineness, cm^2/g	1-day compressive strength, MPa	2-day compressive strength, MPa	7-day compressive strength, MPa	28-day compressive strength, MPa
CEM I 52.5 R	2	3.05	4500	25	36	49	58

Table 2—Properties of employed biochar

Surface area, m^2/g	40.7
Pore volume, cm^3/g	0.06
Water absorption, g	0.69 ± 0.07
Average particle size, μm	13.7

Table 3—Mixture proportions of tested cement pastes

Series No.	Cement, g	Water, g	Biochar, g
OPC	450	157.5	0
BC_1.5	450	157.5	4.5
BC_2	450	157.5	9
BC_3	450	157.5	13.5

assess the specific surface area of the sample. The biochar used in this research is characterized by a surface area of 40.7 m^2/g and a pore volume of 0.06 cm^3/g, according to the Barrett-Joyner-Halenda model.

The water absorption of biochar was evaluated as the mass of absorbed water per gram of dry biochar.[27] The water absorption of adopted biochar is equal to 0.69 ± 0.07 g of water per gram of dry biochar. This property can change the rheological properties of cementitious systems.[17]

The particle-size distribution (PSD) was determined using a laser granulometer equipped with a dry powder disperser. Figure 1 reveals that the PSD is roughly bimodal with an average particle size (d_{50}) equal to 13.7 μm, while the diameters d_{10} and d_{90} corresponding to 10% and 90% of the cumulative curve are 2.31 and 49.9 μm, respectively. This PSD could have a twofold packing effect in the cementitious mixture: on the one hand, it may result in a reduction of the spaces between sand particles; on the other hand, it may contribute to densifying the cementitious matrix. Table 2 summarizes the properties of the biochar.

Mixture proportions

Although the influence of aggregates is lost, it is commonly believed in the relevant literature that the effect of any admixtures on the rheology of concrete and mortar can be reasonably estimated on the basis of their influence in the cement pastes.[17,28] In light of this, the rheological study was carried out on four different cementitious mixtures characterized by the following different biochar-cement ratios: 0%, 1.5%, 2%, and 3% (Table 3). Unfortunately, as previously specified, it was not possible to evaluate the rheological behavior for higher percentages of biochar (7.7%), because very stiff and high-consistency pastes were obtained, which were not compatible with the specified measuring range of the rheometer used. In the analysis of rheological properties, the *w*/*c* was kept constant and equal to 0.35. In fact, for the purpose of this work, it was considered sufficient to study rheological behavior for only one of the *w*/*c* investigated for the mechanical properties and shown herein.

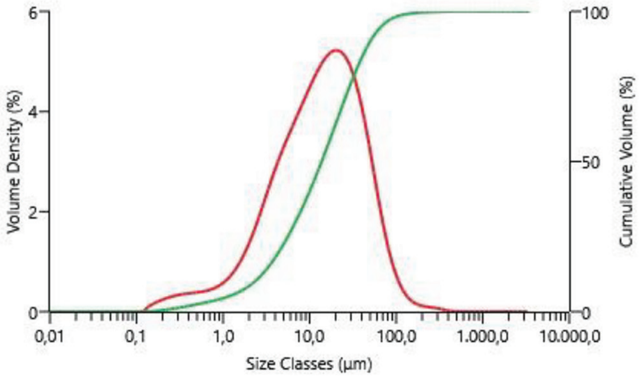

Fig. 1—Biochar PSD.

For the investigation of mechanical properties, all series were realized with the same sand-cement ratio. It is worth noting that in terms of precise terminology, this study refers to mortars and not concrete, as no coarse aggregates were used. As mentioned earlier, this choice was dictated by the constraints on the maximum aggregate particle size imposed by the equipment generally used in the 3-D-printing process, primarily the pump, but especially the end effector and the printhead nozzle. Nevertheless, it is common practice in the technical and scientific literature of the field to refer to such cementitious composites as concrete, even though, more accurately, they should be classified as mortar. Three different *w*/*c* were investigated: 0.28, 0.31, and 0.35. The amount of HRWRA varied between 0.5 and 4% of cement weight. Specifically, as the amount of biochar increased, it was necessary to increase the proportion of HRWRA in the cementitious mixture. Mixtures with a biochar addition of 7.7% (by weight of cement) are identified as BC_I, while those with a biochar addition of 3% are identified as BC_II.

Specimen preparation and curing conditions

To prepare the cement paste and mortar, the components were mixed for 3 minutes with a mortar mixer; the mixing procedure included two different mixing intensities: 80 rpm for the first 60 seconds and 210 rpm for the remaining 120 seconds. Three prismatic specimens of dimensions 40 x 40 x 160 mm were produced for each series in accordance with EN 196-1.

In Table 4, samples whose curing is identified with formwork were demolded after 48 hours of curing and were then air cured at a temperature of 25 ± 2°C and relative humidity (R.H.) of 65 ± 5% until the evaluation of the 28-day mechanical properties. In contrast, samples whose curing is identified with air were demolded immediately after being formed, to simulate the curing effect proper to 3-D printing—that is, directly in air. Through this procedure, any positive influences of the addition of biochar on the degree of hydration

Table 4—Mixture proportions and curing conditions of tested mortars

Series No.	Cement, g	Water, g	Sand, g	HRWRA, g	Biochar, g	Curing condition
REF_28_FMW	800	224	1024	12	0	Formwork
REF_28_AIR	800	224	1024	12	0	Air
BC_I_28_FMW	800	224	1024	32	61.6	Formwork
BC_I_28_AIR	800	224	1024	32	61.6	Air
BC_I_31_FMW	800	248	1024	32	61.6	Formwork
BC_I_31_AIR	800	248	1024	32	61.6	Air
BC_I_35_FMW	800	280	1024	32	61.6	Formwork
BC_I_35_AIR	800	280	1024	32	61.6	Air
BC_II_35_AIR	800	280	1024	6	24	Air
REF_35_AIR	800	280	1024	4	0	Air

of the cement paste can be revealed indirectly—that is, by comparing the mechanical properties of the samples.

Testing conditions

The rheology of the pastes was studied using a rotational rheometer with co-axial cylinders. The gap between the inner and outer cylinders was 1.15 mm, and the gap between the base of the cup and the bob was 5 mm. A Peltier cell was used to keep the system temperature stable at 23 ± 1.0°C. A ramping up of the shear rate from 0 to 200 s^{-1} was performed, followed by a ramping down of the shear rate from 200 to 0 s^{-1}.

Regarding mechanical properties, at the end of the 28-day curing period, all samples were subjected to three-point bending tests and compression tests on the two resulting halves. In accordance with UNI EN 196-1, the three-point bending tests were performed in force-control mode, using a loading rate of 50 N/s; the compression tests were also performed in force-control mode, using a loading rate of 2400 N/s. The equipment for three-point bending tests was a testing machine with a load capacity of 50 kN, operated by a closed-loop control system. A testing machine with a loading capacity of 500 kN was used for compression tests.

EXPERIMENTAL RESULTS AND DISCUSSION

Effect of biochar addition on cementitious pastes flow curves

Three flow curves were performed for each series studied, which revealed excellent repeatability of the test. To make the results obtained more readable, only one representative curve for each of the series was investigated, as shown in Fig. 2. To make the effect of biochar addition on the rheological behavior of cementitious pastes clearer, a magnification of the behavior found during the early stages of the test is also provided.

As the biochar content increases, there is an increase in shear stress for any value of the shear rate. In the reference samples, the cement particles are surrounded by a thin fluid layer that, acting as a lubricant, reduces their friction and allows the cement paste to flow with great ease.

In cases of biochar additions of 1.5 and 2%, the change in slope at shear rates just below 25 s^{-1} is evident, showing a change in rheological behavior. As previously demonstrated, biochar particles can absorb a certain amount of water due to their porous microstructure. However, a further increase in the amount of biochar to 3% of cement weight results in a further change in the initial rheological behavior of the cementitious system. In fact, as shown in Fig. 2(d), there is first a sudden increase in shear stress as shear rate increases with a subsequent abrupt reduction before the classic behavior manifested at lower biochar percentages is resumed. This same behavior at the same shear rate value is confirmed in the downward curve.

This behavior could be justified by considering that as the amount of biochar increases, the possibility of agglomeration of biochar particles that can trap water inside them increases due to their high surface area and surface tension. In fact, the increase in biochar leads to a reduction in the interparticle distance between biochar particles, resulting in the possibility of agglomeration due to increased interparticle attraction forces.[29] This agglomeration, on the one hand, can reduce the free water present in the system, giving rise to an abrupt increase in yield stress,[17] and on the other hand, when the agglomerate is disaggregated, this free water can be released into the system, giving rise to paste lubrication. This leads to a sudden decrease in yield stress values until a new equilibrium state is reached, with recovery of the rheological behavior exhibited in the case of lower biochar contents.

The determined curves are well represented by Bingham's model, Eq. (1). This is a rheological model used, for example, for cementitious pastes with non-zero yield stress and a linear relationship between shear rate and shear stress[10]

$$\tau = \tau_0 + \eta_{pl} \cdot \gamma \tag{1}$$

where τ is the shear stress (Pa); τ_0 is the yield stress (Pa); η_{pl} is the plastic viscosity (Pa·s); and γ is the shear rate (s^{-1}).

As can be observed in Fig. 3(b), which shows the average yield stress value over the three determinations performed, the presence of biochar induces an increase in the yield stress of the cementitious pastes. Furthermore, the yield stress increases again as the percentage of biochar increases: there is an average increase of approximately 84% from a biochar content of 1.5 to 2%, and approximately 68% from a biochar content of 2 to 3%.

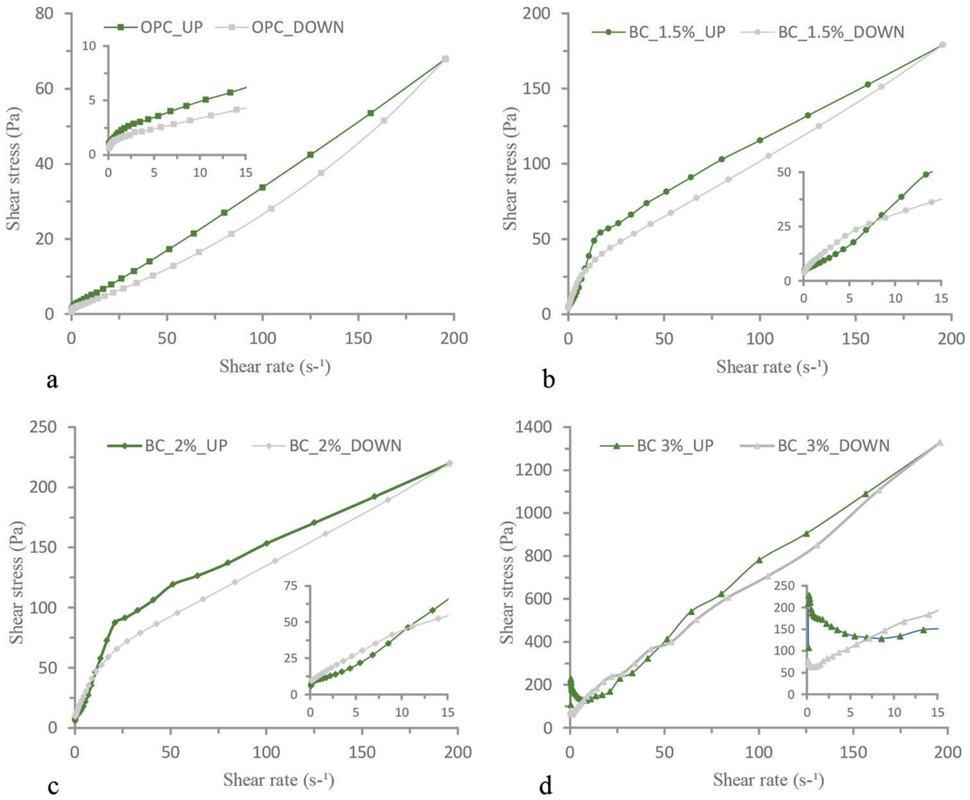

Fig. 2—Effect of biochar content on flow curves of cement pastes (in small graphs, behavior during early stages of test): (a) ordinary portland cement (OPC); (b) biochar addition equal to 1.5% (BC_1.5%); (c) biochar addition equal to 2% (BC_2%); and (d) biochar addition equal to 3% (BC_3%). (Note: _UP stands for upward curve, and _DOWN stands for downward curve.)

From Fig. 3(a), it can be observed that in addition to the increase in the yield stress of cement pastes, as the percentage of biochar increases, there is also an increase in plastic viscosity, which is directly affected by the volume of solids in the mixture.[30] Therefore, the addition of particles characterized by a relatively large specific surface area gives rise to an increase in yield stress[28] and plastic viscosity, also due to the water retention capacity of biochar, a property that is of remarkable relevance to the phenomenon of internal curing. In addition, Fig. 3 also highlights the markedly different behavior characterizing the series with 3% biochar addition, discussed previously.

In light of these results, it can be concluded that biochar acts as a viscosity-enhancing agent, resulting in a significant increase in the yield stress of cementitious pastes.

This property can be exploited in the field of 3-D concrete printing. However, it is also recognized that cementitious mixtures characterized by too high consistency are difficult to use due to obvious problems in both mixing and pumping. The rheological behavior shown in this study is also optimal compared to the results obtained in the work of Zhang et al.[31] In fact, the presence of mechanical action, such as that exerted during the mixing phase, guarantees a cementitious system that is easily mixable, workable, and pumpable. At the end of the mixing phase, thanks to the properties of biochar, the cementitious system becomes capable of self-sustaining without the use of formwork.

Hardened-state properties: flexural strength and compressive strength

Table 5 shows the experimental results obtained; the standard deviation and the coefficient of variation of the evaluated parameters are also given.

The flexural strength values shown in Table 5 represent the average of the three experimental determinations.

The effect of curing conditions and *w*/*c* on the flexural strength are shown in Fig. 4. As expected, the curing that characterizes 3-D-printed concrete adversely affects flexural strength. In fact, in all cases, there is a decrease in flexural strength, which is more pronounced in the case of samples with biochar addition: there is a slight decrease of 5.5% in the case of the reference sample without biochar addition, and an average decrease of approximately 19% in the case of biochar addition. In terms of flexural strength, therefore, there is no beneficial effect due to the addition of biochar for air-cured samples. In fact, in the case of the samples cured for the first 2 days in the formwork and then in air, the presence of 7.7% (BC_I_28) biochar, with respect to cement weight, does not result in an appreciable decrease in flexural strength, which remains close to that characterizing the reference samples (REF_28). In the case of the presence of biochar, moreover, again considering the specimens cured for the first 2 days in the formwork, increasing the *w*/*c* from 0.28 to 0.31 does not lead to a decrease in performance, which is even slightly higher when using the *w*/*c* of 0.31. The absence of a reduction in flexural strength from a *w*/*c* of 0.28 to 0.31 may be due to the marginally improved workability

Table 5—Experimental flexural and compressive strengths for each series investigated

	Mean flexural strength	Standard deviation of flexural strength	COV flexural strength	Mean compressive strength	Standard deviation of compressive strength	COV compressive strength
Series No.	f_t, MPa	σ_{ft}, MPa	COV_{ft}	R_c, MPa	σ_{R_c}, MPa	COV_{R_c}
REF_28_FMW	11.24	1.28	0.11	95.67	3.57	0.04
REF_28_AIR	10.62	0.77	0.07	49.06	1.25	0.03
BC_I_28_FMW	11.06	0.49	0.04	84.88	2.56	0.03
BC_I_28_AIR	8.73	1.18	0.14	54.14	0.04	0.00
BC_I_31_FMW	11.21	0.14	0.01	78.75	5.61	0.05
BC_I_31_AIR	9.04	1.81	0.20	50.22	2.34	0.03
BC_I_35_FMW	9.69	0.49	0.05	73.15	5.23	0.07
BC_I_35_AIR	8.05	0.77	0.10	47.16	1.91	0.04
BC_II_35_AIR	7.44	0.51	0.07	44.69	1.41	0.03
REF_35_AIR	8.62	0.47	0.05	32.60	1.22	0.04

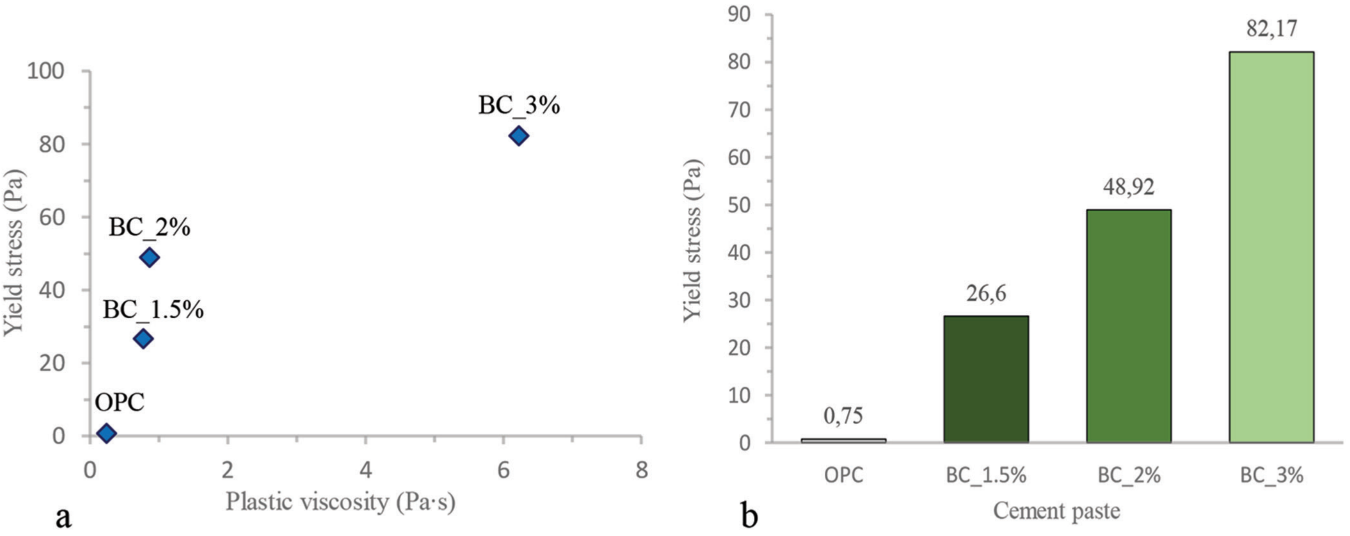

Fig. 3—Effect of biochar content on yield stress and plastic viscosity of cement pastes: (a) yield stress in function of plastic viscosity and biochar content; and (b) effect of biochar content on yield stress.

of the cementitious material with a higher *w/c*, which may have facilitated a more homogenous mixture, minimizing defects and microcracks that could adversely affect flexural strength. On the other hand, the decrease becomes more significant if the *w/c* is increased to 0.35.

Comparing the results of specimens cured for the first 2 days in formwork with those cured directly in air, in specimens with biochar additions, a noticeable trend emerges: the reduction in flexural strength becomes less pronounced as the *w/c* increases. In fact, this percentage drop is equal to 21.07%, 19.36%, and 16.92% in cases of *w/c* of 0.28, 0.31, and 0.35, respectively. These results can be explained by the internal curing effect facilitated by the presence of biochar. Specifically, the increased water content in the mixture provides more moisture that can be absorbed by the biochar particles. Over time, the biochar gradually releases the absorbed water, promoting a more sustained hydration process of the cement paste. This mechanism is similar to the function of superabsorbent polymers, which store and release water to improve hydration and overall performance of the material.

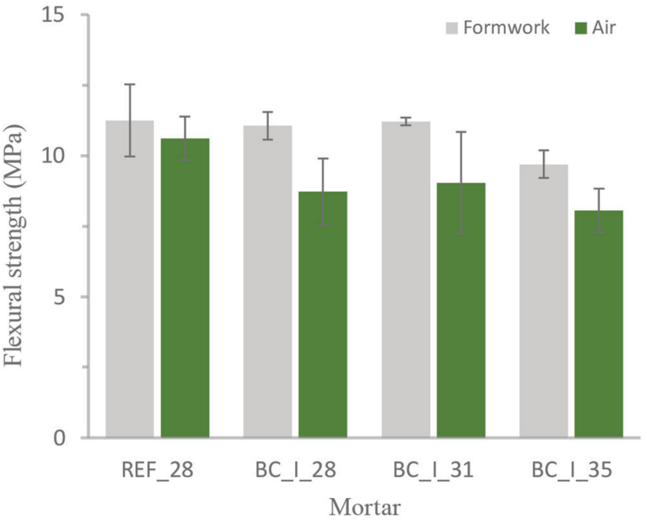

Fig. 4—Effect of curing conditions (formwork for first 48 hours or directly in air, as 3-D-printed materials) and w/c *on flexural strength of tested mortars.*

The same trend can be identified in the results shown in Fig. 5, where the effect of biochar content on flexural strength is shown for the same curing conditions (air) and *w/c* (0.35). In fact, it is evident that the presence of biochar leads to a slight decrease in flexural strength even in the case of *w/c* of 0.35. The decrease in flexural strength in the case of samples with biochar addition is in line with the finding reported by Tan et al.,[32] in which the addition of 5% pyrolyzed biochar resulted in a decrease in flexural strength of approximately 10% at 28 days. However, in addition to confirming this finding, the present study highlights the very interesting aspect previously mentioned: the reduction in the drop of flexural strength as the *w/c* increases, when comparing the results of specimens cured for the first 2 days in molds with those cured directly in air.

The compressive strength values shown in Table 5 represent the average of the experimental determinations carried out on the three specimens. Specifically, the compressive strength of each specimen was evaluated as the average of the two determinations performed on the two halves obtained from the three-point bending test.

Figure 6 shows the effects on compressive strength of the two different curing conditions and *w/c*. A different trend can be seen for formwork-cured samples and air-cured samples. In the former case, the reference specimens without the addition of biochar are characterized by the highest compressive strength, averaging 95.67 MPa. In fact, under formwork curing conditions, the addition of 7.7% biochar (by weight of cement), at the same *w/c*, results in an 11.28% decrease in compressive strength compared to the reference specimens.

In addition, again in the case of the formwork-cured specimens, in the case of the presence of biochar, the increase in the *w/c* from 0.28 to 0.31 and 0.35, respectively, produces a further decrease in compressive strength of 7.22% and 16.92%. The latter observation is also confirmed in the case of air-cured specimens, where a slight decrease in compressive strength as the *w/c* increases is still observed. In fact, compared with specimens characterized by a *w/c* of 0.28, there is a reduction of 7.24% and 14.80% in the case of *w/c* equal to 0.31 and 0.35, respectively. In contrast, continuing to observe the results obtained in the case of air-cured specimens, the highest compressive strength, averaging 54.14 MPa, is associated with specimens with biochar addition at 7.7% by weight of cement and *w/c* of 0.28. Compared to the corresponding reference specimens, these specimens show an increase in compressive strength of 10.35%. As can be seen from the data shown in Table 5 and Fig. 6, the presence of biochar provides compressive strengths in line with (or higher than) those of the reference specimens even when the *w/c* is increased. In fact, comparing the results of specimens cured for the first 2 days in formwork with those cured directly in air, the reference specimens show a 48.7% reduction in compressive strength. In contrast, for specimens with a biochar addition of 7.7%, this reduction is limited to approximately 36%. These results can be justified by the internal curing phenomenon favored by the presence of biochar. In addition, biochar can provide a substrate for the nucleation and growth of hydration products.[33]

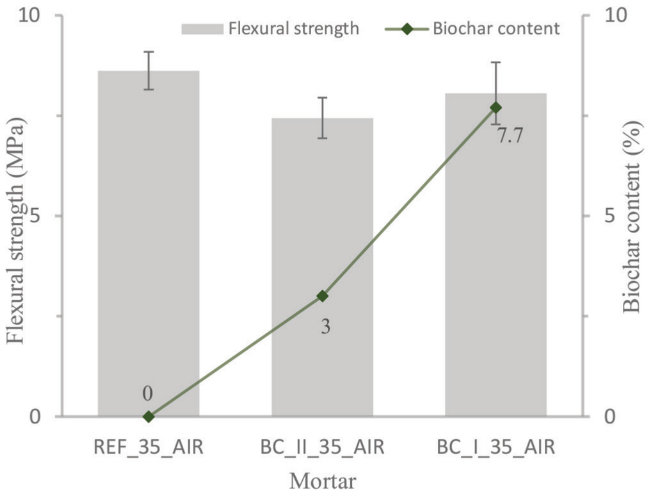

Fig. 5—Mortars with w/c *of 0.35: effect of biochar content on flexural strength of specimens cured directly in air.*

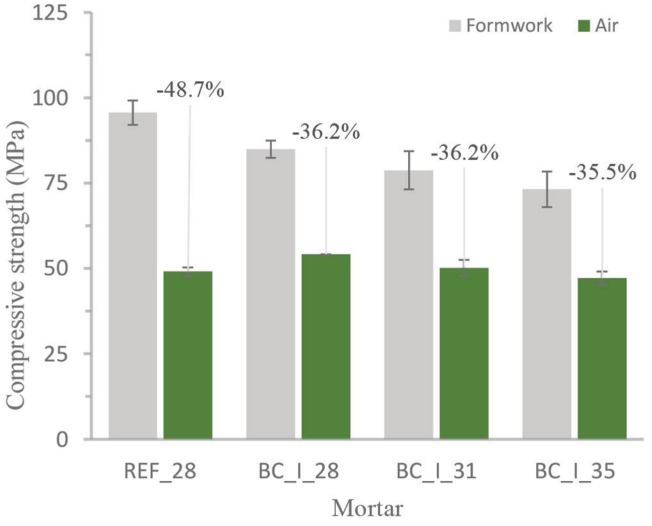

Fig. 6—Effect of curing conditions (formwork for first 48 hours or directly in air, as 3-D-printed materials) and w/c *on compressive strength of tested mortars.*

A similarly interesting result emerges when looking at the comparative histogram shown in Fig. 7, which shows the effect of biochar content on the compressive strength of cementitious mixtures at the same *w/c* (0.35) and curing condition (air). Compared with reference samples without biochar addition, the compressive strength increase is 37.08% and 44.66% when biochar is added in the amount of 3% and 7.7% by weight of cement, respectively.

This further improvement can be justified by considering that there is more water in the mixture that is free to be absorbed by the biochar, which can then release it slowly over time, ensuring a better degree of hydration of the cement paste, similar to what is achieved by the use of superabsorbent polymers. In fact, in the case of the air-cured reference samples, increasing the *w/c* from 0.28 to 0.35 results in a 33.55% reduction in compressive strength. In contrast, this significant decrease is not present in the case of specimens with biochar addition: in fact, under the same conditions there is a percentage reduction of 12.89%. Therefore, biochar under the typical curing conditions of 3-D-printed elements allows a significant increase in *w*/*c* without a simultaneous drastic decrease in compressive strengths. Such evidence could also be due to the ability of biochar to absorb water in the early stages, reducing the effective *w*/*c*, and then slowly release it during the curing stage. This reduces the effect of premature evaporation of water from the surface of the samples and promotes hydration of unreacted cement particles.[34] The very interesting results presented here pave the way for profitable use of biochar in the field of 3-D concrete printing, or even in the case of more traditional construction techniques where faster demolding is needed, turning a low-cost waste product into a resource with twofold value.

CONCLUSIONS

This study focused on the possibility of using a low-cost waste material, biochar, as a resource to be exploited as an internal curing and viscosity-modifying agent in the field of three-dimensional (3-D) printing of concrete, or as an internal curing agent in the case of more traditional construction technologies when faster demolding is needed. Rheological investigations revealed that the incorporation of biochar leads to substantial increase in yield stress and plastic viscosity in cementitious systems. This is attributed to the ability of biochar to absorb water, accelerating internal structuration and flocculation. Specifically, yield stress continues to increase with increasing biochar content, showing an average increase of 84% when biochar content increases from 1.5% to 2%, and 68% when it increases from 2% to 3%, with respect to cement weight. As expected, the curing conditions typical of 3-D-printed concrete have a negative impact on the mechanical properties, especially in terms of compressive strength. However, this study showed the remarkable ability of biochar to act as an internal curing agent, significantly mitigating the negative effects caused by the absence of formwork. The work revealed a completely different trend in compressive strength, with the presence of biochar playing a crucial role in the comparison between samples cured in formwork for the first 2 days and those cured directly in air. In the case of the formwork-cured samples, the reference samples without biochar showed higher compressive strength than those containing biochar under the various conditions analyzed in this study. However, this trend changed significantly in the case of air-cured samples, where the highest compressive strength was associated with the biochar-containing samples, specifically 7.7% with respect to cement weight. In fact, air-cured specimens containing biochar showed a reduction in compressive strength of approximately 36% compared to the corresponding specimens cured in formwork. This reduction was notably smaller than the 48% reduction observed in the reference specimens without biochar under the same curing conditions. This result is more pronounced as the water-cement ratio (*w*/*c*) increases, due to the increased availability of free water. In fact, the beneficial effect of biochar is further emphasized when comparing the results at a *w*/*c* of 0.35 with air curing. In particular, the increased biochar content led to significant improvements in compressive strength, with increases of 37.08% and 44.66% at 3% and 7.7% biochar to cement weight, respectively, compared to the reference sample. These observations are supported by the evaluation of the water absorption capacity of the biochar used, equal to 0.69 ± 0.07 g of water for each gram of dry biochar.

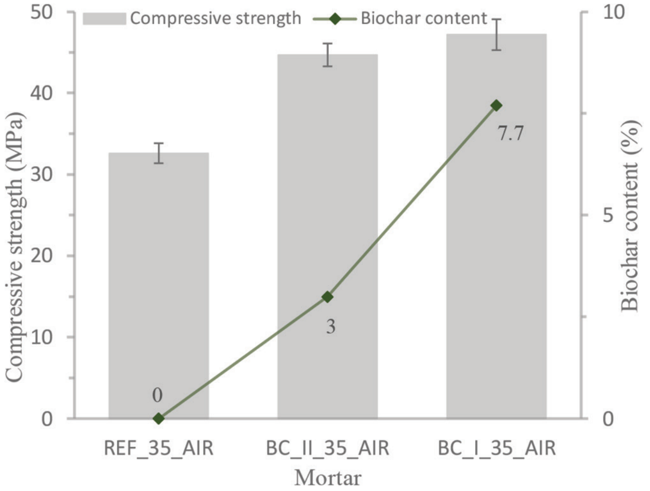

Fig. 7—Mortars with w/c *of 0.35: effect of biochar content on compressive strength of specimens cured directly in air.*

Therefore, the results presented in this study highlight that biochar represents a promising waste material for applications in the field of 3-D concrete printing, both as a viscosity-modifying agent and as an internal curing agent, but also as an internal curing agent when faster demolding is required in more traditional building techniques. Moreover, the synergy between the 3-D-printing process and printable concretes with biochar, a carbon-negative material, may be an important way toward greater sustainability in the field of concrete.

AUTHOR BIOS

Devid Falliano *is an Assistant Professor in the Department of Structural, Geotechnical and Building Engineering at Politecnico di Torino, Turin, Italy. He received his PhD in engineering and chemistry of materials and constructions from the University of Messina, Messina, Italy, in 2018. His research interests include strategies for improving the durability of reinforced concrete structures, theoretical and experimental aspects of three-dimensional (3-D) concrete printing, and experimentation and mechanical characterization of cementitious-based composite materials.*

Luciana Restuccia *is an Associate Professor in the Department of Structural, Geotechnical and Building Engineering at Politecnico di Torino, where she received her PhD in structural engineering in 2016. Her research interests include anti-seismic safety of existing structures, study of innovative materials, 3-D concrete printing, and experimentation and mechanical characterization of cement-based composite materials.*

Jean-Marc Tulliani *is a Professor in the Department of Applied Science and Technology at Politecnico di Torino. He received his PhD in materials engineering from the École Supérieure de l'Énergie et des Matériaux d'Orléans, Orléans, France, in 1997. His research interests include ceramic gas and humidity sensors for ammonia and NOx detection, soil moisture content measurement, and new hybrid consolidants for mortars and stones conservation.*

Giuseppe Andrea Ferro *is a Professor in the Department of Structural, Geotechnical and Building Engineering at Politecnico di Torino, where he received his PhD in structural engineering in 1994. His research interests include the fracture mechanics of concretes, scale effects, mechanical behavior of innovative and sustainable cementitious materials, seismic analysis of existing structures, and bridge assessment.*

ACKNOWLEDGMENTS

The authors would like to acknowledge the support of D. Suarez for his help in evaluating the water absorption of biochar, and the support of

S. Quattrocchi, A. Sciarrone, P. Cosenza, and G. Occhino. The authors also greatly acknowledge the SISCON (Safety of Infrastructures and Constructions) Interdepartmental Laboratory for the use of the rheometer. The work of D. Falliano was carried out within the Ministerial Decree No. 1062/2021 and received funding from the FSE REACT-EU – PON Ricerca e Innovazione 2014-2020.

REFERENCES

1. Reis, D. C.; Quattrone, M.; Souza, J. F.; Punhagui, K. R.; Pacca, S. A.; and John, V. M., "Potential CO_2 Reduction and Uptake Due to Industrialization and Efficient Cement Use in Brazil by 2050," *Journal of Industrial Ecology*, V. 25, No. 2, 2021, pp. 344-358. doi: 10.1111/jiec.13130

2. Mata-Falcón, J.; Bischof, P.; and Kaufmann, W., "Exploiting the Potential of Digital Fabrication for Sustainable and Economic Concrete Structures," *First RILEM International Conference on Concrete and Digital Fabrication – Digital Concrete 2018*, T. Wangler and R. J. Flatt, eds., Springer, Cham, Switzerland, 2019, pp. 157-166. doi: 10.1007/978-3-319-99519-9_14

3. Bak, D., "Rapid Prototyping or Rapid Production? 3D Printing Processes Move Industry Towards the Latter," *Assembly Automation*, V. 23, No. 4, 2003, pp. 340-345. doi: 10.1108/01445150310501190

4. Buchli, J.; Giftthaler, M.; Kumar, N.; Lussi, M.; Sandy, T.; Dörfler, K.; and Hack, N., "Digital in Situ Fabrication-Challenges and Opportunities for Robotic in Situ Fabrication in Architecture, Construction, and Beyond," *Cement and Concrete Research*, V. 112, 2018, pp. 66-75. doi: 10.1016/j.cemconres.2018.05.013

5. Khoshnevis, B., "Automated Construction by Contour Crafting—Related Robotics and Information Technologies," *Automation in Construction*, V. 13, No. 1, 2004, pp. 5-19. doi: 10.1016/j.autcon.2003.08.012

6. Buswell, R. A.; Soar, R. C.; Gibb, A. G.; and Thorpe, A., "Freeform Construction: Mega-Scale Rapid Manufacturing for Construction," *Automation in Construction*, V. 16, No. 2, 2007, pp. 224-231. doi: 10.1016/j.autcon.2006.05.002

7. Roussel, N., "Rheological Requirements for Printable Concretes," *Cement and Concrete Research*, V. 112, 2018, pp. 76-85. doi: 10.1016/j.cemconres.2018.04.005

8. Zhang, Y.; She, W.; Yang, L.; Liu, G.; and Yang, Y., "Rheological and Harden Properties of the High-Thixotropy 3D Printing Concrete," *Construction and Building Materials*, V. 201, 2019, pp. 278-285. doi: 10.1016/j.conbuildmat.2018.12.061

9. Falliano, D.; De Domenico, D.; Ricciardi, G.; and Gugliandolo, E., "3D-Printable Lightweight Foamed Concrete and Comparison with Classical Foamed Concrete in Terms of Fresh State Properties and Mechanical Strength," *Construction and Building Materials*, V. 254, 2020, p. 119271. doi: 10.1016/j.conbuildmat.2020.119271

10. Falliano, D.; Crupi, G.; De Domenico, D.; Ricciardi, G.; Restuccia, L.; Ferro, G.; and Gugliandolo, E., "Investigation on the Rheological Behavior of Lightweight Foamed Concrete for 3D Printing Applications," *Second RILEM International Conference on Concrete and Digital Fabrication – Digital Concrete 2020*, F. P. Bos, S. S. Lucas, R. J. M. Wolfs, and T. A. M. Salet, eds., Springer, Cham, Switzerland, pp. 246-254. doi: 10.1007/978-3-030-49916-7_25

11. Cho, S.; van Rooyen, A.; Kearsley, E.; and van Zijl, G., "Foam Stability of 3D Printable Foamed Concrete," *Journal of Building Engineering*, V. 47, 2022, p. 103884. doi: 10.1016/j.jobe.2021.103884

12. Markin, V.; Krause, M.; and Otto, J., "3D-Printing with Foam Concrete: From Material Design and Testing to Application and Sustainability," *Journal of Building Engineering*, V. 43, 2021, p. 102870. doi: 10.1016/j.jobe.2021.102870

13. Jha, K. N., *Formwork for Concrete Structures*, Tata McGraw-Hill Education Private Limited, India, 2012.

14. Veenendaal, D.; West, M.; and Block, P., "History and Overview of Fabric Formwork: Using Fabrics for Concrete Casting," *Structural Concrete*, V. 12, No. 3, 2011, pp. 164-177. doi: 10.1002/suco.201100014

15. Coppola, L., *Concretum*, McGraw-Hill, Italy, 2007.

16. Hamzah, N.; Mohd Saman, H.; Baghban, M. H.; Mohd Sam, A. R.; Faridmehr, I.; Muhd Sidek, M. N.; Benjeddou, O.; and Huseien, G. F., "A Review on the Use of Self-Curing Agents and its Mechanism in High-Performance Cementitious Materials," *Buildings*, V. 12, No. 2, 2022, p. 152. doi: 10.3390/buildings12020152

17. Gupta, S.; Tulliani, J. M.; and Kua, H. W., "Carbonaceous Admixtures in Cementitious Building Materials: Effect of Particle Size Blending on Rheology, Packing, Early Age Properties and Processing Energy Demand," *The Science of the Total Environment*, V. 807, 2022, p. 150884. doi: 10.1016/j.scitotenv.2021.150884

18. Tan, K. H.; Wang, T. Y.; Zhou, Z. H.; and Qin, Y. H., "Biochar as a Partial Cement Replacement Material for Developing Sustainable Concrete: An Overview," *Journal of Materials in Civil Engineering*, ASCE, V. 33, No. 12, 2021, p. 03121001. doi: 10.1061/(ASCE)MT.1943-5533.0003987

19. Azzi, E. S.; Karltun, E.; and Sundberg, C., "Prospective Life Cycle Assessment of Large-Scale Biochar Production and Use for Negative Emissions in Stockholm," *Environmental Science and Technology*, V. 53, No. 14, 2019, pp. 8466-8476. doi: 10.1021/acs.est.9b01615

20. Chen, L.; Zhang, Y.; Wang, L.; Ruan, S.; Chen, J.; Li, H.; Yang, J.; Mechtcherine, V.; and Tsang, D. C., "Biochar-Augmented Carbon-Negative Concrete," *Chemical Engineering Journal*, V. 431, 2022, p. 133946. doi: 10.1016/j.cej.2021.133946

21. Suarez-Riera, D.; Restuccia, L.; and Ferro, G. A., "The Use of Biochar to Reduce the Carbon Footprint of Cement-Based Materials," *Procedia Structural Integrity*, V. 26, 2020, pp. 199-210. doi: 10.1016/j.prostr.2020.06.023

22. Gupta, S.; Kua, H. W.; and Cynthia, S. Y. T., "Use of Biochar-Coated Polypropylene Fibers for Carbon Sequestration and Physical Improvement of Mortar," *Cement and Concrete Composites*, V. 83, 2017, pp. 171-187. doi: 10.1016/j.cemconcomp.2017.07.012

23. Restuccia, L., and Ferro, G. A., "Promising Low Cost Carbon-Based Materials to Improve Strength and Toughness in Cement Composites," *Construction and Building Materials*, V. 126, 2016, pp. 1034-1043. doi: 10.1016/j.conbuildmat.2016.09.101

24. Falliano, D.; De Domenico, D.; Sciarrone, A.; Ricciardi, G.; Restuccia, L.; Ferro, G.; Tulliani, J. M.; and Gugliandolo, E. "Influence of Biochar Additions on the Fracture Behavior of Foamed Concrete," *Frattura ed Integrità Strutturale*, V. 14, No. 51, 2019, pp. 189-198. doi: 10.3221/IGF-ESIS.51.15

25. Falliano, D.; Restuccia, L.; and Ferro, G. A., "Biochar Addition for 3DCP: A Preliminary Study," *Procedia Structural Integrity*, V. 41, 2022, pp. 699-703. doi: 10.1016/j.prostr.2022.05.079

26. Buswell, R. A.; De Silva, W. L.; Jones, S. Z.; and Dirrenberger, J., "3D Printing Using Concrete Extrusion: A Roadmap for Research," *Cement and Concrete Research*, V. 112, 2018, pp. 37-49. doi: 10.1016/j.cemconres.2018.05.006

27. Gupta, S.; Kua, H. W.; and Low, C. Y., "Use of Biochar as Carbon Sequestering Additive in Cement Mortar," *Cement and Concrete Composites*, V. 87, 2018, pp. 110-129. doi: 10.1016/j.cemconcomp.2017.12.009

28. Ferraris, C. F.; Obla, K. H.; and Hill, R., "The Influence of Mineral Admixtures on the Rheology of Cement Paste and Concrete," *Cement and Concrete Research*, V. 31, No. 2, 2001, pp. 245-255. doi: 10.1016/S0008-8846(00)00454-3

29. Liu, H.; Sun, X.; Du, H.; Lu, H.; Ma, Y.; Shen, W.; and Tian, Z., "Effects and Threshold of Water Film Thickness on Multi-Mineral Cement Paste," *Cement and Concrete Composites*, V. 112, 2020, p. 103677. doi: 10.1016/j.cemconcomp.2020.103677

30. Bonen, D., and Shah, S. P., "Fresh and Hardened Properties of Self-Consolidating Concrete," *Progress in Structural Engineering and Materials*, V. 7, No. 1, 2005, pp. 14-26. doi: 10.1002/pse.186

31. Zhang, C.; Nerella, V. N.; Krishna, A.; Wang, S.; Zhang, Y.; Mechtcherine, V.; and Banthia, N., "Mix Design Concepts for 3D Printable Concrete: A Review," *Cement and Concrete Composites*, V. 122, 2021, p. 104155. doi: 10.1016/j.cemconcomp.2021.104155

32. Tan, K.; Pang, X.; Qin, Y.; and Wang, J., "Properties of Cement Mortar Containing Pulverized Biochar Pyrolyzed at Different Temperatures," *Construction and Building Materials*, V. 263, 2020, p. 120616. doi: 10.1016/j.conbuildmat.2020.120616

33. Wang, L.; Chen, L.; Poon, C. S.; Wang, C. H.; Ok, Y. S.; Mechtcherine, V.; and Tsang, D. C., "Roles of Biochar and CO_2 Curing in Sustainable Magnesia Cement-Based Composites," *ACS Sustainable Chemistry and Engineering*, V. 9, No. 25, 2021, pp. 8603-8610. doi: 10.1021/acssuschemeng.1c02008

ARE YOU A RESEARCHER?

SIGN UP FOR ORCID TODAY!

1. Register
2. Use your ORCID ID
3. Share

ORCID provides a digital identifier that distinguishes you from every other researcher and, through integration in key research workflows such as manuscript and grant submission, supports automated linkages between you and your professional activities, ensuring that your work is recognized.

ORCID services are FREE and it's as easy as **1-2-3**.

WWW.ORCID.ORG

ACI MATERIALS JOURNAL TECHNICAL PAPER

Title No. 122-M28

Carbonated Fly Ash Alkali-Activated Aggregates: Properties, Performance, and Environmental Impact

by Mohd Hanifa, Usha Sharma, P. C. Thapliyal, and L. P. Singh

The production of carbonated aggregates from Class F fly ash (FA) is challenging due to its low calcium content, typically less than 10%. This study investigates the production of carbonated alkali-activated aggregates using FA and calcium carbide sludge (CCS). Sodium hydroxide was used as an activator, and the effects of autoclave treatment on the properties of these aggregates were examined. The optimal mixture, comprising 70% FA and 30% CCS, achieved a single aggregate strength of >5 MPa in autoclave carbonated (AC) aggregates, comparable to the strength obtained after 14 days of water curing without-autoclave carbonated (WAC) aggregates. Both AC and WAC aggregates exhibited a bulk density of 790 to 805 kg/m^3, and the CO_2 uptake was 12.5% and 13.3% in AC and WAC aggregates, respectively. Field-emission scanning electron microscopy (FE-SEM) and Fourier-transform infrared spectroscopy (FTIR) analysis indicated the formation of calcium-aluminum-silicate-hydrate (C-A-S-H) gel in non-carbonated aggregates, while calcite and vaterite, along with sodium-aluminum-silicate-hydrate (N-A-S-H) gel, formed in carbonated aggregates. Concrete incorporating AC and WAC aggregates exhibited compressive strength of 39 and 38 MPa, with concrete density of 2065 kg/m^3 and 2085 kg/m^3, respectively. Furthermore, AC and WAC aggregate concrete showed a reduction in CO_2 emissions of 18% and 31%, respectively, compared to autoclave non-carbonated (ANC) aggregate concrete. These findings highlight the potential of producing carbonated alkali-activated aggregates from FA and CCS as sustainable materials for construction applications.

Keywords: alkali activation; autoclave; carbonated aggregate; CO_2 emissions.

INTRODUCTION

In recent decades, the increase in CO_2 emissions due to human activities has emerged as a pressing global concern. As of 2022, CO_2 concentration reached a record of 417.06 parts per million (ppm), which is 50% higher than the preindustrial levels.[1,2] In response, 196 parties adopted the Paris Agreement at the 2015 United Nations Climate Change Conference (COP21) on December 12, 2015, in Paris, France, aiming to limit the global temperature increase this century to well below 2°C above preindustrial levels.[3] Among the various contributors to environmental impact, the construction industry is a major source of CO_2 emissions. In 2021, the construction sector emitted approximately 10 gigatons of CO_2, as reported in the "2022 Global Status Report for Buildings and Construction."[4]

To mitigate CO_2 emissions from the construction industry, particularly from concrete production, mineral carbonation is a promising method for permanently sequestering CO_2 as stable carbonates. Because aggregates constitute approximately 70% of concrete's volume, using carbonated aggregates can significantly lower CO_2 emissions by up to 80% compared to conventional buildings materials.[5] Research has extensively explored the production of carbonated aggregates using calcium-rich wastes, such as steel slag, paper waste, municipal solid waste, and construction and demolition wastes.[6-12] However, producing carbonated aggregates from calcium-deficient waste such as Class F fly ash (FA) is challenging due to its low CaO content, which is essential for carbonation.

Class F FA is one of the most abundant industrial by-products, with an estimated global annual production of 800 million tons, including 180 million tons generated in India alone.[13] Given its vast availability, using Class F FA for artificial aggregate production can mitigate environmental pollution while providing a viable alternative to natural aggregates. Furthermore, its high aluminum and silica content is crucial for achieving aggregate strength. Extensive research has been conducted on producing artificial aggregates from Class F FA using cold-bonding technology without any activators or binders. However, these aggregates fail to achieve compressive strengths of more than 2 MPa and require prolonged curing times. To overcome these limitations, researchers have developed geopolymer aggregates from Class F FA using highly alkaline solutions (~12 M NaOH) and sodium silicate solutions.[14-17] The primary binding product in geopolymer aggregates is sodium-aluminum-silicate-hydrate (N-A-S-H) gel.[18,19] However, these aggregates are non-carbonatable and generate significant CO_2 emissions during production, as sodium hydroxide and sodium silicate contribute approximately 400 kg and 850 kg of CO_2 equivalent (CO_2e) per ton, respectively.[20] Additionally, the high molarity (~12 M) of sodium hydroxide leads to efflorescence, which degrades the aggregates over time. Another method involves producing sintered aggregates from Class F FA, which requires sintering temperatures above 1000°C. While these aggregates exhibit improved properties, the process is highly energy-intensive and results in substantial CO_2 emissions, making them less sustainable. A summary of aggregates derived from Class F FA is

---

ACI Materials Journal, V. 122, No. 4, July 2025.

MS No. M-2024-365.R1, doi: 10.14359/51746810, received February 18, 2025, and reviewed under Institute publication policies. Pertinent discussion including author's closure, if any, will be published ten months from this journal's date if the discussion is received within four months of the paper's print publication.

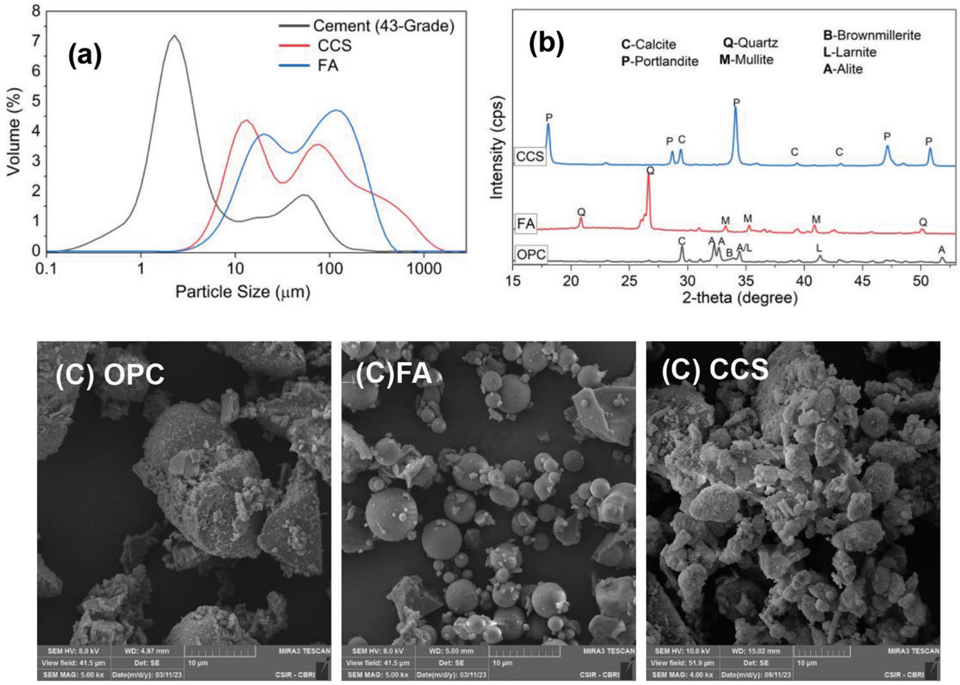

Fig. 1—Characterization of raw materials: (a) particle-size distribution; (b) XRD pattern; and (c) FE-SEM.

provided in Table T1 in the Appendix,* highlighting that all these aggregates are non-carbonated. Overall, the production of carbonated aggregates remains a significant challenge.

Therefore, to produce carbonated aggregates from FA, it is essential to incorporate calcium-rich materials, which facilitate the carbonation reaction. Calcium carbide sludge (CCS), an industrial by-product from the acetylene industry, is composed of approximately 92% calcium hydroxide and is used with FA to produce carbonated aggregates. It is generated in slurry form at a rate of approximately 2.8 tons per ton of acetylene.[21] Due to its high alkalinity, CCS cannot be recycled in carbide production or used as a cementitious material in cement manufacturing.[22-25] However, its high calcium content and alkalinity make it a promising material for producing carbonated aggregates in combination with Class F FA, requiring only 5 M NaOH and eliminating the need for sodium silicate solution (water glass). The production of CCS from the acetylene industry is shown in Eq. (1).[26]

$$CaC_2(s) + 2H_2O(l) \rightarrow C_2H_2(g) + Ca(OH)_2(s) \qquad (1)$$

In this study, alkali-activated cold-bonding pelletization technology was used to prepare carbonated aggregates from FA and CCS as a precursor and sodium hydroxide solution as the activator. The study explored the effects of autoclave treatment and accelerated carbonation on the properties of carbonated alkali-activated aggregates. Characterization methods, including X-ray diffraction (XRD), thermogravimetric analysis (TGA), Fourier-transform infrared spectroscopy (FTIR), and field-emission scanning electron microscopy (FE-SEM)/energy-dispersive X-ray analysis (EDAX), were used to examine the microstructure, CO_2 uptake, and reaction products formed in alkali-activated aggregates. Finally, the compressive strength, density, and environmental assessment of concrete cast with these aggregates were evaluated. The results could provide a solution for preparing carbonated aggregates from FA and CCS with a low-concentration sodium hydroxide solution, leading to the production of concrete with low carbon emissions.

RESEARCH SIGNIFICANCE

The production of artificial aggregates from Class F FA through sintering and alkali activation methods is highly energy-intensive and generates significant CO_2 emissions. Producing carbonated aggregates from FA is particularly challenging due to its low calcium content, which is crucial for the carbonation reaction. Studies on producing carbonated aggregates from FA and CCS (industrial waste) with a low-concentration sodium hydroxide solution are limited in the technical literature. The authors believe that this approach significantly reduces the overall CO_2 emissions of concrete compared to sintered and geopolymer aggregates.

MATERIALS AND METHODS

Materials

In this study, alkali-activated aggregate was prepared from FA and CCS derived from Netra NTPC Limited in Udyog Vihar, Uttar Pradesh, India, and an industrial gases and gas cylinders manufacturer in Rewari, Haryana, India. Sodium hydroxide pellets (>97% purity) were selected as the alkaline activator, purchased from a chemical manufacturing company in Mumbai, India. The particle-size distributions for FA, CCS, and ordinary portland cement (OPC) are shown in Fig. 1(a). The mean particle sizes of FA, CCS, and OPC were 78.794 μm, 115.32 μm, and 12.07 μm, respectively. The chemical compositions of the FA, OPC, and CCS were

---

*The Appendix is available at **www.concrete.org/publications** in PDF format, appended to the online version of the published paper. It is also available in hard copy from ACI headquarters for a fee equal to the cost of reproduction plus handling at the time of the request.

Table 1—Chemical compositions of raw materials

Materials	CaO	SiO_2	Al_2O_3	Fe_2O_3	K_2O	Na_2O	SO_3	MgO	LOI
CCS	74.0	3.1	0.46	0.26	—	—	0.54	0.72	—
FA	1.61	55.27	26.69	8.14	1.76	0.13	0.25	0.39	1.33
OPC	62.85	20.98	5.42	3.92	0.53	0.28	2.36	1.76	1.90

Note: LOI is loss on ignition.

Table 2—Mixture proportions of artificial aggregate and concrete production

Artificial aggregate

Mixtures	FA, wt. %	CCS, wt. %	5 M NaOH solution (solution/solid)	Pelletizer duration, minutes	Mechanical parameters	
					Angle, degrees	Speed, rpm
Mix-1	60	40	0.3	15	45	35 to 40
Mix-2	70	30	0.3	15	45	35 to 40
Mix-3	80	20	0.3	15	45	35 to 40

Concrete, kg/m^3

Concrete	Water	Cement	Sand	High-range water-reducing admixture	Natural aggregates	Artificial aggregates
Natural aggregate	141	402.8	623.41	2.01	1151.5	0
WAC aggregate	141	402.8	623.41	2.01	0	856.50
AC aggregate	141	402.8	623.41	2.01	0	856.50

analyzed using X-ray fluorescence (XRF), and the results are shown in Table 1. The content of CaO was 1.6%, which indicates that the FA was Class F FA according to ASTM C618-19.[27] The XRD patterns of the FA, CCS, and OPC are shown in Fig. 1(b). The FE-SEM images show FA contained spherical particles, whereas CCS and OPC contained large, irregular-shaped particles (Fig. 1(c)). River sand was used as fine aggregate, with a specific gravity of 2.6 and bulk density of 1482.8 kg/m^3, while coarse aggregates were angular granite (12.5 to 20 mm), with a specific gravity of 2.42.

Methods

Artificial aggregates were produced using Class F FA and CCS in three different mixture proportions (Table 2). In Mix-1, Mix-2, and Mix-3, FA was partially replaced with CCS at 40%, 30%, and 20% by weight, respectively. The artificial aggregates were prepared through alkali activation using the cold-bonding pelletization method in a 100 cm diameter disc pelletizer with a 15 cm edge height. The process was conducted with a tilting angle of 45 degrees and a revolution speed of 40 rpm, following optimized parameters from previous studies.[28] Activation was carried out using NaOH solutions of 3, 5, and 7 M concentrations. A detailed analysis of the optimal sodium hydroxide concentration is provided in Fig. S1 in the Appendix, concluding that 5 M is optimal for aggregate production.

First, FA and CCS were thoroughly dry-mixed in a mixing chamber before being transferred to the disc pelletizer. A NaOH solution was sprayed using a water can to achieve a water-to-solid ratio (*w/s*) of 0.3 during granulation. The granulation process continued for 10 minutes, producing spherical aggregates with diameters between 10 and 20 mm. These aggregates were then carbonated in a carbonation chamber and were referred to as without-autoclave carbonated (WAC) aggregates. The aggregates were then water cured for different water-curing ages (3, 7, and 14 days).

Similarly, autoclaved aggregates were produced using the same granulation method but underwent an additional autoclaving process after granulation, resulting in autoclave non-carbonated (ANC) aggregates. These ANC aggregates were subsequently carbonated in the pressurized carbonation chamber for varying durations to achieve maximum carbonation and were referred to as autoclave carbonated (AC) aggregates.

The carbonation process was conducted in the pressurized carbonation chamber. The chamber was initially vacuumed to achieve a pressure of approximately –0.06 MPa. CO_2 gas (99% purity) was then injected into the chamber until a pressure of 4 bar was reached, and this pressure was maintained for durations of 4, 8, 12, and 24 hours. A saturated NaCl solution was used to maintain a relative humidity (RH) of 65 to 70% during carbonation, while silica gel was used to absorb excess moisture.[29,30] A schematic of the carbonation equipment is shown in Fig. S2 in the Appendix.

The autoclaving process was conducted in an autoclave chamber under three different conditions: 1 bar (115°C), 3 bar (130°C), and 5 bar (150°C) for 3 hours. The pressure-temperature relationship in an autoclave follows the principles of gas laws and can be described by the Clausius-Clapeyron equation or the ideal gas law.[31] In this study's autoclave, the selected temperatures and corresponding pressures were as follows: 115°C at approximately 1 atm, 130°C at approximately 3 atm, and 150°C at approximately 5 atm.

As a result, three types of aggregates were produced: WAC aggregates, ANC aggregates, and AC aggregates. These aggregates, with diameters between 12.5 and 20, were used as coarse aggregates, and river sand was used as fine aggregates to prepare concrete with dimensions of 100 x 100 x 100 m^3. Aggregates with a diameter of 12.5 to 20 mm were immersed in water for 24 hours at room temperature. After this duration, the aggregates were removed, and surface water was wiped off until they reached a saturated surface-dry state. The mixture proportions of concrete were designed according to the Indian Standard IS 10262:2019[32] (Table 2). To prepare the concrete, hand-mixing was performed following the guidelines set out in the Indian Standard IS 516-1959,[33] which outlines the procedure for mixing the components to ensure uniformity and consistency in the final mixture. After standard water curing for 7, 14, and 28 days, the concrete specimens were subjected to compression tests.

TESTING METHODS

Properties of artificial aggregates

Both the water absorption and bulk density of artificial aggregates were studied according to the Indian Standard IS:2386 (Part III)-1963.[34]

For water absorption testing, artificial aggregates with a diameter of 12.5 to 20 mm were immersed in water for 24 hours at room temperature. After this duration, the aggregates were removed, and surface water was wiped off until they reached a saturated surface-dry state. The mass was then recorded as M_w. These aggregates were then dried in an oven for 24 hours at 105°C, and their mass was recorded as M_d. The water absorption of the aggregates was calculated using Eq. (2). This procedure was repeated with three different batches, and the average value was used.

$$\text{Water absorption} = \frac{M_w - M_d}{M_d} \times 100\% \tag{2}$$

To determine the bulk density (kg/m^3), artificial aggregates were filled into a container with a volume of V_C, and then the total mass of the artificial aggregates and the container was recorded as M_f. The mass of the container was recorded as M_C. The bulk density of the artificial aggregate can be calculated using Eq. (3).

$$\text{Bulk density} = \frac{M_f - M_C}{V_C} \times 1000 \tag{3}$$

The single aggregate strength of artificial aggregates was tested according to Eq. (4) using the California Bearing Ratio tester, as recommended by the previous studies.[35,36] For each batch, 15 aggregates with sizes between 12.5 and 20 mm were tested, and the average strength was reported.

$$\sigma = \frac{2.8P}{\pi d^2} \tag{4}$$

where σ is the individual aggregate strength in MPa; d is the diameter of the aggregates in mm; and P is the load at failure in N.

CO_2 uptake by artificial aggregates was quantified by TGA. The powder sample underwent a controlled heating process from room temperature to 1000°C with a heating rate of 10°C/min and a flow of N_2 at 100 mL/min. The estimated CO_2 uptake by artificial aggregates was calculated by Eq. (5) and (6).[37,38]

$$\text{Total } CO_2 \text{ (wt. \%)} = \frac{\Delta M_{550°C \text{ to } 800°C}}{M_{950°C}} \times 100 \tag{5}$$

$$\text{Actual } CO_2 \text{ uptake (wt. \%)} = \frac{CO_{2carbonated} - CO_{2initial}}{100 - CO_{2carbonated}} \times 100 \tag{6}$$

where ΔM is mass loss due to the $CaCO_3$ decomposition (550 to 810°C); and $CO_{2initial}$ and $CO_{2carbonated}$ are the weights of CO_2 in artificial aggregates before and after carbonation, respectively.

To determine the pH value of artificial aggregates, powdered samples of aggregates were dissolved in distilled water at a *w/s* of 10:1. The solution was then stirred for 60 minutes. Following this, the pH was measured using a pH electrode.

Mineralogical and morphological analysis of artificial aggregate

The mineralogical compositions of artificial aggregates were examined by X-ray diffractometer (CuKα, 30 kV, 16 mA) with a scanning speed of 1 degree/min and a 2θ range of 10 to 60 degrees. Quantitative analysis of the sample was performed using XRD analysis software using the Crystallography Open Database (COD). FTIR was used to determine the chemical composition, and the spectra were analyzed between 400 cm^{-1} and 4000 cm^{-1}, with a resolution of 4 cm^{-1}. The morphology of the samples was examined using FE-SEM, with an accelerating voltage of 10 to 20 kV. A thin layer of gold was sputtered on the surface using a gold sputter, making it conductive. For elemental analysis and mapping of the sample, an energy-dispersive X-ray attached to the FE-SEM was used.

Properties of concrete

The compressive strength and density of concrete cast with natural and carbonated alkali-activated aggregates were tested at 7, 14, and 28 days of water curing as per IS 516-1959.[33] Three concrete cubes were used for each test, and the average result was reported.

Environmental assessment

The environmental impact of artificial aggregates is assessed by analyzing CO_2 emissions throughout their life cycle, excluding use, end-of-life, and recycling. The study assumes that CCS and FA are industrial wastes with no energy consumption or CO_2 emissions, measured per ton. Material transportation, typically using diesel trucks in India, covers approximately 150 km and requires energy. The impacts were analyzed using GaBi Professional (Version 9.2.1.68). The system boundary included FA, CCS, NaOH, water, raw material transport, and electricity used during alkali-activated aggregates production, as shown in Fig. S3 in the Appendix.

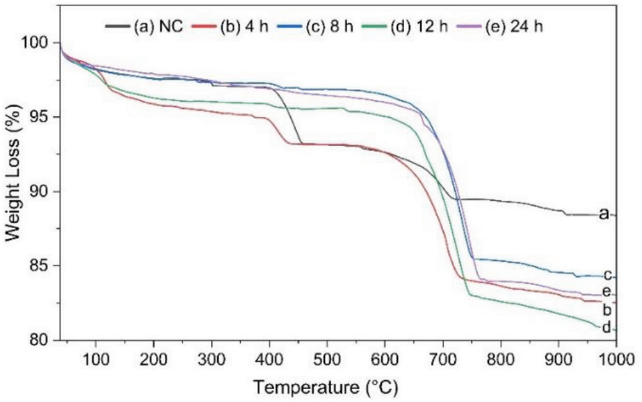

Fig. 2—TGA of artificial aggregates prepared from optimized Mix-2 at different durations of accelerated carbonation: (a) weathering/natural carbonation; (b) 4-hour carbonation; (c) 8-hour carbonation; (d) 12-hour carbonation; and (e) 24-hour carbonation.

Table 3—Estimated CO_2 uptake by artificial aggregate during accelerated carbonation, wt. %

Mixtures	ID	$\Delta M_{500\text{ to }800°C}$	$M_{950°C}$	Total CO_2	Actual CO_2 uptake
Mix-1	ANC	2.9	80.82	3.59	—
	AC	11.94	72.69	16.42	15.35
	WAC	13.05	75.88	17.19	16.42
Mix-2	ANC	2.46	89.19	2.76	—
	AC	10.90	80.44	13.55	12.48
	WAC	11.88	83.89	14.16	13.28
Mix-3	ANC	1.37	87.05	1.57	—
	AC	6.57	80.86	8.20	7.22
	WAC	7.86	83.88	9.37	8.60

Note: Total CO_2 uptake is CO_2 uptake by both natural carbonation and accelerated carbonation; actual CO_2 uptake is CO_2 uptake by accelerated carbonation only.

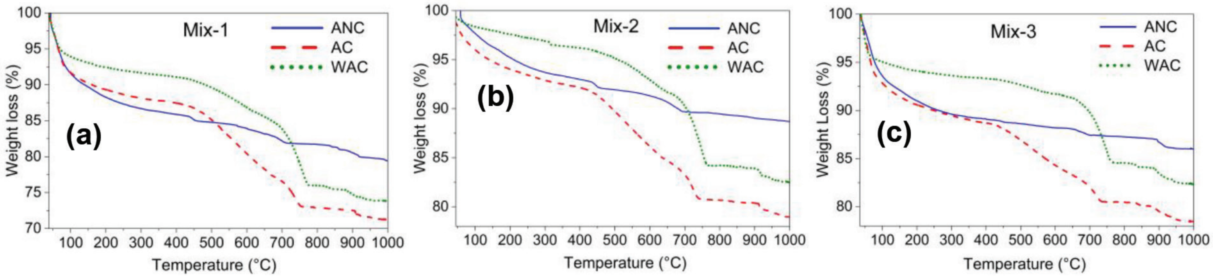

Fig. 3—TGA of: (a) Mix-1 aggregates; (b) Mix-2 aggregates; and (c) Mix-3 aggregates.

The Higg Material Sustainability Index (MSI) values are used to quantify CO_2 emissions associated with concrete production.[39] The MSI occurs by considering energy and material flows in the manufacturing process, which includes energy consumption, waste generation, and pollution.[39,40] The MSI study found that CO_2 emissions for OPC, sand, granite gravel, and water during each phase of production were 930 kg/ton, 23.3 kg/ton, 20 kg/ton, and 1 kg/ton, respectively.[41,42]

EXPERIMENTAL RESULTS

CO_2 uptake of artificial aggregates

CO_2 uptake in artificial carbonated aggregates was calculated by TGA, as shown in Fig. 2. Weight loss in the temperature range of 400 to 450°C corresponded to the dehydration of the portlandite, while weight loss in the temperature range of 550 to 800°C was due to the decarbonation of calcium carbonate.[43,44] The artificial aggregates became fully carbonated after 12 hours of accelerated carbonation, as shown in Fig. 2. The complete disappearance of the portlandite peak, observed at temperatures between 400 and 500°C after 12 hours of carbonation, confirmed complete carbonation. Extending carbonation to 24 hours did not cause additional weight loss, confirming 12 hours as the optimal carbonation duration for artificial aggregates.

The CO_2 uptake of alkali-activated aggregates prepared from Mix-1, Mix-2, and Mix-3 is shown in Fig. 3. CO_2 uptake by artificial aggregates prepared from three different mixtures was in the range of 6.8 to 15.1% (Table 3). Mix-1 aggregates showed a higher CO_2 uptake than Mix-2 and Mix-3, as CO_2 uptake increases with CCS content. In similar mixtures, the weight loss in WAC aggregates was higher than in AC aggregates, as highly polymerized calcium-aluminum-silicate-hydrate (C-A-S-H) gel formed in AC aggregates through autoclaving, which hindered the carbonation reaction, resulting in lower CO_2 uptake compared to WAC aggregates.

Water absorption, bulk density, and pH of artificial aggregates

The single aggregate strength, water absorption, and bulk density of alkali-activated aggregates prepared from Mix-1, Mix-2, and Mix-3 are shown in Fig. 4.

The single aggregate strength achieved by the ANC aggregate of Mix-1, Mix-2, and Mix-3 was 3.2 MPa, 3.9 MPa, and 4.4 MPa, respectively, immediately after the autoclave process (Fig. 4(a)). After accelerated carbonation, the single aggregate strength of the AC aggregates of Mix-1, Mix-2, and Mix-3 increased to 4.1 MPa, 5.4 MPa, and 5 MPa, respectively (Fig. 4(b)). However, the WAC aggregates of Mix-1, Mix-2, and Mix-3 achieved strengths of 3.9 MPa, 5 MPa, and 3.5 MPa, respectively, after 14 days of water curing (Fig. 4(c)). The aggregate strength increased with curing time from 3 to 14 days, due to the activation of FA through water curing, and achieved the maximum strength after 14 days of water curing, which is almost comparable to the AC aggregate strength achieved just after the autoclave process. The results show that without autoclaving,

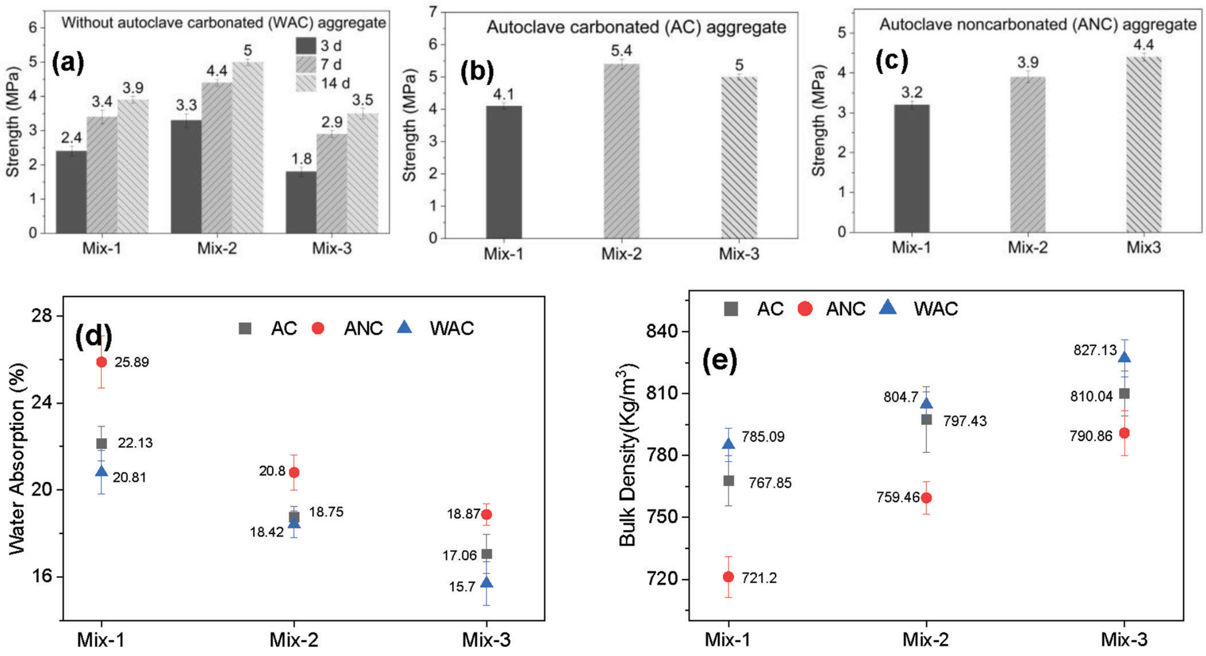

Fig. 4—Single aggregate strength of: (a) WAC aggregate at 3, 7, and 14 days of water curing; (b) ANC aggregate after carbonation; and (c) AC aggregate after carbonation; along with (d) water absorption; and (e) bulk density of artificial aggregates.

aggregates require 14 days of water curing to achieve maximum strength, whereas similar strength is achieved immediately through the autoclaving process.

The water absorption of artificial aggregates of Mix-1, Mix-2, and Mix-3 is shown in Fig. 4(d), indicating water absorption between 15 and 26%. The ANC aggregates of Mix-1 exhibited the highest water absorption (25.89%) compared to AC (22.13%) and WAC (20.81%) aggregates. The water absorption of the ANC aggregates of Mix-2 and Mix-3 was 20.8% and 18.87%, respectively; after carbonation, the water absorption of AC and WAC aggregates decreased to 18.75% and 18.42%, respectively. Similarly, the water absorption of the ANC aggregates of Mix-3 was 18.87%, and it decreased to 17.06% and 15.7% for AC and WAC aggregates, respectively, through carbonation. Similar trends were observed in the artificial aggregates of Mix-1, Mix-2, and Mix-3, where water absorption decreased with increased carbonation. From the aforementioned results, it was observed that water absorption significantly decreased with an increase in FA and CCS content because FA is less porous and absorbs less water than CCS. Further, accelerated carbonation decreased water absorption by forming calcium-carbonated products (calcite, vaterite, and aragonite) within the aggregate matrix. Comparing the carbonated aggregates of Mix-1, Mix-2, and Mix-3, AC aggregates have more water absorption than WAC aggregates due to the formation of vaterite and calcite in AC aggregates. In contrast, only calcite is formed during accelerated carbonation in WAC aggregates. Calcite is a crystalline form of calcium carbonate with a relatively compact and well-ordered crystal structure, which makes it less porous, while vaterite is more porous, which enhances water absorption.

The bulk densities of the ANC, AC, and WAC aggregates of Mix-1, Mix-2, and Mix-3 are shown in Fig. 4(e). The bulk density of aggregates ranged from 721 to 828 kg/m^3, classifying them as lightweight aggregates according to Indian Standard IS:2386 (Part III)-1963.[34]

The ANC aggregates of Mix-1 had the lowest bulk density of 721.2 kg/m^3, compared to AC with 767.85 kg/m^3 and WAC with 785.09 kg/m^3. A similar trend was observed in Mix-2 and Mix-3 aggregates, wherein bulk density increased with carbonation. Compared to the same mixtures of carbonated aggregates, the bulk density increased with carbonation; therefore, WAC aggregates have a higher bulk density than AC aggregates. However, within different mixtures, bulk density depends on the percentage of FA relative to CCS, as the bulk density of FA is higher compared to that of CCS.

The pH of the ANC artificial aggregate ranged from 12.2 to 13.0. After accelerated carbonation, the aggregates' pH decreased to 9 to 9.8 due to the formation of calcium carbonate. WAC aggregates have a lower pH than AC aggregates due to the greater extent of carbonation.

Microstructural studies: mineralogy and morphology of reaction products

The mineralogical and morphological characteristics of artificial aggregates were analyzed using XRD, FTIR, and FE-SEM/EDAX techniques (Fig. 5).

XRD patterns of calcite (2θ = 26.0 and 26.3 degrees), quartz (2θ = 16.46, 20.86, and 26.64 degrees), mullite (2θ = 26.0 and 26.3 degrees), vaterite (2θ = 24.87, 27.28, and 32.74 degrees), and portlandite (2θ = 18.04, 34.12, 47.08, and 50.76 degrees) were observed in the artificial aggregates.[45,46] A comparison of XRD patterns of the ANC and WAC aggregates of Mix-1, Mix-2, and Mix-3 is shown in Fig. 5(a) to (c). The portlandite peaks were less intense in the ANC aggregates before carbonation due to the formation of C-A-S-H gel by consuming the calcium from portlandite through the alkali activation/autoclave process. A comparative analysis of Mix-1, Mix-2, and Mix-3 portlandite

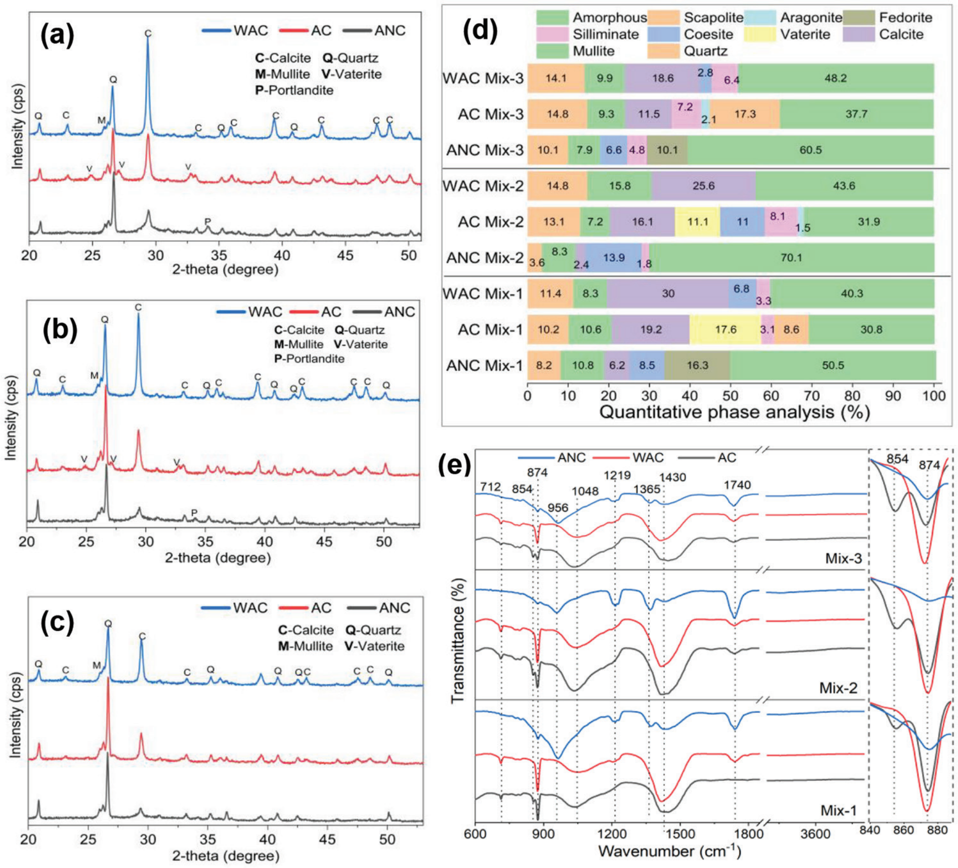

Fig. 5—XRD pattern of: (a) Mix-1 aggregate; (b) Mix-2 aggregate; and Mix-3 aggregate; and their (d) quantitative phases analysis; and (e) comparative FTIR spectra of ANC, WAC, and AC aggregates prepared from Mix-1, Mix-2, and Mix-3.

intensity indicates that Mix-1 had a higher-intensity portlandite peak, followed by Mix-2 and Mix-3. However, the portlandite peak was completely absent in AC and WAC aggregates, indicating the conversion of portlandite into calcium carbonate through carbonation. The calcite peaks in AC aggregates were less intense than in WAC aggregates, as vaterite formed alongside calcite in the AC aggregates. Similar trends were observed in Mix-2 and Mix-3 aggregates (Fig. 5(b) and (c)). Furthermore, the intensity of calcite in different mixtures depends on the percentage of CCS. Mix-1, comprising 40 wt. % CCS, had intense calcite peaks, followed by Mix-2 with 30 wt. % CCS, then Mix-3 with 20 wt. % CCS. The calcite peak in non-carbonated aggregates was due to the weathering or natural carbonation of CCS. Additionally, mullite and quartz were observed along with calcite in the artificial aggregates.

The quantitative analysis of different phases formed in aggregates just after the carbonation of Mix-1, Mix-2, and Mix-3 is shown in Fig. 5(d). The detailed Joint Committee on Powder Diffraction Standards (JCPDS) data are provided in the Appendix. The percentage of amorphous phases found in ANC aggregates of Mix-1, Mix-2, and Mix-3 was approximately 50.5%, 70.1%, and 60.5%, respectively. The percentage of amorphous phases in the AC aggregates of Mix-1, Mix-2, and Mix-3 was 30.8%, 31.9%, and 37.7%, respectively. Similarly, the WAC aggregates of Mix-1, Mix-2, and Mix-3 were 40.3%, 43.6%, and 48.2%. These results show that the ANC aggregates contained more amorphous phases due to the poor crystalline C-A-S-H gel than AC and WAC aggregates, whereas crystalline calcite and vaterite formed in the AC and WAC aggregates through carbonation from C-A-S-H gel. The WAC aggregate of Mix-1 showed the highest calcite content at 30%, whereas the AC aggregate of Mix-3 had the lowest at 11.5%. Other phases, including scapolite, aragonite, fedorite, sillimanite, coesite, mullite, and quartz, were also present in the aggregates.

FTIR spectra of alkali-activated aggregates are shown in Fig. 5(e). In the ANC aggregates, an asymmetrical stretching vibration band obtained at approximately 956 cm^{-1} may be attributed to C-A-S-H gel,[47-49] while the AC and WAC aggregates having the stretching vibration band at ~1048 cm^{-1} may be attributed to N-A-S-H gel.[49-51] Vibration bands observed at 874 cm^{-1}, 712 cm^{-1}, and in the range of 1400 to 1500 cm^{-1} are associated with the asymmetric bending vibrations of the O-C-O bond in the CO_3^{2-} group, indicating natural carbonation in ANC aggregates. These vibration bands were more intense in the AC and WAC aggregates due to the formation of calcite through carbonation.[48,49,52] The band observed at 854 cm^{-1} corresponded to vaterite, observed only in AC aggregates; these results are consistent with the XRD results. The absence of a sharp band at 3642 cm^{-1} indicated complete carbonation in WAC and AC aggregates and formation of C-A-S-H gel in ANC aggregates, as it is associated with stretching vibrations of the O-H bond in portlandite.[53,54]

Further, in FE-SEM analysis, it was observed that the morphology of non-carbonated aggregates was entirely

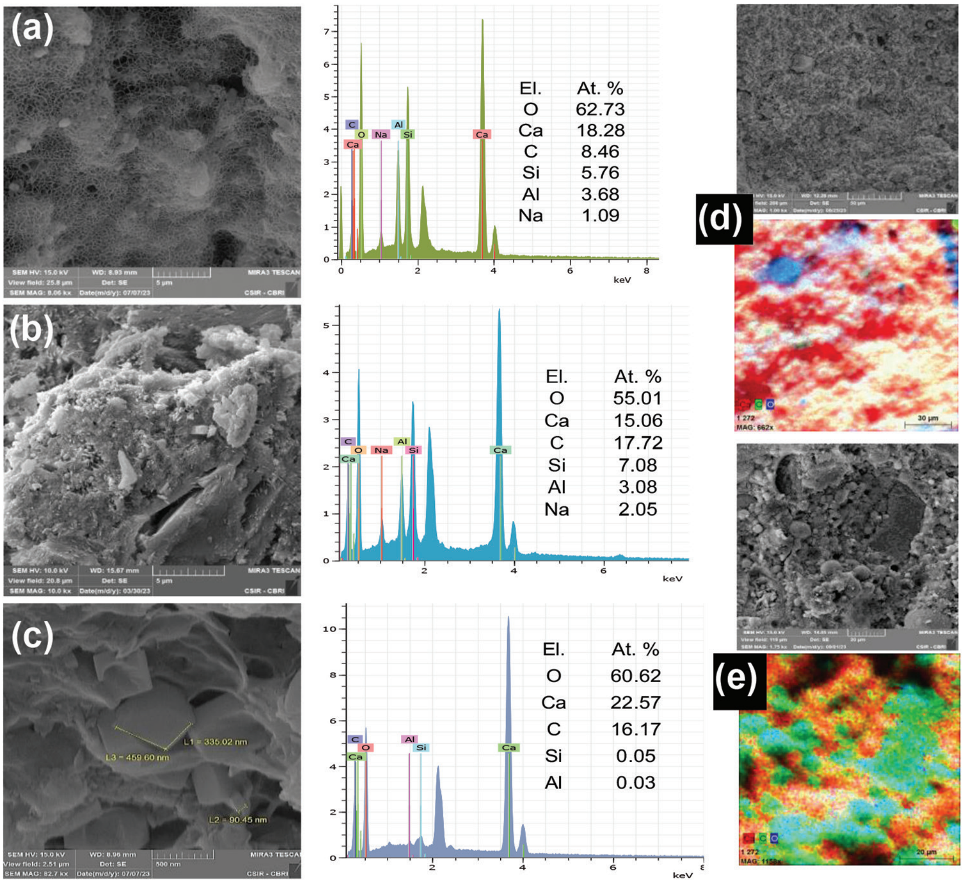

Fig. 6—FE-SEM/EDAX analysis of: (a) non-carbonated aggregates; (b) carbonated aggregates; and (c) rhombohedral calcite formed in carbonated aggregate; and elemental mapping of: (d) carbonated; and (e) non-carbonated aggregates.

different from the carbonated aggregates (Fig. 6). Non-carbonated aggregates exhibited a honeycomb-like structure, similar to that of the C-A-S-H gel (Fig. 6(a)).[55] In contrast, no such structure was observed in the carbonated aggregates (Fig. 6(b)). Instead, carbonated aggregates contained rhombohedral calcite crystals with sizes ranging from 90 to 500 nm (Fig. 6(c)). According to EDAX analysis, the ratio of atomic percentage of C atoms in the non-carbonated aggregate was 8.46%; after accelerated carbonation, carbon atoms increased to 17.72%, showing the formation of calcium carbonate. Elemental mapping performed at low magnification (1 kx) used RGB color coding (red for calcium, green for carbon, and blue for oxygen) to identify elements and their phases according to the provided legend (full-color PDF of this paper is available at www.concrete.org). Carbonated aggregates showed a predominant white color, indicating the presence of calcite, as the white color depicted the combination of Ca (red), C (green), and O (blue) (Fig. 6(d)). However, in non-carbonated aggregates, no such color was observed (Fig. 6(e)).

Studies on concrete incorporating alkali-activated carbonated aggregates

Concrete performance—The compressive strength of concrete largely depends on the strength of artificial aggregates, and to reduce CO_2 emissions during concrete production, it is imperative that the artificial aggregates sequester the maximum CO_2 during carbonation.[56] Therefore, in this study, two important factors were considered to optimize the mixture composition (FA and CCS): the aggregate strength and the CO_2 uptake. As shown in Fig. 7(a), the AC and WAC aggregates of Mix-2 achieved a maximum aggregate strength of 5.4 MPa and 5 MPa, respectively, and a CO_2 uptake of more than 10%. Aggregate strength is the key factor affecting concrete's compressive strength; increases in artificial aggregate strength increase compressive strength. Sim et al.[56] reported that the compressive strength of concrete depends on the artificial aggregate strength.

Therefore, the AC and WAC aggregate of this mixture was selected for casting concrete specimens with dimensions of 100 x 100 x 100 mm^3. The compressive strength of natural aggregate concrete after 7, 14, and 28 days of water curing was 32 MPa, 40 MPa, and 45 MPa, respectively (Fig. 7(b)). In comparison, concrete cast with AC aggregates achieved compressive strengths of 24, 33, and 39 MPa, while concrete cast with WAC aggregates achieved compressive strengths of 31, 29, and 38 MPa (Fig. 7(b)).

Furthermore, the concrete density of concrete is directly proportional to the bulk density of aggregates, as reported by Liu et al.[40] Concrete density results showed that with 100% replacement of natural aggregates with AC and WAC aggregates, concrete density decreased to 2065 kg/m^3 and 2085 kg/m^3, respectively, compared to the density of natural aggregate concrete of 2452 kg/m^3 (Fig. 7(b)). Concrete cast with WAC aggregates had a higher density than AC

Table 4—Calculated CO_2 emissions from artificial aggregate production, kg CO_2e

Aggregates	Process				CO_2 uptake	Total CO_2 emissions
	Autoclave process	Transport	Electricity	NaOH		
ANC	73	23	19	113	—	228
WAC	—	23	19	113	133	22
AC	73	23	19	113	125	103

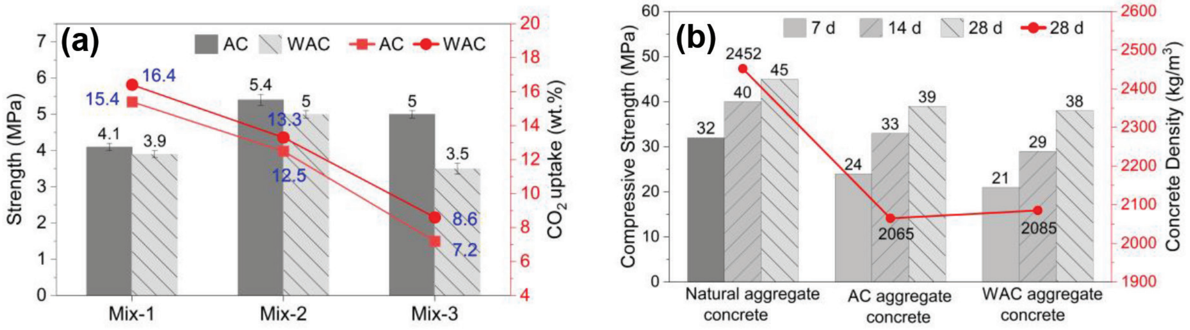

Fig. 7—(a) Optimization of mixture for production of carbonated alkali-activated aggregates; and (b) comparison of compressive strength and bulk density of concrete.

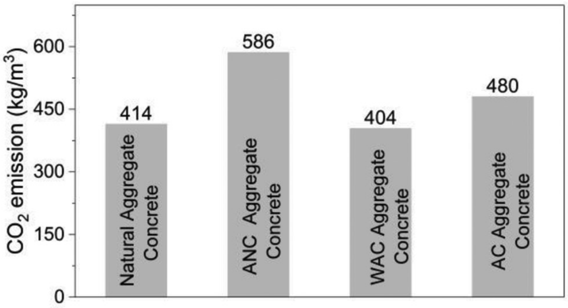

Fig. 8—Comparison of CO_2 emissions of concrete prepared with natural, ANC, WAC, and AC aggregates.

aggregate concrete, due to the higher bulk density of WAC aggregates compared to AC aggregates.

Environmental assessment—The global warming potential (GWP) of different types of artificial aggregates based on Class F FA and the CCS is shown in Table 4. Accordingly, the GWP of artificial aggregates is mainly attributed to the autoclave process and the sodium hydroxide solution, accounting for 113 and 73.4 kg CO_2e, respectively. After the accelerated carbonation, the CO_2 uptake of WAC and AC aggregates was 125 and 130 kg CO_2e, respectively.

The CO_2 emissions from natural aggregate concrete, ANC aggregate concrete, WAC aggregate concrete, and AC aggregate concrete are shown in Fig. 8. ANC aggregate concrete emitted 586 kg/m^3, WAC aggregate concrete emitted 404 kg/m^3, AC aggregate concrete emitted 480 kg/m^3, and natural aggregate concrete emitted 414 kg/m^3. Further, a general comparison of CO_2 emissions of artificial aggregate concrete with the previously reported data is shown in Fig. 9. Sarabèr et al.[57] reported the CO_2 emissions for sintered FA aggregate concrete and hydrothermal FA aggregate concrete produced approximately 607 and 523 kg/m^3. Liu et al.[40] also reported that CO_2 emissions by artificial aggregate concrete

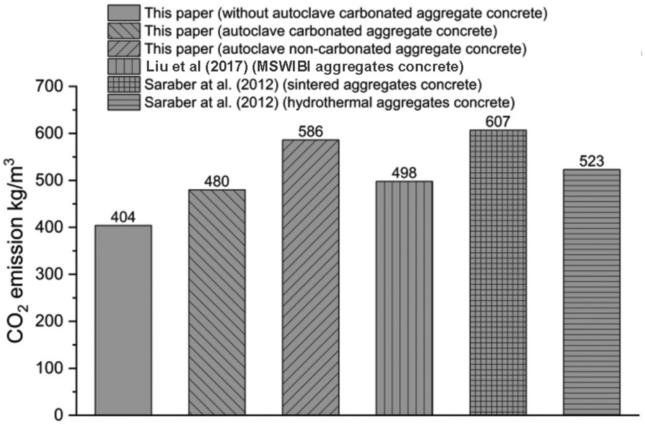

Fig. 9—Comparison of CO_2 emissions of concrete prepared in this study with concrete reported in literature.

were 498 kg/m^3. In comparison, the CO_2 emissions of concrete made with AC and WAC aggregates in this study were relatively lower.

DISCUSSION

Currently, the production of carbonated aggregates from Class F FA is limited due to its low calcium content. Geopolymer and sintered aggregates produced from Class F FA require energy-intensive processes and are not environmentally friendly. Geopolymer aggregates require higher-molarity sodium hydroxide (~12 M) and sodium silicate (water glass) solution to achieve adequate single aggregate strength and are non-carbonatable due to the formation of N-A-S-H gel. Similarly, sintered aggregates produced at temperatures above 1000°C require an energy-intensive process and are non-carbonatable. To address these challenges, this study demonstrated the production of carbonated alkali-activated aggregates produced from Class F FA and CCS using only a 5 M sodium hydroxide solution.

CCS, due to its strong alkalinity, cannot be used directly in construction because of its corrosive nature. However, this strong alkaline nature of CCS facilitates the production of carbonated aggregates at low-molarity sodium hydroxide and eliminates the need for sodium silicate solutions. The developed aggregates achieved a maximum single aggregate strength of ~5 MPa after 14 days of water curing. To achieve earlier strength, these aggregates were autoclaved, achieving the desired single aggregate strength just after carbonation. XRD and FTIR results show that before carbonation, the main reaction product in these aggregates was C-A-S-H gel, which converted to N-A-S-H gel and calcium carbonate after carbonation. FE-SEM results show that the microstructure of carbonated aggregates is denser due to the formation of nanosized calcium carbonate crystals (90 to 500 nm). These nanosized calcium carbonate crystals fill all the pores; thus, the single aggregate strength of carbonated aggregates is higher than that of non-carbonated aggregates. The bulk density of these aggregates ranged from 721 to 828 kg/m^3, classifying them as lightweight aggregates. The specific gravity of Class F FA is approximately 2.6, while that of CCS is approximately 2.2. Consequently, in different mixtures, bulk density primarily depends on the percentage of FA. However, within the same mixture, bulk density is influenced by the degree of carbonation, as the FA percentage remains constant. Therefore, in the same mixture, WAC aggregates with higher carbonation exhibit greater bulk density than AC aggregates. These aggregates are used in concrete as a replacement for natural aggregates.

Concrete specimens incorporating AC and WAC aggregates exhibited compressive strength of approximately 39 MPa and 38 MPa, respectively, after 28 days of water curing, making them suitable for reinforced concrete structures. The density of concrete with WAC and AC aggregates was reduced to 2085 and 2065 kg/m^3, compared to 2452 kg/m^3 for natural aggregate concrete.

The GWP of artificial aggregates mainly depends on the sodium hydroxide solution and CO_2 uptake through carbonation. The maximum CO_2 uptake by WAC and AC aggregates prepared from optimized Mix-2 was 13.3 wt. % and 12.5 wt. %, respectively. With the reduction in sodium hydroxide molarity from 12 to 5 M and increased CO_2 through accelerated carbonation, the GWP of these aggregates is significantly lower compared to geopolymer and sintered aggregates. Therefore, concrete incorporating these aggregates—that is, WAC and AC aggregates—reduced the overall CO_2 emissions of concrete compared with the concrete prepared with the geopolymer, sintered, and hydrothermal aggregates. Compared with sintered FA aggregate concrete, the CO_2 emissions of WAC and AC aggregate concrete are reduced by 33% and 21%, respectively.[57]

Therefore, incorporating these carbonated aggregates into concrete can significantly reduce the overall CO_2 emissions, contributing to a more sustainable and eco-friendly building material. Further research will focus on eliminating the use of sodium hydroxide without compromising strength, while aiming to enhance CO_2 uptake of artificial aggregates. Additionally, the use of different calcium-rich wastes with Class F FA will be explored to produce carbonated aggregates.

CONCLUSIONS

In this study, carbonated lightweight aggregates were developed from fly ash (FA) and calcium carbide sludge (CCS) using the alkali-activated cold-bonding pelletization method. The effect of autoclaving on the properties of aggregate strength was thoroughly examined. Additionally, the performance of concrete cast with these aggregates and the environmental assessment were also investigated. The following conclusions can be drawn:

1. A mixture of 70% FA and 30% CCS was selected as the optimal composition for producing alkali-activated lightweight carbonated aggregates, achieving a single aggregate strength in the range of 5 to 5.4 MPa and a bulk density of 721 to 828 kg/m^3. Autoclaving accelerates FA activation, achieving maximum strength in 3 days compared to 14 days without autoclaving. Additionally, CO_2 uptake by carbonated aggregates was in the range of 6.8 to 15.1%.
2. Fourier-transform infrared spectroscopy (FTIR) and field-emission scanning electron microscopy (FE-SEM) analyses revealed that calcium-aluminum-silicate-hydrate (C-A-S-H) gel formed in the non-carbonated aggregates, whereas after carbonation, sodium-aluminum-silicate-hydrate (N-A-S-H) gel was formed. The microstructure of carbonated aggregates is denser compared to non-carbonated aggregates. Carbonation resulted in the formation of rhombohedral calcites ranging from 90 to 500 nm in the carbonated aggregates.
3. The concrete using the optimized without-autoclave carbonated (WAC) and autoclave carbonated (AC) lightweight aggregates exhibited a compressive strength of 38 MPa and 39 MPa, respectively, after 28 days of water curing. The density of concrete with WAC and AC aggregates was reduced to 2065 kg/m^3 and 2080 kg/m^3, compared to 2452 kg/m^3 for natural aggregate concrete.
4. The total CO_2 emissions from autoclave non-carbonated (ANC), WAC, and AC aggregates are 229 kg CO_2e, –16 kg CO_2e, and 105 kg CO_2e, respectively. Concrete cast with WAC and AC aggregates achieved reductions in CO_2 emissions of 31% and 18%, respectively, compared to concrete cast with ANC aggregates.

The study presents an innovative approach to recycling a large volume of industrial waste (FA and CCS) to develop carbonated aggregates through the alkali activation process and accelerated carbonation. It demonstrates a viable alternative to replace natural aggregates with carbonated aggregates in concrete. Adopting these methodologies is imperative to achieving net-zero emissions by the end of the century.

AUTHOR BIOS

Mohd Hanifa *is a Researcher at the CSIR-Central Building Research Institute (CBRI), Roorkee, Uttarakhand, India, and a Doctoral Student at the Academy of Scientific and Innovative Research (AcSIR), Ghaziabad, Uttar Pradesh, India. He received his BSc and MSc from Banaras Hindu University, Varanasi, Uttar Pradesh, India. His research interests include the use of* CO_2 *in cement-based materials.*

Usha Sharma *is a Research Associate at CSIR-CBRI. She received her PhD from AcSIR. Her research interests include nanotechnology, cement chemistry, and carbon capture and use.*

P. C. Thapliyal *is a Chief Scientist at CSIR-CBRI and a Professor at AcSIR. He received his PhD from the University of Delhi, New Delhi, India. His research interests include corrosion, coating, nanotechnology, and building materials.*

L. P. Singh *is a distinguished scientist and currently serves as the Director General of the National Council for Cement and Building Materials and is also a Professor at AcSIR. He received his PhD from the University of Roorkee (now the Indian Institute of Technology [IIT] Roorkee), Roorkee, Uttarakhand, India. His research interests include cement, building materials, nanotechnology, and carbon capture and use in industrial waste.*

ACKNOWLEDGMENTS

The author M. Hanifa (Award number_191620059131) is grateful for the financial support provided by the UGC, New Delhi, India.

REFERENCES

1. NOAA, "Carbon Dioxide Now More than 50% Higher than Pre-industrial Levels," National Oceanic and Atmospheric Administration, Washington, DC, June 3, 2022, https://www.noaa.gov/news-release/carbon-dioxide-now-more-than-50-higher-than-pre-industrial-levels. (last accessed June 5, 2025)

2. Wikipedia, "Carbon Dioxide in Earth's Atmosphere," Wikimedia Foundation, last modified June 8, 2025, https://en.wikipedia.org/wiki/Carbon_dioxide_in_Earth%27s_atmosphere. (last accessed June 10, 2025)

3. Fawzy, S.; Osman, A. I.; Doran, J.; and Rooney, D. W., "Strategies for Mitigation of Climate Change: A Review," *Environmental Chemistry Letters*, V. 18, No. 6, Nov. 2020, pp. 2069-2094. doi: 10.1007/s10311-020-01059-w

4. United Nations Environment Programme, "2022 Global Status Report for Buildings and Construction: Towards a Zero-Emissions, Efficient and Resilient Buildings and Construction Sector," UNEP, Nairobi, Kenya, 2022, 101 pp.

5. Grand View Research, Inc., "Recycled Concrete Aggregates Market Size, Share & Trends Analysis Report By Product (Unprocessed, Processed), By Application (Bridges, Concrete Manufacturing, Roadway & Pavement), By Region, And Segment Forecasts, 2021 - 2028," Grand View Research, San Francisco, CA, 2023, 100 pp.

6. Qian, L.-P.; Wang, Y.-S.; Alrefaei, Y.; and Dai, J.-G., "Experimental Study on Full-Volume Fly Ash Geopolymer Mortars: Sintered Fly Ash Versus Sand as Fine Aggregates," *Journal of Cleaner Production*, V. 263, Aug. 2020, Article No. 121445. doi: 10.1016/j.jclepro.2020.121445

7. Tajra, F.; Abd Elrahman, M.; and Stephan, D., "The Production and Properties of Cold-Bonded Aggregate and Its Applications in Concrete: A Review," *Construction and Building Materials*, V. 225, Nov. 2019, pp. 29-43. doi: 10.1016/j.conbuildmat.2019.07.219

8. Gesoğlu, M.; Özturan, T.; and Güneyisi, E., "Effects of Cold-Bonded Fly Ash Aggregate Properties on the Shrinkage Cracking of Lightweight Concretes," *Cement and Concrete Composites*, V. 28, No. 7, Aug. 2006, pp. 598-605. doi: 10.1016/j.cemconcomp.2006.04.002

9. Gesoğlu, M.; Özturan, T.; and Güneyisi, E., "Effects of Fly Ash Properties on Characteristics of Cold-Bonded Fly Ash Lightweight Aggregates," *Construction and Building Materials*, V. 21, No. 9, Sept. 2007, pp. 1869-1878. doi: 10.1016/j.conbuildmat.2006.05.038

10. Wei, Y.-L.; Cheng, S.-H.; Ou, K.-T.; Kuo, P.-J.; Chung, T.-H.; and Xie, X.-Q., "Effect of Calcium Compounds on Lightweight Aggregates Prepared by Firing a Mixture of Coal Fly Ash and Waste Glass," *Ceramics International*, V. 43, No. 17, Dec. 2017, pp. 15573-15579. doi: 10.1016/j.ceramint.2017.08.110

11. Colangelo, F.; Messina, F.; and Cioffi, R., "Recycling of MSWI Fly Ash by Means of Cementitious Double Step Cold Bonding Pelletization: Technological Assessment for the Production of Lightweight Artificial Aggregates," *Journal of Hazardous Materials*, V. 299, Dec. 2015, pp. 181-191. doi: 10.1016/j.jhazmat.2015.06.018

12. Tang, P., and Brouwers, H. J. H., "The Durability and Environmental Properties of Self-Compacting Concrete Incorporating Cold Bonded Lightweight Aggregates Produced from Combined Industrial Solid Wastes," *Construction and Building Materials*, V. 167, Apr. 2018, pp. 271-285. doi: 10.1016/j.conbuildmat.2018.02.035

13. Das, D., and Rout, P. K., "Coal Fly Ash Utilization in India," *New Horizons for Industry 4.0 in Modern Business*, A. Nayyar, M. Naved, and R. Rameshwar, eds., Springer, Cham, Switzerland, 2023, pp. 233-251.

14. Provis, J. L., and Bernal, S. A., "Geopolymers and Related Alkali-Activated Materials," *Annual Review of Materials Research*, V. 44, 2014, pp. 299-327. doi: 10.1146/annurev-matsci-070813-113515

15. Zhang, Z.; Wang, H.; Provis, J. L.; Bullen, F.; Reid, A.; and Zhu, Y., "Quantitative Kinetic and Structural Analysis of Geopolymers. Part 1. The Activation of Metakaolin with Sodium Hydroxide," *Thermochimica Acta*, V. 539, July 2012, pp. 23-33. doi: 10.1016/j.tca.2012.03.021

16. Palomo, A., and Glasser, F. P., "Chemically-Bonded Cementitious Materials Based on Metakaolin," *British Ceramic Transactions and Journal*, V. 91, No. 4, 1992, pp. 107-112.

17. Shivaprasad, K. N., and Das, B. B., "Determination of Optimized Geopolymerization Factors on the Properties of Pelletized Fly Ash Aggregates," *Construction and Building Materials*, V. 163, Feb. 2018, pp. 428-437. doi: 10.1016/j.conbuildmat.2017.12.038

18. Xu, L.-Y.; Alrefaei, Y.; Wang, Y.-S.; and Dai, J.-G., "Recent Advances in Molecular Dynamics Simulation of the N-A-S-H Geopolymer System: Modeling, Structural Analysis, and Dynamics," *Construction and Building Materials*, V. 276, Mar. 2021, Article No. 122196. doi: 10.1016/j.conbuildmat.2020.122196

19. Xu, L.-Y.; Qian, L.-P.; Huang, B.-T.; and Dai, J.-G., "Development of Artificial One-Part Geopolymer Lightweight Aggregates by Crushing Technique," *Journal of Cleaner Production*, V. 315, Sept. 2021, Article No. 128200. doi: 10.1016/j.jclepro.2021.128200

20. Habert, G., and Ouellet-Plamondon, C., "Recent Update on the Environmental Impact of Geopolymers," *RILEM Technical Letters*, V. 1, 2016, pp. 17-23. doi: 10.21809/rilemtechlett.2016.6

21. Wittcoff, H. A.; Reuben, B. G.; and Plotkin, J. S., *Industrial Organic Chemicals*, third edition, John Wiley & Sons, Inc., Hoboken, NJ, 2012, 848 pp.

22. Guo, J., and Zheng, D., "Thermodynamic Analysis of Low-Rank-Coal-Based Oxygen-Thermal Acetylene Manufacturing Process System," *Industrial & Engineering Chemistry Research*, V. 51, No. 41, Oct. 2012, pp. 13414-13422. doi: 10.1021/ie301986q

23. Schobert, H., "Production of Acetylene and Acetylene-based Chemicals from Coal," *Chemical Reviews*, V. 114, No. 3, Feb. 2014, pp. 1743-1760. doi: 10.1021/cr400276u

24. Makaratat, N.; Jaturapitakkul, C.; Namarak, C.; and Sata, V., "Effects of Binder and $CaCl_2$ Contents on the Strength of Calcium Carbide Residue-Fly Ash Concrete," *Cement and Concrete Composites*, V. 33, No. 3, Mar. 2011, pp. 436-443. doi: 10.1016/j.cemconcomp.2010.12.004

25. Suttiprapa, P.; Tangchirapat, W.; Jaturapitakkul, C.; Rattanasak, U.; and Jitsangiam, P., "Strength Behavior and Autogenous Shrinkage of Alkali-Activated Mortar Made from Low-Calcium Fly Ash and Calcium Carbide Residue Mixture," *Construction and Building Materials*, V. 312, Dec. 2021, Article No. 125438. doi: 10.1016/j.conbuildmat.2021.125438

26. Sun, H.; Li, Z.; Bai, J.; Memon, S. A.; Dong, B.; Fang, Y.; Xu, W.; and Xing, F., "Properties of Chemically Combusted Calcium Carbide Residue and Its Influence on Cement Properties," *Materials*, V. 8, No. 2, 2015, pp. 638-651. doi: 10.3390/ma8020638

27. ASTM C618-19, "Standard Specification for Coal Fly Ash and Raw or Calcined Natural Pozzolan for Use in Concrete." ASTM International, West Conshohocken, PA, 2019, 5 pp.

28. Ren, P.; Ling, T.-C.; and Mo, K. H., "Recent Advances in Artificial Aggregate Production," *Journal of Cleaner Production*, V. 291, Apr. 2021, Article No. 125215. doi: 10.1016/j.jclepro.2020.125215

29. Takahashi, H.; Kou, T.; Kato, Y.; and Kato, E., "Effect of Water Saturation in Hardened Mortar Around a Steel Bar on Corrosion Considering Exposure History," *Journal of Building Engineering*, V. 98, Dec. 2024, Article No. 111213. doi: 10.1016/j.jobe.2024.111213

30. Zheng, J.; Zhou, Y.; Zhi, Y. T.; Su, W.; and Sun, Y., "Sorption Equilibria of CO_2 on Silica-Gels in the Presence of Water," *Adsorption*, V. 18, No. 2, Oct. 2012, pp. 121-126. doi: 10.1007/s10450-012-9387-1

31. Thompson, J. E., and Paluch, A. S., "Revisiting the Clausius/Clapeyron Equation and the Cause of Linearity," *Thermo*, V. 3, No. 3, Sept. 2023, pp. 412-423. doi: 10.3390/thermo3030025

32. IS 10262:2019, "Concrete Mix Proportioning — Guidelines (Second Revision)," Bureau of Indian Standards, New Delhi, India, 2019, 44 pp.

33. IS 516-1959, "Method of Tests for Strength of Concrete (Reaffirmed 2004)," Bureau of Indian Standards, New Delhi, India, 1959, 30 pp.

34. IS:2386 (Part III)-1963, "Methods of Test for Aggregates for Concrete: Part III Specific Gravity, Density, Voids, Absorption and Bulking (Reaffirmed 2002)," Bureau of Indian Standards, New Delhi, India, 1963, 22 pp.

35. Qian, L.-P.; Xu, L.-Y.; Huang, B.-T.; and Dai, J.-G., "Pelletization and Properties of Artificial Lightweight Geopolymer Aggregates (GPA): One-Part vs. Two-Part Geopolymer Techniques," *Journal of Cleaner Production*, V. 374, Nov. 2022, Article No. 133933. doi: 10.1016/j.jclepro.2022.133933

36. Alqahtani, F. K.; Rashid, K.; Zafar, I.; and Khan, M. I., "Assessment of Morphological Characteristics and Physico-Mechanical Properties of Geopolymer Green Foam Lightweight Aggregate Formulated by Microwave Irradiation," *Journal of Building Engineering*, V. 35, Mar. 2021, Article No. 102081. doi: 10.1016/j.jobe.2020.102081

37. Wu, Y.; Mehdizadeh, H.; Mo, K. H.; and Ling, T.-C., "High-Temperature CO_2 for Accelerating the Carbonation of Recycled Concrete Fines," *Journal of Building Engineering*, V. 52, July 2022, Article No. 104526. doi: 10.1016/j.jobe.2022.104526

38. Mehdizadeh, H.; Shao, X.; Mo, K. H.; and Ling, T.-C., "Enhancement of Early Age Cementitious Properties of Yellow Phosphorus Slag via CO_2 Aqueous Carbonation," *Cement and Concrete Composites*, V. 133, Oct. 2022, Article No. 104702. doi: 10.1016/j.cemconcomp.2022.104702

39. Yang, E.-H.; Yang, Y.; and Li, V. C., "Use of High Volumes of Fly Ash to Improve ECC Mechanical Properties and Material Greenness," *ACI Materials Journal*, V. 104, No. 6, Nov.-Dec. 2007, pp. 620-628.

40. Liu, J.; Li, Z.; Zhang, W.; Jin, H.; Xing, F.; and Tang, L., "The Impact of Cold-Bonded Artificial Lightweight Aggregates Produced by Municipal Solid Waste Incineration Bottom Ash (MSWIBA) Replace Natural Aggregates on the Mechanical, Microscopic and Environmental Properties, Durability of Sustainable Concrete," *Journal of Cleaner Production*, V. 337, Feb. 2022, Article No. 130479. doi: 10.1016/j.jclepro.2022.130479

41. Hammond, G., and Jones, C., "Embodied Carbon: The Inventory of Carbon and Energy (ICE): A BSRIA Guide," BSRIA 10/2011, F. Lowrie and P. Tse, eds., BSRIA Limited, Bracknell, Berkshire, UK, 2011, 136 pp.

42. Choi, W.-C.; Yun, H.-D.; Kang, J.-W.; and Kim, S.-W., "Development of Recycled Strain-Hardening Cement-Based Composite (SHCC) for Sustainable Infrastructures," *Composites Part B: Engineering*, V. 43, No. 2, Mar. 2012, pp. 627-635. doi: 10.1016/j.compositesb.2011.11.060

43. Shah, V.; Scrivener, K.; Bhattacharjee, B.; and Bishnoi, S., "Changes in Microstructure Characteristics of Cement Paste on Carbonation," *Cement and Concrete Research*, V. 109, July 2018, pp. 184-197. doi: 10.1016/j.cemconres.2018.04.016

44. Khachani, M.; El Hamidi, A.; Halim, M.; and Arsalane, S., "Non-isothermal Kinetic and Thermodynamic Studies of the Dehydroxylation Process of Synthetic Calcium Hydroxide $Ca(OH)_2$," *Journal of Materials and Environmental Science*, V. 5, No. 2, 2014, pp. 615-624.

45. Fletcher, D. A.; McMeeking, R. F.; and Parkin, D., "The United Kingdom Chemical Database Service," *Journal of Chemical Information and Computer Sciences*, V. 36, No. 4, July 1996, pp. 746-749. doi: 10.1021/ci960015+

46. Niu, T.; Xu, J.; and Huang, J., "Growth of Aragonite Phase Calcium Carbonate on the Surface of a Titania-Modified Filter Paper," *CrystEngComm*, V. 16, No. 12, Mar. 2014, pp. 2424-2431. doi: 10.1039/C3CE42322K

47. Bernal, S. A.; Provis, J. L.; Rose, V.; and Mejía de Gutierrez, R., "Evolution of Binder Structure in Sodium Silicate-Activated Slag-Metakaolin Blends," *Cement and Concrete Composites*, V. 33, No. 1, Jan. 2011, pp. 46-54. doi: 10.1016/j.cemconcomp.2010.09.004

48. Garcia-Lodeiro, I.; Palomo, A.; Fernández-Jiménez, A.; and Macphee, D. E., "Compatibility Studies between N-A-S-H and C-A-S-H Gels. Study in the Ternary Diagram Na_2O–CaO–Al_2O_3–SiO_2–H_2O," *Cement and Concrete Research*, V. 41, No. 9, Sept. 2011, pp. 923-931. doi: 10.1016/j.cemconres.2011.05.006

49. Walkley, B.; San Nicolas, R.; Sani, M.-A.; Rees, G. J.; Hanna, J. V.; van Deventer, J. S. J.; and Provis, J. L., "Phase Evolution of C-(N)-A-S-H/N-A-S-H Gel Blends Investigated via Alkali-Activation of Synthetic Calcium Aluminosilicate Precursors," *Cement and Concrete Research*, V. 89, Nov. 2016, pp. 120-135. doi: 10.1016/j.cemconres.2016.08.010

50. Fernández-Jiménez, A., and Palomo, A., "Mid-Infrared Spectroscopic Studies of Alkali-Activated Fly Ash Structure," *Microporous and Mesoporous Materials*, V. 86, No. 1-3, Nov. 2005, pp. 207-214. doi: 10.1016/j.micromeso.2005.05.057

51. Fang, G., and Zhang, M., "Multiscale Micromechanical Analysis of Alkali-Activated Fly Ash-Slag Paste," *Cement and Concrete Research*, V. 135, Sept. 2020, Article No. 106141. doi: 10.1016/j.cemconres.2020.106141

52. dos Santos, V. H. J. M.; Pontin, D.; Ponzi, G. G. D.; Stepanha, A. S. G.; Martel, R. B.; Schütz, M. K.; Einloft, S. M. O.; and Dalla Vecchia, F., "Application of Fourier Transform Infrared Spectroscopy (FTIR) Coupled with Multivariate Regression for Calcium Carbonate ($CaCO_3$) Quantification in Cement," *Construction and Building Materials*, V. 313, Dec. 2021, Article No. 125413. doi: 10.1016/j.conbuildmat.2021.125413

53. Yi, H.; Zhan, W.; Zhao, Y.; Qu, S.; Wang, W.; Chen, P.; and Song, S., "A Novel Core-Shell Structural Montmorillonite Nanosheets/Stearic Acid Composite PCM for Great Promotion of Thermal Energy Storage Properties," *Solar Energy Materials and Solar Cells*, V. 192, Apr. 2019, pp. 57-64. doi: 10.1016/j.solmat.2018.12.015

54. Yi, H.; Ai, Z.; Zhao, Y.; Zhang, X.; and Song, S., "Design of 3D-Network Montmorillonite Nanosheet/Stearic Acid Shape-Stabilized Phase Change Materials for Solar Energy Storage," *Solar Energy Materials and Solar Cells*, V. 204, Jan. 2020, Article No. 110233. doi: 10.1016/j.solmat.2019.110233

55. Zhao, D.; Gao, Y.; Nie, S.; Liu, Z.; Wang, F.; Liu, P.; and Hu, S., "Self-Assembly of Honeycomb-Like Calcium-Aluminum-Silicate-Hydrate (C-A-S-H) on Ceramsite Sand and Its Application in Photocatalysis," *Chemical Engineering Journal*, V. 344, July 2018, pp. 583-593. doi: 10.1016/j.cej.2018.03.074

56. Sim, J.-I.; Yang, K.-H.; Kim, H.-Y.; and Choi, B.-J., "Size and Shape Effects on Compressive Strength of Lightweight Concrete," *Construction and Building Materials*, V. 38, Jan. 2013, pp. 854-864. doi: 10.1016/j.conbuildmat.2012.09.073

57. Sarabèr, A.; Overhof, R.; Green, T.; and Pels, J., "Artificial Lightweight Aggregates as Utilization for Future Ashes – A Case Study," *Waste Management*, V. 32, No. 1, Jan. 2012, pp. 144-152. doi: 10.1016/j.wasman.2011.08.017

ACI MATERIALS JOURNAL TECHNICAL PAPER

Title No. 122-M29

Advances in Engineered Cementitious Composites: A Comprehensive Review

by N. M. Sutan, F. Amsyar Redzuan, A. R. B. A. Karim, N. M. Sa'don, Y. S. S. Hui, and C. C. Y. Jie

Engineered cementitious composites (ECC) represent a significant innovation in construction materials due to their exceptional flexibility, tensile strength, and durability, surpassing traditional concrete. This review systematically examines the composition, mechanical behavior, and real-world applications of ECC, with a focus on how fiber reinforcement, mineral additives, and micromechanical design improve its structural performances. The present study reports on the effects of various factors, including different types of mineral admixtures, aggregate sizes, fiber hybridization, and specimen dimensions. Key topics include ECC's strain-hardening properties, its sustainability, and its capacity to resist crack development, making it ideal for high-performance infrastructure projects. Additionally, the review discusses recent advancements in ECC technology such as hybrid fiber reinforcement and the material's growing use in seismic structures. The paper also addresses the primary obstacles, including high initial costs and the absence of standardized specifications, while proposing future research paths aimed at optimizing ECC's efficiency and economic viability.

Keywords: bendable concrete; engineered cementitious composites (ECC); high-performance concrete; hybrid fiber reinforcement; mineral additives; sustainable construction.

INTRODUCTION

Most of the present construction and infrastructure relies heavily on concrete, a fundamental material composed of cement and fine and coarse aggregates.[1] Concrete's importance in modern construction has led to significant advancements, one of which is the development of engineered cementitious composites (ECC).[2] ECC is an ultra-ductile, cement-based material engineered for cost-effective, large-scale construction. Also known as bendable concrete, ECC represents a unique subset of fiber-reinforced concrete (FRC), which incorporates fibers into a cementitious matrix to achieve superior mechanical properties.[3,4] The cement-based, strain-hardening nature of ECC allows it to exhibit tensile strain capacities 300 to 500 times higher than traditional concrete.[4] ECC, recognized as a high-performance fiber-reinforced cementitious composite (HPFRCC),[1] achieves its outstanding performance through the precise balance of its core components: cement, fine silica sand, polymer fibers, fly ash, water, and high-range water-reducing admixtures (HRWRAs). Notably, coarse aggregates are intentionally omitted to improve its ductility.[5] Despite its established composition, ECC lacks standardized international specifications due to its versatility and unique performance attributes, which include superior ductility, workability, and resistance to fire and water—qualities that make it comparable to ultra-high-performance concrete (UHPC).[6]

However, the use of ECC is limited by its higher initial costs, primarily attributed to the exclusion of coarse aggregates. Despite this, ECC technology is steadily gaining global recognition due to its long-term advantages, positioning it as a strong material for commercialization. Ongoing research and development continue to explore its extensive capabilities, solidifying ECC's place as a vital material for the future of construction.[7] Figure 1 illustrates a flowchart of ECC research, highlighting its evolution from material design to commercial application. This review explores the theoretical principles, mechanical performance, and practical uses of ECC, while also addressing the challenges and future outlook for this innovative material in modern construction. The authors envision that by consistently disseminating new insights and advancements in ECC technology, its growth and implementation will rapidly advance over the next decade.

RESEARCH SIGNIFICANCE

This paper highlights ECC as revolutionary materials in construction. ECC offers exceptional flexibility, compressive and tensile strengths, and durability, making it ideal for high-performance infrastructure projects. This review examines its strain-hardening behavior, self-healing properties, and the durability of ECC under extreme environmental conditions. It also emphasizes the ability of ECC to prevent structural damage, improve seismic resilience, and control cracking, while promoting the use of hybrid fiber reinforcement and sustainable materials to develop more durable, cost-effective, and feasible infrastructure solutions for the future.

ENGINEERING PROPERTIES OF ECC

A range of systematic design methods has been proposed and refined to achieve the optimal mechanical properties of ECC, grounded in the fundamentals of fracture mechanics and micromechanics. These approaches ensure that ECC meets the optimal strength, ductility, and energy absorption criteria, which are crucial for fostering the

---

ACI Materials Journal, V. 122, No. 4, July 2025.

MS No. M-2024-374.R3, doi: 10.14359/51746811, received April 14, 2025, and reviewed under Institute publication policies. Pertinent discussion including author's closure, if any, will be published ten months from this journal's date if the discussion is received within four months of the paper's print publication.

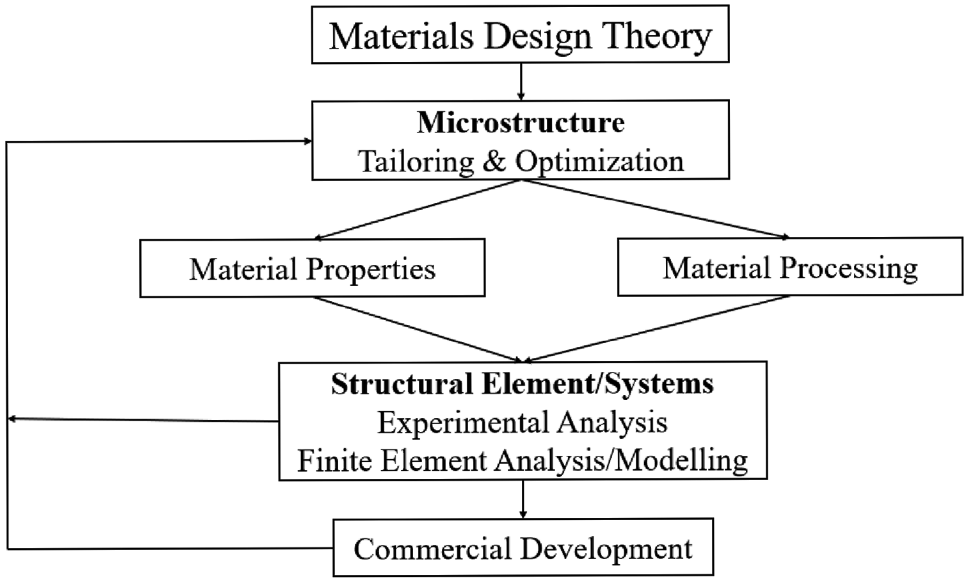

Fig. 1—Flowchart illustrating key elements in research and development of ECC.[2]

necessary interactions between the matrix and fibers, ultimately enhancing the composite's overall performance.[8,9]

Strength incorporated with mineral admixtures

ECC have garnered significant attention due to their remarkable ductility, which provides a substantial advantage over conventional normalweight concrete by reducing the risk of structural failure from fractures.[2] Conventionally, structural strength has been closely associated with the concrete's compressive strength. However, recent studies indicate that higher compressive strength does not always translate to ultimate overall structural performance. For instance, Billington and Yoon[10] highlighted this through cyclic shear load tests, where an ECC panel with a compressive strength of 41 MPa outperformed a conventional concrete panel with 50 MPa, demonstrating a structural strength of 56 kN versus 38 kN, respectively. This finding underscores ECC's potential to deliver enhanced structural performance, even with lower compressive strength. To address this issue, an increasing volume of research has focused on understanding how different materials and mineral admixtures impact ECC's performance. Meng et al.[11] demonstrated that the replacement of silica sand with lightweight aggregates such as dune sand maintained compressive strength while improving ultimate tensile and flexural strengths, though tensile strain capacity decreased. Similarly, Li and Yang[12] showed that recycled concrete fines (RCF) can maintain typical ECC compressive strength, but lead to reduced performance with larger RCF sizes and higher content levels. However, higher sand content significantly diminished these properties, highlighting the delicate balance between mixture design and performance.[13-16] Huang et al.[17] replaced iron ore tailings with fly ash cenosphere (FAC), resulting in improved tensile strain capacity despite reductions in compressive strength.

The role of mineral admixtures in improving ECC's compressive strength is critical, particularly when used with fine aggregates that contribute to a dense microstructure. This strength is further bolstered by short fibers that enhance load transfer and crack resistance, as discussed by Barbhuiya et al.[7] Researchers such as Wang and Li,[18] Yu et al.,[19] and Sahmaran et al.[20] have conducted extensive studies on ECC's mechanical characteristics, including compressive, flexural, and tensile strengths, as well as its fire resistance and the use of predictive models to enhance performance. Yu et al.[21] also examined a high-volume limestone-calcined clay blend for medium-strength ECC, showing that this mixture not only delivers favorable mechanical properties but also helps to reduce environmental impact. Huang et al.[17] demonstrated that ECC/strain-hardening cementitious composites (SHCC) can achieve ultra-high compressive strengths above 210 MPa, showing their applicability in high-strength engineering fields. Collectively, most studies demonstrate that ECC's performance is highly dependent on the type and size of aggregates, mineral admixtures, and fibre content, highlighting its versatility in achieving both structural performance and sustainability goals.[22-24] Various mineral admixtures—including fly ash, palm oil fuel ash, ground-granulated blast-furnace slag (GGBS), and recycled concrete fines—have been successfully incorporated into ECC, replacing traditional cement and silica sand components.[1] Table 1 provides a summary of previous research studies conducted by various researchers on the properties of ECC, focusing on the partial or full replacement of sand and cement with different mineral admixtures.

Ductility behavior

The strain capacity of ECC has garnered a decent trending, as it can range from 3 to 8%, particularly enhancing its ductility when compared to typical normalweight concrete. This exceptional strain capacity allows ECC to undergo significant deformation without failure, positioning it as a highly flexible and resilient material in modern construction. The higher strain capacity of ECC, coupled with multiple fine cracking, results in improved strength, ductility, fracture energy, and tighter crack widths, particularly under tensile loading.[1] When comparing typical concrete, FRC,

Table 1—Overview of previous research studies on properties of ECC with partial and full replacement of sand and cement using various mineral admixtures

Reference	Type of fine aggregate used	Replacement, %	Compressive strength	Tensile strength	Ultimate tensile strength	Flexural strength	Crack width	Drying shrinkage
Meng et al.[11]	Local dune sand	100%	Almost same as normalweight concrete	81 MPa	15 MPa	9 MPa	—	—
Li and Yang[12]	Recycled concrete fines (RCF)	100%	22 MPa by increasing the size of RCF	Almost same as normalweight concrete	—	3 MPa with 600 μm RCF	—	—
Huang and Zhang[13]	FAC (fly ash cenosphere)	Up to 100% (almost double the strength of normalweight concrete)	8 MPa	25 MPa	20 MPa	—	58 μm	—
Huang et al.[15]	Silica sand with silica fume	65% below 300 μm silica sand	21 to 22 MPa	15.6 to 16.2 MPa	3.4 to 5.2%	—	71.2 to 112.3 μm	—
Huang et al.[17]	Local dune sand	100%	Almost same as normalweight concrete	Slightly lower than normalweight concrete (decrease)	17 MPa	—	—	—
Sahmaran et al.[20]	Lightweight aggregate (LWA)	Up to 20%	25 MPa	21 MPa	19 MPa	13 MPa	9 μm	37
Altwair et al.[25]	Palm oil fuel ash (POFA)	55% with mass of cement	3 MPa (with 18% of POFA)	—	—	7 MPa (with 18% of POFA)	—	—
Zhu et al.[26]	Tire rubber	Up to 40%	74 MPa at 40% replacement	67 MPa	36 MPa	—	13 μm	50
Zhang and Qian[27]	Crumb rubber	Up to 25%	35 MPa	—	—	Slightly lower than the traditional concrete	29 μm	—
Ling et al.[28]	Iron ore tailings (IOTs)	Up to 80%	35 MPa	28 MPa	13 MPa	—	36 μm at ultimate stress	—
Gulghane and Bari[29]	Slag sand (replacement of cement)	Up to 30%	28 to 42 MPa (for 7 and 28 days)	2 to 5.8 MPa (for 7 and 28 days)	7 MPa	—	—	—
Turk and Demirhan[30]	Limestone powder replaced by microsilica sand	25%, 50%, 75%, and 100%	29 to 68 MPa (up to 90-day curing period)	8 to 12 MPa subjected to large deflection	—	1.3 to 11.4 MPa (up to 90-day curing period)	3 to 5.8 μm	—
Raza et al.[31]	Yellow River sand replacement	0%, 25%, 50%, 75%, and 100%	26 to 35 MPa	—	—	79% improved compared to typical concrete	Up to 6 μm crack width	—

and ECC under tensile stress, traditional concrete displays brittle behavior, while FRC exhibits tension-softening after the initial crack, demonstrating a clear distinction in performance, as illustrated in Fig. 2.[32]

The tension-softening behavior in FRC is primarily caused by the propagation of cracks and fiber rupture, which ultimately reduces its stress-carrying capacity. Conversely, ECC shows a strain-hardening response, characterized by multiple cracks resulting from the slip-hardening behavior of its fibers.[33,34] This difference highlights ECC's superior capacity to withstand tensile forces without compromising its structural integrity. Moreover, as compressive strength increases, studies have consistently shown a concurrent rise in brittleness or ductility, further emphasizing the material's robustness.[25,26] This property has significant implications for the application of ECC in seismic elements, where its high ductility can considerably enhance a structure's seismic resilience. The incorporation of low-modulus fibers such as polyvinyl alcohol (PVA),[18] polypropylene (PP), and polyethylene (PE) has also been recognized for their ability to significantly reduce cracking and improve the ductility of concrete mixtures. These fibers enhance tensile strain capacity and ductility while minimizing interfacial bonding and friction, particularly when coated with oil to optimize their performance within the matrix.[35-38] Such findings are corroborated by Li,[3] who demonstrated that the ductility or

Table 2—Comprehensive summary of key international testing methods for assessing uniaxial tensile strength of ECC

Testing outcome	Testing standards	Description
Uniaxial tensile strength	AASHTO T 132-87[39]	Standard method of test for tensile strength of hydraulic cement mortars.
	RILEM TC 162-TDF[40]	Test and design methods for steel FRC. Recommendations for uniaxial tension test.
	AFGC[41]	Ultra-high-performance FRC, interim recommendations.
	JSCE[42]	Recommendations for design and construction of high-performance FRC composites with multiple fine cracks.
Flexural strength	ASTM C293/C293M-10[43]	Standard test method for flexural strength of concrete (using simple beam with center-point loading).
	ASTM C78/C78M-10[44]	Standard test method for flexural strength of concrete (using simple beam with third-point loading).
Residual strength	ASTM C1399/C1399M-10[45]	Test method for obtaining average residual-strength of FRC.
	ASTM C1609/C1609M-12[46]	Test method for flexural performance of FRC.
	RILEM TC 162-TDF[47]	Test and design methods for steel FRC; bending test.
	BS EN 14651[48]	Test method for metallic fiber concrete. Measuring the flexural tensile strength (limit of proportionality [LOP], residual).

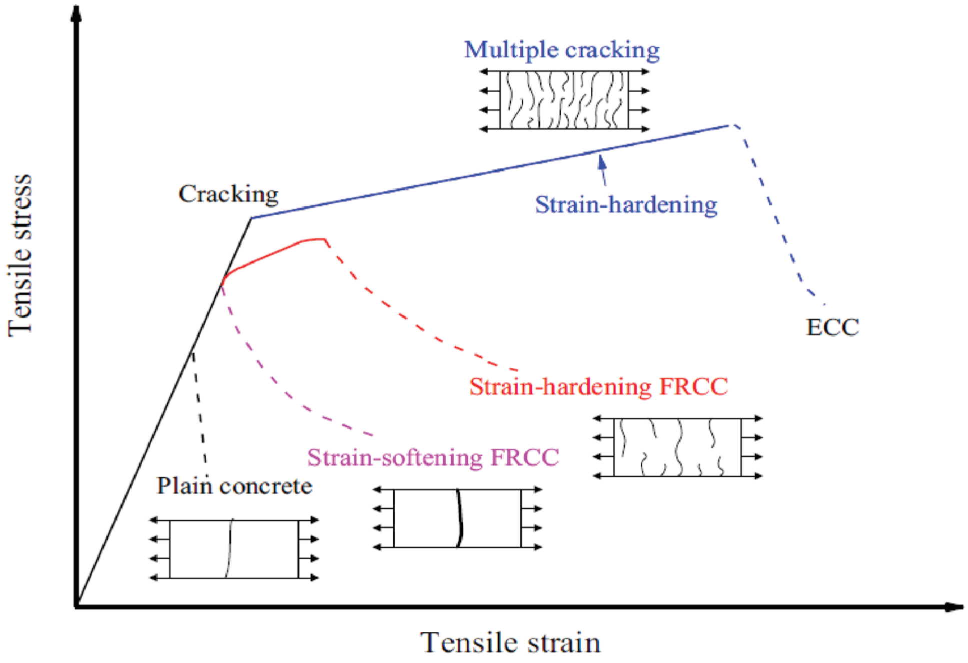

Fig. 2—Stress-strain curves illustrating tensile response of typical normalweight concrete, FRC, and ECC under tensile loading.[32]

brittleness of concrete is directly proportional to its strength, thereby increasing the risk of sudden fracture failure, which underscores the need for materials such as ECC in high-performance applications.

A comprehensive summary of testing methods, including international standards, supporting the material's performance is tabulated in Table 2. Further research has focused on using discontinuous microfibers as intrinsic reinforcement in ECC to improve its toughness and structural performance.[49] Additionally, studies have demonstrated ECC's enhanced resistance to chloride diffusion during wetting-and-drying cycles, greatly increasing its long-term durability.[50] The self-healing properties of ECC, as shown by Li and Li,[51] also help to mitigate chloride ingress by limiting crack growth. Recent research has confirmed ECC's effectiveness against chloride penetration, with Sun et al.[52] and Shumuye et al.[53] noting improvements in both self-healing and chloride resistance. In addition, Wang et al.[54] confirmed that ECC sustains its chloride resistance even under continuous flexural loading, making it highly suitable for structures requiring strong chloride protection.

Workability related to water-cement content

In addition to its strength, ECC offers good workability, including self-consolidating characteristics.[55] Its versatility allows ECC to be applied in different forms, whether cast, extruded, or sprayed, making it adaptable to various construction techniques. Unlike traditional concrete, ECC develops a more compact structure due to its finer particles filling the spaces left by larger ones, which enhances its workability performance and durability in challenging environments. Research conducted by Altwair et al.,[25] Sasmal and Avinash,[56] Pan et al.,[57] Zhu et al.,[58] and Yang et al.[59] observed that increasing the water-cement ratio (*w*/*c*), particularly between 0.30 and 0.38, leads to a noticeable reduction in compressive strength, initial crack strength, and flexural strength. Despite these reductions in mechanical properties, a higher *w*/*c* significantly enhances the workability of the mixture, making it easier to handle during construction.[25,56-59] Additionally, a higher *w*/*c* improves strain hardening, promotes multiple cracking, and increases flexural deflection capacity. In contrast, a lower *w*/*c* yields greater strength but less ductility.[25,56,57] Şahmaran et al.[60] demonstrated that adjusting the *w*/*c* and HRWRA dosage can optimize ECC's workability. Fischer and Wang[61] highlighted the importance of mixture design and fiber content in improving ECC's flowability. Kim et al.[62] found that the addition of GGBS improved tensile strength and fiber distribution while also enhancing workability when used with the correct *w*/*c*. These studies highlight the importance of optimizing mixture designs and using supplementary materials to maximize ECC's workability for various construction applications.

Durability performance

Durability is a fundamental requirement for construction materials, especially when used in long-term engineering projects.[32] In conventional normalweight concrete, increasing durability often involves enhancing its strength and Young's modulus, but this comes at the cost of brittleness and a greater tendency to failure-crack. Thereby, ECC offers an alternative solution by providing durability without brittle failure, while maintaining a lightweight structure, high strength, and significant strain capacity.[63] ECC's ability to perform well in challenging conditions is largely due to its use of PVA fibers, which meet the micromechanical requirements for strain-hardening behavior, ensuring that ECC can maintain durability without cracking.[64] Unlike typical concrete, which relies on density for durability, ECC achieves this through its microcracking behavior and self-healing properties. These characteristics, along with its large fiber content, allow ECC to outperform regular concrete in freezing-and-thawing cycles, carbonization, permeability, and high-temperature conditions.[64-67] To maintain high durability with optimal strength, it is essential that the crack width in ECC remains below 100 μm.[66] In their study, Şahmaran et al.[68] found that adding PVA fibers eliminated explosive spalling in ECC, while the inclusion of fly ash further enhanced its heat resistance. According to Yu et al.,[69] this reduction in strain-hardening capacity is caused by a decrease in the number of microcracks. Mechtcherine et al.[70] concurrently found that at 100°C, PVA-ECC's strain capacity improves with strain rate, but at 150°C, ECC loses its ductility and starts showing strain rate effects. In conclusion, ECC's unique combination of microcracking behavior, fiber reinforcement, and self-healing capacity makes it a highly durable material, capable of performing under a variety of harsh and ultimate environmental conditions, from freezing-and-thawing cycles to high-temperature scenarios.

Ultra-high performance

The need for ultra-high-performance materials in contemporary construction has driven the advancement of ECC as a pivotal innovation.[19,21,71] As infrastructure projects grow more complex, including super-tall skyscrapers, long-span bridges, and large-scale dams, conventional concrete encounters significant challenges in terms of strength, durability, and energy absorption. Ultra-high-performance ECC, especially when reinforced with fibers such as PE, has proven to be a better solution, delivering exceptional mechanical properties that meet the stringent demands of modern engineering. High-strength (HS) ECC with excellent performance, as demonstrated in Fig. 3, is designed to meet the rigorous strength and durability requirements of modern building materials, as highlighted by Huang et al.[15] and Ding et al.[72] Ran et al.[73-75] made advancements in ECC technology by developing a multifunctional ultra-lightweight (ULW) ECC incorporating FAC and PE fibers. This material achieved a density under 1400 kg/m^3, a compressive strength greater than 60 MPa, and tensile strength and strain capacity above 6 MPa and 3%, respectively. ECC has also progressed significantly in Japan and Europe, where it is

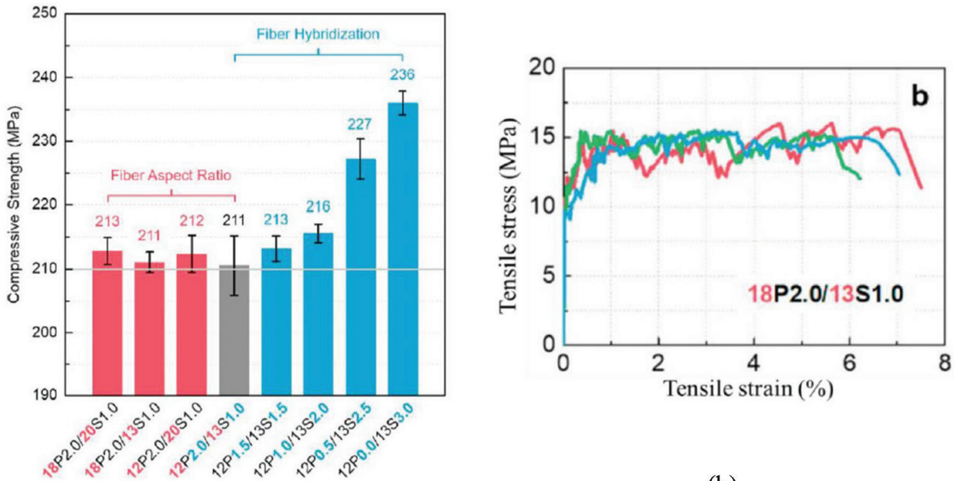

(a)

(b)

Fig. 3—Mechanical engineering properties of HS-ECC: (a) compressive strength; and (b) tensile strength behavior.[20,72]

Table 3—Summary of various fiber types integrated with ECC, as documented by different researchers in previous studies

Main category of fibers	Types of fibers used	Reference
Synthetic fibers	Polyvinyl alcohol fiber (PVA)	Meng et al.,[11] Li and Yang,[12] Huang and Zhang,[13] Zhou et al.,[14] Huang et al.,[17] Sahmaran et al.,[20] Altwair et al.,[25] Zhang and Qian,[27] Lepech and Li,[32] Soe et al.,[36] Kawamata et al.,[37] Lawler et al.,[38] Sasmal and Avinash,[56] Pan et al.,[57] Şahmaran et al.,[60] Pakravan et al.,[88] Alrefaei et al.,[89] Gadhiya et al.,[90] Mohammed et al.,[91] Ali et al.,[92] Said et al.,[93] Keoleian et al.,[94] Thaishnavi et al.,[95] Gencturk and Hosseini,[96] Wang et al.,[97] Al-Gemeel et al.[98]
	Polypropylene fiber (PP)	Pakravan et al.,[88] Thaishnavi et al.,[95] Gencturk and Hosseini,[96] Felekoglu et al.,[99] Afefy and Mahmoud[100]
	Polyethylene fiber (PE)	Kawamata et al.,[37] Lawler et al.,[38] Said et al.,[93] Maalej et al.,[101] Fischer et al.,[102] Yu et al.[103]
	Polymeric fiber	Singh et al.[104]
	Shape memory alloy (SMA)	Qiu and Yang[105]
Metallic fibers	Steel fiber (SE)	Soe et al.,[36] Kawamata et al.,[37] Lawler et al.,[38] Tian and Zhang,[84,86] Tian et al.,[85] Yang and Li,[87] Gadhiya et al.,[90] Wang et al.,[97] Maalej et al.[101]
	Tire-wire fiber	Mohammed et al.[91]
Glass fiber		Thaishnavi et al.[95]
Natural fibers	Bagasse fiber	Tian and Zhang,[84,86] Tian et al.[85]
	Basalt	Wang et al.,[97] Al-Gemeel et al.[98]

called ultra-high-performance fiber-reinforced cementitious composites (UHPFRCC) in Japan[76] and SHCC in Europe.[77]

PERFORMANCE OF SYNTHETIC FIBERS IN ECC

The incorporation of synthetic fibers in ECC is vital for enhancing its mechanical properties, durability, and structural integrity, which in turn extends its service life. While synthetic fibers such as PP are commonly used to enhance the mechanical performance of ECC, the environmental impact of synthetic fibers remain a growing concern, particularly regarding to their non-biodegradability and potential for microplastic release.[78-80] Singh et al.[1] found that a fiber volume fraction of approximately 2% typically results in significant strain-hardening behavior, improving ECC's capacity to endure high stress. In addition to steel bars, fibers such as synthetic, basalt, and hybrid are often used to increase the tensile strength of concrete, making ECC particularly effective in resisting tension-related cracking. PVA fibers, in particular, have gained widespread use in ECC due to their excellent dispersion and their ability to promote strain-hardening.[81] Other polymer fibers similarly contribute to strengthening ECC, while various aggregates influence the material's fracture energy.[26,78,82,83] While PVA fibers are the most commonly used, studies have also explored the use of natural fibers,[84-87] as detailed in Table 3. Although the use of fibers in ECC results in better performance, the side effects related to environmental and health concerns cannot be neglected.[78,79,106] The degradation of bagasse fiber in cementitious composites may raise health concerns due to the release of organic material under harsh environmental conditions, which may lead to biohazards if not properly managed.[83,86] Additionally, the use of PP fibers in ECC can potentially release fibers during production and handling, leading to concerns about the inhalation of fine particles, which may cause respiratory issues.[78-80,107]

Effect of hybrid fibers on ECC

When different fibers are combined in ECC, it is referred to as hybrid fiber incorporated ECC. This combination of fibers significantly influences the ECC's overall performance. For example, partially replacing PVA fibers blended with PP fibers can increase the deformability of ECC while reducing costs.[88] Hybrid fibers offer synergistic benefits by blending the unique properties of various fiber types. The selection of fibers in hybrid ECC depends on the desired mechanical properties, durability, and cost-effectiveness.[7] Research by Pan et al.[57] demonstrated that hybrid PVA fibers reduced the complementary energy of ECC but improved strain-hardening and multiple cracking behavior, while also reducing the material costs. High-modulus hybrid fibers are effective at increasing strength, whereas low-modulus fibers improve ductility and strain-hardening, resulting in finer cracks and reduced crack widths.[36,88,89,101] In terms of flexural strength, Gadhiya et al.[90] found that increasing the volume of steel fibers from 3 to 4% combined with PVA fibers from 1.5 to 2.0% improved flexural strength significantly by 15 to 20%. Mohammed et al.[91] further investigated hybridization by incorporating tire-wire and PVA fibers. They observed improvements in flexural strength, tensile strength, and modulus of elasticity, though there was a decrease in workability.

Effect of length, shape, and orientation of fibers on ECC

Fiber-reinforced ECC is a composite material that incorporates fibers of different lengths and orientations, which significantly impact its mechanical performance. This selection of fibers, whether steel, glass, synthetic, or natural, can be arranged either in parallel or randomly dispersed within the matrix.[1,38,108] Plenty of research has focused on fibers with various lengths ranging from 6 to 16 mm, and findings show that increasing both the fiber volume fraction and the length-to-diameter ratio (*L*/*D*) enhances the flexural and ultimate strengths of ECC, though it may decrease compressive strength and the load at the first crack.[56,93] Under compression, fibers orient due to shear forces, with circular fibers exhibiting more rotation compared to triangular or trilobal fibers.[93] Previous research by Yu et al.[21] explored how fiber orientation, specifically with PE fibers, affects ultra-high-performance ECC. Their findings revealed that controlling fiber orientation not only improved mechanical properties but also increased durability by influencing ECC's anisotropic behavior and crack resistance.[21] Even with smaller fiber inclination angles (0 to 40 degrees), Wang et al.[109] observed a notable improvement in crack-bridging capacity and crack resistance in hybrid steel-PVA ECC. Conversely, they concluded that fibers misaligned or oriented at steeper angles (for example, greater than 45 degrees) tend to reduce the strain-hardening efficiency and increase the risk of fiber rupture.[108,109] Supporting this, Ge et al.[108] examined the influence of extrusion-based processes on fiber alignment, highlighting that precise fiber orientation significantly contributes to the enhanced mechanical performance of ECC. Improvements in casting methods, modeling models, and three-dimensional (3-D) printing technology have further demonstrated that directly configurating fiber characteristics such as orientation angle, arrangement, and geometry can greatly improve the overall strength and ductility of ECC, making it suitable for broader structural applications.[108-111] Additionally, Dong et al.[112] emphasized that well-distributed and uniformly oriented fibers enhance crack-bridging efficiency, allowing the cementitious composite to exhibit strain-hardening behavior and improved energy absorption.

ECC IN COMMON STRUCTURAL PERFORMANCE

Removal or reduction use of shear reinforcement

ECC has been proven to work effectively with reinforcing bars, providing excellent shear capacity, increased damage tolerance, and effective crack control.[6,113] This was demonstrated in the Ohno shear beam test, where ECC developed multiple cracks perpendicular to the main tensile direction when subjected to shear forces.[113] Because ECC exhibits ductile tensile behavior, its shear response is also ductile, allowing for the possibility of reducing or even eliminating conventional steel shear reinforcement in R/ECC (reinforced) elements. Li and Wang[114] examined ECC beams lacking shear reinforcement and found that R/ECC beams outperformed high-strength concrete (HSC) beams with closely spaced steel stirrups, suggesting ECC can replace conventional concrete without the need for additional shear reinforcement. Further studies on unbonded post-tensioned precast columns featuring ECC hinge zones[10] and R/ECC columns[102] also confirmed that ECC enhances column integrity, even in the absence of seismic shear detailing, and delivers superior performance under cyclic loading. Yuan et al.,[115] in addition, confirmed that increasing the reinforcement ratio from 0.73 to 1.5% improved the ultimate drift ratio from 12 to 17% of R/ECC beams under cyclic loading.

Sustaining large deformation

ECC, known for its unique tensile strain-hardening properties and high tensile strain capacity, is able to endure significant deformations without localized damage. As highlighted by Zhu et al.[116] and Zhang et al.,[117] numerous studies have focused on the deformation performance of ECC, revealing significant increases in tensile strain capacity due to its ability to develop multiple cracks and undergo strain hardening. Research indicates that ECC can achieve tensile strain capacities of 3 to 5%, far exceeding that of conventional concrete.[117] This impressive performance is largely attributed to the inclusion of fibers, which bridge cracks and enhance strain capacity, enabling ECC to sustain large deformations while maintaining strength.[117] Similarly, the use of alternative materials such as rice husk ash (RHA) has further enhanced strain capacity, although with a slight reduction in tensile strength. This makes ECC a highly versatile and resilient material, particularly well-suited for structures that experience large deformations, such as those in seismic structural applications. Li[2] and Larson[118] noted that ECC is particularly beneficial in link slabs, where it can replace traditional joints in concrete bridge decks, absorbing movements and massive deflections caused by shrinkage, temperature fluctuations, or creep, thus improving deck durability. Full-scale testing by Kim et al.[119] further confirmed the practical application of ECC link-slab technology, showing its ability to handle large deck movements while maintaining structural integrity. Fischer and Li[120] also evaluated the deformation characteristics of ECC reinforced with fiber-reinforced polymer (FRP) by examining flexural load-deformation behavior, residual deflection, and damage progression. Their findings suggest that the combination of elastic FRP reinforcement and the ductile ECC matrix results in a nonlinear flexural response, stable hysteresis, minimal residual deflection, and gradual failure in compression.[120,121]

APPLICATION AREAS

ECC has proven its effectiveness in key sectors such as transportation, commercial construction, water infrastructure, and geotechnical and soil applications, highlighting its critical role as a high-performance material within the construction industry.[2,3,5,6,35,72,94,122,123] According to Park et al.,[6] Lepech and Li,[123] and Keoleian et al.,[94] ECC has successfully been applied in transportation infrastructures, particularly highway pavements and bridge components, due to its exceptional durability, lower maintenance demands, and increased service life as compared to conventional concrete. Further evidence provided by Krouma and Syed[122] in their comparative review of ECC and FRC highlights ECC's enhanced mechanical properties, showing notably higher ultimate tensile strength (4.6 MPa versus 4.3 MPa) and compressive strength (68.5 MPa versus 55 MPa) compared to FRC. In addition to that, ECC's unique self-healing capability, reduced permeability, and strong resistance to environmental impacts such as corrosion significantly benefit its suitability for bridge construction and rehabilitation, thereby improving structural longevity and lowering life-cycle maintenance expenses.[122,123] For structural applications, ECC's enhanced tensile strain capacity and effective crack control make it particularly advantageous for seismic retrofitting, strengthening reinforced concrete beams, and repairing unreinforced masonry structures.[35] Moreover, the emphasis on ECC's sustainability attributes has contributed significantly to promoting environmentally sustainable practices in infrastructure projects.[3,116,124]

Building infrastructure

In seismic regions, buildings are often designed or retrofitted to resist earthquake forces and improve safety. ECC has emerged as a highly effective material in this context, offering both durability and aesthetic versatility, making it an excellent choice for building façades.[15,76] One of the early application findings by Li and Kanda[125] demonstrated the structural effectiveness of ECC in critical load-bearing elements such as bridge decks, floor slabs, and coupling beams in tall buildings. Its advantageous ability to absorb energy and control crack propagation significantly enhances the durability of these components, while also lowering long-term maintenance requirements.[94,119,125] Additionally, ECC allows for the maximization of usable floor space by reducing the number of required columns and beams.[125] In Japan, ECC has been practically implemented in coupling beams of core structural walls in high-rise buildings like the 27-story Glorio Tower in Tokyo and the 60-story Kitahama Tower in Osaka.[2] This technique has also been effectively employed in other skyscrapers across Japan, including the 41-story Nabule Tower in Yokohama, where ECC coupling beams integrated with durable core walls notably improved seismic resistance.[2,76,77] ECC has also proven valuable in rehabilitation projects. For instance, Singh and Munjal[126] demonstrated that bonding precast ECC panels onto masonry walls improved both their out-of-plane load resistance and overall ductility, making it a viable solution for strengthening aging or vulnerable structures. In terms of technological innovation, 3-D-printable ECC (3DP-ECC) was developed to facilitate automated digital construction without the need for conventional steel reinforcement.[19] Yu et al.[19] confirmed that 3DP-ECC preserved essential properties such as strain-hardening behavior and microcrack formation, thus aligning with the goals of sustainable and modern construction. Fire performance of the ECC applications has been studied, where ECC maintained its structural integrity at temperatures up to 400°C, while avoiding explosive spalling. This is due to the melting of PVA fibers, which create escape channels for vapor, thus reducing internal pressure buildup—an essential safety feature for high-rise buildings.[20,68,69]

Transportation and bridge infrastructure

One of the most promising applications of ECC is in highway infrastructure, particularly in the construction of highway bridges, due to its unique characteristics such as high tensile ductility, excellent crack-width control, and self-healing capabilities.[35,55,102] These structures are continuously exposed to extreme environmental conditions, leading to issues such as cracking, expansion, water damage, chloride-induced corrosion, and uneven settlement between the pavement, slab, and bridge supports.[118,122,123] For instance, studies by the Nevada Department of Transportation demonstrated that ECC overlays exhibit enhanced durability, low permeability, and excellent resistance to freezing-and-thawing damage and abrasion, leading to significantly extended service life and lower long-term maintenance compared to conventional concrete overlays.[5] Furthermore, evaluations by the Texas Department of Transportation emphasized ECC's cost-efficiency based on life-cycle cost and environmental impact analyses, particularly in pavement overlays and bridge joint replacements.[6] ECC provides significant benefits in terms of weather resistance and longevity, making it a highly suitable material for bridge construction.[94] Tests demonstrated that after 26 weeks of immersion in hot water, ECC's tensile strain capacity decreases by only 1.75%—a performance that is 250 times better than that of conventional concrete.[127] ECC plays a crucial role in jointless bridge designs, where it replaces traditional mechanical expansion joints with ECC link slabs. A life-cycle analysis (LCA) comparing ECC link slabs with conventional steel expansion joints over a 60-year span highlighted that ECC extends the service life of bridges while reducing the need for maintenance.[94] The self-healing properties of ECC also contribute to its long-term durability by minimizing issues such as shrinkage and damage caused by traffic loads.[7] Studies, such as those by Kim et al.,[62] demonstrate ECC's effectiveness in enhancing crack control and service life in bridge deck link slabs. Traditionally, expansion joints are used to manage temperature-induced movements in bridge decks, preventing cracks.[62,119] The application of ECC not only lowered greenhouse gas emissions and energy consumption but also extended maintenance intervals. In addition, recent work by Mishra et al.[124] discussed the environmental and operational benefits of combining ECC with drone-based inspection technologies to improve the sustainability and resilience of bridge assets. Collectively, these findings reinforce ECC's viability for use in demanding infrastructure environments, offering a durable and economically sustainable alternative that supports both structural integrity and long-term performance goals.[94,119,124]

Geotechnical underground and soil applications

Researchers acknowledged that ECC offer significant advantages for applications involving large deformation structures due to their strain-hardening properties and effective crack control.[51,83,120] These attributes make ECC an ideal choice for applications such as underground infrastructure, concrete pipes, and other scenarios where high structural flexibility, energy absorption, and precise control of crack width under significant strain are crucial.[34] In the realm of underground structures like tunnels and foundations, soil movement can result in uncertain stress distribution and cracking in standard concrete.[54,55,72] ECC's ability to handle substantial deformations while preserving structural integrity provides a distinct advantage in these situations. It efficiently absorbs and redistributes stresses, which reduces the likelihood of failure due to soil displacement.[128] When it comes to concrete pipes used in underground infrastructure, ECC's strain-hardening properties make it proficient at managing

Table 4—ECC structural applications across different infrastructure types[3]

Infrastructure type	Application	Problem solved	ECC property used	Processing method
Building	Coupling beams in building core	Rapid recovery following seismic events due to ECC's tolerance to damage; decreased need for replacement or repairs; quicker building installation and shorter construction times, resulting in more usable floor space.	Tensile ductility; damage tolerance; energy absorption under shear; fire resistance	Precast in factory
	External insulation wall	Lower construction costs, labor, and time; minimize the risk of inconsistent construction quality on-site.	Durability against drying and thermal cycles	Precast in factory
Transportation	Bridge deck and road pavement link-slab retrofits	Lower the frequency and expense of bridge deck maintenance; reduce traffic noise.	Tensile ductility to accommodate thermal deformation; tight crack width; fatigue resistance; wear durability	Cast-in-place or precast in factory
	Composite bridge deck	Minimize the risk of fatigue failure in steel decks; reduce both cost and weight.	Tensile ductility; fatigue resistance	Cast-in-place
	Tunnel linings repair and retrofit	Cut down on labor and expenses; decrease maintenance requirements.	Tensile ductility; watertightness; carbonation resistance; freezing-and-thawing resistance	Spraying
Water infrastructure	Retrofit of Mitaka Dam	Mitigate the risk of dam leakage and failure; extend its operational lifespan.	Crack and spall resistance; watertightness	Spraying
	Repair of dam of hydraulic powerplant	Lower the risk of reflective cracking; prevent water leakage.	Tensile ductility; watertightness	Spraying
	Retrofit of water tunnel for water treatment facility	Prevent water loss; reduce the frequency and cost of maintenance.	Tensile ductility; watertightness; enhanced durability	Injection pumping

both internal pressures and external soil loads.[129] Leakage prevention is also a critical issue for underground structures and concrete pipes. ECC's tightly controlled microcracking behavior prevents the formation of large cracks, which are common pathways for water ingress. Li[3] provides a detailed overview of all these applications in Table 4, showcasing ECC's broad impact across various sectors.

Cost analysis and feasibility of ECC in construction

The cost-effectiveness and feasibility of ECC have become a growing point of interest, particularly in balancing advanced mechanical performance with sustainable and economical construction.[6,19] Multiple studies have highlighted that although ECC is initially more expensive because of its reliance on synthetic fibers such as PVA and its higher cement content, its innovative mixture designs and material substitutions can significantly reduce cost while maintaining desirable performance characteristics.[106,130,131] In their study, Arce et al.[130] demonstrated that ECC with a reduced PVA content (1.5% volume) and 75% cement replacement using fly ash still achieved high tensile ductility (2.61%) and flexural strength (9.85 MPa), making it suitable for pavement applications. Similarly, a follow-up report by the same research group further showed that the use of locally sourced materials including river sands and crumb rubber enabled additional reduction in cost without severely compromising mechanical integrity.[131] In a separate study, Radhakrishnan et al.[106] explored the use of bio-fiber-based green ECC by employing flax, hemp, kenaf, and pineapple fibers as replacements for synthetic PVA. This substitution drastically reduced environmental and economic burdens, with LCA results showing significant reductions in embodied energy and CO$_2$ emissions. Specifically, kenaf- and pineapple-based ECC achieved high strain capacities (2.0 to 2.5%) with minimal performance loss while being markedly more sustainable than synthetic fiber alternatives.[106] These findings are consistent with other references in the literature. For instance, Keoleian et al.[94] reported that ECC link slabs reduce life-cycle costs by minimizing long-term maintenance, while Lepech and Li[123] supported the economic feasibility of ECC overlays in pavements. Altwair et al.[25] and Zhang et al.[117] further demonstrated how substituting cement with RHA or palm oil fuel ash improves both sustainability and cost efficiency in the Malaysian context. Also, Mishra et al.[124] highlighted ECC's role in reducing carbon footprint and life-cycle cost when used in modern bridge design. The integration of locally sourced fillers, recycled materials, and bio-based fibers provides a viable path forward to mainstream ECC adoption in cost-sensitive construction projects.

CONCLUSIONS

Engineered cementitious composites (ECC) mark a significant leap forward in construction materials, combining innovative engineering principles with sustainability. Their outstanding ductility, high tensile strength, and self-healing properties address many of the weaknesses found in typical conventional concrete, offering a versatile and robust solution for today's infrastructure challenges. Through its ability to accommodate large deformations, resist cracking, and enhance structural resilience, ECC effectively tackles critical challenges in modern infrastructure development, particularly in seismic zones, transportation networks, and underground applications. Its wide range of applications, together with the environmental benefits through material optimization and waste use, make ECC a promising solution for future construction needs. Although certain challenges remain, such as high initial costs and the lack of standardized guidelines, ongoing research continues to improve ECC's performance and economic feasibility. As the industry moves toward sustainable and durable construction practices, ECC stands out not just as an innovation, but as a reliable and practical material ready to meet the complex and evolving demands of modern construction.

AUTHOR BIOS

Norsuzailina Mohamed Sutan *is an Associate Professor at Universiti Malaysia Sarawak (UNIMAS), Kota Samarahan, Malaysia. She received her PhD in civil engineering, with a research focus on advanced concrete technologies. Her research interests include material characterization and the development of sustainable concrete using supplementary cementitious materials.*

Faisal Amsyar Redzuan *is a Civil Engineering Lecturer at UNIMAS. He received his PhD in civil engineering, specializing in composite steel structures, from Universiti Teknologi Malaysia (UTM), Johor Bahru, Malaysia. His research interests include composite steel structures, semi-rigid steel connections, lightweight concrete, steel confinement, cold-formed steel, and finite element analysis.*

Abdul Razak Bin Abdul Karim *is an Associate Professor of Civil Engineering at UNIMAS. He received his PhD in civil engineering from The University of Auckland, Auckland, New Zealand. His research interests include structural engineering, particularly in bolted timber connections and low-carbon concrete.*

Norazzlina M. Sa'don *is an Associate Professor in Civil Engineering at UNIMAS. She received her PhD in civil engineering from The University of Auckland. Her research interests include geotechnical engineering, soil stabilization, and earthquake engineering.*

Yoeng Sebastian Shun Hui *is a Postgraduate Student pursuing a master's degree in civil engineering at the Department of Civil Engineering, Faculty of Engineering, UNIMAS.*

Chin Cerries Yee Jie *is a Postgraduate Student pursuing a master's degree in civil engineering at the Department of Civil Engineering, Faculty of Engineering, UNIMAS.*

ACKNOWLEDGMENTS

The authors would like to express their sincere gratitude to the Malaysia Ministry of Higher Education and Universiti Malaysia Sarawak (INT/F02/UPJ/86237/2023 and UNI/F02/CATALYST/86462/2025) for their invaluable support and contributions, which played a crucial role in enabling this research.

DECLARATION OF COMPETING INTEREST

The authors affirm that this manuscript is an original submission, has not been published previously, and is not being considered for publication by any other journal. Furthermore, they declare that there are no conflicts of interest, financial or otherwise, that may have impacted the research, writing, or submission of this work.

REFERENCES

1. Singh, M.; Saini, B.; and Chalak, H. D., "Performance and Composition Analysis of Engineered Cementitious Composite (ECC): A Review," *Journal of Building Engineering*, V. 26, 2019, pp. 1-8. doi: 10.1016/j.jobe.2019.100851

2. Li, V. C., "On Engineered Cementitious Composites (ECC): A Review of the Material and its Applications," *Journal of Advanced Concrete Technology*, V. 1, No. 3, 2003, pp. 215-230. doi: 10.3151/jact.1.215

3. Li, V. C., *Engineered Cementitious Composites (ECC): Bendable Concrete for Sustainable and Resilient Infrastructure*, Springer, Berlin, Germany, 2019.

4. Bentur, A., and Mindess, S., *Fibre Reinforced Cementitious Composites*, second edition, E & FN Spon, London, UK, 2007.

5. Hajj, E.; Sanders, D. H.; and Weitzel, N. D., "Development of Specifications for Engineered Cementitious Composites for Use in Bridge Deck Overlays," University of Nevada, Reno, Reno, NV, 2016.

6. Park, P.; Jones, R.; Castillo, L.; Vallangca, M.; and Cantu, F., "Engineered Cementitious Composites (ECC) for Applications in Texas," Technical Report 0-7030-1, TxDOT Project Number 0-7030, The University of Texas Rio Grande Valley, Edinburg, TX, 2020.

7. Barbhuiya, S.; Das, B. B.; and Adak, D., "Advances and Perspectives in Engineered Cementitious Composites (ECC): A Comprehensive Review," *Magazine of Concrete Research*, V. 76, No. 20, 2024, pp. 1165-1184. doi: 10.1680/jmacr.24.00047

8. Deng, B. Y.; Li, L. Z.; Tan, D.; Uddin, M. N.; Cai, Z. W.; and Yu, K. Q., "Sustainable and Cost-Effective Ultra-Lightweight Engineered Cementitious Composite: Design and Material Characterization," *Cement and Concrete Composites*, V. 136, 2023, p. 104895. doi: 10.1016/j.cemconcomp.2022.104895

9. Liao, Q.; Su, Y. R.; Yu, J. T.; and Yu, K. Q., "Compression-Shear Performance and Failure Criteria of Seawater Sea-Sand Engineered Cementitious Composites with Polyethylene Fibers," *Construction and Building Materials*, V. 345, 2022, p. 128386. doi: 10.1016/j.conbuildmat.2022.128386

10. Billington, S. L., and Yoon, J. K., "Cyclic Response of Unbonded Posttensioned Precast Columns with Ductile Fiber-Reinforced Concrete," *Journal of Bridge Engineering*, ASCE, V. 9, No. 4, 2004, pp. 353-363. doi: 10.1061/(ASCE)1084-0702(2004)9:4(353)

11. Meng, D.; Huang, T.; Zhang, Y. X.; and Lee, C. K., "Mechanical Behaviour of a Polyvinyl Alcohol Fibre Reinforced Engineered Cementitious Composite (PVA-ECC) Using Local Ingredients," *Construction and Building Materials*, V. 141, 2017, pp. 259-270. doi: 10.1016/j.conbuildmat.2017.02.158

12. Li, J., and Yang, E. H., "Macroscopic and Micro Structural Properties of Engineered Cementitious Composites Incorporating Recycled Concrete Fines," *Cement and Concrete Composites*, V. 78, 2017, pp. 33-42. doi: 10.1016/j.cemconcomp.2016.12.013

13. Huang, T., and Zhang, Y. X., "Mechanical Properties of a PVA Fiber Reinforced Engineered Cementitious Composites," *Sustainable Solutions in Structural Engineering and Construction*, 2014, pp. 439-444.

14. Zhou, J.; Quian, S.; and Breugel, K. V., "Engineered Cementitious Composites with Low Volume of Cementitious Materials," *Fracture Mechanics of Concrete and Concrete Structures: Proceedings of FraMCoS-7, 2010 May 23-28*, 2010, pp. 1551-1556.

15. Huang, B. T.; Weng, K. F.; Zhu, J. X.; Xiang, Y.; Dai, J. G.; and Li, V. C., "Engineered/Strain-Hardening Cementitious Composites (ECC/SHCC) with an Ultra-High Compressive Strength over 210 MPa," *Composites Communications*, V. 26, 2021, p. 100775. doi: 10.1016/j.coco.2021.100775

16. Zhou, J.; Pan, J.; and Leung, C. K., "Mechanical Behavior of Fiber-Reinforced Engineered Cementitious Composites in Uniaxial Compression," *Journal of Materials in Civil Engineering*, ASCE, V. 27, No. 1, 2015, p. 04014111. doi: 10.1061/(ASCE)MT.1943-5533.0001034

17. Huang, X.; Ranade, R.; Zhang, Q.; Ni, W.; and Li, V. C., "Mechanical and Thermal Properties of Green Lightweight Engineered Cementitious Composites," *Construction and Building Materials*, V. 48, 2013, pp. 954-960. doi: 10.1016/j.conbuildmat.2013.07.104

18. Wang, S. X., and Li, V. C., "Polyvinyl Alcohol Fiber Reinforced Engineered Cementitious Composites: Materials Design and Performances," *International RILEM Workshop on High Performance Fiber Reinforced Cementitious Composites (HPFRCC) in Structural Applications*, G. Fischer and V. C. Li, eds., Honolulu, HI, 2005, pp. 65-73.

19. Yu, K.; McGee, W.; Ng, T. Y.; Zhu, H.; and Li, V. C., "3D-Printable Engineered Cementitious Composites (3DP-ECC): Fresh and Hardened Properties," *Cement and Concrete Research*, V. 143, 2021, p. 106388. doi: 10.1016/j.cemconres.2021.106388

20. Sahmaran, M.; Lachemi, M.; and Li, V. C., "Assessing Mechanical Properties and Microstructure of Fire-Damaged Engineered Cementitious Composites," *ACI Materials Journal*, V. 107, No. 3, May-June 2010, pp. 297-304.

21. Yu, K. Q.; Yu, J. T.; Dai, J. G.; Lu, Z. D.; and Shah, S. P., "Development of Ultra-High Performance Engineered Cementitious Composites Using Polyethylene (PE) Fibers," *Construction and Building Materials*, V. 158, 2018, pp. 217-227. doi: 10.1016/j.conbuildmat.2017.10.040

22. Li, V., "Tailoring ECC for Special Attributes: A Review," *International Journal of Concrete Structures and Materials*, V. 6, No. 3, 2012, pp. 135-144. doi: 10.1007/s40069-012-0018-8

23. Zhou, Y. W.; Xi, B.; Yu, K. Q.; Sui, L. L.; and Xing, F., "Mechanical Properties of Hybrid Ultra-High Performance Engineered Cementitious Composites Incorporating Steel and Polyethylene Fibers," *Materials*, V. 11, No. 8, 2018, p. 1448. doi: 10.3390/ma11081448

24. Ajith, G.; Shanmugasundaram, N.; and Praveenkumar, S., "Effect of Mineral Admixtures and Manufactured Sand on Compressive Strength of Engineered Cementitious Composite," *Journal of Building Pathology and Rehabilitation*, V. 6, No. 1, 2021, p. 38. doi: 10.1007/s41024-021-00137-y

25. Altwair, N. M.; Magat Johari, M. A.; and Saiyid Hashim, S. F., "Flexural Performance of Green Engineered Cementitious Composites Containing High Volume of Palm Oil Fuel Ash," *Construction and Building Materials*, V. 37, 2012, pp. 518-525. doi: 10.1016/j.conbuildmat.2012.08.003

26. Zhu, J. X.; Xu, L. Y.; Huang, B. T.; Weng, K. F.; and Dai, J. G., "Recent Developments in Engineered/Strain-Hardening Cementitious Composites (ECC/SHCC) with High & Ultra-High Strength," *Construction and Building Materials*, V. 342, 2022, p. 127956. doi: 10.1016/j.conbuildmat.2022.127956

27. Zhang, Z., and Qian, S., "Influence of Crumb Rubber on the Mechanical Behavior of Engineered Cementitious Composites," *VIII International Conference on Fracture Mechanics of Concrete and Concrete Structures FraMCOS-8*, Toledo, Spain, 2013, pp. 1-10.

28. Ling, G.; Shui, Z.; Gao, X.; Sun, T.; Yu, R.; and Li, X., "Utilizing Iron Ore Tailing as Cementitious Material for Eco-Friendly Design of Ultra-High-Performance Concrete (UHPC)," *Materials*, V. 14, No. 8, 2021, p. 1829. doi: 10.3390/ma14081829

29. Gulghane, A. A., and Bari, C., "Comparative Analysis of ECC by Partial Replacement of Cement with Slag Sand," *Smart Technologies for Energy, Environment and Sustainable Development - Select Proceedings of ICSTEESD 2018*, M. L. Kolhe, P. K. Labhasetwar, and H. M. Suryawanshi, eds., Springer, Singapore, 2019, pp. 427-435.

30. Turk, K., and Demirhan, S., "The Mechanical Properties of Engineered Cementitious Composites Containing Limestone Powder Replaced by Microsilica Sand," *Canadian Journal of Civil Engineering*, V. 40, No. 2, 2013, pp. 151-157. doi: 10.1139/cjce-2012-0281

31. Raza, A.; Zhang, J.; Xu, S.; Umar, M.; and Yuan, C., "Experimental Analysis of Frost Resistance and Failure Models in Engineered Cementitious Composites with the Integration of Yellow River Sand," *Science and Engineering of Composite Materials*, V. 31, No. 1, 2024, pp. 1-19. doi: 10.1515/secm-2024-0017

32. Lepech, M. D., and Li, V. C., "Water Permeability of Engineered Cementitious Composites," *Cement and Concrete Composites*, V. 31, No. 10, 2009, pp. 744-753. doi: 10.1016/j.cemconcomp.2009.07.002

33. Maalej, M., and Li, V. C., "Introduction of Strain-Hardening Engineered Cementitious Composites in the Design of Reinforced Concrete Flexural Members for Improved Durability," *ACI Structural Journal*, V. 92, No. 2, Mar.-Apr. 1995, pp. 167-176.

34. Li, V. C., "Engineered Cementitious Composites - Tailored Composites through Micromechanical Modeling," *Fiber Reinforced Concrete: Present and the Future*, N. Banthia, A. Bentur, and A. Mufti, eds., Canadian Society for Civil Engineering, Montreal, QC, Canada, 1998, pp. 64-97.

35. Maalej, M.; Quek, S. T.; Ahmed, S. F. U.; Zhang, J.; Lin, V. W. J.; and Leong, K. S., "Review of Potential Structural Applications of Hybrid Fiber Engineered Cementitious Composites," *Construction and Building Materials*, V. 36, 2012, pp. 216-227. doi: 10.1016/j.conbuildmat.2012.04.010

36. Soe, K. T.; Zhang, Y. X.; and Zhang, L. C., "Material Properties of a New Hybrid Fiber-Reinforced Engineered Cementitious Composite," *Construction and Building Materials*, V. 43, 2013, pp. 399-407. doi: 10.1016/j.conbuildmat.2013.02.021

37. Kawamata, A.; Mihashi, H.; and Fukuyama, H., "Properties of Hybrid Fiber Reinforced Cement-Based Composites," *Journal of Advanced Concrete Technology*, V. 1, No. 3, 2003, pp. 283-290. doi: 10.3151/jact.1.283

38. Lawler, J. S.; Zampini, D.; and Shah, S. P., "Micro Fiber and Macro Fiber Hybrid Fiber-Reinforced Concrete," *Journal of Materials in Civil Engineering*, ASCE, V. 17, No. 5, 2005, pp. 595-604. doi: 10.1061/(ASCE)0899-1561(2005)17:5(595)

39. AASHTO T 132-87(R2013), "Standard Method of Test for Tensile Strength of Hydraulic Cement Mortars," American Association of State Highway and Transportation Officials, Washington, DC, 2013.

40. RILEM TC 162-TDF, "Uni-Axial Tension Test for Steel Fibre Reinforced Concrete," *Materials and Structures*, V. 34, No. 1, 2001, pp. 3-6. doi: 10.1007/BF02482193

41. AFGC, *Ultra-High-Performance Fibre-Reinforced Concretes—Interim Recommendations*, AFGC Scientific and Technical Documents, Association Française de Génie Civil, Paris, France, 2002.

42. JSCE Concrete Committee, *Recommendations for Design and Construction of High-Performance Fiber Reinforced Cement Composites with Multiple Fine Cracks (HPFRCC)*, Japan Society of Civil Engineers, Tokyo, Japan, 2008.

43. ASTM C293/C293M-10, "Standard Test Method for Flexural Strength of Concrete (Using Simple Beam with Center-Point Loading)," ASTM International, West Conshohocken, PA, 2010.

44. ASTM C78/C78M-10, "Standard Test Method for Flexural Strength of Concrete (Using Simple Beam with Third-Point Loading)," ASTM International, West Conshohocken, PA, 2010.

45. ASTM C1399/C1399M-10, "Standard Test Method for Obtaining Average Residual-Strength of Fiber-Reinforced Concrete," ASTM International, West Conshohocken, PA, 2010.

46. ASTM C1609/C1609M-12, "Standard Test Method for Flexural Performance of Fiber-Reinforced Concrete (Using Beam with Third-Point Loading)," ASTM International, West Conshohocken, PA, 2012.

47. RILEM TC 162-TDF, "Test and Design Methods for Steel Fiber Reinforced Concrete: Bending Test," *Materials and Structures*, V. 35, No. 9, 2002, pp. 579-582.

48. BS EN 14651:2005+A1:2007, "Test Method for Metallic Fibre Concrete: Measuring the Flexural Tensile Strength (Limit of Proportionality (LOP), Residual)," British Standards Institution, London, UK, 2007.

49. Zhang, D.; Yu, J.; Wu, H.; Jaworska, B.; Ellis, B. R.; and Li, V. C., "Discontinuous Micro-Fibers as Intrinsic Reinforcement for Ductile Engineered Cementitious Composites (ECC)," *Composites Part B: Engineering*, V. 184, 2020, p. 107741. doi: 10.1016/j.compositesb.2020.107741

50. Sun, R.; Hu, X.; Ling, Y.; Zuo, Z.; Zhuang, P.; and Wang, F., "Chloride Diffusion Behavior of Engineered Cementitious Composite under Dry-Wet Cycles," *Construction and Building Materials*, V. 260, 2020, p. 119943. doi: 10.1016/j.conbuildmat.2020.119943

51. Li, M., and Li, V. C., "Cracking and Healing of Engineered Cementitious Composites under Chloride Environment," *ACI Materials Journal*, V. 108, No. 3, May-June 2011, pp. 333-341.

52. Sun, R.; Lu, W.; Ma, C.; Tawfek, A. M.; Guan, Y.; Hu, X.; Zhang, H.; Ling, Y.; and Savija, B., "Effect of Crack Width and Wet-Dry Cycles on the Chloride Penetration Resistance of Engineered Cementitious Composite (ECC)," *Construction and Building Materials*, V. 352, 2022, p. 129030. doi: 10.1016/j.conbuildmat.2022.129030

53. Shumuye, E. D.; Li, W.; Liu, J.; Wang, Z.; Yu, J.; and Wu, H., "Self-Healing Recovery and Micro-Structural Properties of Slag/Fly-Ash Based Engineered Cementitious Composites under Chloride Environment and Tidal Exposure," *Cement and Concrete Composites*, V. 134, 2022, p. 104789. doi: 10.1016/j.cemconcomp.2022.104789

54. Wang, L.; Han, X.; Tian, L.; Wang, P.; and Sun, X., "Influence of Frost Damage on Performance of Engineered Cementitious Composites," *Journal of Advanced Concrete Technology*, V. 21, No. 12, 2023, pp. 971-982. doi: 10.3151/jact.21.971

55. Hou, L.; Xu, R.; Chen, D.; Xu, S.; and Aslani, F., "Seismic Behavior of Reinforced Engineered Cementitious Composite Members and Reinforced Concrete/Engineered Cementitious Composite Members: A Review," *Structural Concrete*, V. 21, No. 1, 2020, pp. 199-219. doi: 10.1002/suco.201800269

56. Sasmal, S., and Avinash, G., "Investigations on Mechanical Performance of Cementitious Composites Micro-Engineered with Polyvinyl Alcohol Fibers," *Construction and Building Materials*, V. 128, 2016, pp. 136-147. doi: 10.1016/j.conbuildmat.2016.10.025

57. Pan, Z.; Wu, C.; Liu, J.; Wang, W.; and Liu, J., "Study on Mechanical Properties of Cost-Effective Polyvinyl Alcohol Engineered Cementitious Composites (PVA-ECC)," *Construction and Building Materials*, V. 78, 2015, pp. 397-404. doi: 10.1016/j.conbuildmat.2014.12.071

58. Zhu, M.; Chen, B.; Wu, M.; and Han, J., "Effects of Different Mixing Ratio Parameters on Mechanical Properties of Cost-Effective Green Engineered Cementitious Composites (ECC)," *Construction and Building Materials*, V. 328, 2022, p. 127093. doi: 10.1016/j.conbuildmat.2022.127093

59. Yang, Y.; Gao, X.; Deng, H.; Yu, P.; and Yao, Y., "Effects of Water/Binder Ratio on the Properties of Engineered Cementitious Composites," *Journal of Wuhan University of Technology. Materials Science Edition*, V. 25, No. 2, 2010, pp. 298-302. doi: 10.1007/s11595-010-2298-7

60. Şahmaran, M.; Bilici, Z.; Ozbay, E.; Erdem, T. K.; Yucel, H. E.; and Lachemi, M., "Improving the Workability and Rheological Properties of Engineered Cementitious Composites Using Factorial Experimental Design," *Composites Part B: Engineering*, V. 45, No. 1, 2013, pp. 356-368. doi: 10.1016/j.compositesb.2012.08.015

61. Fischer, G., and Wang, S. X., "Design of Engineered Cementitious Composites (ECC) for Processing and Workability Requirements," *Brittle Matrix Composites 7*, A. M. Brandt, V. C. Li, and I. H. Marshall, eds., Woodhead Publishing, Sawston, UK, 2003, pp. 29-36.

62. Kim, J. K.; Kim, J. S.; Ha, G. J.; and Kim, Y. Y., "Tensile and Fiber Dispersion Performance of ECC (Engineered Cementitious Composites) Produced with Ground Granulated Blast Furnace Slag," *Cement and Concrete Research*, V. 37, No. 7, 2007, pp. 1096-1105. doi: 10.1016/j.cemconres.2007.04.006

63. Nicolaides, D.; Kanellopoulos, A.; Petrou, M.; Savva, P.; and Mina, A., "Development of a New Ultra-High-Performance Fiber Reinforced Cementitious Composite (UHPFRCC) for Impact and Blast Protection of

Structures," *Construction and Building Materials*, V. 95, 2015, pp. 667-674. doi: 10.1016/j.conbuildmat.2015.07.136

64. Ma, H.; Yi, C.; and Wu, C., "Review and Outlook on Durability of Engineered Cementitious Composite (ECC)," *Construction and Building Materials*, V. 287, 2021, p. 122719. doi: 10.1016/j.conbuildmat.2021.122719

65. Xu, S. L., and Cai, X. H., "Experimental Study of the Durability Properties of Ultra-High Toughness Cementitious Composites under Freeze and Thawing Cycles," *Tumu Gongcheng Xuebao*, V. 42, No. 9, 2009, pp. 42-46.

66. Xu, S. L., and Cai, X. H., "Experimental Studies on Permeability and Carbonation Properties of Ultra-High Toughness Cementitious Composites," *Acta Materiae Compositae Sinica*, V. 27, No. 3, 2010, pp. 177-183.

67. Ranjith, S.; Venkatasubramani, R.; and Sreevidya, V., "Comparative Study on Durability Properties of Engineered Cementitious Composites with Polypropylene Fiber and Glass Fiber," *Archives of Civil Engineering*, V. 63, No. 4, 2017, pp. 83-101. doi: 10.1515/ace-2017-0042

68. Şahmaran, M.; Ozbay, E.; Yucel, H. E.; Lachemi, M.; and Li, V., "Effect of Fly Ash and PVA Fiber on Microstructural Damage and Residual Properties of Engineered Cementitious Composites Exposed to High Temperatures," *Journal of Materials in Civil Engineering*, ASCE, V. 23, No. 12, 2011, pp. 1735-1745. doi: 10.1061/(ASCE)MT.1943-5533.0000335

69. Yu, J. T.; Lin, J. H.; Zhang, Z. G.; and Li, V., "Mechanical Performance of ECC with High-Volume Fly ash after Sub-Elevated Temperature," *Construction and Building Materials*, V. 99, 2015, pp. 82-89. doi: 10.1016/j.conbuildmat.2015.09.002

70. Mechtcherine, V.; Silva, F. A.; Müller, S.; Jun, P.; and Filho, R. D. T., "Coupled Strain Rate and Temperature Effects on the Tensile Behavior of Strain-Hardening Cement-Based Composites (SHCC) with PVA Fibers," *Cement and Concrete Research*, V. 42, No. 11, 2012, pp. 1417-1427. doi: 10.1016/j.cemconres.2012.08.011

71. Ranade, R.; Heard, W. F.; and Williams, B. A., "Multi-Scale Mechanical Performance of High Strength-High Ductility Concrete," *Dynamic Behavior of Materials, Volume 1 - Proceedings of the 2015 Annual Conference on Experimental and Applied Mechanics*, B. Song, L. Lamberson, D. Casem, and J. Kimberley, eds., Springer, Cham, Switzerland, 2016, pp. 93-101.

72. Ding, Y.; Yu, K.; and Mao, W., "Compressive Performance of All-Grade Engineered Cementitious Composites: Experiment and Theoretical Model," *Construction and Building Materials*, V. 244, 2020, p. 118357. doi: 10.1016/j.conbuildmat.2020.118357

73. Ran, H. Y.; Elchalakani, M.; Boussaid, F.; Yehia, S.; Sadakkathulla, M. A.; and Yang, B., "Development and Evaluation of Conductive Ultra-Lightweight Cementitious Composites for Smart and Sustainable Infrastructure Applications," *Construction and Building Materials*, V. 375, 2023, p. 131017. doi: 10.1016/j.conbuildmat.2023.131017

74. Ran, H. Y.; Elchalakani, M.; Liu, H. Y.; Yehia, S.; and Yang, B., "Development and Characteristics of Multifunctional Ultra-Lightweight Engineered Cementitious Composites Incorporating Cenospheres and PE Fibre," *Cement and Concrete Composites*, V. 140, 2023, p. 105084. doi: 10.1016/j.cemconcomp.2023.105084

75. Ran, H. Y.; Elchalakani, M.; Yehia, S.; Cai, J. M.; and Yang, B., "Self-Sensing High-Performance Ultra-Lightweight Engineered Cementitious Composites Using Calcined Petroleum Coke," *Journal of Cleaner Production*, V. 418, 2023, p. 138241. doi: 10.1016/j.jclepro.2023.138241

76. Kanda, T.; Lin, Z.; and Li, V., "Tensile Stress-Strain Modeling of Pseudostrain Hardening Cementitious Composites," *Journal of Materials in Civil Engineering*, ASCE, V. 12, No. 2, 2000, pp. 147-156. doi: 10.1061/(ASCE)0899-1561(2000)12:2(147)

77. Schröfl, C.; Mechtcherine, V.; Kaestner, A.; Vontobel, P.; Hovind, J.; and Lehmann, E., "Transport of Water through Strain-Hardening Cement-Based Composite (SHCC) Applied on Top of Cracked Reinforced Concrete Slabs with and without Hydrophobization of Cracks-Investigation by Neutron Radiography," *Construction and Building Materials*, V. 76, No. 1, 2015, pp. 70-86. doi: 10.1016/j.conbuildmat.2014.11.062

78. Shabakhty, N.; Karimi, H. R.; and Bakhtiary, A. Y., "Statistical Evaluation of Fracture and Mechanical Performance of Engineered Cementitious Composites (ECC), Containing Different Percentages of Glass, Polypropylene, Polyvinyl-Alcohol Fibers, and Fly Ash," *Construction and Building Materials*, V. 417, 2024, p. 135247. doi: 10.1016/j.conbuildmat.2024.135247

79. Shabakhty, N.; Karimi, H. R.; and Yeganeh Bakhtiary, A., "Effect of Short to Long Hybrid Elastic/Hyperelastic (Glass/PP) Fibers on High-Strength Engineered Cementitious Composites (ECC), Along with Presenting a Constitutive Model," *Journal of Building Engineering*, V. 89, 2024, p. 109215. doi: 10.1016/j.jobe.2024.109215

80. Saljoughian, A.; Bahmani, H.; Ansari, Z.; Jafari, N.; and Mostofinejad, D., "An Eco-Friendly ECC with High Slag and Polypropylene Fiber Content for High-Tensile Strain Applications," *Journal of Building Engineering*, V. 91, 2024, p. 109726. doi: 10.1016/j.jobe.2024.109726

81. Lee, B. Y.; Kim, J. K.; Kim, J. S.; and Kim, Y. Y., "Quantitative Evaluation Technique of Polyvinyl Alcohol (PVA) Fiber Dispersion in Engineered Cementitious Composites," *Cement and Concrete Composites*, V. 31, No. 6, 2009, pp. 408-417. doi: 10.1016/j.cemconcomp.2009.04.002

82. Sherir, M. A.; Hossain, K. M.; and Lachemi, M., "Fracture Energy Characteristics of Engineered Cementitious Composites Incorporating Different Aggregates," *CSCE 2014 4th International Structural Specialty Conference*, Halifax, NS, Canada, 2014.

83. Said, S. H.; Razak, H. A.; and Othman, I., "Strength and Deformation Characteristics of Engineered Cementitious Composite Slabs with Different Polymer Fibers," *Journal of Reinforced Plastics and Composites*, V. 34, No. 23, 2015, pp. 1950-1962. doi: 10.1177/0731684415607393

84. Tian, H., and Zhang, Y. X., "Ageing Effect on Tensile and Shrinkage Behaviour of New Green Hybrid Fibre-Reinforced Cementitious Composites," *Cement and Concrete Composites*, V. 75, 2017, pp. 38-50. doi: 10.1016/j.cemconcomp.2016.11.005

85. Tian, H.; Zhang, Y. X.; Ye, L.; and Yang, C., "Mechanical Behaviours of Green Hybrid Fibre-Reinforced Cementitious Composites," *Construction and Building Materials*, V. 95, 2015, pp. 152-163. doi: 10.1016/j.conbuildmat.2015.07.143

86. Tian, H., and Zhang, Y. X., "The Influence of Bagasse Fibre and Fly Ash on the Long-Term Properties of Green Cementitious Composites," *Construction and Building Materials*, V. 111, 2016, pp. 237-250. doi: 10.1016/j.conbuildmat.2016.02.103

87. Yang, E.-H., and Li, V. C., "Strain-Hardening Fiber Cement Optimization and Component Tailoring by Means of a Micromechanical Model," *Construction and Building Materials*, V. 24, No. 2, 2010, pp. 130-139. doi: 10.1016/j.conbuildmat.2007.05.014

88. Pakravan, H. R.; Jamshidi, M.; and Latifi, M., "The Effect of Hybridization and Geometry of Polypropylene Fibers on Engineered Cementitious Composites Reinforced by Polyvinyl Alcohol Fibers," *Journal of Composite Materials*, V. 50, No. 8, 2016, pp. 1007-1020. doi: 10.1177/0021998315586078

89. Alrefaei, Y.; Rahal, K.; and Maalej, M., "Shear Strength of Beams Made Using Hybrid Fiber-Engineered Cementitious Composites," *Journal of Structural Engineering*, ASCE, V. 144, No. 1, 2018, p. 04017177. doi: 10.1061/(ASCE)ST.1943-541X.0001924

90. Gadhiya, S.; Patel, T. N.; and Shah, D., "Parametric Study on Flexural Strength of ECC," *International Journal of Science Research and Development*, V. 3, No. 4, 2015, pp. 1494-1497.

91. Mohammed, B. S.; Khed, V. K. C.; and Liew, M. S., "Optimization of Hybrid Fibers in Engineered Cementitious Composites," *Construction and Building Materials*, V. 190, 2018, pp. 24-37. doi: 10.1016/j.conbuildmat.2018.08.188

92. Ali, M. A. E. M.; Soliman, A. M.; and Nehdi, M. L., "Hybrid-Fiber Reinforced Engineered Cementitious Composite under Tensile and Impact Loading," *Materials & Design*, V. 117, 2017, pp. 139-149. doi: 10.1016/j.matdes.2016.12.047

93. Said, S. H.; Razak, H. A.; and Othman, I., "Flexural Behavior of Engineered Cementitious Composite (ECC) Slabs with Polyvinyl Alcohol Fibers," *Construction and Building Materials*, V. 75, 2015, pp. 176-188. doi: 10.1016/j.conbuildmat.2014.10.036

94. Keoleian, G. A.; Kendall, A.; Dettling, J. E.; Smith, V. M.; Chandler, R. F.; Lepech, M. D.; and Li, V. C., "Life Cycle Modeling of Concrete Bridge Design: Comparison of Engineered Cementitious Composite Link Slabs and Conventional Steel Expansion Joints," *Journal of Infrastructure Systems*, ASCE, V. 11, No. 1, 2005, pp. 51-60. doi: 10.1061/(ASCE)1076-0342(2005)11:1(51)

95. Thaishnavi, A.; Suryaprakash, S.; and Krishnaraja, A. R., "Experimental Studies on Properties of Engineered Cementitious Composites," *South Asian Journal of Engineering and Technology*, V. 2, No. 21, 2016, pp. 217-222.

96. Gencturk, B., and Hosseini, F., "Evaluation of Reinforced Concrete and Reinforced Engineered Cementitious Composites (ECC) Members and Structures Using Small-Scale Testing," *Canadian Journal of Civil Engineering*, V. 42, No. 3, 2015, pp. 164-177. doi: 10.1139/cjce-2013-0445

97. Wang, Q.; Yi, Y.; Ma, G.; and Luo, H., "Hybrid Effects of Steel Fibers, Basalt Fibers and Calcium Sulfate on Mechanical Performance of PVA-ECC Containing High-Volume Fly Ash," *Cement and Concrete Composites*, V. 97, 2019, pp. 357-368. doi: 10.1016/j.cemconcomp.2019.01.009

98. Al-Gemeel, A. N.; Zhuge, Y.; and Youssf, O., "Experimental Investigation of Basalt Textile Reinforced Engineered Cementitious Composite under Apparent Hoop Tensile Loading," *Journal of Building Engineering*, V. 23, 2019, pp. 270-279. doi: 10.1016/j.jobe.2019.01.037

99. Felekoglu, B.; Tosun-Felekoglu, K.; Ranade, R.; Zhang, Q.; and Li, V. C., "Influence of Matrix Flowability, Fiber Mixing Procedure, and Curing Conditions on the Mechanical Performance of HTPP-ECC," *Composites Part B: Engineering*, V. 60, 2014, pp. 359-370. doi: 10.1016/j.compositesb.2013.12.076

100. Afefy, H. M. E. D., and Mahmoud, M. H., "Structural Performance of RC Slabs Provided by Pre-Cast ECC Strips in Tension Cover Zone," *Construction and Building Materials*, V. 65, No. 29, 2014, pp. 103-113. doi: 10.1016/j.conbuildmat.2014.04.096

101. Maalej, M.; Quek, S. T.; and Zhang, J., "Behavior of Hybrid-Fiber Engineered Cementitious Composites Subjected to Dynamic Tensile Loading and Projectile Impact," *Journal of Materials in Civil Engineering*, ASCE, V. 17, No. 2, 2005, pp. 143-152. doi: 10.1061/(ASCE)0899-1561(2005)17:2(143)

102. Fischer, G.; Fukuyama, H.; and Li, V. C., "Effect of Matrix Ductility on the Performance of Reinforced ECC Column Members under Reversed Cyclic Loading Conditions," *Proceedings of the DFRCC International Workshop*, Takayama, Japan, 2002, pp. 269-278.

103. Yu, K.; Wang, Y.; Yu, J.; and Xu, S., "A Strain-Hardening Cementitious Composites with the Tensile Capacity Up to 8%," *Construction and Building Materials*, V. 137, 2017, pp. 410-419. doi: 10.1016/j.conbuildmat.2017.01.060

104. Singh, S. B.; Munjal, P.; and Thammishetti, N., "Strengthening of Masonry Beam with ECC as Bed Joint," *Journal of Engineering Science and Technology*, V. 10, 2015, pp. 29-39.

105. Qiu, J., and Yang, E. H., "Micromechanics-Based Investigation of Fatigue Deterioration of Engineered Cementitious Composite (ECC)," *Cement and Concrete Research*, V. 95, 2017, pp. 65-74. doi: 10.1016/j.cemconres.2017.02.029

106. Radhakrishnan, N.; Chellapandian, M.; and Singh, S. B., "Engineering Characteristics, Techno-Economic Feasibility and Life Cycle Assessment of Bio-Fiber Based Green Engineered Cementitious Composites," *Journal of Building Engineering*, V. 96, 2024, p. 110521. doi: 10.1016/j.jobe.2024.110521

107. Tian, J.; Zhu, W.; Wu, X.; Yuan, J.; Zheng, Y.; Wang, W.-W.; Wei, L.; Zhang, W.; and Zheng, M., "Investigation on Shear Performance and Prediction Model of CFRP-ECC-Concrete Composite Interface Suffered from Anodic Polarization and Environmental Degradation," *Developments in the Built Environment*, V. 18, 2024, p. 100422. doi: 10.1016/j.dibe.2024.100422

108. Ge, Z.; Tawfek, A. M.; Zhang, H.; Yang, Y.; Yuan, H.; Sun, R.; and Wang, Z., "Influence of an Extrusion Approach on the Fiber Orientation and Mechanical Properties of Engineered Cementitious Composite," *Construction and Building Materials*, V. 306, 2021, p. 124876. doi: 10.1016/j.conbuildmat.2021.124876

109. Wang, Z.; Wang, P.; and Zhu, F., "Synergy Effect of Hybrid Steel-Polyvinyl Alcohol Fibers in Engineered Cementitious Composites: Fiber Distribution and Mechanical Performance," *Journal of Building Engineering*, V. 62, 2022, p. 105348. doi: 10.1016/j.jobe.2022.105348

110. Lu, C., and Leung, C. K. Y., "Theoretical Evaluation of Fiber Orientation and its Effects on Mechanical Properties in Engineered Cementitious Composites (ECC) with Various Thicknesses," *Cement and Concrete Research*, V. 95, 2017, pp. 240-246. doi: 10.1016/j.cemconres.2017.02.024

111. Pang, Z.; Lu, C.; Li, B.; and Wang, J., "A Multiscale Model for Quantifying Fiber Orientation Effects on the Tensile Properties of 3D Printed Engineered Cementitious Composites (3DP-ECC)," *Journal of Building Engineering*, V. 68, 2023, p. 106090. doi: 10.1016/j.jobe.2023.106090

112. Dong, B.; Liu, C.; Shumuye, E. D.; Zhang, Y.; Zhong, H.; and Fang, G., "Effect of Nano-Silica on Mechanical Properties and Microstructure of Engineered Geopolymer Composites," *Cement and Concrete Composites*, V. 156, 2025, p. 105849. doi: 10.1016/j.cemconcomp.2024.105849

113. Li, V. C.; Mishra, D. K.; Naaman, A. E.; Wight, J. K.; LaFave, J. M.; Wu, H. C.; and Inada, Y., "On the Shear Behavior of Engineered Cementitious Composites," *Advanced Cement Based Materials*, V. 1, No. 3, 1994, pp. 142-149. doi: 10.1016/1065-7355(94)90045-0

114. Li, V. C., and Wang, S., "Failure Mode and Structural Ductility of GFRP Reinforced Engineered Cementitious Composite Beams," *ACI Materials Journal*, V. 99, No. 1, Jan.-Feb. 2002, pp. 11-21.

115. Yuan, F.; Pan, J.; Dong, L.; and Leung, C. K. Y., "Mechanical Behaviors of Steel Reinforced ECC or ECC/Concrete Composite Beams under Reversed Cyclic Loading," *Journal of Materials in Civil Engineering*, ASCE V. 26, No. 8, 2014, p. 04014047. doi: 10.1061/(ASCE)MT.1943-5533.0000935

116. Zhu, H.; Zhang, D.; Wang, T.; McBain, M.; and Li, V. C., "Intrinsic Self-Stressing and Low Carbon Engineered Cementitious Composites (ECC) for Improved Sustainability," *Cement and Concrete Research*, V. 149, 2021, p. 106580. doi: 10.1016/j.cemconres.2021.106580

117. Zhang, Z.; Liu, S.; Yang, F.; Weng, Y.; and Qian, S., "Sustainable High Strength, High Ductility Engineered Cementitious Composites (ECC) with Substitution of Cement by Rice Husk Ash," *Journal of Cleaner Production*, V. 317, 2021, p. 128379. doi: 10.1016/j.jclepro.2021.128379

118. Larson, M. B., "Bridge Decks Going Jointless: Cementitious Composites Improve Durability of Link Slabs," *Construction and Technology Research Record*, V. 100, 2005, pp. 342-348.

119. Kim, Y. Y.; Fischer, G.; and Li, V. C., "Performance of Bridge Deck Link Slabs Designed with Ductile Engineered Cementitious Composites," *ACI Structural Journal*, V. 101, No. 6, Nov.-Dec. 2004, pp. 792-801.

120. Fischer, G., and Li, V. C., "Deformation Behavior of Fiber-Reinforced Polymer Reinforced Engineered Cementitious Composite (ECC) Flexural Members under Reversed Cyclic Loading Conditions," *ACI Structural Journal*, V. 100, No. 1, Jan.-Feb. 2003, pp. 25-34.

121. Kanda, T.; Watanabe, S.; and Li, V. C., "Application of Pseudo Strain Hardening Cementitious Composites to Shear Resistant Structural Elements," *Fracture Mechanics of Concrete Structures, Proceedings FRAMCOS-3*, AEDIFICATIO Publishers, Freiburg, Germany, 1998, pp. 1477-1490.

122. Krouma, A., and Syed, Z. I., "A Review on the Use of Engineered Cementitious Composite in Bridges," *Materials Science Forum*, V. 860, No. 1, 2016, pp. 125-134. doi: 10.4028/www.scientific.net/MSF.860.125

123. Lepech, M., and Li, V. C., "Sustainable Pavement Overlays Using Engineered Cementitious Composites," *International Journal of Pavement Research and Technology*, V. 3, No. 5, 2010, pp. 241-250.

124. Mishra, D. K.; Ranjan, P.; Sun, H.; Yu, J.; and Ng, P. L., "Applications of Drone Inspection and Use of Strain-Hardening Cementitious Composites (ECC/SHCC) in Lowering Carbon Footprint and Lifecycle Cost of Bridges," *Life-Cycle of Structures and Infrastructure Systems*, 2023, pp. 4029-4036.

125. Li, V. C., and Kanda, T., "INNOVATIONS FORUM: Engineered Cementitious Composites for Structural Applications," *Journal of Materials in Civil Engineering*, ASCE, V. 10, No. 2, 1998, pp. 66-69. doi: 10.1061/(ASCE)0899-1561(1998)10:2(66)

126. Singh, S. B., and Munjal, P., "Engineered Cementitious Composite and its Applications," *Materials Today: Proceedings*, V. 32, No. 4, 2020, pp. 797-802. doi: 10.1016/j.matpr.2020.03.743

127. Şahmaran, M., and Li, V. C., "Durability of Mechanically Loaded Engineered Cementitious Composites under Highly Alkaline Environments," *Cement and Concrete Composites*, V. 30, No. 2, 2008, pp. 72-81. doi: 10.1016/j.cemconcomp.2007.09.004

128. Shanmugasundaram, N., and Praveenkumar, S., "Mechanical Properties of Engineered Cementitious Composites (ECC) Incorporating Different Mineral Admixtures and Fibre: A Review," *Journal of Building Pathology and Rehabilitation*, V. 7, No. 1, 2022, p. 40. doi: 10.1007/s41024-022-00182-1

129. Li, V. C., "Large Volume, High-Performance Applications of Fibers in Civil Engineering," *Journal of Applied Polymer Science*, V. 83, No. 3, 2002, pp. 660-686. doi: 10.1002/app.2263

130. Arce, G.; Noorvand, H.; Hassan, M.; Rupnow, T.; and Hungria, R., "Cost-Effective ECC with Low Fiber Content for Pavement Application," *MATEC Web of Conferences*, V. 271, 2019, p. 07001.

131. Arce, G.; Rupnow, T.; and Hassan, M., "Evaluation of the Performance and Cost-Effectiveness of Engineered Cementitious Composites (ECC) Produced from Region 6 Local Materials," *Project No. 17CLSU05*, Transportation Consortium of South-Central States (Tran-SET), Louisiana State University, Baton Rouge, LA, 2018.

NOTES:

aci® in Your Classroom

Integrate aci® into your classroom!

To support future leaders, ACI has launched several initiatives to engage students in the Institute's activities and programs – select programs that may be of interest to Educators are:

- **Free student membership –** encourage students to sign up
- **Special student discounts on *ACI 318 Building Code Requirements for Structural Concrete*, *ACI 530 Building Code Requirements and Specification for Masonry Structure*, & *Formwork for Concrete* manual.**
- **Access to *Concrete International* –** free to all ACI student members
- **Access to *ACI Structural Journal* and *ACI Materials Journal* –** free to all ACI student members
- **Free sustainability resources –** free copies of Sustainable Concrete Guides provided to universities for use in the classroom
- **Student competitions –** participate in ACI's written and/or team-based competitions
- **Scholarships and fellowships –** students who win awards are provided up to $15,000 and may be offered internships and paid travel to attend ACI's conventions
- **ACI Award for University Student Activities –** receive local and international recognition for your University's participation in concrete-related activities
- **Free access to the *ACI Collection of Concrete Codes, Specifications, and Practices* –** in conjunction with ACI's chapters, students are provided free access to the online ACI Collection
- **ACI online recorded web sessions and continuing education programs –** online learning tools ideal for use as quizzes or in-class study material

https://www.concrete.org/educatorsandresearchers/aciinyourclassroom.aspx

NEW Symposium Publications from ACI

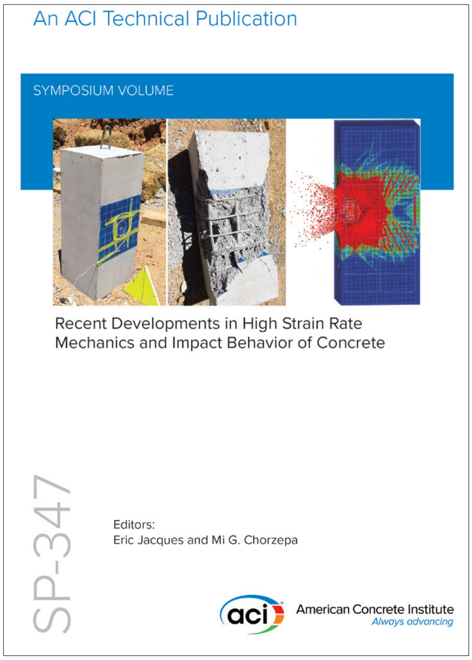

An ACI Technical Publication
SYMPOSIUM VOLUME
Recent Developments in High Strain Rate Mechanics and Impact Behavior of Concrete
SP-347
Editors:
Eric Jacques and Mi G. Chorzepa
aci American Concrete Institute
Always advancing

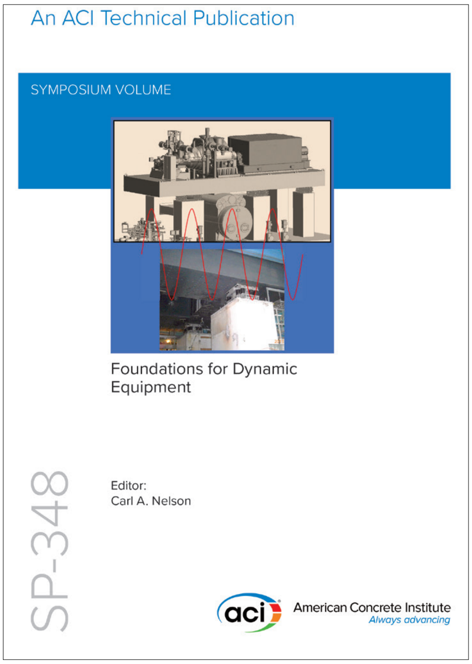

An ACI Technical Publication
SYMPOSIUM VOLUME
Foundations for Dynamic Equipment
SP-348
Editor:
Carl A. Nelson
aci American Concrete Institute
Always advancing

SP-347: Recent Developments in High Strain Rate Mechanics and Impact Behavior of Concrete

This Symposium Volume reports on the latest developments in the field of high-strain-rate mechanics and behavior of concrete subject to impact loads. This effort supports the mission of ACI Committee 370, Blast and Impact Load Effects, to develop and disseminate information on the design of concrete structures subjected to impact, as well as blast and other short-duration dynamic loads.

Available in PDF format: $69.50
(ACI members: $39.00) ($30.50 savings)

SP-348: Foundations for Dynamic Equipment

This special publication grew out of the Technical Session titled “Application of ACI 351-C Report on Dynamic Foundations,” held at the ACI Spring 2019 Convention in Québec City, Québec. Following this event, ACI Committee 351 decided to undertake a special publication with contributions from those session participants willing to develop their presentations into full-length papers. Three papers included in the current publication were contributed by these presenters and their coauthors, with six additional papers provided by others.

Available in PDF format: $69.50
(ACI members: $39.00) ($30.50 savings)

aci American Concrete Institute
+1.248.848.3700 • www.concrete.org

CALL FOR ACTION

ACI Invites You To...

Share your expertise

Do you have EXPERTISE in any of these areas?

- BIM
- Chimneys
- Circular Concrete Structures Prestressed by Wrapping with Wire and Strand
- Circular Concrete Structures Prestressed with Circumferential Tendons
- Concrete Properties
- Demolition
- Deterioration of Concrete in Hydraulic Structures
- Electronic Data Exchange
- Insulating Concrete Forms, Design, and Construction
- Nuclear Reactors, Concrete Components
- Pedestal Water Towers
- Pipe, Cast-in-Place
- Strengthening of Concrete Members
- Sustainability

Become a Reviewer for the ACI Journals

Then become a REVIEWER for the *ACI Structural Journal* or the *ACI Materials Journal*.

How to become a Reviewer:

1. Go to: **http://mc.manuscriptcentral.com/aci**;
2. Click on "Create Account" in the upper right-hand corner; and
3. Enter your E-mail/Name, Address, User ID and Password, and Area(s) of Expertise.

Update your Manuscript Central user account information

Did you know that the database for MANUSCRIPT CENTRAL, our manuscript submission program, is separate from the ACI membership database?

How to update your user account:

1. Go to **http://mc.manuscriptcentral.com/aci**;
2. Log in with your current User ID & Password; and
3. Update your E-mail/Name, Address, User ID and Password, and Area(s) of Expertise.

QUESTIONS?

E-mail any questions to Journals.Manuscripts@concrete.org.

aci®

American Concrete Institute

Always advancing

ACI Foundation Seeks Research Needs, Industry Problem Statements, and Ideas for Innovation

aci Foundation

Building the Future

The ACI Foundation is committed to impacting ACI and the concrete industry through concrete research and innovative initiatives.

We are seeking your ideas, research needs and problem statements that advance the knowledge and use of concrete materials, structures, and construction, as well as new technologies and innovations that provide solutions to industry issues.

The ACI Foundation will evaluate, and prioritize submissions based on impact, relevancy, and urgency. There are a variety of ways the ACI Foundation can provide support, such as hosting stakeholder meetings, funding a road map, business plan, document development, or standard research.

We are interested in both small discreet needs or large-scale interdisciplinary projects and visionary topics. We value collaboration and strategic partnerships with ACI committees and industry stakeholders outside of the ACI community to fully leverage the ACI Foundation's resources.

Visit **acifoundation.org/research/solicitations** for additional information, the submission form, and detailed instructions

ACI
MATERIALS
JOURNAL

aci®

American Concrete Institute